Exploring the Effect of a Potential Barrier on the Molecular Rotation-Vibration Structure

by

Jun Jiang

B.S., Dickinson College (2012)

Submitted to the Department of Chemistry
in partial fulfillment of the requirements for the degree of

Doctor of Philosophy

at the

MASSACHUSETTS INSTITUTE OF TECHNOLOGY

September 2017

Signature redacted
Author ....
Department of Chemistry
August 11, 2017

Signature redacted
Certified by ....
Robert W. Field
Haslam and Dewey Professor of Chemistry
Thesis Supervisor

Signature redacted
Accepted by ....
Robert W. Field
Chairman, Departmental Committee on Graduate Students

This doctoral thesis has been examined by a Committee of the
Department of Chemistry as follows:

Signature redacted

Professor Troy Van Voorhis.......
Chairman, Thesis Committee
Haslam and Dewey Professor of Chemistry

Signature redacted

Professor Sylvia T. Ceyer.........
Member, Thesis Committee
John C Sheehan Professor

Signature redacted

Professor Robert W. Field..............
Thesis Supervisor
Haslam and Dewey Professor of Chemistry

Exploring the Effect of a Potential Barrier on the Molecular Rotation-Vibration Structure

by

Jun Jiang

Submitted to the Department of Chemistry
on August 11, 2017, in partial fulfillment of the
requirements for the degree of
Doctor of Philosophy

Abstract

The goal of this thesis is to explore the effect of a potential barrier on the rotation-vibration structure of the sulfur dioxide (SO_2) $\tilde{C}$ state and the acetylene (HCCH) $\tilde{A}$ state. The minimum-energy geometry of both electronically excited states is qualitatively different from their respective electronic ground state geometry. The SO_2 $\tilde{C}$ state exhibits a barrier ($\sim$100 cm^{-1}) at the C_{2v} geometry along the antisymmetric-stretching direction, separating two equivalent minimum-energy configurations with C_s geometry. The HCCH $\tilde{A}$-state potential energy surface (PES) supports both *trans*- and *cis*-bent conformers (but not a linear configuration). The *trans*- and *cis*-conformer-wells are separated by a barrier of $\sim$5000 cm^{-1} (above the *trans*-bent minimum energy). For both the SO_2 $\tilde{C}$ state and the HCCH $\tilde{A}$ state, the presence of a potential barrier greatly complicates the rotation-vibration structure of the molecule. Interpretation of these barrier-related spectroscopic patterns requires both new experimental observations and new analysis tools, both of which are discussed in this thesis.

For the SO_2 $\tilde{C}$ state, an IR-UV double-resonance excitation scheme enables direct observations of levels with odd quanta in the antisymmetric-stretching vibrational mode (ν_3). A new anharmonic force field is derived for the SO_2 $\tilde{C}$ state, which allows accurate determination of the shape of the barrier on the $\tilde{C}$-state PES. In addition, we develop tools, based on perturbation theory, the polyad model, and semiclassical analysis, to interpret the effect of the barrier on the $\tilde{C}$-state rotation-vibration structure.

The *cis-trans* isomerization in the HCCH $\tilde{A}$-state has been the focus of the Field group acetylene project for the past ten years. However, the diminishing detection efficiency of the laser-induced fluorescence (LIF) scheme (due to acetylene predissociation), combined with a partial breakdown of the polyad fit model, has made it increasingly difficult to understand the HCCH $\tilde{A}$-state level-structure near the top of the *cis-trans* isomerization barrier. Two new sensitive and convenient action schemes are reported in this thesis to detect predissociated $\tilde{A}$-state rovibrational levels. The first scheme is based on detection of H-atoms by two-photon laser-induced ($3d \leftarrow 1s$)

fluorescence ($3d \rightarrow 2p$), and the second scheme is based on fluorescence detection of C_2 and C_2H fragments, photolyzed via resonance with the probed $\tilde{\mathrm{A}}$-state levels. The photodissciation processes that give rise to the strong photofragment fluorescence signals are also studied in this thesis.

Thesis Supervisor: Robert W. Field
Title: Haslam and Dewey Professor of Chemistry

Acknowledgments

First, I would like to thank my thesis advisor, Bob Field, for all his encouragement and support throughout my time at MIT. Bob trusts me and gives me tremendous amount of freedom to develop my own instinct in molecular spectroscopy. He encourages me to look beyond molecular constants and to seek cause-and-effect mechanism to explain patterns and anomalies in the spectra. In the past five years, I have been trained to become an independent scientist. I am very proud to be Bob's student.

I have also benefited tremendously from interactions with a number of people both inside and outside the lab. Josh Baraban suggested two excellent start-up projects on S_1 acetylene (included in Chapter 2 and Chapter 9 of this thesis) to me when I first joined the group. The success of these two projects gave me a lot of confidence. The H-atom fluorescence detection (Chapter 3) was also based on his idea. I have also benefited greatly from conversations with Byran Changala, the best undergraduate student the Field group has ever had, as well as email correspondence with Professor Anthony Merer (UBC, IAMS). During my first two years, I also worked closely with Peter Richter in the lab. Near the end of my second year, I started to collaborate substantially with Barratt Park on the SO_2 $\tilde{C}$ state. It was a great success, and I am very proud of what we were able to accomplish. I am also grateful to Barratt's detailed and extremely helpful mark-ups to my SO_2 force-field paper.

I had the pleasure of working closely with two excellent undergraduate students: Catherine Saladrigas and Angelar Muthike. Catherine joined the group when she was a sophomore at MIT and stayed in the group for the rest of her time at MIT. Catherine is smart and hard-working, and I had a lot of fun working with her. Despite her somewhat "scandalous" act of joining the Rydberg project at the end, I wish her best of luck at UC Berkeley. (The history seems to have repeated itself. Clare Keenan, a new undergraduate student of the acetylene project, also recently switched to the Rydberg project.) Angelar Muthike, who was a student at Spelman College, spent a summer at MIT. Even during this short period of time, we successfully set up the dispersed fluorescence experiment and identified the photofragments resulting from multi-photon dissociation of acetylene. The productivity in that summer owes much to the many hours that Angelar spent after 6 pm in the lab (when I already left for home). Angelar will attend graduate school at the University of Michigan in Ann Arbor in the fall of 2017.

I also worked closely with Trevor Erickson on the development of the acetylene photofragment fluorescence detection scheme. I enjoyed working with Trevor. When I had a question or idea, he was the first one who I turned to. Carrie Womack and I, in collaboration with Matt Nava from Kit Cummins' group at MIT, worked together on the LIF detection of HCP. Alex Hull and I also worked together briefly on the chirp-pulse mm-wave setup. I have also interacted with Clare who had helped on the acetylene photofragment detection work. Near the end of my PhD, I had a fruitful collaboration with Professor Zhenhui Du, a visiting scholar from Tianjin University, using the frequency-modulation spectroscopy. Greg Hall, from Brookhaven National Laboratory, lent us a number of FM components and provided advice on the FM setup.

I also had the fortune of being labmates with a number of excellent scientists on the Rdyberg projects. Yan Zhou is knowledgeble of essentially every aspects of physics and many other things in the lab. David Grimes, who sat at the desk right next to me for three years (before he eventually got bored of me and switched seat to the other side of the office), gave me a lot of useful information on the operation of this lab. Tim Barnum is not only a very good experimentalist, but also knows a lot of things about diatomic molecules (I frequently asked him stupid and naive questions about diatomics). He is also an expert on labview (or really any computer/electronic-related things). The success of the dispersed fluorescence experiment owes much to Tim's generous assistance in setting up the thirty-year-old monochromator. I look forward to working with him in the next year or so. I also enjoyed interactions with Ethan Klein, who was a major player in that memorable afternoon in Ohio state in the summer of 2013 ("No more Mr. Nice Bob", "Gravitational waves", and "the Mexican restaurant spicy food challenge", just to name a few). Steve Coy and John Muenter are both extremely knowledgeable in the field of molecular spectroscopy and

I have learned a great deal from discussions with them.

I have also interacted with a number of former Field group members and collaborators: Tony Colombo, Kirill Prozument, Alice Green, Julia Berk, Celina Bermudez, Georg Melau, Wilton Virgo, and Adam Steeves, who were all willing to provide input and assistance on many issues despite our relatively brief encounters. I am also thankful to Peter Giunta, who is an extremely competent administrator.

I would also like to thank my parents, whose constant support and love keep me going forward.

My final thanks goes to Yujia Zhou. Yujia and I were married during my third year as a graudate student. As Yujia told me (jokingly?) the other day (although she denies it now), I would live a rather boring life if I had not met her. Well, she is certainly not wrong. Being with her has added a lot of color to my life. Rather soon (in two weeks or so), Anya will be born. I am really looking forward to raising our kid together, who will grow up with the best possible sister, Dao-Gao, our two-year-old golden retriever.

Contents

List of Figures

List of Tables

Chapter 1

Introduction

My work in the Field group mainly involves two molecular electronic states, the SO_2 $\tilde{C}$ state (with origin at v_{00}=42573.45 cm^{-1}) and the HCCH $\tilde{A}$ state (with origin at v_{00}=42197.57 cm^{-1}). These two electronically-excited states share a common feature in that the minimum-energy geometry of both states is qualitatively different from their respective electronic ground state geometry. The electronic ground state of acetylene (S_0, $\tilde{X}^1\Sigma_g^+$) is a linear closed-shell molecule, containing a triple-bond between the two carbon atoms. It was first established over 60 years ago, by Ingold and King [75] and Innes [76], that acetylene changes its point-group on electronic excitation and becomes *trans*-bent in its first singlet excited state (S_1, $\tilde{A}^1A_u$). In addition, the S_1 potential energy surface (PES) supports a *cis*-bent conformer ($\tilde{A}^1A_2$), which was only recently observed by our group [12, 105]. The S_1 *cis*- and *trans*-conformer-wells are separated by a barrier of ~5000 cm^{-1} (above the *trans*-bent minimum energy) [10, 11, 13].[1] Similarly, the electronic ground state of sulfur dioxide ($\tilde{X}^1A_1$) is well-known to be of C_{2v} geometry. Pioneering work by Hoy and Brand in the 1970s [22, 70], based on earlier analysis by Coon and co-workers [36, 80], established the presence of a double-well structure (with a barrier of ~100 cm^{-1}) in

---

[1] The S_1 PES also supports a vinylidene conformer, which is calculated to be a global minimum on the S_1 PES. However, since the S_1(vinylidene, $^1A_2$)$\leftarrow$$S_0$ transition is not one-photon-allowed, and the barrier separating the S_1 *trans*- (which is optically-accessible) and vinylidene-conformer wells is high (~2 eV) [150], the S_1 vinylidene conformer is unlikely to play any role in the spectral region of current interest (~5000 cm^{-1} above the zero-point level of the S_1 *trans*-conformer).

the anti-symmetric stretching coordinate (q_3) of the $\tilde{\mathrm{C}}$-state ($^1B_2$ in C_{2v}) PES. The minimum-energy geometry of the SO_2 $\tilde{\mathrm{C}}$ state has unequal S-O bond lengths.

For both the SO_2 $\tilde{\mathrm{C}}$ state and the HCCH $\tilde{\mathrm{A}}$ state, the presence of a potential barrier greatly complicates the rotation-vibration structure of the molecule. Interpretation of these barrier-related spectroscopic patterns requires both new experimental observations (using both conventional and novel detection schemes) and new analysis tools, both of which are discussed in this thesis. A complete understanding of these patterns allows us to solve the ultimate inverse problem in spectroscopy: how are the dynamics of the molecule encoded in its spectra?

1.1 Some General Remarks

One great lesson that I learned from reading these early spectroscopic work on the SO_2 $\tilde{\mathrm{C}}$ state and the HCCH $\tilde{\mathrm{A}}$ state is that a good spectroscopist should always look for a model that fits, not just one, but *all* of the available observations. Such a model is able to reliably predict molecular properties that are not directly observable in the experiments. For example, in the work of Brand and Hoy [22, 70], even though SO_2 $\tilde{\mathrm{C}}$-state levels with odd quanta in ν_3 were not directly observed (discussed in Section 1.2), the ν_3 fundamental frequency was estimated based on the effective value of the Coriolis-perturbed C rotational constant of the (0,0,2) level. The estimated value of the ν_3 fundamental frequency is unusually low (213 cm^{-1}), but is consistent with *all* other anomalies of the $\tilde{\mathrm{C}}$ state that were known at the time, such as the large isotope shift and inertial defect of the zero-point level. Given that the predicted (0,0,1) level lies less than half-way in energy between (0,0,2) (561 cm^{-1}) and (0,0,0) (0 cm^{-1}), the antisymmetric stretching motion must involve a double-minimum potential. As it turns out, the estimated ν_3 fundamental frequency by Brand and Hoy is remarkably close to our observation (212.576 cm^{-1}), measured directly using an IR-UV double-resonance excitation scheme. (A bit of luck was perhaps involved in the remarkable agreement between the estimated and measured $\tilde{\mathrm{C}}$-state ν_3 fundamental frequency, as discussed in Ref [131]).

Now, with advances in quantum chemical calculations, theoreticians are able to obtain increasingly accurate *ab initio* PES of molecules. Rovibrational energies and wavefunctions can be calculated from the PES. For small molecules, such as SO_2 and HCCH, it is possible to derive an empirical PES (or an effective Hamiltonian), based on a fit to experimental data, which is even more accurate than the *ab initio* PES. For the SO_2 $\tilde{C}$ state, the discrepancies in vibrational level-positions (<3000 cm^{-1} above the $\tilde{C}$-state zero-point level) between the experimental data and the empirical fit result are <1 cm^{-1}; in comparison, the discrepancies are typically <20 cm^{-1} between the *ab initio* values and the experiment. Guided by these results (from either *ab initio* or empirical calculations), one might argue that spectral assignments, at least the vibrational assignments, should become straightforward, if one simply counted the number of nodes in the vibrational wavefunctions. However, as I will demonstrate in Chapter 8 (where an accurate empirical PES of the SO_2 $\tilde{C}$ state is derived), node-counting is not a reliable way to assign vibrational levels of even a triatomic molecule, especially when there are significant interactions among all internal degrees of freedom of the molecule. When strong mode-mixing is present, it is difficult to visualize a wavefunction that has more than two degrees of freedom (which is the case for all molecules that are not diatomics) without being biased by arbitrarily-selected slices of the wavefunction.

An eigenvector-based approach, which is used in our studies of the SO_2 $\tilde{C}$ and HCCH $\tilde{A}$ states, avoids such bias, although there is still a question of optimal choice of basis used in the analysis. With a good set of basis states (which are molecule-dependent), features in the spectra can usually be explained by simple first and/or second-order non-degenerate perturbation theory. When non-degenerate perturbation theory starts to fail, it is often a sign that a new set of basis states is needed, in order to explain the qualitatively new features emergent in the spectra, such as *cis-trans* isomerization in the HCCH $\tilde{A}$ state as opposed to localized motion in the *trans*-well. The goodness of a basis is certainly subject to interpretation, but it is ultimately judged by its utility in enabling spectroscopists to understand the observed level-patterns and possibly to make predictions about molecular properties. When a good basis is found and constructed (discussed in Chapter 8), secure vibrational assignments (or sometimes leading-character eigenvector compositions) can be made, and these are consistent with *all* of the spectroscopic properties of the level, such as its rotational constants and intensity patterns in the electronic spectrum. I must emphasize that the purpose of level-assignment is that one can directly infer from the assignment properties of the level, without inspecting the wavefunction (which is subject to interpretation). Level-assignment should *not* be reduced to a list of ill-defined quantum numbers. Finding a good basis for the problem is what I consider to be one of the most crucial parts of understanding the molecular structure and dynamics.

In Section 1.2, I provide a brief overview of the spectroscopy of the SO_2 $\tilde{C}$ state, focusing on the motivation of this work. An overview of the spectroscopy of the HCCH $\tilde{A}$ state is provided separately in Chapter 2, where I incorporate into the discussion some experimental results obtained during my second year.

1.2 The SO_2 $\tilde{C}$ State

The SO_2 $\tilde{C}$ state exhibits a barrier at the C_{2v} geometry along q_3, separating two equivalent minimum-energy configurations with C_s geometry. The barrier at C_{2v} is small ($\sim$100 cm^{-1}) and is an even function of q_3, so there are no terms in the vibrational Hamiltonian that break the vibrational symmetries in the representations of C_{2v}. Therefore, the low-lying levels of the $\tilde{C}$ state conserve a_1 (even quanta of ν_3) and b_2 (odd quanta of ν_3) vibrational symmetries, and the vibrational selection rule in the $\tilde{C}-\tilde{X}$ spectrum is such that the vibrational symmetry remains unchanged. For convenience, the molecule is treated in C_{2v} symmetry throughout this work.

All previous analyses of the SO_2 $\tilde{C}$ state were based on spectra recorded with single-resonance UV excitation, which allowed direct observations of $\tilde{C}$-state levels exclusively with even quanta in ν_3. Transitions into $\tilde{C}$-state levels with odd quanta in ν_3 are forbidden from the ground vibrational level of the $\tilde{X}$ state. As mentioned earlier, the identification of a double-well structure on the $\tilde{C}$-state PES was based on indirect

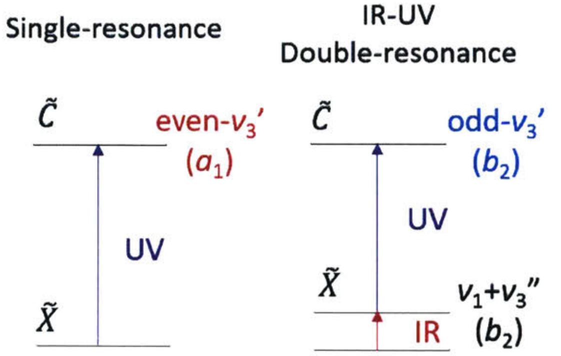

Figure 1-1: Level diagrams of UV single resonance transition and IR-UV double resonance transition to the SO_2 $\tilde{C}$ state.

(but convincing) spectroscopic evidence. However, without direct observations of the odd-quanta levels, the shape of the barrier (i.e. its height and width) separating the two C_s geometry wells could not be determined accurately. Using an IR-UV double-resonance excitation scheme (see Fig. 1-1), where the IR photon is used to populate the $\nu_1 + \nu_3''$ vibrational level of the $\tilde{X}$ state, we made the first direct observations of the eight lowest-energy b_2 symmetry vibrational levels of the $\tilde{C}$ state [131]. Combining the previously-observed a_1 levels and the newly-obtained b_2 levels, we observe the characteristic staggered energy-level pattern between even- and odd-ν_3 levels due to the presence of a double well, e.g. in all ν_3 progressions shown in Fig. 1-2, the $(0,\nu_2,1)$ level lies lower in energy than the average of $(0,\nu_2,0)$ and $(0,\nu_2,2)$ levels. In addition, we are able to study directly and systematically the strong Coriolis interactions between a_1 and b_2 levels, which were known to exist in the $\tilde{C}$ state, but could not be deperturbed properly in all previous work on the SO_2 $\tilde{C}$ state [22, 62, 70, 182], due to lack of direct observation of b_2 levels. The IR-UV work is included in Dr. Barratt Park's Ph.D. thesis [128], and is not repeated in this thesis.

Our direct high resolution measurements of both a_1 and b_2 symmetry vibrational levels led us to derive a new anharmonic force field for the SO_2 $\tilde{C}$ state, with the initial goal of accurately determing the shape of the barrier at the C_{2v} geometry. As we show here, the presence of the double-well structure makes the SO_2 $\tilde{C}$ state special. The ν_3 frequency is lowered due to the double-well. Consequently, there is a strong 1:2

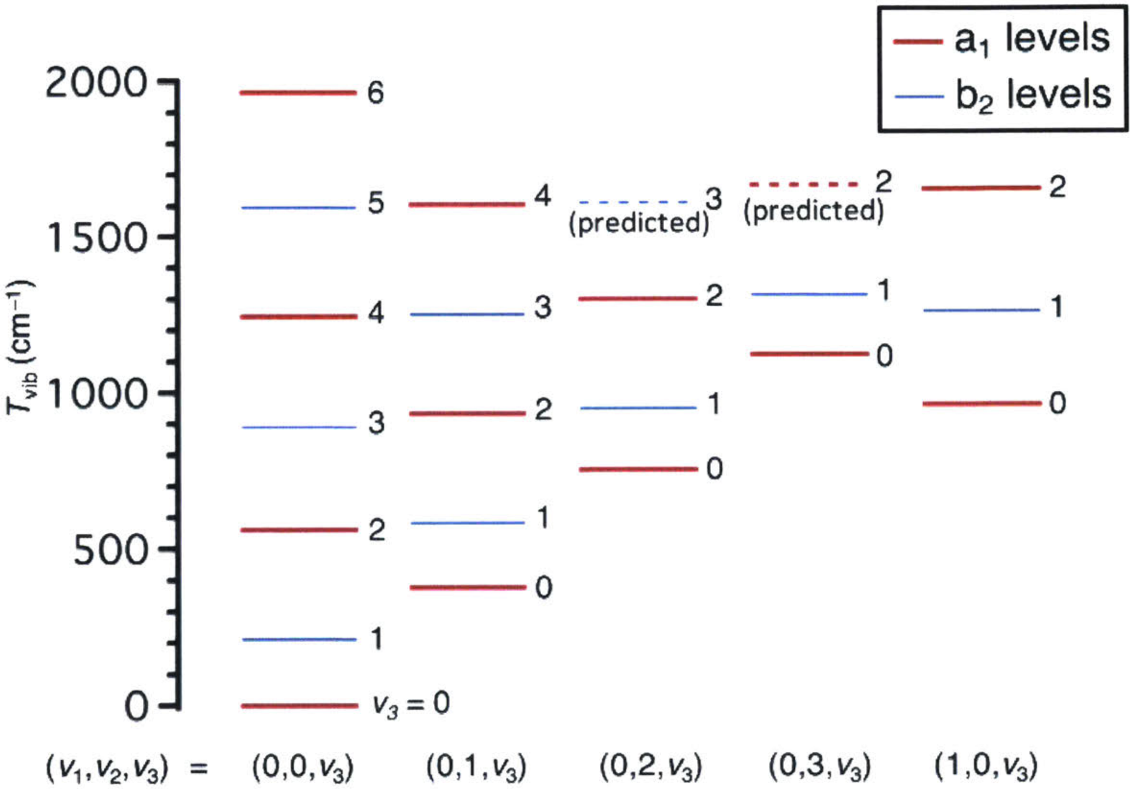

Figure 1-2: The low-lying vibrational level structure of the $\tilde{\mathrm{C}}$ state of SO_2 is shown (adapted from Ref [130]), arranged as progressions in ν_3. The b_2 levels were observed by our IR-UV double-resonance experiments [131].

Fermi interaction between the ν_1 (symmetric-stretch) and ν_3 (antisymmetric-stretch) vibrational modes (i.e. $\nu_1 \approx 2\nu_3$). The two stretching modes typically have similar frequencies (in all symmetric triatomic molecules) and interact via 2:2 Darling-Dennison interaction instead of 1:2 Fermi interaction. As a result of a depressed ν_3 frequency, the $\tilde{\mathrm{C}}$-state ν_2 (bend) and ν_3 modes (the former is typically much lower in frequency than the latter in a symmetric triatomic) become coupled strongly via c-axis Coriolis interaction. The matrix elements of the 2:2 Darling-Dennison interaction between ν_2 and ν_3 are smaller than that of the 1:2 Fermi interaction between ν_1 and ν_3, but are by no means negligible in the $\tilde{\mathrm{C}}$ state. *All* three vibrational modes *and* the rotation interact strongly as a result of the double-well structure on the $\tilde{\mathrm{C}}$-state PES. Misassignments of the $\tilde{\mathrm{C}}$-state rotation-vibration levels are quite common in the literature, because at least one of these interactions was either neglected or treated incorrectly. To understand the complicated rotation-vibration structure of the $\tilde{\mathrm{C}}$ state, we develop tools, based on perturbation theory, the polyad model, and semiclassical analysis (on a Fermi-resonance system), to explain the observed spectroscopic patterns in a way that is as quantitative as possible. Interestingly, using the tools that we develop, we identify a few interesting spectroscopic patterns (i.e. a zigzag trend in the rotational constants of levels in a vibrational progression) associated with the presence of the double-well, which were not initially obvious to us.

The newly-derived force field is able to quantitatively reproduce essentially all of the spectroscopic observations of the SO_2 $\tilde{\mathrm{C}}$ state, but it does not explain why the two S-O bond lengths are different. Mulliken [117] suggested that an unsymmetrical distortion of the S-O bond lengths minimizes the antibonding in the SO_2 $\tilde{\mathrm{C}}$ state, but Innes [77] argued that the asymmetry in the potential is likely the result of vibronic interaction of a ${}^1B_2$ state with a higher lying $2\,{}^1A_1$ state (the so-called pseudo Jahn-teller effect). Innes thought that the distortion of the $\tilde{\mathrm{C}}$-state PES (i.e. having a minimum-energy configuration with C_s geometry, instead of a C_{2v} as in the SO_2 $\tilde{\mathrm{X}}$ state) is too large to be accounted for by the electronic factor alone. We believe that Innes' argument is the best explanation, because the vibronic coupling model is not only able to reproduce the observed staggered energy level pattern, but also predicts the presence of a seam of intersection between the ${}^1B_2$ and $2\,{}^1A_1$ surfaces at a large bend angle. These empirically-based conclusions agree with quantum chemical calculations [20, 83]. The vibronic coupling work is included in Dr. Barratt Park's Ph.D. thesis [128] (also reported in Ref [130]), and is not repeated in this thesis.

1.3 Thesis Outline

I have arranged my thesis chapters into two major parts. The first part (Chapters $2-6$) deals with experimental work and analysis on S_1 acetylene and its photodissociation process. A common theme for the second part of this thesis (Chapters $7-9$) is force-field determination, and how we use the derived force field in order to understand the details of the rotation-vibration structure of the molecule.

- In Chapter 2, I provide an overview of the ongoing spectroscopic characterizations of the acetylene S_1 state, focusing on the current remaining theoretical and experimetal challenges. Experimental results obtained during my second year in the Field group are incorporated into the discussion. Predissociation of S_1 acetylene, HCCH (S_1)→ C_2H ($\tilde{X}^2\Sigma^+$)+H(^2S), greatly reduces the detection efficiency of the laser-induced fluorescence (LIF) technique, which has been the most commonly used technique in the study of S_1 acetylene. Work in the remaining chapters of the first part of this thesis is motivated by attempts to increase the detection efficiency of the S_1 levels.

- In Chapter 3, I report two new sensitive and convenient action schemes to detect predissociated S_1 levels. The first scheme is based on detection of H-atom $3d \rightarrow 2p$ fluorescence (the H-atom $3d$ level is populated by a two-photon resonance transition at 205.14 nm), and the second scheme is based on fluorescence detection of C_2 and C_2H fragments, photolyzed via resonance with the probed S_1 levels.

- In Chapter 4, I discuss the identification of photofragments (which are identified as the C_2 $C^1\Pi_g$ and $d^3\Pi_g$ states, and electronically-excited C_2H with unknown assignment) used in the second detection scheme described in Chapter 3. The multi-photon UV dissociation mechanism is also proposed here.

- In Chapter 5, I introduce a method, based on a slight modification of conventional frequency-modulation (FM) spectroscopy, which allows one to determine, from the *phase* of the FM signal, the sign of the population difference in a two-level system (i.e. whether the system is inverted). This method is used in the work described in Chapter 6.

- As discussed in Chapter 4, the C_2 $C^1\Pi_g$ and $d^3\Pi_g$ states are generated from one-color (~220 nm), resonance-enhanced (S_1-S_0), multi-photon dissociation of acetylene. Populations in the C_2 $A^1\Pi_u$ and $X^1\Sigma_g^+$ states, however, cannot be measured based on the technique used in Chapter 4. In Chapter 6, we determine the population difference between the C_2 A and X states, using the FM technique described in Chapter 5. We are interested in whether there is population inversion between the C_2 A and X states following the ~220 nm acetylene photolysis. The C_2 A state is known to be significantly more populated than the X state, following 193 nm ArF photolysis of acetylene [39, 148].

- In Chapter 7, I report a new harmonic force field for the S_1 acetylene *trans*-conformer. The acetylene S_1-S_0 transition probabilities calculated [127, 129, 132] based on the new S_1 harmonic force field are in better agreement with experiment, compared to transition probabilities calculated based on a previous S_1 harmonic force field [161].

- In Chapter 8, I derive an anharmonic force field of the SO_2 $\tilde{C}$ state from the experimental data. The motivation behind this work is described in Section 1.2. This force field is used to explain the peculiar features in the $\tilde{C}$-state rotation-vibration structure.

- In Chapter 9, I report a preliminary result of using a two-state interaction model to explain the rotation-vibration features of the C_2 $C^1\Pi_g$ state. This is still an ongoing project, and we are hoping to improve the fit model further to spectroscopic accuracy (i.e. <0.1 cm^{-1}) by incorporating new *ab initio* results (in collaboration with Hongzhou Ye from Professor Van Voorhis' group at MIT). The analysis of the C_2 $C^1\Pi_g$ state is a spin-off project from the acetylene photolysis work.

Chapter 2

An Overview of the Spectroscopy on the S_1 State of Acetylene

In this chapter, I provide an overview of the ongoing spectroscopic characterizations of the S_1 state of acetylene, focusing on the remaining theoretical and experimental challenges. Those challenges have motivated a large part of my thesis work. The experimental results presented in this chapter are based on IR-UV double-resonance (DR) laser-induced fluorescence (LIF) detection, carried out during my second year in the Field lab, working closely with Peter Richter. Catherine Saladrigas also assisted with the experiments. Due to the introductory nature of this chapter, experimental details, which have been described in Chapter I of Dr. Joshua Baraban's thesis [9], are not provided here.

2.1 Spectroscopic Analysis of the S_1 State of Acetylene

The electronic ground state of acetylene (S_0 $\tilde{X}^1\Sigma_g^+$) is well-known to be a linear closed-shell molecule, containing a triple-bond between the two carbon atoms. When one of the π-electrons is excited to the anti-bonding π^* orbital, the resulting ${}^1\Sigma_u^+$ configuration state becomes unstable with respect to the *trans* and *cis* geometries [9,

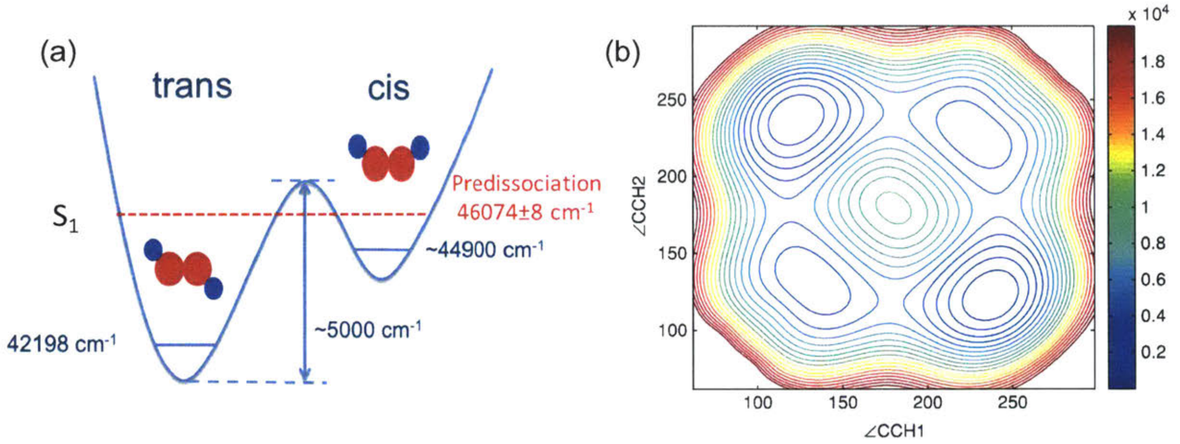

Figure 2-1: The S_1 potential energy surface. (a) A schematic drawing of a 1D slice of the PES. Numbers in the figure are based on the latest spectroscopic information [9–14, 75, 76, 105, 112, 174]. (b) The *ab initio* 2D in-plane bending potential, with R_{CC} and R_{CH} at the *trans*-bent equilibrium values. Reproduced from Ref [10]. The *cis*-bent minima are located in the lower left and upper right, and the trans minima are in the upper left and lower right. The energy scale is in cm^{-1}, and the contour spacing is 10^3 cm^{-1}.

75, 76, 82, 92]. The presence of the *trans*-bent conformer on the potential energy surface (PES) of the first singlet excited state of acetylene (S_1) was estabilished in groundbreaking works of Ingold and King [75], and Innes [76]. The most prominent feature in the acetylene S_1-S_0 absorption spectrum is the long $\nu_3' \leftarrow 0$ Franck-Condon progression [75, 76, 127, 169, 170, 173, 174], due to large change in the *trans*-bending angle between the S_1 *trans*-conformer (122.8°) [78] and the linear S_0 state. The S_1-S_0 transition was identified as a *c*-type $\tilde{A}^1A_u - \tilde{X}^1\Sigma_g$ transition, with a corresponding $K_a' - l'' = \pm 1$ selection rule (for convenience, the subscript, a, in K_a' is dropped in the following discussion). Transitions from the S_0 state into S_1 *cis*-conformer levels, with $^1A_2$ electronic symmetry in the C_{2v} point group, are forbidden by the electric dipole selection rule. A cartoon 1D slice of the S_1 PES is given in Fig. 8-1a, where the numbers in the figure are based on the latest spectroscopic information [9–14, 75, 76, 105, 112, 174]. A physically more complete description of the S_1 PES is provided in Fig. 8-1b, which shows two equivalent *cis* and *trans* wells on the 2D in-plane bending potential energy surface (reproduced from Ref [10]).

Detailed analyses by various groups [12, 104, 106, 107, 111, 154, 155, 160, 168–

170, 174] led to essentially complete vibrational and rotational assignments of S_1 *trans*-conformer levels up to 4500 cm^{-1} above the S_1 *trans* zero-point level (42198 cm^{-1}). Given that the *cis-trans* isomerization barrier is ~5000 cm^{-1} above the *trans* minimum energy [10, 11, 13], the possibility of *cis-trans* tunneling arises in the >4000 cm^{-1} energy region (above the *trans* zero-point level). Recent work [12, 105], led by Professor Anthony Merer, resulted in the discovery of several S_1 *cis*-conformer levels (which obtain their intensity by mixing with nearby *trans* levels) in this energy region. According to *ab initio* calculations [10] and modeling of experimental data [11], the minimum energy *cis-trans* isomerization pathway (via a half-linear transition-state) involves a CC-H local bending motion, which is a combination of the Q_3 and Q_6 normal coordinates for both conformers (see Fig. 2-2 for illustrations of the normal-mode motions). Combination levels with excitation in ν_3 and ν_6 are barrier-proximal, meaning that those levels have considerable amplitude directed toward the *cis-trans* isomerization transition state. The energies of the barrier-proximal states are strongly affected by the extremely anharmonic isomerization path.

Fundamental frequencies of normal modes of S_1 *trans*- and *cis*-conformers (and those of S_0 acetylene) are included in Fig. 2-2 for reference. For the S_1 *trans*-conformer, one-photon excitation from the S_0 ground vibrational level can only reach S_1 levels with *gerade* vibrational symmetry. To reach S_1 levels with *ungerade* vibrational symmetry, IR-UV DR excitation, via the S_0 ν_3'', $\nu_3 + \nu_4''$, or $\nu_1 + \nu_5''$ vibrational states, is needed.

2.1.1 The Polyad Model

An essential tool in the systematic analysis of the S_1 acetylene levels is a polyad fit model, based on an effective Hamiltonian for the *trans*-conformer [107, 154]. A brief discussion of the polyad model is provided in this section. Weak bands terminating in levels which cannot be fitted in the *trans*-manifold effective Hamiltonian are assigned to the S_1 *cis*-state [12, 105]. The assignments of these observed *cis* interloper levels have been further supported based on ^{13}C isotope shifts, upper state lifetimes, and the rotational structure of these bands [105]. Results from high-level *ab initio*

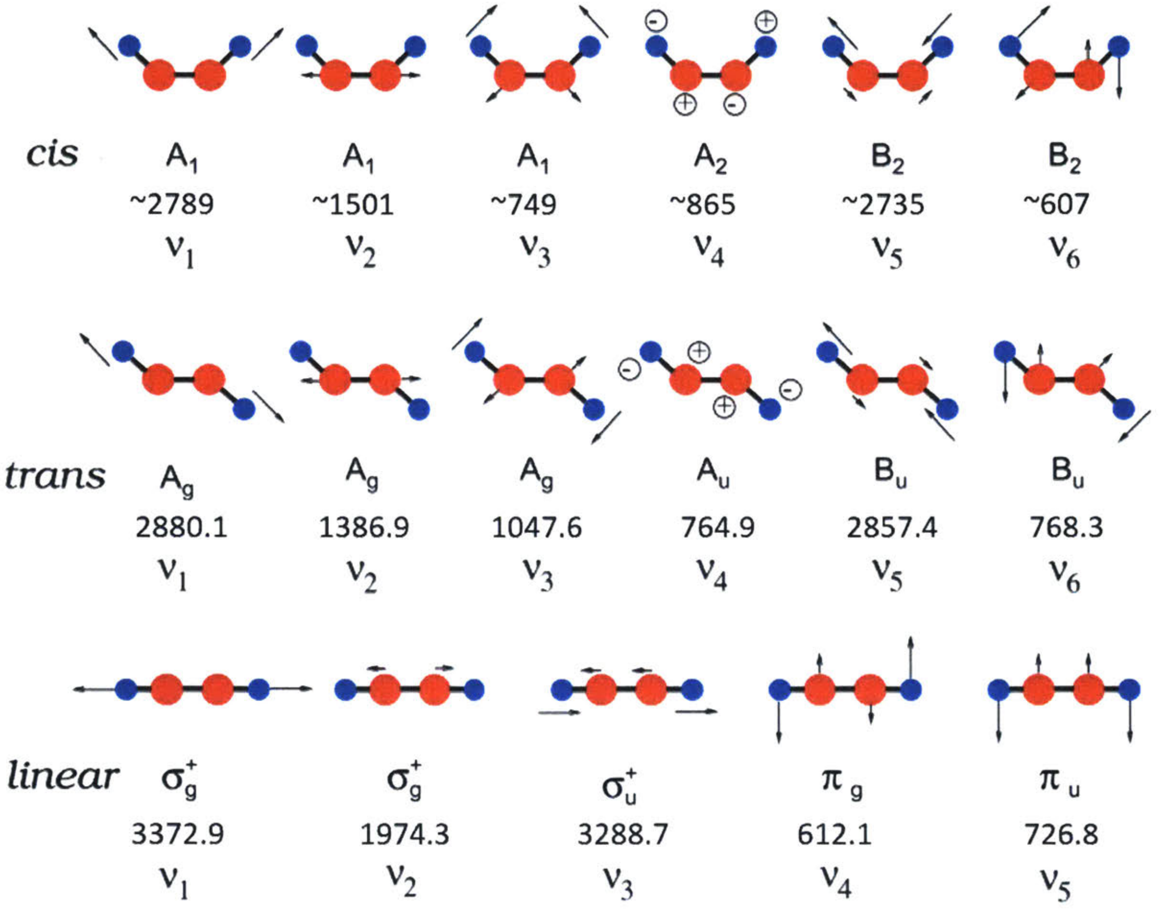

Figure 2-2: Normal modes of the S_1 *cis*-conformer (C_{2v}), S_1 *trans*-conformer (C_{2h}), and S_0 linear acetylene ($D_{\infty h}$). Numbers (in units of cm^{-1}) under the point-group symmetry labels of each normal-mode motion are the fundamental frequency of the corresponding normal mode. For S_1 *trans*- and S_0 linear acetylene, the experimental fundamental frequencies are used. For the S_1 *cis*-conformer, the listed fundamental frequencies are based on *ab initio* calculations in Ref [14]. For the ν_4 and ν_6 fundamental frequencies of the *cis*-conformer, empirical corrections have been applied to the calculated values (see Table 3 of Ref [14]).

calculations [14, 30, 32] are also crucial to confirm the *cis* assignments.

As shown in Fig. 2-2, for the S_1 *trans*-conformer, the torsional (ν_4, A_u) and *cis*-bend (ν_6, B_u) vibrational frequencies are nearly degenerate. Overtones and combination levels of those two bending vibrations interact strongly by Darling-Dennison and Coriolis (a and b axis) interactions. As a result, zero-order vibrational states with the same value of $v_4 + v_6$ interact strongly, and form polyads, denoted by B^{v4+v6}, where B means "bending". While the g/u vibrational symmetry is preserved under Coriolis interactions, the distinction between A and B irreducible representation is lost for the vibrational symmetries of the *trans*-conformer. The S_1 *trans* rotational structure, despite being highly irregular, can be effectively modeled by the polyad. An essential feature of polyads is that interaction matrix elements determined from relatively simple low-energy polyads conform to known vibrational quantum number scalings and selection rules for higher-lying polyads. Such patterns have made it possible to accurately predict (typically within a few cm^{-1} from the predictions) the energies of a significant portion of the unobserved *trans*-conformer levels below 46700 cm^{-1}, which can now be securely assigned.

Within the polyad model, addition of the *trans*-bending vibrational mode, ν_3, to the bending polyad (i.e. forming the $3^m B^n$ polyad) should not significantly alter the polyad structure (i.e. the predictive power of the polyad fit model should still be good). However, even in the region >500 cm^{-1} below the top of *cis-trans* isomerization barrier (~47200 cm^{-1}), there are signs of failure of the *trans*-conformer effective Hamiltonian in modeling the $3^m B^n$ polyad structure, due to *cis-trans* isomerization [12, 154]. For example, the structure of the $3^2 B^3$ polyad (located in the 46400 cm^{-1} region), which contains barrier-proximal members such as $3^2 6^3$, is not as well predicted as other polyads in the same energy region, e.g. B^5 which does not contain barrier-proximal members [12]. In general, *cis-trans* isomerization affects the energies of the barrier-proximal states in two major ways, as discussed in Section 2.1.2.

2.1.2 Effects of *cis-trans* Isomerization on the Energy-level Structure

The *cis-trans* isomerization saddle point on the S_1 PES results in very large and negative anharmonicity in the *trans* 3^m6^n combination levels [14, 30, 32, 154]. Based on a global fit to the $J = K = 0$ level-structure up to 3000 cm^{-1} above the *trans* zero-point level [14], the x_{36} cross-anharmonicity of the *trans*-conformer is found to be -33.45 cm^{-1}. A direct result of the negative and large value of x_{36} is that the zero-order states in the 3^mB^n polyad become more spread-out in energy compared to the zero-order states in the pure bending B^n polyad. For example, while the zero-order 4^1 and 6^1 states are nearly degenerate, the 3^44^1 state lies ~170 cm^{-1} higher in energy than the 3^46^1 state (the 3^4B^1 polyad is analyzed in Section 9.4). Consequently, the interaction between the 3^44^1 and 3^46^1 zero-order states is significantly reduced compared to that between 4^1 and 6^1. This isomerization-induced polyad-breaking is beautifully presented in Fig. 4 of Ref [32] (which is a reduced-dimension rovibrational variational calculation), where we can see that the lowest-energy polyad member (3^26^4), which is the most isomerization-prone state within the 3^2B^4 polyad, is the first to be decoupled from the rest of the polyad.

The rotational structure of barrier-proximal vibrational states is also significantly altered due to a *cis-trans* quantum tunneling effect, in the form of even-odd staggering of their rotational K-structures [32, 68, 105]. There are two mechanisms by which K-staggering occurs. The first mechanism is via tunneling interactions between degenerate vibrational states that belong to identical wells (i.e. *cis-cis* or *trans-trans* tunneling), analyzed by Hougen and Merer by group theory [68]. To fulfill the requirement of a single-valued total wavefunction, symmetric tunneling components are allowed to have only even-K states, and antisymmetric tunneling components are allowed to have only odd-K states. In S_1 acetylene, tunneling splittings are thus manifest as a staggering between even- and odd-K levels of a vibrational state. In addition, interactions between *cis* and *trans* levels at similar energies also give rise to staggering between the even- and odd-K-structures, because the selection rules for *cis-trans* interactions are different for even and odd K-values [32, 105]. As demonstrated in Fig. 6 of Ref [32], the even-K levels of the *trans* $3^4 6^2$ state interact with the *cis* $3^2 6^2$ state, while the odd-K levels of the *trans* state interact with the *cis* $3^3 6^1$ level. The level-shifts are thus different for the even *vs.* odd-K levels. Combining the two mechanisms above, K-staggering varies in an apparently random fashion from level to level, and is especially sensitive to local resonances.

From an experimental point of view, since typically only the $K = 0 - 2$ structures of a given vibrational state are conveniently observed in our experiments (due to the $K' - l'' = \pm 1$ selection rule), K-staggering is manifest as a deviation of the $K = 1$ structure from its unperturbed position with respect to $K = 0$ and 2 levels. However, given the strong a-axis Coriolis interaction in the S_1 *trans*-conformer, it is difficult to disentangle K-staggering from the a-axis Coriolis effect. For the $3^4 B^1$ polyad, a nearly complete disentanglement is possible, due to the large x_{36} cross-anharmonicity. As I demonstrate in Section 9.4, the quantum-tunneling affects the barrier-proximal $3^4 6^1$ state (46827 cm^{-1}) to a much larger extent than the isomerization-inert $3^4 4^1$ state (46996 cm^{-1}), even though the former lies $\sim$170 cm^{-1} lower in energy. Similarly, the level structure of the observed *trans* $3^2 5^1$ vibrational state (47113 cm^{-1}), which is not expected to be sensitive to isomerization effects due to lack of *simultaneous* excitation in ν_3 and ν_6, is minimally affected by isomerization.

2.2 Predissociation in the S_1 state of acetylene

Laser-induced fluorescence (LIF) detection has been the most commonly used technique in the study of S_1 acetylene. However, a rapid fall-off in the fluorescence quantum yield is observed in the >46300 cm^{-1} region (just above the energy of the $K = 2$ level of the *trans* 3^4 vibrational state) [60], due to acetylene predissociation, which produces $C_2H(\tilde{X}^2\Sigma^+)$ + $H(^2S)$ fragments. Using high-resolution H-atom photofragment translation spectroscopy, Mordaunt et al. [112] determined the predissociation threshold to be 46074±8 cm^{-1}, $\sim$1100 cm^{-1} below the top of the *cis-trans* isomerization barrier. *Ab initio* calculations [38] of low lying singlet and triplet states of

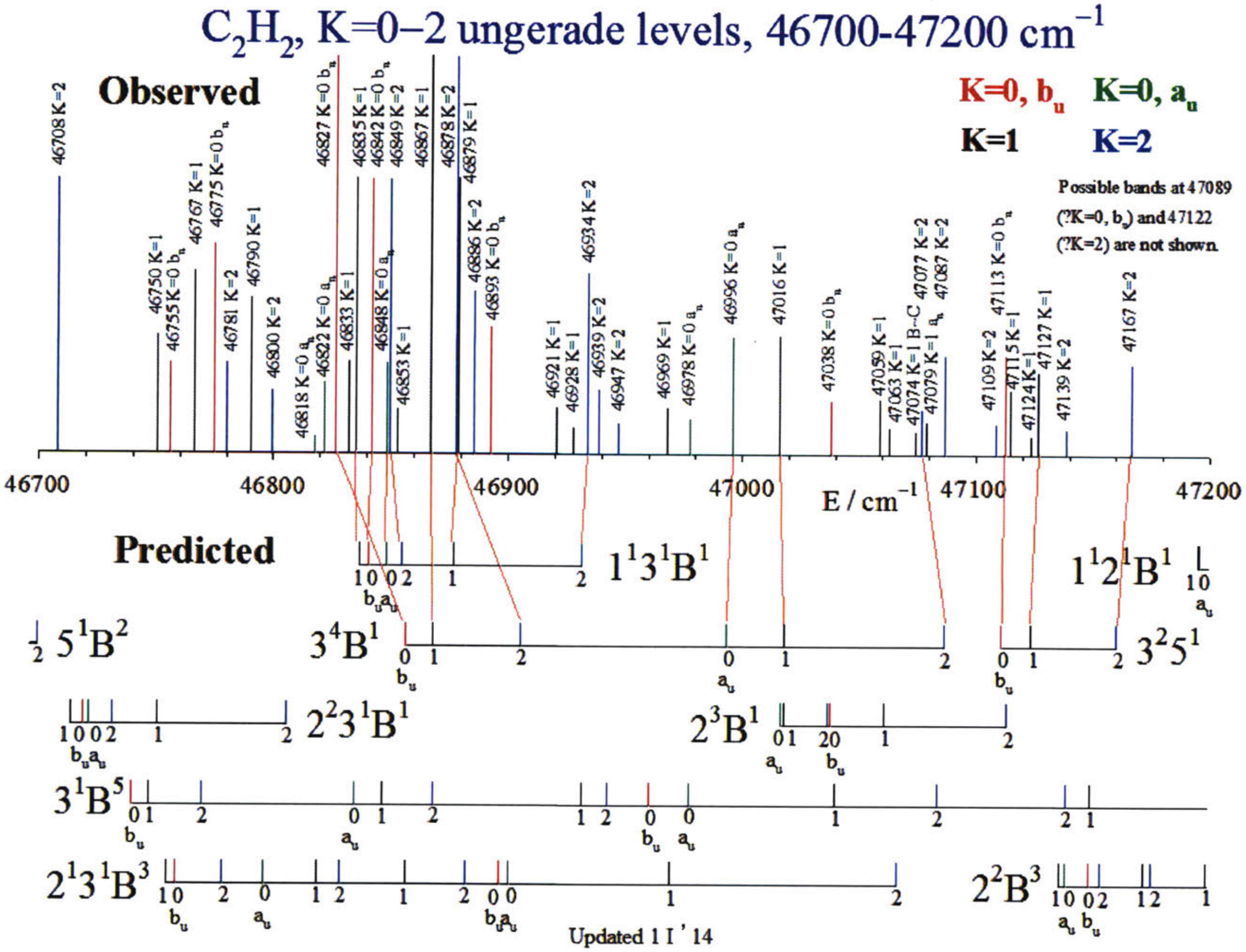

Figure 2-3: A summary of the observed (IR-UV DR LIF detection) and predicted (ungerade *trans*-conformer levels) S_1 vibrational states and their K-structures in the 46700 − 47200 cm^{-1} total energy region (4500 − 5000 cm^{-1} above the *trans* zero-point level). Orange lines are used to indicate assignments of some of the observed levels. The predicted level positions have been provided by Professor Anthony Merer.

acetylene suggest a sequential S_1-T_3-T_2-T_1 predissociation pathway, with an exit barrier on the T_1 PES. From the translational energy release of the H-atoms (measured from the Doppler profile), the exit barrier is extrapolated to be ~560 cm^{-1} [64, 158]. The presence of this barrier explains the observation that the onset of the rapid fluorescence fall-off lies higher in energy than the predissociation threshold.

Due to the sequential nature of the predissocation pathway, which is faciliated by weak spin-orbit interactions, LIF signals can still be observed from S_1 levels >1000 cm^{-1} above the predissociation threshold, although the detection quantum efficiency of those predissociated levels is greatly diminished. In addition, since LIF signals from the predissociated levels have a laser-pulse limited temporal profile (the non-predissociated S_1 levels typically have lifetime of $200 - 300$ ns), it is no longer possible to reduce the effect of laser scatter-light by a gating window on the fluorescence time-trace after laser excitation. As a result of significantly reduced signal-to-noise (s/n) ratio, only two-thirds of the expected *trans*-conformer ungerade vibrational levels in the 46700 – 47200 cm^{-1} energy region could be observed in the LIF experiment, as shown in Fig. 2-3, where both the observed and predicted $K = 0 - 2$ *trans* ungerade vibrational levels are shown. Given that the current energy region lies just below the top of the isomerization barrier, it is also likely that some of the observed levels are *cis*-conformer levels, which gain significant oscillator strength by interacting with nearby *trans* levels. If this were the case, the total number of observed *trans* levels is an even smaller fraction of the total number of expected *trans* levels.

As mentioned in Section 2.1.1, unambiguous identification of the *cis*-conformer levels relies on the ability to observe and assign essentially all of the possible *trans*-conformer levels within an energy region. Vibrational assignment of the *trans* levels is based on the effective Hamiltonian polyad model. Near the top of the isomerization barrier, the polyad model, which does not directly take into account the presence of the *cis* well on the PES, is unable to reproduce the energy level structure of the *trans*-conformer to the same level of accuracy as it does in the <46700 cm^{-1} region (typically a few cm^{-1}). The possible appearance of the *cis*-conformer levels in the spectra further complicates the assignments. In the energy region of current interest, we encounter a situation where both the detection and the vibrational assignments become challenging. An improvement in the detection efficiency is a crucial first step in assigning the complicated energy level-structure in the barrier region. With a nearly complete observation of all of the possible states in this region, it might become possible to sort out the *trans* level structure, guided (with caution) by predictions from the polyad model. The *cis*-interloper levels, which are still relatively sparse in the 46700 – 47200 cm^{-1} region, might be identified with more certainty.

To increase the detection efficiency, 2+1 resonance-enhanced multi-photon ionization (REMPI) detection of H atoms and 1+1 REMPI detection of acetylene have both been previously applied in our lab [31]. Problems and difficulties associated with those two detection schemes are discussed in Chapter 3 of this thesis. Part of my thesis work is focused on developing sensitive detection schemes for predissociated S_1 levels. Given that a laser scan in the S_1 acetylene experiments typically spans several hundreds of wavenumbers (in double-resonance experiments, the same energy region must be scanned multiple times to record all J levels), and it is carried out semi-continuously for months, I consider experimental convenience to be almost as important as detection sensitivity, because the reproducibility and quality of the experimental data cannot be guaranteed if difficult laser alignments are regularly needed.

2.3 Results and Discussions

2.3.1 Ungerade Vibrational States in the 46700 – 47200 cm^{-1} Region

Despite decreased detection efficiency and partial breakdown of the polyad model, definite vibrational assignments of some of the *trans* levels are still possible in the 46700 – 47200 cm^{-1} region, thanks to our detailed knowledge of the *trans* level structure in the lower energy region. In this section, I provide an analysis of the observed *trans* 3^4B^1 polyad and the *trans* 3^25^1 state, both of which provide nice illustrations of the effect of isomerization on the *trans* level structure, discussed in Section 2.1.2.

I must point out that the two zero-order vibrational states in the 3^4B^1 polyad, 3^46^1 and 3^44^1, are separated by >150 cm^{-1}, due to large x_{36} cross-anharmonicity induced by *cis-trans* isomerization. The energy separation between the two zero-order states is much larger than the interaction matrix element (i.e. the a-axis Coriolis matrix element between two zero-order $K = 1$ levels of the two vibrational states is expected to be ~30 cm^{-1}). Consequently, all of the observed eigenstates within the 3^4B^1 polyad have predominantly one vibrational character, and they will be refered to, in the following discussions, by their dominant vibrational assignment.

The three spectrally-brightest levels in the 46800-46900 cm^{-1} total energy region (see Fig. 2-3) can be assigned unambiguously to be $K = 0 - 2$ levels of the *trans* 3^46^1 vibrational state, which is predicted to lie in this energy region by the effective Hamiltonian polyad model. The 3^44^1 state is expected to lie higher in energy by ~150 cm^{-1} than 3^46^1. Transitions into $K = 0 - 2$ levels of 3^44^1 are also expected to be stronger than transitions into other predicted states in the same energy region (47000 – 47100 cm^{-1}), based on LIF studies near 46000 cm^{-1}, where the 3^34^1 state is observed [12]. As a result, I assign the observed $K = 0$, A_u-symmetry level at 46996 cm^{-1}, $K = 1$ level at 47016 cm^{-1}, and $K = 2$ level at 47077 cm^{-1} to be, respectively, $K = 0 - 2$ levels of the *trans* 3^44^1 state.[1] Based on predictions from the polyad model, the observed $K = 0$ B_u-symmetry level at 47113 cm^{-1}, $K = 1$ level at 47127 cm^{-1}, and $K = 2$ level at 47167 cm^{-1} are assigned to 3^25^1. The observed transition

---

[1] Based on the LIF spectrum, there is some ambiguity in the assignment of the $K = 2$ level of 3^46^1, due to proximity of two observed $K = 2$ levels near 47080 cm^{-1}. The 47087 cm^{-1} state shows up more intensely in the LIF spectrum compared to the 47077 cm^{-1} state, which suggests that the former should correspond to the $K = 2$ level of 3^44^1. However, for predissociated levels, the observed LIF intensity does not necessarily correspond closely with the absolute transition probability, due to possibility of level-dependent predissociation rate. In the photofragment (C_2 and C_2H) fluorescence detection scheme (discussed in Chapter 3), the transition into the 47077 cm^{-1} level is approximately three times more intense than that into the 47087 cm^{-1} level in the resulting action spectrum. Given that signal intensities obtained in the photofragment fluorescence action spectrum appear to reflect more closely the acetylene S_1-S_0 transition probabilities (as discussed in Section 3.4 of Chapter 3), it is more likely that the 47077 cm^{-1} level corresponds to the $K = 2$ level of 3^44^1, which is the assignment adopted in my analysis. Relative LIF intensities of other levels in the 46700-47200 cm^{-1} region appear to agree qualitatively with photofragment fluorescence action intensities.

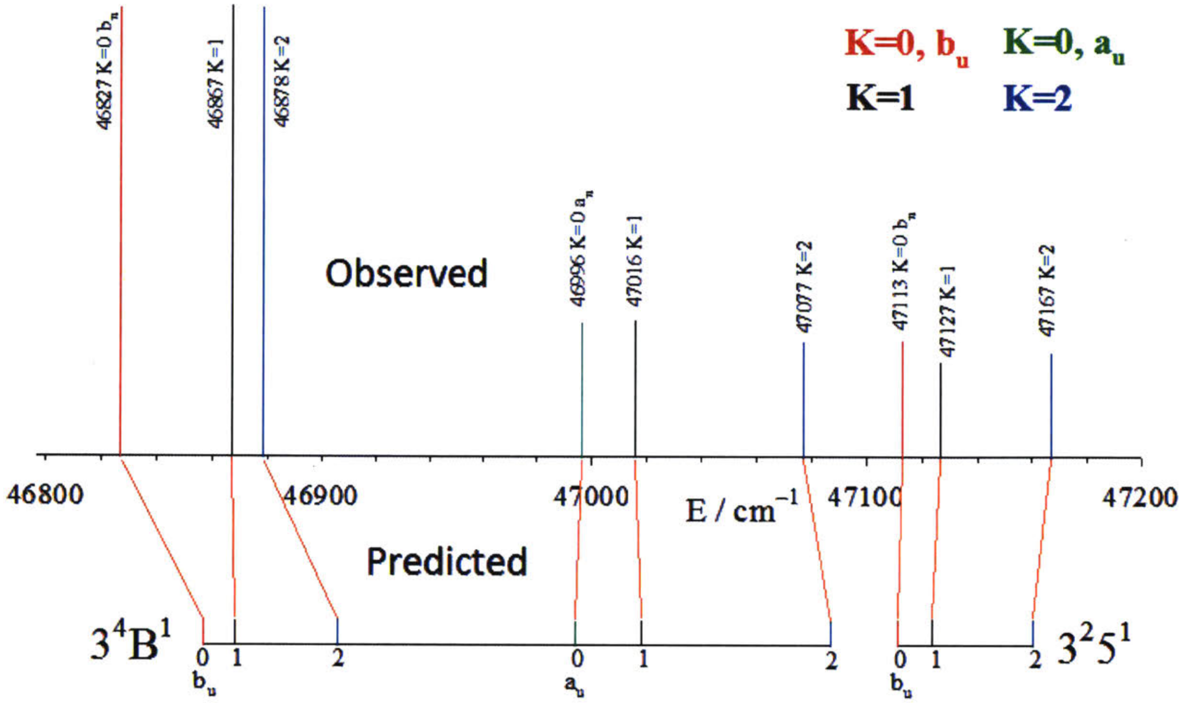

Figure 2-4: Observed and predicted (based on the *trans* polyad model) level positions of 3^4B^1 and 3^25^1. Levels in Fig. 2-3 irrelevant to discussions in Section 9.4 are omitted for clarity. Orange lines are used to indicate assignments.

intensities into the three K-levels also agree with the expectation that 3^25^1 is the spectrally-brightest vibrational state in the $47100-47200$ cm^{-1} energy region. The assignments of the K-structure of 3^4B^1 and 3^25^1 are further supported by results from least-squares fitting, discussed later in this section.

The assigned and predicted level positions of 3^4B^1 and 3^25^1 are shown in Fig. 2-4, where levels in Fig. 2-3 irrelevant to my discussion in this section are omitted for clarity. As can be seen from Fig. 2-4, while the observed $K = 0-2$ levels of 3^25^1 and 3^44^1 agree reasonably well (<10 cm^{-1} discrepancies) with predictions based on the polyad model, the agreement is significantly worse ($\sim$30 cm^{-1} discrepancies) for the $K = 0$, 2 levels of 3^46^1. The energies of the two even-K levels seem to have both been shifted down by $\sim$30 cm^{-1} with respect to the energy of the odd $K = 1$ level of 3^46^1, characteristic of tunneling-induced K-staggering discussed in Section 2.1.2. The 3^46^1 state, with *simultaneous* excitations in both ν_3 and ν_6, is a barrier-proximal state and tunnels readily into the *cis* wells, while 3^25^1 and 3^44^1 are less prone to isomerize,

Table 2.1: Rotational constants from least-squares fitting of the *trans* 3^4B^1 polyad. Values are in cm^{-1}. The *rms* of the fit is 0.034 cm^{-1}.

	3^46^1	3^44^1
T_o	46826.67(2)	46995.65(2)
A	20.276(171)	15.200(168)
B	1.1278(32)	1.1198(23)
C	1.0138(21)	1.0270(18)
D_{JK}	0.0065(6)	-0.0023(3)
$2A\zeta_a^{46}$	32.86(38)	
$B\zeta_b^{46}$	0.7618(359)	
K-staggering	28.98(3)	

despite the fact that the two states lie higher in energy than 3^46^1.

Given that Coriolis interactions (especially a-axis Coriolis) are non-neglible betweeen the 3^46^1 and 3^44^1 states, to accurately determine the degree of K-staggering in 3^46^1, it is necessary to fit the observed $K = 0 - 2$ structures of both states simultaenously, with a model that includes both a and b-axis Coriolis interactions (the Darling-Dennison interaction is absent in the 3^4B^1 polyad). To account for an apparently staggered K-structure, a K-staggering parameter is included for the zero-order 3^46^1 state. The K-staggering parameter is assumed to be a constant, and it effectively shifts the position of the $K = 1$ level with respect to $K = 0$ and 2. The K-structure of 3^46^1 no longer follows the patterns of an asymmetric top.

The PGOPHER program is used for the least-squares fitting, and the results are given in Table 2.1. The Coriolis matrix elements used in my fit are defined similarly as in Ref [107]. Note that the *rms* of the fit is significantly reduced (0.078 cm^{-1}→0.034 cm^{-1}) by including D_{JK} terms for both vibrational states. The D$_{JK}$ terms should be considered correction terms to the fit, similar to the small centrifugal distortion correction terms used in the polyad fit of Refs [107, 154]. The values of all other rotational constants in Table 2.1 are reasonable. For example, the value of $2A\zeta_a^{46}$, which increases rapidly with addition of ν_3 (~3 cm^{-1} per quantum of ν_3), is predicted to be ~30 cm^{-1} for the 3^4B^1 polyad. The value of $B\zeta_b^{46}$, which is relatively insensitive to addition of ν_3, is predicted to be ~0.78 cm^{-1}(derived from the B^1 polyad) [168].

Table 2.2: Rotational constants from least-squares fitting of the *trans* $3^2 5^1$ state. Values are in cm^{-1}. The *rms* of the fit is 0.029 cm^{-1}.

	$3^2 5^1$
T_o	47112.42(1)
A	14.6522(33)
B	1.1278(32)
C	1.0202(32)
K-staggering	0.927(13)

Based on the least-squares fit results, it is clear that the tunneling-induced level shift of the $3^4 6^1$ $K = 1$ level (+29 cm^{-1}, with respect to the even-K manifold) is significantly larger than the Coriolis-induced level shift (-7.5 cm^{-1}). Within the experimental resolution, there is no observable K-staggering in the $3^4 4^1$ level, which is a further indication that $3^4 4^1$ is not tunneling-active.

A similar least-squares fit is carried out for the $3^2 5^1$ state. The results are shown in Table 2.2. There are definite signs that a small amount of K-staggering (0.93 cm^{-1}) is present in $3^2 5^1$. Without the K-staggering parameter, a nearly constant fit residual of around +0.9 cm^{-1} is present for all observed J-levels within the $K = 1$ structure. By incorporating the K-staggering parameter, I am able to obtain a fit, with $rms = 0.029$ cm^{-1}. A small but non-negligible K-staggering indicates that the $3^2 5^1$ state, which does not have excitation in ν_6, is also barrier-proximal, although to a much lesser extent compared to $3^4 6^1$. The small degree of tunneling activity in $3^2 5^1$ might be related to the fact that excitation in ν_5 (the antisymmetric stretching mode) is necessary to reach the *cis-trans* isomerization transition state, which has unequal CH bond lengths.

As discussed in Section 2.2, vibrational assignments become challenging in the 46700 – 47200 cm^{-1} region. Currently, we do not have a model which allows prediction of the energy level structure of the barrier-proximal states, especially their rotational K-structure. This is particularly problematic for $3^m B^n$ polyads, with small m and large n values, e.g. $3^1 B^5$, because those polyads have multiple polyad members (six in the case of 3^1B^5), with varying degree of barrier-proximity, and Coriolis interactions among the polyad members are by no means negligble. The resulting K-structure becomes unpredictable (for the current model). However, as pointed out in Section 2.2, an improved detection efficiency will get us significantly closer to a full understanding of the complicated energy level structure near the top of the S_1 *cis-trans* isomerization barrier, especially given that we are already equipped with detailed knowledge of the *trans* (and *cis*) level structure below 46700 cm^{-1}, as well as a qualitative understanding of the effect of isomerization on the energy-level structure.

Secure vibrational assignments of S_1 levels near the top of the isomerization barrier are also crucial for future SEP experiments to detect S_0 local-bender levels, because the ideal "local-bender pluck" S_1 acetylene levels are those with many quanta in ν_6', as well as some additional quanta in ν_3' to improve the Franck-Condon intensity [129, 132]. In other words, in the energy region where the S_1 level structure has been explored in detail (i.e. up to 47200 cm^{-1}), S_1 barrier-proximal states, such as 3^16^5 (not yet securely identified, but is expected to be located in the 46700 – 47200 cm^{-1} region), will possibly grant the best access to local benders in S_0.

2.3.2 Collisonal Relaxation

All of the recent LIF spectra of S_1 acetylene from our group are collected in the collision-free region (also known as the zone of silence) of a supersonic jet, generated from a pulsed-valve. The collision-free region typically lies >10 nozzle-diameters downstream from the face-plate of the pulse-valve. The rotational temperature of the beam in the collision-free region is ~10 K. However, collisional relaxation is still sometimes observed, especially when the laser beam intersects the supersonic molecular beam upstream of the zone of silence. The effects of collisional relaxation are most prominently observed in IR-UV DR experiments, where the acetylene molecules are first pumped by an IR photon to an intermediate S_0 rovibrational level with ungerade vibrational symmetry, e.g. the ν_3'' fundamental (Σ_u^+) or the $\nu_3 + \nu_4''$ combination level (Π_u). Collisional relaxation results in population in levels that are not initially populated by the IR photon. The UV laser, which is intended to excite

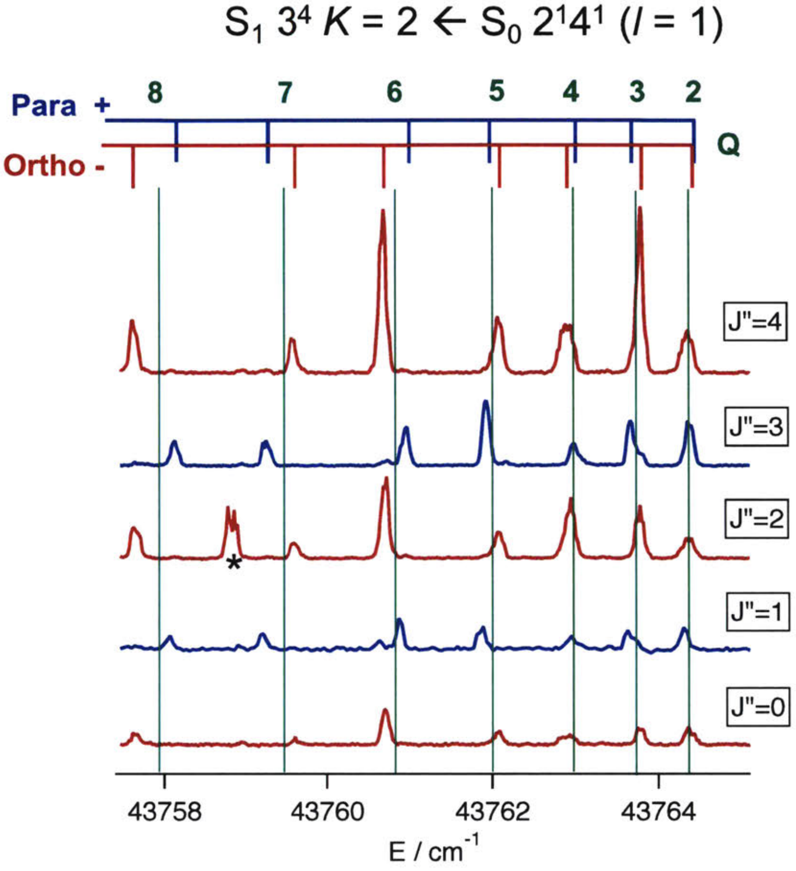

Figure 2-5: The observed collisionally-induced transitions from the S_0 $\nu_2 + \nu_4''$ levels into S_1 *trans*-3^4 $K = 2$ levels. The $J'' = 0 - 4$ levels of ν_3'' are individually pumped by the IR laser, and the five resulting spectra are shown in the figure. The spectra are color-coded according to the nuclear-spin ortho/para symmetry of the collision precursor ν_3'' levels, i.e. red for even-J'' levels with ortho symmetry and blue for odd-J'' levels with para symmetry. The Q-branch assignments are shown by the tie-lines, for which transitions originating from S_0 $2^1 4^1$ rotational levels with ortho and para symmetry are shown, respectively, in red and blue. The peak labeled by an asterisk in the $J'' = 2$ spectrum is an IR-UV transition originating from the IR-pumped ν_3'' $J'' = 2$ level.

S_1-S_0 transitions from the IR-populated S_0 level, also excites transitions from the collisionally-populated S_0 levels. While the dynamics of collisionally-induced energy transfer are interesting (see Refs [53, 54, 125]), the presence of collisional relaxation is a nuisance in collecting IR-UV DR spectra, because additional IR-dependent lines (which complicate spectra-assignments) can appear in the spectra as a result of collisional relaxation. Given that collisional relaxation is one of the most frequently encountered sources of unwanted signals in the IR-UV DR spectra, I describe this problem in this section. In particular, I focus on the rotational selection rules of the relaxation process. Understanding the relaxation selection rules facilitates identification and assignment of those collisionally-induced peaks in the spectra.

In IR-UV DR experiments via the S_0 ν_3'' fundamental level, $J'' = 0 - 4$ levels of ν_3'' are individually pumped by the IR laser (in five different experiments). At UV excitation energy of $\sim$43764 cm^{-1}, transitions from the S_0 $\nu_2 + \nu_4''$ levels into S_1 *trans*-3^4 $K = 2$ levels can be definitively assigned in all five IR-UV DR spectra, each of which should only contain transitions from one of the five individually-selected IR-pumped ν_3'' levels. Vibrational relaxation, $\nu_3'' \rightarrow \nu_2 + \nu_4''$, must have occurred prior to UV excitation ($\sim$20 ns after IR). The rotational quantum number, J, of the collision precursor ν_3'' level, is randomized by collisions, and multiple J-levels of $\nu_2 + \nu_4''$ are populated, as can be seen in all five spectra in Fig. 2-5. To help understand the patterns in the spectra, I include the rotational level structures (with parity and symmetry labels) of $\nu_2 + \nu_4''$ and ν_3'' in Fig. 2-6a. If both l-components of the $\nu_2 + \nu_4''$ state were collisionally-populated *without* bias from a given J''-level of ν_3'', each observed Q-branch transition in Fig. 2-5 would be split into two lines, centered around one of the green vertical lines in Fig. 2-5. However, as can be seen from all five spectra in Fig. 2-5, only one member of the doublet is present for each of the observed Q-branch transitions. According to my rotational assignments, when the collision-precursor levels are even-J'' levels of ν_3'', rotational levels of $\nu_2 + \nu_4''$ with *ortho* nuclear-spin configuration (and + parity) are selectively populated; when the collision-precursor levels are odd-J'' levels of ν_3'', rotational levels of $\nu_2 + \nu_4''$ with *para* nuclear-spin configuration (and - parity) are selectively populated. Given that even-

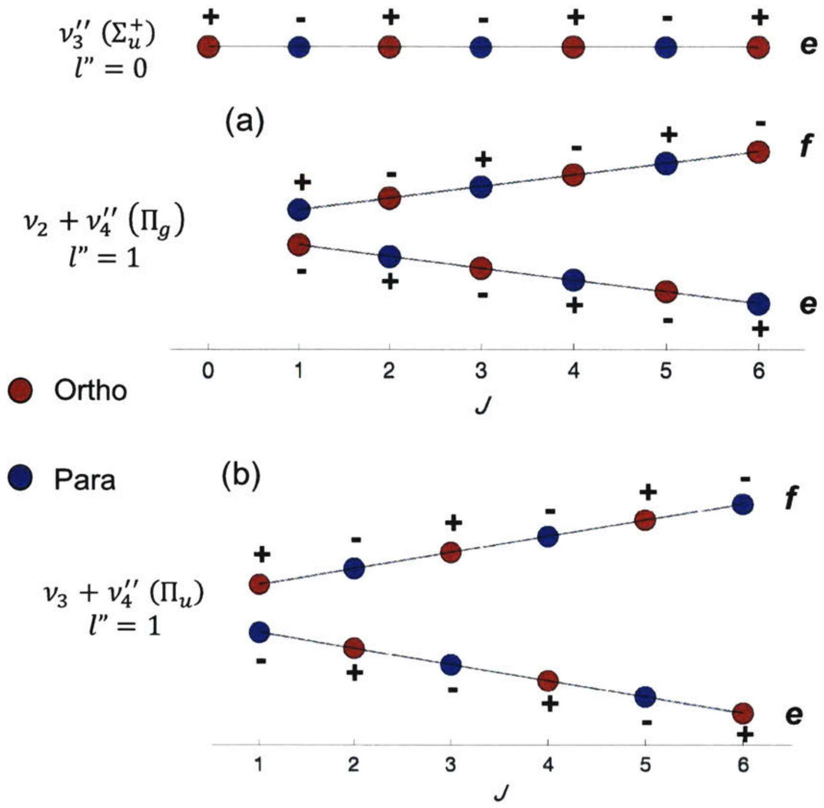

Figure 2-6: Rotational level-structure of (a) ν_3'' and $\nu_2 + \nu_4''$ and (b) $\nu_3 + \nu_4''$, with $+/-$, e/f, and *ortho*/*para* labels.

and odd-J'' levels of ν_3'' have, respectively, ortho and para nuclear-spin symmetry (see Fig. 2-6a), nuclear-spin symmetry appears to be conserved during $\nu_3'' \rightarrow \nu_2 + \nu_4''$ vibrational relaxation. Conservation of nuclear-spin symmetry is expected, because collisions, which do not generally involve magnetic perturbations, are unable to induce a nuclear-spin flip. The observed vibrational relaxation also obeys the $+ \leftrightarrow -$ parity selection rule. This parity selection rule, however, is not universally applicable to all types of collisional relaxations, such as rotational relaxation (discussed below).

Rotational relaxation (i.e. J-changing collisions within a vibrational level) is also observed in the supersonic jet. Specifically, after the $J = 4{+}e$ level of the S_0 $\nu_3 + \nu_4''$ combination level is initially populated by an IR photon, rotational relaxation from $J = 4{+}e$ into $J = 3{+}f$ and $J = 5{+}f$ levels is observed during IR-UV DR experiments that probe the S_1 $3^4 6^1$ $K = 0f$ levels (IR-UV DR transitions into $3^4 6^1$

are strong). As a result of rotational relaxation, extra $P_{ff}(3)$ and $P_{ff}(5)$ lines show up in the DR spectrum, in addition to the expected $Q_{fe}(4)$ transition. The parity of the rotational levels appears to be conserved during rotational relaxation, i.e. $+ \leftrightarrow +$, which is different from the parity selection rule associated with vibrational relaxation, $+ \leftrightarrow -$, discussed in the previous paragraph. However, if I consider the nuclear-spin state of the involved rotational levels, nuclear-spin symmetry is also conserved during rotational relaxation. As can be seen from Fig. 2-6b, the intially-populated $\nu_3 + \nu_4'' \ J = 4{+}e$ level has the same nuclear-spin symmetry (ortho) as the collisionally-populated $J = 3{+}f$ and $J = 5{+}f$ levels. Conservation of ortho-para symmetry is thus a more rigorous selection rule in collisional relaxation processes.

Chapter 3

Probing the Predissociated Levels of the S_1 State of Acetylene via H-atom Fluorescence and Photofragment Fluorescence Action Spectroscopy

Abstract

In this work, I report two new experimental schemes to obtain high-resolution spectra of predissociated S_1 acetylene levels. In the first method, H-atoms from the predissociated S_1 acetylene levels are probed by two-photon laser-induced fluorescence. Specifically, the H-atoms are pumped to the $3d$ (and $3s$) level by the two-photon resonance transition at 205.14 nm. The resulting $3d - 2p$ fluorescence signals (654.5 nm) are collected by a photomultiplier tube (PMT). This new H-atom fluorescence detection scheme is an improvement over the more widely used H-atom resonance-enhanced multiphoton ionization (REMPI) detection, both in terms of the signal-to-noise (s/n) ratio of the resultant H-atom action spectra of S_1 acetylene, and experimental convenience (due to higher number-density of molecules that can be used in the fluorescence detection than in the REMPI detection). In the second method, fluorescence from the electronically excited C_2 and C_2H photofragments of S_1 acetylene are detected. The photofragment fluorescence detection results in the best s/n ratio in the action spectra of predissociated acetylene levels, compared to the H-atom ion-detection and laser-induced-fluorescence (LIF) detection methods. In addition, a *single* UV laser beam is used as both the excitation and probe beams, which greatly simplifies the laser alignment process for the photofragment fluorescence detection scheme.

The H-atom fluorescence detection work described in this chapter was performed

with C. A. Saladrigas. The photofragment fluorescence action detection scheme was performed with T. J. Erickson, including contributions from C. L. Keenan.

3.1 Introduction

The study of the first electronically excited singlet (S_1) state of the acetylene molecule dates back more than one hundred years, when Stark and Lipp published the first absorption spectrum of gas-phase acetylene from 2200 to 1900 Å [151]. Groundbreaking works from Ingold and King [75], and Innes [76], demonstrated that the excited state observed in the absorption spectrum has a *trans*-bent structure (C_{2h} point group), instead of the linear structure of the electronic ground states (S_0). From the observed rotational selection rule, the S_1-S_0 transition was identified as a *c*-type $\tilde{A}^1A_u - \tilde{X}^1\Sigma_g$ transition. Detailed analyses by various groups [12, 104, 106, 107, 111, 154, 155, 160, 168–170, 174] led to essentially complete vibrational and rotational assignment up to 4500 cm^{-1} above the zero-point level of the S_1 *trans* conformer, and recent work from our group resulted in the discovery of several S_1 *cis*-conformer levels [12, 105]. The *cis* conformer levels borrow transition intensities by interaction with nearby S_1 *trans* levels. High-level *ab initio* calculations [13] and modeling of the experimental data [11] have located the *cis-trans* isomerization barrier at ~5000 cm^{-1} above the *trans* minimum energy.

We have encountered both theoretical and experimental difficulties in extending the vibrational assignments to levels above 4500 cm^{-1} [31]. The *cis-trans* isomerization process greatly alters the energy-level structures of both *trans* and *cis*-conformer levels near the top of the isomerization barrier [105]. Our polyad fit model, based on an effective Hamiltonian of the *trans*-conformer (i.e. the presence of the *cis*-conformer on the potential energy surface is not directly taken into account), fails to accurately predict positions of levels above 4500 cm^{-1}. The possible appearances of the *cis*-conformer levels in the spectra further complicate the assignments. In addition, the predissociation threshold of acetylene (46074±8 cm^{-1}) [112] lies ~1000 cm^{-1} below the top of the isomerization barrier. The detection efficiency of the laser-induced fluorescence (LIF) technique (the most commonly used technique in the study of the S_1 acetylene) diminishes greatly for the predissociated levels. As a result, only about half of the expected levels near 5000 cm^{-1} could be observed in the LIF experiment. Combined with the partial breakdown of our polyad fit model, secure vibrational and conformer assignments of those observed levels became challenging.

To increase the detection efficiency, resonance-enhanced multi-photon ionization (REMPI) detection of H atoms (2+1 REMPI) has been previously applied in our lab [31]. The signal-to-noise (s/n) ratio of the H-atom REMPI detection, however, is not significantly better than acetylene LIF in the energy region of interest (~5000 cm^{-1} above the *trans* minimum, and ~1000 cm^{-1} above the predissociation threshold), although it does permit observation, with reasonable signal-to-noise, of one predissociated band that is barely observable by LIF detection. REMPI detection of acetylene (1+1 REMPI) has also been applied to study predissociated S_1 levels [31, 164], and the s/n ratio of the resultant spectrum is better than that of H-atom ion-detection and acetylene LIF.

In this chapter, I report two new experimental strategies to obtain rotationally-resolved high-resolution spectra of predissociated S_1 acetylene levels. In the first method, instead of detecting the H atoms via 2+1 REMPI, I detect the H-atoms by monitoring two-photon laser-induced fluorescence. In addition to probing the predissociated S_1 levels, the H-atom fluorescence action spectra, in combination with the LIF spectra, also allows a rotationally-resolved study of the predissociation process in S_1 acetylene. In the second method, fluorescence from the electronically excited photodissociation products of S_1 acetylene (C_2 and C_2H) are detected. The second method offers significantly higher s/n ratio, compared to LIF and the two H-atom detection techniques (direct comparison with acetylene 1+1 REMPI detection is not currently avaliable). It is also the easiest method to implement, because a *single* UV laser beam is used for both $\tilde{A} \leftarrow \tilde{X}$ excitation and the immediate multi-photon fragmentations. No additional probe laser beam is needed.

3.2 Experimental Details

Both H-atom and photofragment (C_2 and C_2H) fluorescence detection experiments are carried out in a vacuum chamber, fitted with a diffusion pump (Varian, VHS-6), which achieves an ultimate pressure of 10^{-6} torr. A molecular beam of acetylene is expanded through a pulsed valve (General Valve, Series 9, d=1.0 mm) into the vacuum chamber. A mixture of acetylene (13%) in Ar with 3 atm backing pressure is used in the H-atom experiment, and neat acetylene with 1 atm backing pressure is used in the carbon-fragment detection scheme. Under gas load, the chamber pressure is $2 - 5 \times 10^{-5}$ torr.

The laser beams used in the experiments are produced from two tunable dye lasers, FL2002 and FL3002E (Lambda Physik), pumped, respectively, by the second and third harmonics of a Q-switched, injection-seeded, Nd:YAG laser (Spectra Physics, Pro-270), operating at 20 Hz. Nonlinear processes are applied to generate the desired wavelengths for specific experiments (see Sections 3.2.1 and 3.2.2). The resulting laser beams intersect the molecular beam at ~1.5 cm downstream from the pulsed nozzle orifice. Fluorescence signals, collected by f/1.2 optics, are observed at an angle mutually perpendicular to the laser path and the molecular beam, and recorded by a photomultiplier tube (PMT) (Hamamatsu R375), with appropriate filter choice (see Sections 3.2.1-3.2.2). To minimize scattered laser light in the fluorescence detection, the laser beams enter and exit the chamber through Brewster windows attached at the end of two long arms, each of which is equipped with two iris baffles (SM1 components, Thorlabs). The PMT signal is split and one part of it is input to a 30 dB voltage amplifier (Femto DHPVA-200), with 1.8 ns rise-time at 200 MHz bandwidth. The two output signals are monitored simultaneously on a digital oscilloscope (LeCroy, 9360), and the data is transferred to a computer for storage and post-processing.

3.2.1 H-atom fluorescence action spectroscopy

Two counter-propagating laser beams are used in the H-atom fluorescence experiments. The pump laser beam, weakly focused by an f = 50 cm lens, is used to

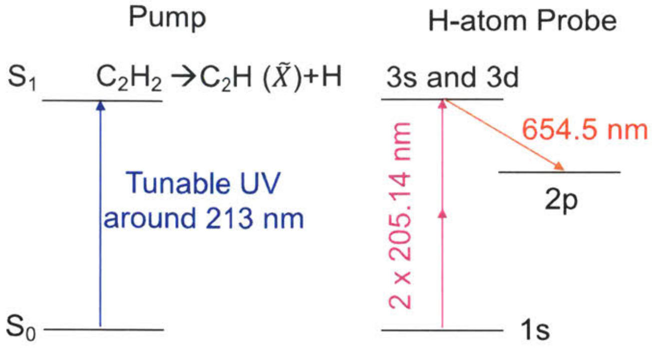

Figure 3-1: Level diagrams (not drawn to scale) relevant to the acetylene pump and subsequent H-atom probe scheme. H-atom fluorescence signals at 654.5 nm are collected by a PMT.

excite the Ã-X̃ transition to a predissociated S_1 level. To probe the resulting H-atom photofragment, a second focused laser beam (f = 30 cm lens), delayed by 5 ns with respect to the excitation laser beam, excites the H-atoms into the $3s$ and $3d$ levels by a two-photon transition at 205.14 nm. The counter-propagating beam configuration is crucial for maximizing spatial overlap between the two laser beams. Fluorescence (654.5 nm) from the $3s$ and $3d$ levels into the $2p$ level is detected by the PMT. A 630 nm long-pass filter (Newport, CGA-630) is used to minimize residual scattered light and fluorescence from photofragments of S_1 acetylene, e.g. C_2 Swan band emission. The acetylene excitation and subsequent H-atom probe scheme is summarized in Fig. 3-1. Given that the two-photon $3d \leftarrow 1s$ transition is approximately an order of magnitude stronger than the two-photon $3s \leftarrow 1s$ transition [58, 172], the H-atom fluorescence signals are dominated by the $3d \rightarrow 2p$ emission, which has a lifetime of <20 ns [177]. The $3s \rightarrow 2p$ emission signal (>100 ns lifetime) [177] is much weaker.

The excitation laser radiation is produced by the FL-3002E dye laser (Stilbene 420 dye). The dye laser output (420-430 nm) is frequency-doubled with a β-barium borate crystal (BBO), and a small portion of the fundamental is used for $^{130}Te_2$ frequency calibration. An intracavity etalon reduces the spectral width to 0.04 cm^{-1} and the UV excitation power is approximately 100 μJ/pulse. The H-atom probe laser beam at 205.14 nm is produced by frequency-tripling the output of the FL2002 dye laser at 615.42 nm (Rhodamine 640 dye). The wavelength of the fundamental beam is monitored by a wavemeter (Wavemaster, Coherent). Specifically, a combination of two BBO crystals and a zero-order half-wave plate (Thorlabs, WPH05M-308) was used to achieve frequency-tripling. The grating-limited spectral width of the 205 nm beam is 0.2 cm^{-1}, with a pulse-energy of ~500 μJ/pulse.

I must emphasize that the power of the UV S_1-S_0 excitation beam is intentionally kept at a relatively low level (100 μJ/pulse) in the H-atom fluorescence experiment. On each $\tilde{A}$-$\tilde{X}$ resonance, I observe, in addition to the H-atom signal, a long lifetime fluorescence signal, which is not dependent on the presence of the H-atom probe beam. In fact, the intensity of the long lifetime signal can completely overwhelm the H-atom signal, if the power of the UV pump laser is high (>250 μJ/pulse). To suppress the 'unwanted' signal (so that it is at least an order of magnitude smaller than the H-atom signal), the UV pump power must be decreased. As I discuss in Section 3.2.2, the 'unwanted' signal turns out to be the basis of our second (preferred) detection strategy for predissociated S_1 levels.

3.2.2 Photofragment fluorescence action spectroscopy

The Photofragment Fluorescence Action Spectroscopy technique (or PFAS) is based on one-color, multi-photon excitation of acetylene, resonance-enhanced at the one-photon level by a rotationally-resolved $\tilde{A}$-$\tilde{X}$ transition. A single UV laser beam (focused by an f = 70 cm lens) excites the $\tilde{A}$-$\tilde{X}$ transition, and immediately causes dissociation of the S_1 acetylene into electronically excited C_2 and C_2H fragments. Swan band emissions of C_2 and fluorescence of C_2H are detected by the PMT, with a 550 nm long-pass filter (Thorlabs, FGL550S). A 2 μs duration fluorescence time-trace is recorded by the oscilloscope, and integrated to generate the action spectrum.

Since a single UV laser beam serves both as the excitation and the probe beam, the laser-alignment process is greatly simplified. This is demonstrated by our successful implementation of an IR-UV double-resonance $\tilde{A}$-$\tilde{X}$ excitation scheme. In that case, the IR laser, focused by an f = 40 cm lens, simultaneously excites acetylene into $J = 1 - 5$ f-symmetry rotational levels of the S_0 $\nu_3 + \nu_4''$ combination level, by Q-branch pumping. A focused UV beam excites the vibrationally excited molecules

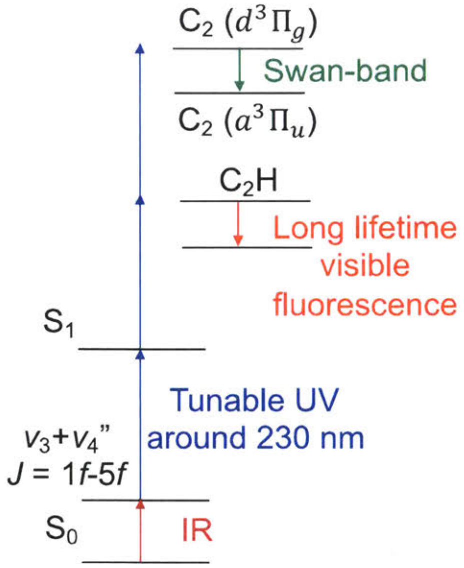

Figure 3-2: Level diagram (not drawn to scale) relevant to the photofragment fluorescence detection scheme. The C_2 $d^3\Pi_g$ state is generated with three same-color UV photons from the IR-populated S_0 $\nu_3 + \nu_4''$ levels. The assignment of the electronically excited C_2H fragments is currently unknown, although the fragments are believed to be generated by two rather than three UV photons, discussed in Chapter 4. The C_2 Swan-band and C_2H visible emission signals are collected by a PMT.

into a selected S_1 rovibrational level, and subsequently produces the photofragment signals. The photofragment detection scheme is summarized in Fig. 3-2.

The UV excitation beam (230-235 nm) is generated with an etalon-narrowed (0.04 cm^{-1} spectral width) FL-3002E dye laser (Coumarin 460 dye), and has an energy of approximately 300-400 μJ/pulse. The IR radiation (~2500 nm) is provided by difference frequency generation in a $LiNbO_3$ crystal, using the fundamental of the injection-seeded Nd:YAG laser (1064 nm) and the near IR (740-750 nm) output of the FL-2002 dye laser (LDS 751 dye). The IR radiation has an energy of approximately 1.5 mJ/pulse, and a grating-limited spectral width of 0.10 cm^{-1}.

In applying the PFAS method, one should be aware of the possibility of accidental two-photon resonance excitations into high-lying Rydberg states of acetylene. Fortunately, two-photon resonant transitions can usually be distinguished from the target $\tilde{A}$-$\tilde{X}$ transitions, because the linewidth of the two-photon resonant transitions are expected to be significantly broader (given the presence of a facile dissociation channel in the two-photon energy region [3, 21, 26, 92, 98–100, 162, 163]) than the target one-photon resonant transitions. In the experiment, the UV excitation beam is only weakly focused (i.e. the beam, focused by an $f = 70$ cm lens, intersects the molecular beam ~2 cm away from the beam waist) to avoid accidental two-photon resonant transitions, none of which have so far been observed in the acetylene experiment.

3.3 H-atom Fluorescence Action Spectroscopy

3.3.1 Results

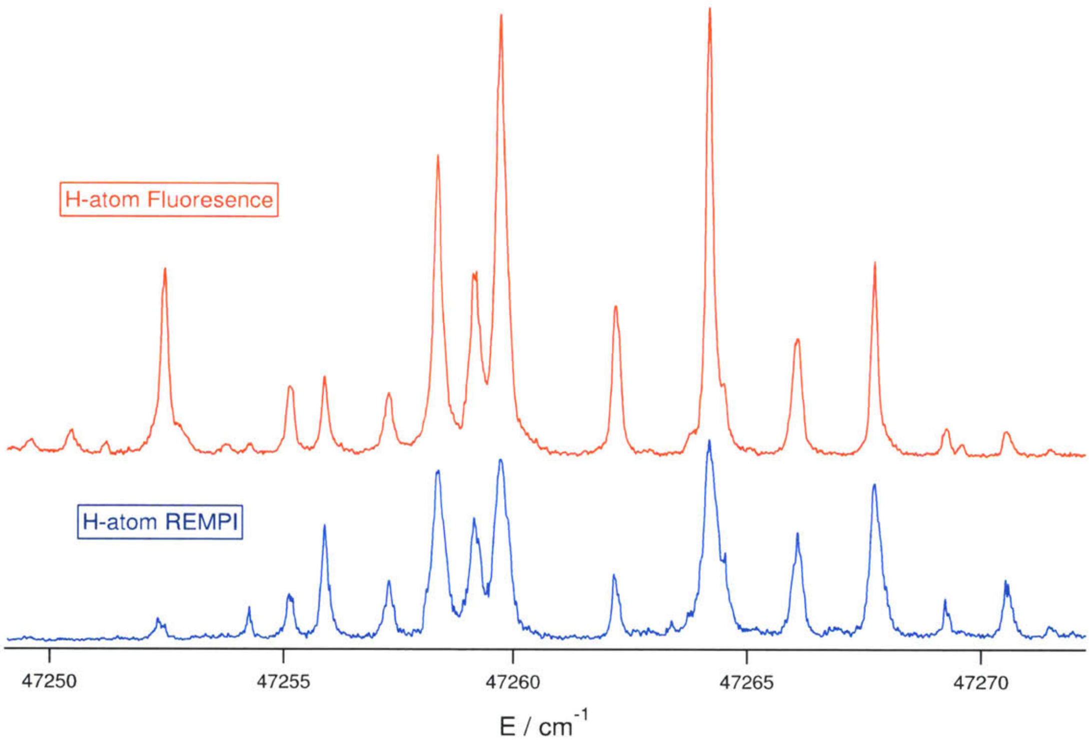

Figure 3-3: Comparison of action spectra of 3^5 $K = 1$ rotational levels of S_1 acetylene, recorded by H-atom fluorescence (orange) and H-atom REMPI (blue) detection schemes. The experimental conditions of the H-atom REMPI detection scheme were described in full detail in Ref [31]. The REMPI spectrum in the figure was recorded with similar excitation and probe laser powers as the H-atom fluorescence spectrum. The two spectra are scaled to a similar noise level.

High-resolution H-atom fluorescence-detected action spectra are recorded in the 47130-47280 cm^{-1} region (1050-1200 cm^{-1} above the predissociation limit). The s/n ratio of the H-atom fluorescence action spectrum is consistently better (by approximately a factor two) than the H-atom REMPI action spectrum (recorded with similar laser powers), as shown in Fig. 3-3 for the 3^5 $K = 1$ levels of S_1 acetylene.

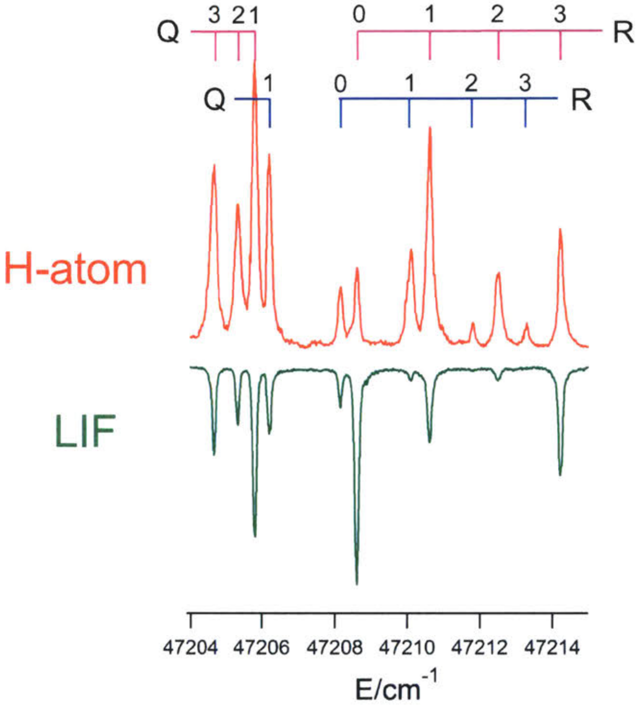

Figure 3-4: J-dependent rotational level predissociation. The H-atom fluorescence action spectrum is plotted in orange and the acetylene LIF spectrum in green. Rotational assignments for the two vibrational levels present in this region are given, respectively, in magenta (assigned as the $3^4 6^2$ $K = 1$ level) and in blue (a state that perturbs the $3^4 6^2$ level, but its vibrational assignment is yet to be determined).

The H-atom fluorescence action spectra, in combination with the LIF spectra (recorded with the same experimental conditions, except that the UV pump beam was unfocused), also allow rotationally-resolved study of the predissociation process of S_1 acetylene. As shown in Fig. 3-4, we have observed clear evidence of rotational level-dependent predissociation. The relative intensities of R(0) and R(1) lines of the $3^4 6^2$ level (magenta) are drastically different in the H-atom and LIF spectra. The $J = 1$ e-symmetry level (reached by the R(0) transition) appears to be more weakly predissociated, compared to the $J = 2$ e-symmetry level (reached by the R(1) transition). In addition, the rate of predissociation seems to be vibrational level-dependent.

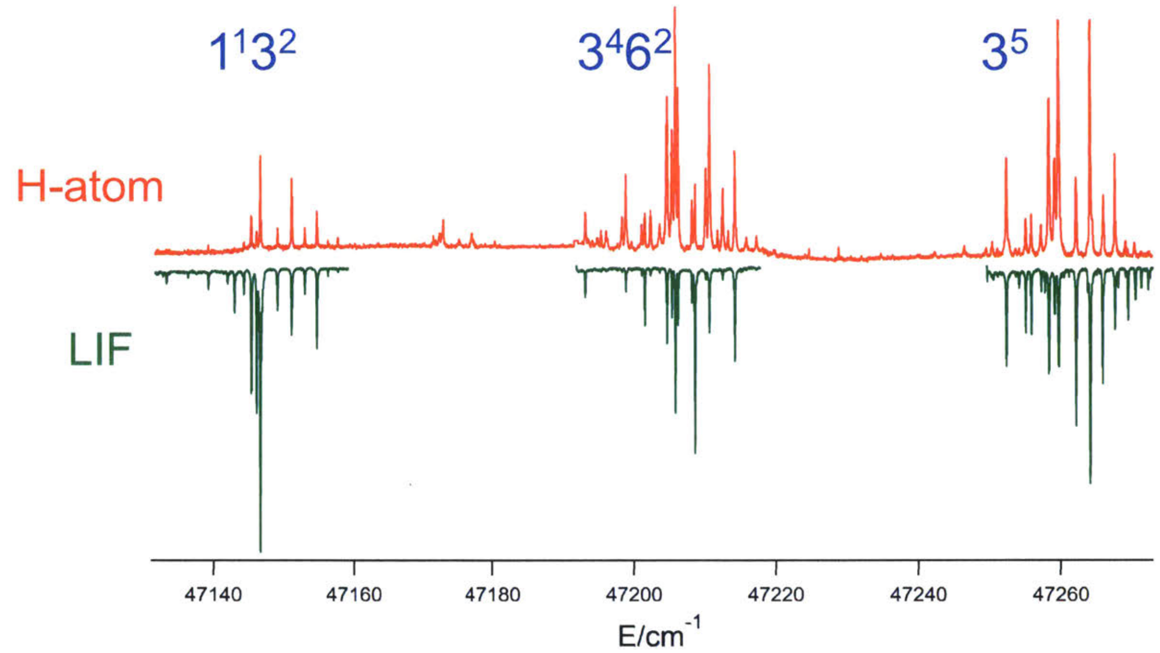

Figure 3-5: Vibrational level-dependent predissociation. The H-atom fluorescence action spectrum is plotted in orange and the acetylene LIF spectrum in green. The vibrational level assignments are given above the spectra.

In Fig. 3-5, the ratio of the LIF signal to the H-atom signal is much larger for the 1^13^2 level than for 3^46^2 and 3^5, which means that the predissociation rate is slower for the 1^13^2 level than 3^46^2 and 3^5. The observed level-dependent predissociation is consistent with the sequential S_1-T_3-T_2-T_1 predissociation pathway [38, 113], with the proposed T_3-mediated doorway interaction model [19, 42].

3.3.2 Discussion

The superior s/n ratio of the H-atom fluorescence detection over the H-atom REMPI detection might be unexpected, given that REMPI has near-unity detection efficiency, while fluorescence detection is reduced by both finite detection solid-angle and PMT quantum yield ($<$ 5% detection efficiency of REMPI). We believe that two factors contribute to the improved s/n ratio in the H-atom fluorescence detection scheme. The total number of acetylene molecules, and consequently the total number of H-atoms resulting from the $\tilde{A}$-$\tilde{X}$ excitation, was significantly larger in the H-atom fluorescence experiment than the H-atom REMPI experiment (differing by at least one order of magnitude)[1], because fluorescence detection does not require such low pressure conditions as are needed for REMPI detection (typically operated at $<5 \times 10^{-6}$ torr). In addition, the linewidth of the probe laser used in the H-atom fluorescence experiment (0.2 cm^{-1}) was about five times larger than that used in the REMPI experiment (0.04 cm^{-1}) [31]. Given that the Doppler linewidth of H-atoms from the predissociated S_1 levels of interest is $\sim$3 cm^{-1} [158], the percentage of probed H-atoms was about five times larger in the current H-atom fluorescence experiment than in the REMPI experiment.

One of the other advantages of H-atom fluorescence detection over REMPI detection is that laser alignment is significantly easier in the fluorescence detection scheme than the REMPI scheme. Even though the two detection schemes involve the same number of focused laser beams, with more H-atoms available in the detection chamber, it is considerably easier to achieve good initial laser alignment in the fluorescence detection scheme (the signals can usually be increased by an additional factor of two upon further beam adjustments). In addition, compared to the REMPI scheme, the H-atom fluorescence detection method is more applicable in experimental conditions where high-vacuum condition is not possible, e.g. in a cell (with typical pressure >1 mtorr), or in conditions where ion-detection is undesirable, i.e. to avoid stray electric fields >50 mV/cm, which is difficult.

The signal strength can potentially be improved by an order of magnitude if the two-photon Doppler-free detection scheme [43] would be applied to probe the H-atoms (e.g. a configuration with two counter-propagating H-atom probe beams), considering that the Doppler linewidth of the H-atom transition (3 cm^{-1}) [158] is significantly wider than the probe laser linewidth (0.20 cm^{-1}). A Doppler-free detection scheme would be challenging to implement in a laser beam configuration in which the pump beam is collinear with the two counter-propagating H-atom probe beams (the most ideal configuration which would maximize spatial overlaps among the laser beams),

---

[1] This estimate is based on the experimental condition described in Ref [31]. In the H-atom REMPI experiment, a skimmer with 1 mm orifice diameter was placed approximately 5 cm downstream from the position of the supersonic nozzle (1 mm orifice diameter).

because an optical beam-combiner for the acetylene pump beam (212 nm) and one of the two counter-propagating H-atom probe beams (205 nm) is not readily available.

The limiting factor in the s/n ratio of the current H-atom fluorescence action spectrum is the presence of a non-zero background signal, which is *independent* of the UV pump beam (212 nm), but *dependent* on the presence of both the H-atom probe beam (205 nm) and acetylene molecules. The background signal has the same fluorescence decay time as the H-atom fluorescence signal resulting from acetylene transitions near 212 nm (the desired $\tilde{\mathrm{A}} - \tilde{\mathrm{X}}$ transitions probed in the experiment), but the background is more sensitive to the power of the 205 nm beam than the desired H-atom signal. It seems most likely that the background signal also comes from H-atom fluorescence, and it is a result of a one-color 1+2 process. The first 205 nm photon excites the acetylene molecule (either resonantly or near-resonantly) into strongly predissociated S_1 levels. The resulting H-atoms are probed by two additional 205 nm photons, which gives rise to the constant background signal. Note that a weak acetylene absorption band has been observed near 205.19 nm [170], which is close to the wavelength of the H-atom probe beam (205.14 nm).

In practice, given that the background signal has higher-order power dependence on the 205 nm beam than the desired H-atom signal (due to acetylene transitions near 212 nm), the optimal s/n ratio is achieved when the 205 nm probe beam is weakly focused at the center of the molecular beam (i.e. the 205 nm beam interacts with the molecular beam ~1 cm away from the tightest focal spot), so that the background is reduced while the desired H-atom signal still remains strong.

3.4 Photofragment Fluorescence Action Spectroscopy

3.4.1 Results

Given that a *single* UV laser beam is used for both $\tilde{\mathrm{A}} - \tilde{\mathrm{X}}$ excitation and immediate photo-fragmentations, the photofragment fluorescence detection method is exceptionally easy to implement. Even IR-UV double-resonance $\tilde{\mathrm{A}} - \tilde{\mathrm{X}}$ excitation, which

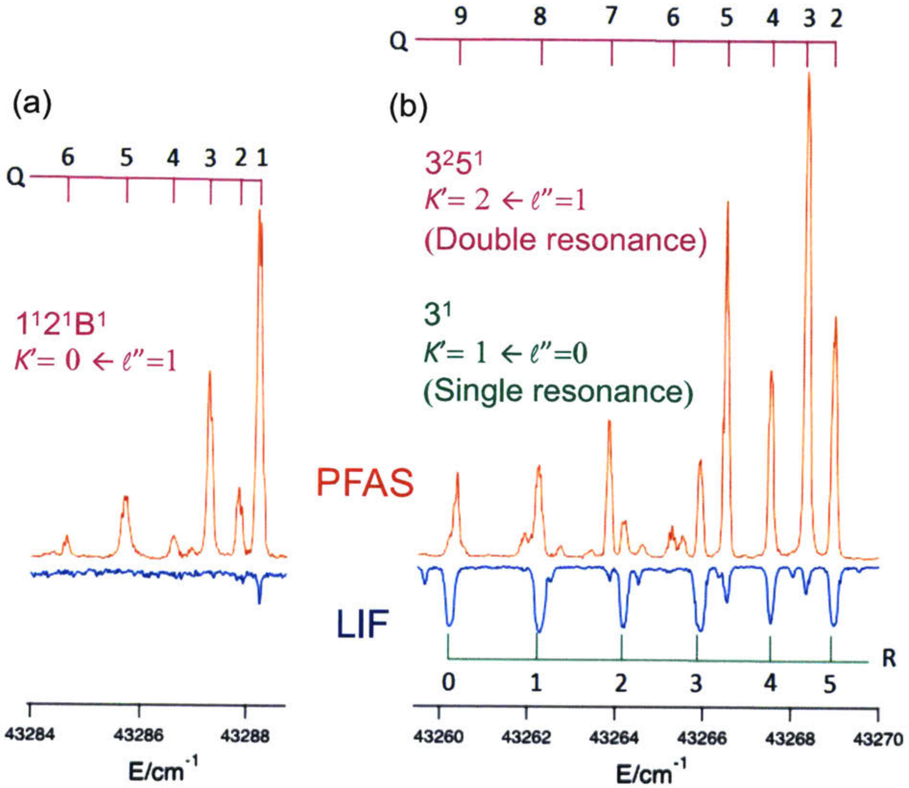

Figure 3-6: Comparison of spectra obtained with PFAS (upward-pointing spectra, orange) and IR-UV double-resonance LIF (downward-pointing spectra, blue). The horizontal-axis represents the energy of the excitation UV-photon used in IR-UV double-resonance excitation scheme. (a) IR-UV double-resonance excitation spectrum of the $1^12^1B^1$ $K = 0$ level. The rotational assignments are shown as horizontal tie-lines in magenta. (b) IR-UV double-resonance excitation spectrum of 3^25^1 $K = 2$ level (only the Q-branch spectrum is shown). The rotational assignments are shown as horizontal tie-lines in magenta. The IR-UV double-resonance spectrum accidentally overlaps with the R-branch of strong single-resonance excitations into 3^1 $K = 1$ rotational levels. The rotational assignments of the single-resonance transitions are shown as horizontal tie-lines in green. Note that the oscilloscope is intentionally saturated for the single-resonance signals in order to reveal much weaker double-resonance signals. In addition, only the early (20 ns) fluorescence time-window is integrated to generate the LIF spectrum. Therefore, the total single-resonance LIF signals are at least an order of magnitude stronger than it appears to be in part (b).

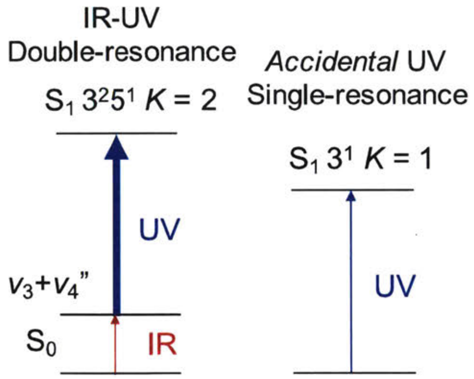

Figure 3-7: Level diagrams of IR-UV double resonance transitions into $S_1\ 3^2 5^1\ K = 2$ levels and *accidental* single-resonance UV transitions into $S_1\ 3^1\ K = 1$ levels. The expected relative strengths of the two types of UV transitions are illustrated by the relative thicknesses of the blue arrows.

is challenging to apply in the H-atom fluorescence detection (which involves precise alignment of an additional focused UV probe laser with two focused IR and UV pump beams), can be easily implemented in the PFAS scheme. The IR-UV double-resonance spectra provide information about the ungerade S_1 vibrational levels, which are inaccessible by single-resonance UV excitation.

The PFAS scheme is applied to record high-resolution IR-UV double-resonance (via $J = 1-5$, f-symmetry rotational levels of the $\nu_3+\nu_4''$ IR combination level) action spectrum of S_1 acetylene, in the 46700-47200 cm^{-1} region (600-1200 cm^{-1} above the predissociation limit). Among all the techniques (LIF, H-atom fluorescence, H-atom REMPI, and PFAS) used to study predissociated S_1 levels in the 47000 cm^{-1} region, the PFAS method has the highest s/n ratio (the other three techniques have similar s/n ratio in this energy region). As shown in Fig 3-6(a), transitions into $1^1 2^1 B^1$ $K = 0$ rotational levels (>1100 cm^{-1} above the predissociation limit) are much more prominent in the PFAS spectrum compared to the LIF spectrum (i.e. only the Q(1) transition is observed in the LIF spectrum).

The PFAS signals are observed for levels both below and above the predissociation limit. In the UV scan region of Fig. 3-6(b), there exists both IR-UV double-resonance transitions into $3^2 5^1$ $K = 2$ rotational levels (~1000 cm^{-1} above the predissociation threshold) and *accidental* single-resonance (UV) transitions into 3^1 $K = 1$ rotational levels ($\sim$2000 cm^{-1} below the predissociation threshold). The level diagrams associated with the two types of transitions are shown in Fig. 3-7. Without predissociation, the UV transitions in the IR-UV double-resonance excitation are expected to be approximately an order of magnitude stronger than the single-resonance UV transition, based on observed absorption intensity as a function of quanta in ν_3' [75, 127, 173]. The actual observed ratio is expected to be smaller, due to the fact that the IR-UV signals are subject to finite IR-pumping efficiency. By comparing the relative intensity of the $3^2 5^1$ Q(3) peak (labeled by the magenta tie-line) and the 3^1 R(3) peak (labeled by the green tie-line) in the PFAS and LIF spectra of Fig. 3-6b,[2] it is clear that the intensity ratio in the PFAS spectrum agrees with the expectation, but in the LIF spectrum, single-resonance transitions into the non-predissociated 3^1 level are at least an order of magnitude stronger than the double-resonance transitions into the predissociated $3^2 5^1$ level (note that the single-resonance LIF signals are saturated, as specified in the caption of Fig. 3-6). This implies that, while the LIF signals are strongly affected by predissociation, the PFAS signals are not. This is expected, because the PFAS signal originates from excitation of S_1 acetylene (discussed in Chapter 4) and should therefore scale linearly with the S_1 population, which is proportional to the $\tilde{A}$-$\tilde{X}$ transition probability. Dependence of the S_1 photodissociation cross-section on the identity of the S_1 level could potentially spoil the proportionality between the PFAS signal and the $\tilde{A}$-$\tilde{X}$ transition probability. However, I do not expect significant level-dependence, based on the study of PFAS signals originating from the close-lying S_1 *trans*-conformer 3^4 and *cis*-conformer $3^1 6^1$ levels (discussed in Chapter 4).

3.4.2 Discussion

Due to large wavelength differences between the excitation laser (212-235 nm) and the detected fluorescence (visible), scattered laser light can be essentially eliminated in the PFAS detection scheme. This significantly reduces the noise level in the PFAS detection. In comparison, both LIF and H-atom fluorescence detection of predissociated

---

[2] The $3^2 5^1$ Q(3) peak and 3^1 R(3) peak are chosen for the comparison, because those two peaks are not accidentally overlapped with other single-resonance and double-resonance transitions.

S_1 levels suffer from a significant background signal (among other problems). Due to the similarity in wavelength between the UV excitation and fluorescence wavelength (<100 nm apart), as well as short lifetime of the LIF signal (which precludes gating of the fluorescence), it is difficult to minimize the background UV scattered light in the LIF detection scheme. The background in the H-atom fluorescence scheme has been discussed in 3.2.1, and it is intrinsic to the technique and the molecular system studied, although it can be minimized by using a lower H-atom probe power density.

Investigations of the mechanisms of the PFAS signals are the subject of Chapter 4, and the spectroscopic characters of the PFAS signals are only briefly discussed here. The PFAS signals are in the visible range (fluorescence from the S_1 levels is concentrated around 300 nm, although this fluorescence does extend into the visible). It has a non-linear dependence on the power of the $\tilde{A}$-$\tilde{X}$ pump laser (power-index of 1.6, which implies some laser-saturation effect). The fluorescence time-dependence of the PFAS signal has at least a bi-exponential decay pattern, with ~120 ns and ~2 μs decay times, respectively (in comparison, LIF signals from predissociated S_1 levels have sub-10 ns lifetimes). There appears to be another even faster decay process present in the PFAS signal (~20 ns), but it is difficult to determine the lifetime accurately from the recorded 2 μs-long signal. By dispersing the visible fluorescence using a monochromator, as well as careful analysis of the undispersed PFAS fluorescence time-traces (both of which are discussed in Chapter 4), I am able to show that one-color multi-photon excitation of acetylene results in three main emission features. The strongest feature is due to C_2 Swan-band emission ($d^3\Pi_g - a^3\Pi_u$, which corresponds to the observed 120 ns decay), centered strongly at 470 nm, followed by weaker C_2 Deslandres-d'Azambuja band emissions centered around 380 nm ($C^1\Pi_g - A^1\Pi_u$, which corresponds to the fastest decay). Underlying the strong discrete features is a near-continuum long lifetime (>2 μs) background emission, the intensity of which grows steadily from 400 nm to the red. The long lifetime visible fluorescence has been observed in previous VUV photodissociation studies of acetylene [21, 26, 157], and was attributed to C_2H emissions (as far as I know, none of the available ab initio calculations, e.g. Refs [21] and [141], have been able to yield unambiguous assignments of the observed electronic transitions). It seems likely that the filter choice in the initial PFAS experiments is far from optimal. Nevertheless, the s/n ratio of the PFAS spectra with a 550 nm long-pass filter is already superior to the s/n ratio in any other techniques applied to the S_1 predissociated levels.

The most likely path for the generation of the detected photofragments is as follows: the acetylene molecules are pumped by the initial UV excitation into an S_1 level. The same focused UV beam (which competes with S_1 predissociation) immediately excites the S_1 molecule into the ~90000 cm^{-1} energy region, where a fast dissociation channel into electronically-excited C_2H is known to exist [3, 21, 26, 92, 98–100, 162, 163]. The resulting electronically excited C_2H fragments (which are long-lived) are subsequently excited by another UV photon into even higher-lying states, which dissociate into $d^3\Pi_g$ and $C^1\Pi_g$ states of C_2.

Given the observed intensity of the photofragment emission signals, photodissociation by excitation from the S_1 state must be fairly efficient and selective. The $d^3\Pi_g$ and $C^1\Pi_g$ states of C_2, both of which have a π^3 electronic configuration [27, 28], are selectively populated after photodissociation of the S_1 state, which has $\pi^3\pi^*$ configuration [82, 92]. I believe that the C_2 Swan band detection scheme can be a generalized sensitive detection method for alkyne and alkyne derivatives (R_1CCR_2). Assuming that the electronic structures of R_1CCR_2 and the C_2R fragment are similar to those of C_2H_2 and C_2H (as far as the π electrons are concerned), I expect that photodissociation from the S_1 level of R_1CCR_2 will lead to a similarly efficient production of the C_2 $d^3\Pi_g$ state.

3.5 Conclusion

I introduce two new experimental detection schemes to obtain high-resolution action spectra of predissociated S_1 acetylene levels. The development of those new experimental techniques is essential to the ongoing study of the S_1 *cis-trans* isomerization process, which has been hindered by the reduced LIF signals due to S_1 predissociation.

H-atom fluorescence detection is an improvement over the more widely-used H-atom REMPI detection, both in terms of improved s/n ratio and experimental convenience. It is also valuable for characterizing the predissociation mechanisms of the S_1 state of acetylene. The new H-atom fluorescence detection can be easily applied to other predissociated (and dissociated) molecular systems, where H-atoms are produced.

The photofragments (C_2 and C_2H) fluorescence detection scheme provides the highest s/n ratio among all of the other techniques used in my experiments (LIF, H-atom fluorescence, and H-atom REMPI detection) to study predissociated S_1 levels in the 47000 cm^{-1} region. The PFAS technique is easy to implement, because only a single UV laser beam is used for both $\tilde{A}-\tilde{X}$ excitation and subsequent level-probing. The superior s/n ratio of the PFAS method relies on the high efficiency of multi-photon dissociation from S_1 acetylene to produce fluorescing photofragments, and its usefulness might be general to S_1 acetylene and similar π^3 systems.

Chapter 4

One-color (212 – 220 nm), Resonance-enhanced (S_1–S_0), Multi-photon Dissociation of Acetylene

Abstract

One-color (212 – 220 nm), multi-photon dissociation of acetylene, resonance-enhanced by rotation-vibration lines of the S_1-S_0 transition, gives rise to strong photofragment fluorescence signals in the visible and near UV regions. The photofragment fluorescence detection scheme has been applied to obtain high-resolution action-spectra of predissociated S_1 acetylene levels near 47000 cm^{-1} (discussed in Chapter 3), and provides significantly higher signal-to-noise ratio than acetylene S_1 LIF, H-atom fluorescence, and H-atom REMPI detections. In this work, fluorescence signals from the photofragments, excited via three intermediate S_1 levels ($K = 1$, $J = 6$, e-symmetry levels of *trans* 3^4, *trans* 3^5, and *cis* $3^1 6^1$ vibrational states), are studied, both in a flow cell and under supersonic jet conditions. In the flow cell (~3 torr), dispersed fluorescence (DF) spectra of the photofragments are obtained. For all three S_1 levels, we observe C_2 Swan band ($d^3\Pi_g \rightarrow a^3\Pi_u$) and C_2 Deslandres-d'Azambuja band ($C^1\Pi_g \rightarrow A^1\Pi_u$) fluorescence. Under the supersonic jet conditions (collision-free), fluorescence time-traces at selected wavelength regions are analyzed. We confirm the presence of the two C_2 emission band systems. The relative intensities of the two emission bands are also in agreement with what we observe in the DF spectra. In addition, we observe a long-lifetime visible fluorescence signal (>3 μs lifetime), which is likely due to emission from electronically-excited C_2H fragments. The

photodissociation mechanism is inferred, based on our analysis of the DF spectra and the fluorescence time-traces obtained under the supersonic jet conditions. The electronically-excited C_2H is generated from two-photon photodissociation of acetylene (resonance-enhanced by the acetylene S_1-S_0 transition), and an additional photon photolyzes the C_2H fragment, producing the C_2 C and d states.

The dispersed fluorescence work described in this chapter was performed with Angelar Muthike, including significant contributions from T. J. Barnum, who helped me set up the monochromator. T. J. Erickson and C. L. Keenan also helped with initial setup of the experiment.

4.1 Introduction

In Chapter 3, I describe a new detection scheme for S_1 acetylene levels, based on photofragment emission. The signal-to-noise ratio of the photofragment fluorescence action spectra (PFAS) of predissociated S_1 levels is superior to the laser-induced fluorescence (LIF) and the two H-atom (H-atom fluorescence and REMPI) detection methods. The PFAS scheme is also easy to implement, because a *single* UV laser beam is used for both S_1-S_0 excitation and the subsequent multi-photon dissociation. Given the observed bi-exponential decay pattern (observed using a 550 nm long-pass filter), with $\sim$120 ns and $\sim$2 μs decay times, the C_2 Swan-band emission ($d^3\Pi_g - a^3\Pi_u$) and emission from electronically highly excited C_2H fragments, which have been observed in earlier vacuum UV (VUV) studies of acetylene [17, 21, 26, 63, 122, 123, 138, 156, 157], are present.

In this chapter, the photofragment fluorescence signals are studied in detail. Specifically, I choose the $K = 1$, $J = 6$, e-symmetry levels of S_1 *trans* 3^4, *trans* 3^5 and *cis* 3^16^1 vibrational levels as the intermediate S_1 levels *en route* to photofragmentation. The fluorescence signals from all three S_1 levels are dispersed by a monochromator so that the identities of the photofragments are determined unambiguously (the dispersed fluorescence experiments are carried out in a flow cell, with an effective pressure of 3 torr). The fluorescence time-traces of the photofragments generated in the collision-free supersonic-jet condition are also analyzed, and the results agree with the interpretation of the dispersed fluorescence spectra recorded at the considerably higher pressure flow-cell condition.

Among the three groups of S_1 levels, only the *trans* 3^5 are predissociated. The *trans* 3^4 and *cis* $3^1 6^1$ $K = 1$ levels are not detectably predissociated (despite the fact that the energies of both levels lie slightly higher than the acetylene predissociation limit at 46074±8 cm^{-1} [112], as discussed in the last paragraph of Section 4.4). In addition, the *cis* $3^1 6^1$ level is qualitatively different from the two *trans* levels, because this *cis* level is largely localized in the S_1 *cis*-conformer well, while the two *trans* levels are localized in the *trans* well. Analyses of photofragments from those three distinctively different S_1 acetylene levels provide insight into the mechanism of the one-color (212-220 nm), resonance-enhanced (S_1-S_0), multi-photon dissociation of acetylene, which is qualitatively different from the widely-studied one-color photolysis of acetylene using a 193 nm ArF laser [5, 39, 40, 101, 124, 148, 167, 179] (discussed in Section 4.5.3).

4.2 Experiments

4.2.1 Dispersed fluorescence experiment in a flow cell

The dispersed fluorescence (DF) spectra of photodissociation products of $K = 1$, $J = 6$, e-symmetry levels of S_1 *trans* 3^4, *trans* 3^5 and *cis* $3^1 6^1$ states are studied in this work. The UV excitation laser beam is focused by an $f = 50$ cm lens into a cell. A constant flow of acetylene (BOC, atomic absorption grade 2.6, 99.6% purity) is added to the cell, which is actively pumped by a rotary-vane pump (Edwards, E2M1.5). The acetylene flow rate is controlled by a needle valve, and the effective cell pressure is ∼3 torr during the experiments, measured by a MKS Baratron (Model 626) pressure gauge.

The fluorescence from photodissociation products is collected and imaged onto the entrance slit of a 3/4 meter monochromator (Spex 750M), by a two-lens system ($f/6$). The monochromator is equipped with a 2400 grooves/mm grating blazed at

400 nm. In all of the DF experiments described in this work, the entrance and exit slit-widths of the monochromator are fixed at 1 mm (which corresponds to a spectral resolution of ~0.4 nm at 600 nm). The monochromator is scanned (0.125 nm/step) during the experiment, and the dispersed fluorescence at each step of the grating position is detected by a photomultiplier tube (PMT, Hamamatsu R928). The PMT output signal is monitored on a digital oscilloscope (LeCroy, 9310), and the data are transferred to a computer for storage and post-processing. The fluorescence time-trace (total of 1 μs) at each grating position is integrated numerically to generate the DF spectrum. Typically, the signal is averaged for $20 - 30$ laser shots at each grating step. The wavelength of the monochromator ($300 - 700$ nm) is calibrated by an iron-neon hollow cathode lamp (Starna Cells) to an accuracy of ±0.02 nm (recorded with a slit-width of 0.3 mm).

Given that typical acetylene S_1 LIF signals are in the UV ($230 - 350$ nm), the second-order dispersed light from the LIF interferes with the first-order dispersed light from the visible fluorescence from the photofragments. To avoid interference, a 400-nm long-pass filter (Thorlabs) is placed after the entrance slit of the monochromator to block the second-order S_1 LIF (i.e. the monochromator is effectively operated in the first order of the grating).

The UV excitation beam ($212 - 220$ nm) is generated by a Sirah Cobra-Stretch dye laser, pumped by the third harmonic of a Q-switched, injection-seeded Nd:YAG laser (Spectra-Physics PRO-270), operating at 20 Hz. The dye laser output ($420 - 440$ nm) is frequency-doubled with a β-barium borate crystal (BBO) to produce the UV radiation, with an energy of 150-250 μJ/pulse. The fundamental frequency of the dye laser is monitored by a wavemeter (Coherent, WaveMaster).

4.2.2 Photofragment fluorescence detection in a supersonic jet

To verify the results from the flow-cell DF experiments, total fluorescence signals are collected by a PMT (Hamamatsu, R331) under the supersonic jet conditions, described in detail in Chapter 3. Specifically, the $K = 1$, $J = 2$, e-symmetry levels of *trans* 3^4 and *cis* $3^1 6^1$ vibrational states are studied. Four band-pass filters

(FWHM=10 nm) (Thorlabs) are used to sample the photofragment fluorescence signals at 360 nm, 430 nm, 470 nm, and 514.5 nm. A 400 nm long-pass filter (Thorlabs, FGL400S) is also used to collect total photofragment fluorescence signal at wavelength >400 nm. Normal acetylene S_1 LIF signals from the two S_1 levels are collected (using a UG-5 filter), with an unfocused UV excitation laser beam.

4.3 Dispersed Fluorescence Spectra of the Photofragments

DF spectra of photodissociation products of S_1 *trans* 3^4, *trans* 3^5, and *cis* $3^1 6^1$ levels are shown in Fig.4-1. Four main features appear in each spectrum. The strongest fluorescence signals come from C_2 Swan-band emission ($d^3\Pi_g - a^3\Pi_u$), centered at 470 nm, followed by weaker (by approximately a factor of four) C_2 Deslandres-d'Azambuja band emissions centered around 380 nm ($C^1\Pi_g - A^1\Pi_u$). In addition, there is a relatively weak feature at ~430 nm which can be assigned as a CH $A^2\Delta - X^2\Pi$ band. In the UV region (240-320 nm), weak and short-lived S_1 LIF signals (~10 ns) are observed from the predissociated *trans* 3^5 level; relatively strong and longer-lived S_1 LIF signals (~100 ns) are observed from the *trans* 3^4 level; LIF signals are not observed from the *cis* $3^1 6^1$ level. Note that fluorescence from the *trans* 3^4 level extends into the near-UV region, and overlaps with the C_2 Deslandres-d'Azambuja emission band.

The absence of LIF from the *cis* $3^1 6^1$ level is likely a consequence of collisional quenching. From the observed shortened lifetime of the LIF signal from the *trans* 3^4 level (250 ns → 100 ns), the collision-limited lifetime in our gas flow cell is estimated to be ~100 ns, which is significantly shorter than the lifetime of the *cis* $3^1 6^1$ level (>1 μs). In addition, the *cis* $3^1 6^1$ level, with a calculated *b*-axis electric dipole moment of 2.5 Debye, is likely more subject to collisional quenching than the *trans* level, which does not have a permanent electric dipole moment. I believe that the vast majority of the LIF from the *cis*-conformer is collisionally quenched, and thus not observable

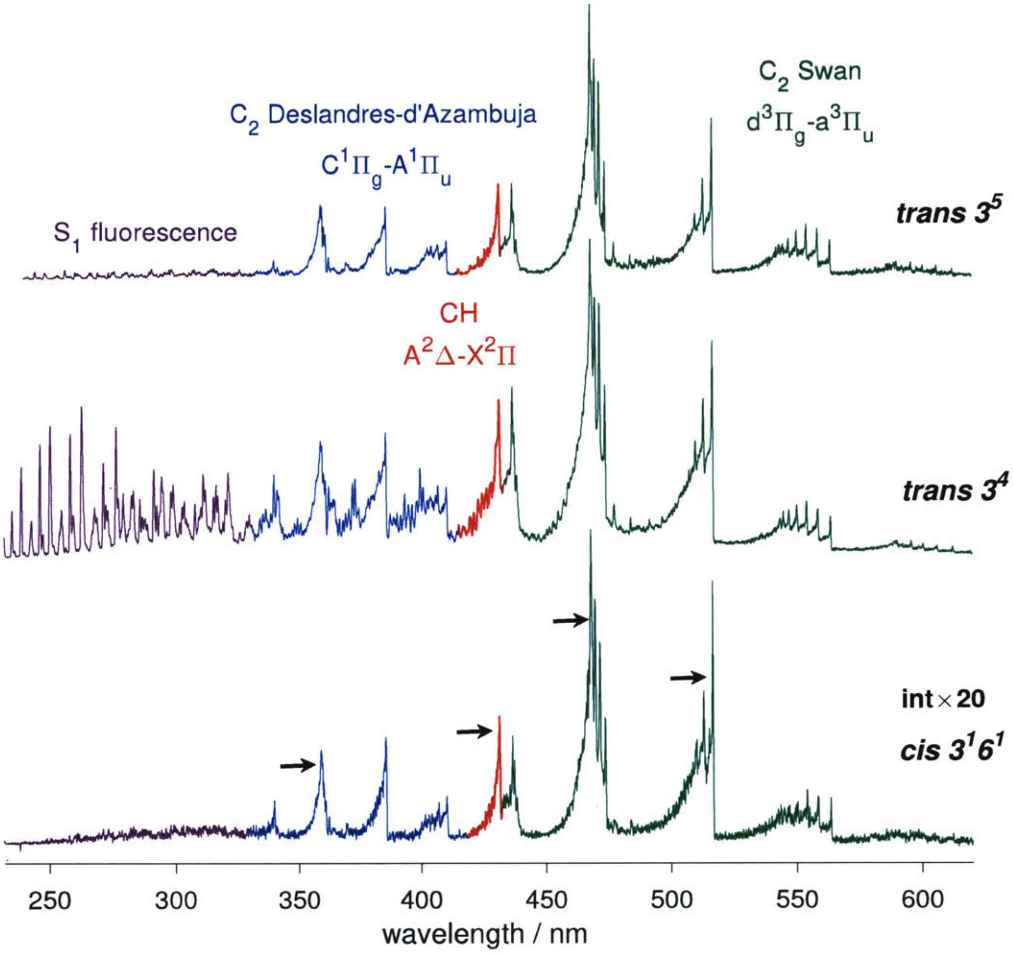

Figure 4-1: Dispersed fluorescence spectra of photodissociation products from $K = 1$, $J = 6$, e-symmetry levels of S_1 *trans* 3^5 (top panel), *trans* 3^4 (middle panel), and *cis* 3^16^1 (bottom panel) vibrational states. The signal intensities are scaled to correct for the wavelength-dependent quantum yield of the PMT. The four main emission features are color-coded on each DF spectrum. In the supersonic-jet setup, four band-pass filters (FWHM=10 nm) are used to sample the total fluorescence signals near 360 nm, 430 nm, 470 nm, and 514.5 nm, which correspond, respectively, to the locations of the four peaks marked by arrows on the bottom graph. The DF spectrum from the *cis* 3^16^1 level is magnified 20× in order to be shown on the same intensity scale as the other two spectra.

in the experimental conditions. The measured lifetimes of both C_2 emission bands agree to within 20% of the literature values [16, 41, 119], which indicates that the C_2 signals are not significantly quenched in the cell. The fluorescence lifetime of the CH emission is collisionally shortened from 500 ns [15, 101] to 150 ns.

4.3.1 Population distribution of the C_2 $C^1\Pi_g$ and $d^3\Pi_g$ states

In order to gain information regarding the C_2 rovibrational population in the $C^1\Pi_g$ and $d^3\Pi_g$ states, I carry out contour fits to the observed C_2 $C-A$ and $d-a$ emission bands from the DF spectra. The C_2 rovibrational population in each electronic state (C or d) is fitted with one vibrational and one rotational temperature, both of which are assumed to follow a Boltzmann distribution. The $C-A$ and $d-a$ transition probabilities, and rotational constants of vibrational levels of all four electronic states are needed for the contour fits. Specifically, $d-a$ Franck-Condon factors, based on RKR calculation in Ref [149] and molecular constants from Ref [159], are used for the $d-a$ transitions. The determination of $C-A$ transition probabilities requires explicit deperturbation of electrostatic interactions between at least two electronic configurations, which are discussed in detail in Chapter 9. The $C-A$ transition probabilities used in this chapter are based on results from Chapter 9.

In this work, the rotational and vibrational temperatures of the C_2 C and d states are derived from the DF spectrum of *trans* 3^5 in Fig.4-1, using the contour-fitting function in Pgopher [176]. Rotational and vibrational temperatures derived from all three DF spectra in Fig. 4-1 are expected to be similar, given qualitative similarities among the three spectra in the $350-600$ nm region. I choose the DF spectrum from

Table 4.1: Derived effective rotational and vibrational temperatures of C_2 in the $C^1\Pi_g$ and $d^3\Pi_g$ states, based on the DF spectrum of *trans* 3^5 level in Fig.4-1.

	T_{rot}/K	T_{vib}/K
$C^1\Pi_g$	3711(70)	4672(55)
$d^3\Pi_g$	4432(46)	8954(60)

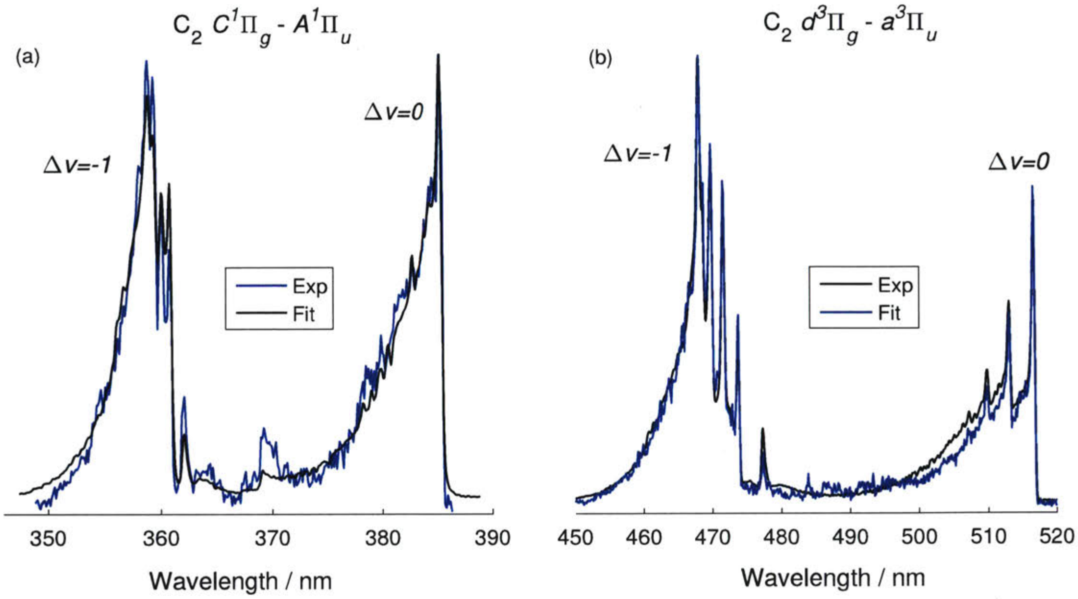

Figure 4-2: The fitted (black) and experimental (blue) DF spectra of C_2 $C^1\Pi_g$ (a) and $d^3\Pi_g$ (b) states (excited via the *trans* 3^5 level). To fit to the low-resolution DF spectrum in Fig.4-1, each transition is assumed to have a Voigt profile (as modeled in the contour-fit).

the *trans* 3^5 level for the fitting, because the photofragment signals in the 3^5 DF spectrum are not overlapped by the S_1 LIF signal, as in the 3^4 DF spectrum, and the signal-to-noise ratio of the 3^5 DF spectrum is better than that of *cis* $3^1 6^1$. The derived C_2 rotational and vibrational temperatures in the C and d states are given in Table 4.1, and the fitted rotational and vibrational contours are shown in Fig. 4-2. It is clear that both C and d states of C_2 are generated with moderately high vibrational excitation (e.g. vibrational levels with $v = 5$ and above are observed for both C and d states) and substantial rotational excitation (i.e. the maximum in the rotational population is broadly around $J \approx 30$ for both the C and d states).

The quality of the fit to the C_2 $C - A$ emission is not as good as the fit to the C_2 $d - a$ emission, especially for the $C - A$ $\Delta v = -1$ band. I believe that the rotational temperature of the $v = 0$ level of the C_2 C state is accurately determined, because the rotational contour of the $C - A$ $\Delta v = 0$ band, dominated by the $0 - 0$ transition (approximately an order of magnitude stronger than the $1 - 1$ transition), is well-fitted. It also seems that a single rotational temperature can be used to describe the rotational population of all the observed C-state vibrational levels. As shown in Fig. 4-2a, even for the $C-A$ $\Delta v=-1$ band, the rotational contour in the $350-360$ nm region, composed of several C-state levels with $v \geq 1$, is relatively well-reproduced with the C-state rotational temperature given in Table 4.1. Therefore, the problem with fitting the $\Delta v=-1$ band seems to indicate that the derived vibrational temperature of the C_2 C state might not be accurate. There are two possible causes for this. First, the $C-A$ transition probabilities might not be accurately determined, despite my attempts to deperturb the interactions between different electronic configurations (discussed in Chapter 9). A comparison with results from high-level *ab initio* calculations is needed to confirm the accuracy of my deperturbation. It is also possible that the vibrational distribution of the C_2 C state does not resemble a Boltzmann distribution as closely as that of the C_2 d state. However, given that the $v=5$ C-state vibrational level has been observed (e.g. the $v=5 \rightarrow 4$ transitions at ~362 nm), in agreement with the C-state vibrational temperature obtained from the contour fit, I believe that the derived C-state vibrational temperature properly characterizes the C_2 C-state vibrational popolation. From the ratio of the total emission intensity[1] between the C_2 $C-A$ and $d-a$ emission bands in Fig. 4-1, I estimate that total population in the d state is approximately four times larger than that in the C state.

4.4 Photofragment Fluorescence under Collision-free Conditions

Since the observed fluorescence intensities in the flow cell are subject to collisional quenching, it is necessary to compare the DF results in Fig. 4-1 with experiments carried out in the collision-free environment, in which the fluorescence is not dispersed. Specifically, photofragment fluorescence signals from close-lying *trans* 3^4 and *cis* $3^1 6^1$ levels are generated in the collision-free region of the supersonic expansion (described

---

[1] The total $C-A$ and $d-a$ emission intensities are obtained, respectively, by numerically integrating (over wavelength) the DF spectrum of *trans* 3^5 (Fig.4-1) in the $330-415$ nm and $432-615$ nm regions.

in detail in Chapter 3). Four band-pass filters (FWHM=10 nm) are used to sample the total fluorescence signals at 360 nm, 430 nm, 470 nm, and 514.5 nm, which correspond, approximately, to the locations of the four peaks marked by arrows on the bottom section of Fig. 4-1. The peak at 360 nm is dominated by the $\Delta v = -1$ transitions of the C_2 $C - A$ band (where Δv is the change in the vibrational quantum numbers during emission); the peak at 430 nm is dominated by the CH emission; and the last two peaks correspond, respectively, to $\Delta v = -1$ and $\Delta v = 0$ transitions of the C_2 $d-a$ band system. If results from the cell experiment are valid, all three photofragments (the C_2 C and d states, and the CH A state) should be present in the collision-free environment. The relative emission intensities of the three photofragments in the four chosen fluorescence wavelength regions should also be similar in the two experimental conditions.

From the collision-free photofragment fluorescence signals, it is obvious that there is an additional long lifetime component (>2 μs) in the fluorescence time-traces of both *trans* 3^4 and *cis* 3^16^1 levels (the species responsible for the long-lived signal will be discussed in detail later in this section). Similar long lifetime signals have also been observed from $K = 1$ rotational levels of *trans* 3^1 and *trans* 3^5 vibrational levels, and from all of the ungerade vibrational levels in the $46700 - 47200$ cm^{-1} region (observed via the IR-UV double resonance experiment described in Chapter 3). The long lifetime signal is not observed in the DF experiment in the cell, likely due to collisional quenching. The long lifetime signal has been observed in previous VUV photodissociation studies of acetylene [17, 21, 26, 63, 122, 123, 138, 156, 157], and that signal was attributed to emission from electronically excited C_2H fragments (C_2H^*). The electronic assignment of the observed C_2H^* emission is, however, not well-estabilished (see discussions in Section 4.5.3).

4.4.1 Analysis of the photofragment fluorescence time-traces

To obtain relative intensities of various emissive species in the undispersed fluorescence signals from the *trans* 3^4 and *cis* 3^16^1 levels (collected with band-pass filters centered at 360 nm, 430 nm, 470 nm, and 514.5 nm), the fluorescence time-traces are fitted to multiple-exponential decay curves. Given that a pulsed-laser is used to generate the photofragments, the fluorescence time-trace has a sharp 10 ns turn-on (i.e. it takes ~10 ns for the signal to increase from zero to maximum intensity) before the decay (see Fig. 4-3). Only the decay portion of the signal is included in the fit. Each of the four main emission features in Fig. 4-1 is assumed to have a single characteristic decay time. Given that C_2H^* fluorescence is also observed in the supersonic jet setup, I include one additional time constant in the fit for the long lifetime signal. To avoid overfitting (i.e. preventing the fitted amplitude from becoming negative for certain species at some wavelength), decisions must be made regarding which emissive species to include at each wavelength, based on the observed DF spectrum in Fig. 4-1. By using the following fitting strategy, I am able to obtain, for each of the fitted time-traces, an R^2 coefficient at least greater than 0.995.

Before I fitted the time-trace at the four wavelengths, I did two additional experiments to accurately determine the lifetimes of the S_1 *trans* 3^4 and *cis* $3^1 6^1$ levels. In those two experiments, the UV excitation lasers are unfocused, and only the UV fluorescence is collected (by using a UG-5 filter). At 514.5 nm, the photofragment fluorescence signal is fitted to a bi-exponential decay (C_2 Swan band and C_2H^* signal). At 470 nm, it is necessary to include the S_1 LIF decay in the fit, in addition to the Swan band and C_2H^* emissions. At 360 nm, a short lifetime ~30 ns decay (C_2 Deslandres d'Azambuja) is present, and the C_2H^* signal is absent. At 430 nm, the C_2 Deslandres d'Azambuja, C_2H^*, and S_1 fluorescence signals are present, but the CH $A - X$ emission, with expected lifetime of ~500 ns [15, 101], is absent from the fluorescence time-trace obtained in the collision-free experiment, as shown in Fig. 4-3 for the *cis* $3^1 6^1$ level. The observed CH population in the $A^2\Delta$ state in the flow cell environment might be a result of secondary chemical reactions (i.e. the CH $A^2\Delta$ fragment could have been generated from chemical reactions between acetylene and an electronically excited species, instead of directly photo-induced). Given that fluorescence signals from CH have a laser-pulse limited rise-time at cell pressure as low as 280 mtorr (which corresponds to a mean collisional time >100 ns), at least one of the precursor molecules to the CH $A^2\Delta$ state must be short-lived (<10 ns lifetime).

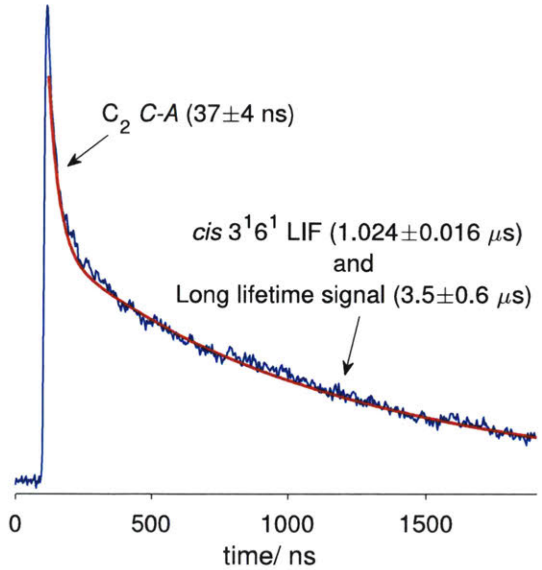

Figure 4-3: The fluorescence time-trace (recorded with a 430 nm band-pass filter) resulting from photodissociation via the *cis*-$3^1 6^1$ level. The experimental time-trace is shown in blue, and the fitted time-trace in red. The CH $A - X$ emission, with expected lifetime of ~500 ns, is not present in the time-trace.

The fit allows me to determine the total integrated fluorescence intensity of all three photofragments (C_2 C and d states, and C_2H^*) in each of the four chosen fluorescence wavelength regions. For the C_2 C state, given its relatively short fluorescence lifetime (37 ns, see Table 4.2), it is necessary to include its fluorescence intensity in the sharp turn-on region (10 ns) of the fluorescence signal.[2] The wavelength-dependent quantum yield of the PMT (Hamamatsu, R331) is corrected for in the fluorescence signals, based on the information provided by the manufacturer, so that fluorescence intensities in the four wavelength regions can be compared.

Fluorescence intensities of the two C_2 species at the four fluorescence wavelength regions (normalized to the intensity obtained at 470 nm) are shown in Fig. 4-4a. The C_2 fragments resulting from photodissociation of the S_1 *trans* 3^4 and *cis* $3^1 6^1$ levels in the supersonic-jet setup have essentially the same emission pattern, in agreement with DF spectra taken in the cell condition (Fig. 4-1). The derived (collision-free) fluores-

---

[2] For simplicity, the fluorescence intensity is assumed to increase at a constant rate from zero to the maximum intensity in 10 ns. The integrated fluorescence intensity in the turn-on region of the fluorescence signal is added to the integrated fluorescence intensity in the decay region to obtain the *total* integrated fluorescence intensity.

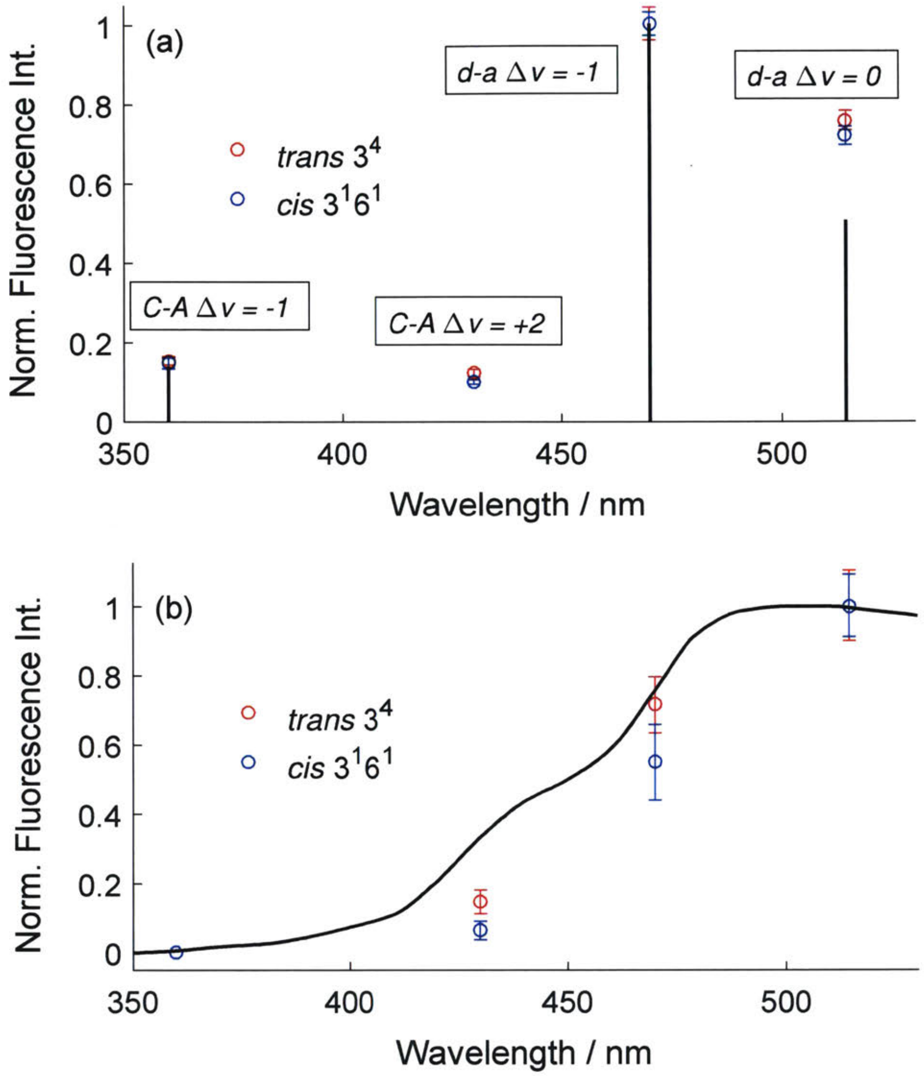

Figure 4-4: Normalized fluorescence intensities of (a) C_2 (normalized to the intensity at 470 nm) and (b) C_2H^* (normalized to the intensity at 514.5 nm) in the four chosen wavelength regions. In both (a) and (b), the red and blue circles are used to indicate, respectively, the derived fluorescence intensities of relevant photofragments from *trans* 3^4 and *cis* $3^1 6^1$ levels, generated in the supersonic-jet condition. The error bars represent 2σ uncertainties. In (a), the vertical sticks are used to indicate the integrated DF signals (integrated over wavelength) of *cis* $3^1 6^1$ level (Fig. 4-1) in the 360 nm, 470 nm, and 515 nm regions. The DF signals are weighted by the measured transmission of the band-pass filters, as specified by the manufacturer (Thorlabs). In (b), the experimental DF spectrum of the C_2H^* fragment (black curve) is shown (obtained from Ref [21]). The C_2H^* fragments were generated from VUV photodissociation of acetylene at 11 eV.

Table 4.2: Derived lifetimes of the observed photofragments generated from photodissociation of S_1 acetylene in the collision-free condition. The literature value of the C_2 d-state lifetime is taken as the averaged value of measured lifetimes of $v = 0 - 2$ levels (supersonic jet condition). The literature value of the C_2 C-state lifetime is taken as the averaged value of measured lifetimes of $v = 0 - 4$ levels (cell condition, with zero-pressure extrapolations). Numbers in parentheses are 2σ uncertainites of the last digits.

	This work		This work	Literature
trans 3^4	257(4) ns	C_2 $C^1\Pi_g$	37(4) ns	33(1) ns [41]
cis 3^16^1	1.024(16) μs	C_2 $d^3\Pi_g$	126(2) ns	103(6) ns [16, 119]
		C_2H^*	3.5(6) μs	$3 - 6$ μs [17, 21, 138]

cence intensities near 360 nm, 470 nm, and 514.5 nm can also be compared directly to the integrated DF signals (Fig. 4-1) at the three wavelength regions (weighted by the transmission of the band-pass filters).[3] The relative fluorescence intensity of the C_2 $C - A$ $\Delta v = -1$ band and the $d - a$ $\Delta v = -1$ band, derived from the supersonic-jet experiments, agree well with the DF result obtained in the flow-cell condition. In addition, the intensity ratio between $d - a$ $\Delta v = -1$ and $\Delta v = 0$ bands, which provides information regarding the vibrational temperature of the C_2 $d^3\Pi_g$ state, agree reasonably well (differing by ~25%) in the two experimental conditions (given that maximum peak intensities in pulsed dye laser experiments have typically 10 – 20% uncertainties for the number of averages used in our experiment). Considering near-quantitative agreement between the cell and supersonic jet experiments, it seems reasonable to assume that information about the C_2 fragments (e.g. vibrational and rotational temperatures given in Table 4.1) can be extracted reliably from the DF spectra (Fig. 4-1).

In Fig. 4-4b, normalized fluorescence intensities of C_2H^* at the four fluorescence wavelengths (normalized to the intensity obtained at 514.5 nm) are shown, along with the experimental DF spectrum [21] of the C_2H^* fragment (black curve, similarly normalized), generated from VUV photodissociation of acetylene at 11 eV (~0.6 eV lower than the two-photon energy of our UV excitation laser). The normalized fluorescence

---

[3] Comparison at 430 nm is not included, because the DF signal at 430 nm (obtained in the cell condition) is dominated by the collisionally-induced CH $A - X$ emission band.

Table 4.3: The ratios between the total integrated C_2H^* fluorescence intensity and the Swan band emission intensity (second–fourth column) at selected wavelength regions. The C_2H^*/LIF ratio in the >400 nm region is also included (fifth column). Numbers in parenthesis are 2σ uncertainty of the last digit. The derived ratios of total C_2H^* fluorescence with respect to the total Swan band (fourth column) and LIF emission (fifth column) in the >400 nm wavelength region are most likely the lower limits of the ratios, due to sharp decrease in PMT quantum yield at wavelengths longer than 520 nm (see discussion in the text).

ratio range	C_2H^*/Swan 470±10 nm	C_2H^*/Swan 514.5±10 nm	C_2H^*/Swan >400 nm	C_2H^*/LIF >400 nm
trans 3^4	1.4(1)	2.2(2)	>5(1)	>1.3(3)
cis 3^16^1	2.2(4)	4.7(3)	>9(3)	>1.6(4)

intensities of C_2H^* resulting from photodissociation of the two S_1 vibrational levels are similar to each other at the four selected wavelengths, and they agree qualitatively with the C_2H^* DF spectrum from the earlier study [21]. The lifetime of the C_2H^* fragment (see Table 4.2) also agrees with earlier measurements [17, 21, 138]. It seems likely that the long lifetime species observed in our supersonic expansion conditions is the same C_2H^* species observed in the VUV photodissociation studies of acetylene.

4.4.2 Relative population of C_2H^* and the C_2 *d*-state fragments

The ratios of total integrated C_2H^* fluorescence intensities with respect to the Swan band emission at selected wavelength regions are listed in Table 4.3 for excitation resonant with the *trans* 3^4 and *cis* 3^16^1 levels. Also included is the ratio between the C_2H^* fluorescence and the S_1 LIF signal in the >400 nm region. Given that the PMT used in the supersonic jet experiment is not red-sensitive (i.e. the PMT quantum yield is 2% at 600 nm, compared to ~30% at 420 nm), it is likely that most of C_2H^* fluorescence signal, which was observed by Boyé et al. [21] in the 550-800 nm region (following VUV photolysis of acetylene), is not detected in our supersonic jet experiment. In comparison, a significantly larger fraction of the C_2 Swan band emission and the acetylene S_1 LIF signal in the >400 nm region are detected, because the strongest region of the C_2 Swan band emission occurs at ~500 nm (~15% PMT quantum yield), and the visible wavelength region of the S_1 LIF signal is concentrated in the 400–450 nm region (~30% PMT quantum yield). As a result, the ratio of C_2H^* fluorescence with respect to the total Swan band (the fourth column in Table 4.3) and acetylene LIF emission (the fifth column in Table 4.3) in the >400 nm region are likely only the lower limit of the ratio.

Given that the observed quantities in *both* numerator and denominator in all four ratios in Table 4.3 are proportional to the S_1-S_0 transition probability (which is different between the two S_1 conformer levels), the S_1-S_0 transition intensity factor is canceled in the calculation of the intensity ratio. Each ratio thus reflects relative population of the two fluorescing species given in the numerator and denominator of the ratio. Since the C_2H^*/LIF ratio is observed here to be similar for the *trans* 3^4 and *cis* 3^16^1 vibrational states, photodissociation cross-sections to produce C_2H^* fragments from both of the S_1 conformer levels (i.e. the cross-section of HCCH $(S_1)\xrightarrow{h\nu}H+C_2H^*$) appear to be similar, assuming that the fraction of total LIF emission (which is proportional to the total number of S_1 molecules) in the >400 nm region is approximately the same for the two S_1 conformer levels.[4] The yield of the C_2 *d* state (the upper state of the Swan band emission), however, seems to be approximately twice as large from the *trans* 3^4 level compared to the *cis* 3^16^1 level. From the ratio between the total C_2H^* and Swan band emission (the fourth column in Table 4.3), I conclude that the population of the C_2H^* fragments is (at least) an order of magnitude larger than that of the C_2 *d* state.

4.4.3 The fluorescence lifetimes

I must point out that the derived lifetime of the C_2 *d* states (Table 4.2) in the supersonic jet condition of this work differs from the lifetime measured in earlier studies. I believe that the discrepancy comes from the fact that the lifetime derived

---

[4] A more careful investigation into the difference in photodissociation cross-sections between the two S_1 conformer levels is needed, because the C_2H^*/LIF ratio is only measured in the >400 nm region, while the majority of the acetylene LIF signal is expected to be around 300 nm and the emissions patterns can be different between the two S_1 levels.

in the current experiment is the lifetime averaged over several C_2 vibrational levels and a large number of rotational levels, because the band-pass filters used in our measurements have FWHM of 10 nm, and the C_2 d state is generated with high rotational ($J_{max} \approx 30$) and vibrational (i.e. vibrational levels with $v > 4$ are observed) excitations. In comparison, the listed literature value of the C_2 d-state lifetime is the averaged lifetime of the $v = 0-2$ vibrational levels at low J (the vast majority of the measured levels have $J < 4$). It is possible that there is a small vibration-rotation level-dependence (10%) in the d-state lifetime, which could account for the difference between my value and the earlier measurements.

Given that the radiative lifetime (see Table 4.2) of the *trans* 3^4 level is similar to the typical lifetime of non-predissociated S_1 *trans* levels, and that the lifetime of *cis* 3^16^1 is >1 μs (the extra-long lifetime of the *cis* level is a consequence of the fact that $\tilde{A}-\tilde{X}$ transition is electronically forbidden at the S_1 *cis* geometry), the predissociation rates of both *trans* 3^4 (46290 cm^{-1}) and *cis* 3^16^1 (46192 cm^{-1}) levels are slow (or nearly zero), despite the fact that both levels lie above the S_1 predissociation limit (46074 cm^{-1}). The unexpectedly long lifetime of the *trans* 3^4 and *cis* 3^16^1 levels is a consequence of the fact that there is a ~560 cm^{-1} exit barrier along the S_1 predissociaiton path [38, 158], and that both *trans* 3^4 and *cis* 3^16^1 $K = 1$ levels lie >300 cm^{-1} below the top of that barrier. In the discussion below, those two levels are treated as if they were non-predissociated.

4.5 Photodissociation Mechanism

In this section, the mechanism of the observed resonance-enhanced (S_1-S_0) photodissociation of acetylene is discussed, based on my analysis of the flow cell DF spectra and the photofragment fluorescence time-traces obtained in the supersonic jet conditon.

4.5.1 C_2H^* fragments

The observed long-lived photofragments in the supersonic jet experiment have similar properties as the C_2H^* fragment, which was observed in VUV (11 eV) photodissociation of acetylene [17, 21, 26, 63, 122, 123, 138, 156, 157]. Given that the two-photon energy of our UV excitation laser is ~11.7 eV, it seems likely that the C_2H^* fragment observed in our experiments is generated via a two-photon process (that is, one additional photon excitation from the resonance selected rotation-vibration level of the S_1 state). There are two likely paths to generate C_2H^* from the S_1 level,

$$\mathrm{C_2H_2\,(S_1)} + h\nu \rightarrow \mathrm{C_2H_2^*} \rightarrow \mathrm{C_2H^*} + \mathrm{H} \tag{4.1}$$

$$\begin{aligned} &\mathrm{C_2H_2\,(S_1)} \rightarrow \mathrm{C_2H}\,(\tilde{X}^2\Sigma_g^+) + \mathrm{H} \\ &\mathrm{C_2H}(\tilde{X}) + h\nu \rightarrow \mathrm{C_2H^*}. \end{aligned} \tag{4.2}$$

The second path (Eqs. 4.2) would be applicable only to predissociated S_1 acetylene levels. In the supersonic-jet experiments, the C_2H^* signals are observed from $K = 1$ rotational levels of *trans* 3^1, *trans* 3^4, *trans* 3^5, and *cis* 3^16^1, and IR-UV double resonance-excited levels in the $46700-47200\,\mathrm{cm}^{-1}$ region (observations of the *trans* 3^1 and IR-UV-excited levels are discussed in Chapter 3). Among those levels, the *trans* 3^5 level and all of the IR-UV-excited levels are predissociated (with an estimated lifetime of ~1 ns), and yield significant C_2H ($\tilde{X}$) fragments.

Since the C_2H^* fluorescence signals are observed from non-predissociated S_1 levels, the process given by Eq. 4.1 must be active for all of the non-predissociated levels. If the process given by Eqs. 4.2 is active instead for predissociated levels, a significant change in the yield of C_2H^* might be expected for photodissociation from a non-predissociated *vs.* a predissociated S_1 level, because the two pathways given by Eq. 4.1 and Eqs. 4.2 involve two completely different excitation and dissociation schemes. However, as illustrated in Fig. 3-6b of Chapter 3, C_2H^* fluorescence intensity from the non-predissociated *trans* 3^1 and predissociated *trans* 3^25^1 levels appears to be proportional to their respective S_1-S_0 transition probabilities. This suggests that the photodissociation cross-sections from the two S_1 levels are similar and are *not* affected by predissociation (and the presence of the C_2H $\tilde{X}$-state fragments). It is thus likely that, for acetylene photodissociation via predissociated S_1 vibrational levels near 47000 cm^{-1} (e.g. *trans* 3^5 $K = 1$ level), the observed C_2H^* fragments are not produced from excitation of the C_2H $\tilde{X}$-state fragments (Eqs. 4.2). Direct one-photon photodissociation of the S_1 level (Eq. 4.1) is the only pathway by which C_2H^* is generated. A two-color pump-probe time-delay experiment is proposed in Section 4.5.4 to confirm this hypothesis.

I must point out that while the S_1 lifetime is ~10 ps in the >48500 cm^{-1} region (based on linewidth measurements)[4], the S_1 predissociation rate is relatively slow near 47000 cm^{-1} (~1000 cm^{-1} above the predissociation threshold) and has a reaction time of ~10 ns, estimated based on the rise time of the H-atom REMPI signal measured in a pump-probe time-delay experiment [158]. Given the high-fluence of the laser beam (focused, 7 ns, ~200 μJ/pulse), direct one-photon photodissociation (Eq. 4.1) is possible and can still be efficient for predissociated S_1 levels with >1 ns lifetime.

4.5.2 C_2 fragments

Energetically (with a UV photon of 5.85 eV), the C_2 C and d states can be generated via two different paths from the S_1 levels,

$$C_2H_2\,(S_1) + h\nu \rightarrow C_2H_2^* \rightarrow C_2(C^1\Pi_g \text{ or } d^3\Pi_g) + H_2(X^1\Sigma_g), \tag{4.3}$$

$$\begin{aligned} &C_2H_2\,(S_1) + h\nu \rightarrow C_2H_2^* \rightarrow C_2H^{*'} + H \\ &C_2H^{*'} + h\nu \rightarrow C_2H^{**} \rightarrow C_2(C^1\Pi_g \text{ or } d^3\Pi_g) + H, \end{aligned} \tag{4.4}$$

where $C_2H_2^*$, $C_2H^{*'}$, and C_2H^{**} are species with currently unidentified electronic assignments. The prime label on $C_2H^{*'}$ in Eq. 4.4 is used to distinguish it from the observed C_2H^* species, which gives rise to the long lifetime visible fluorescence signal. For simplicity, in Eqs. 4.3 and 4.4, the same labels are used for the intermediate predissociated states, $C_2H_2^*$ and C_2H^{**}, for the production of both C_2 C and d states.

Table 4.4: Thermodynamic thresholds of the H_2 elimination (elim.) path and sequential (seq.) bond-breaking path for the generation of C_2 $C^1\Pi_g$ and $d^3\Pi_g$ state from S_0 acetylene, based on the dissociation energies of C_2H_2 [112], C_2H [34], and H_2 [72], as well as the relative energies of C_2 d and C states with respect to the X state [72]. Using the photon energy of 5.85 eV (the excitation energy of the *trans* 3^5 level), the total laser excitation energies (two photons for H_2 elim. and three for Seq.) are given at the bottom row.

	H_2 elim.	Seq.
C_2 $C^1\Pi_g$	10.4 eV	14.9 eV
C_2 $d^3\Pi_g$	8.6 eV	13.1 eV
total energy	11.7 eV	17.6 eV

In fact, given that the two C_2 electronic states have identical dominant electronic orbital configurations, the intermediate predissociated states that lead to the C_2 C and d states likely have similar electronic configurations.

Including the first photon needed for the initial S_1-S_0 excitation, the H_2 elimination path (Eq. 4.3) requires a total of two photons, and the sequential C-H bond-breaking path (Eq. 4.4) requires a total of three photons. The thermodynamic thresholds for processes given by Eqs. 4.3 and 4.4 are summarized in Table 4.4. While the H_2 elimination path is also allowed with three-photon excitation, it is not expected to be an efficient dissociation path with three photons because acetylene states in the 11 eV energy region are known be highly dissociative [21, 26, 157]. A three-photon H_2 elimination path would have to compete with this fast decay channel at the two-photon excitation region, and is thus unlikely to be as efficient as other possible dissociation paths. For this reason, in the following discussion, it is assumed that the H_2 elimination path involves only two-photon excitation from S_0 acetylene. In addition, since S_1 acetylene is a singlet state, the H_2 elimination path (Eq. 4.3) is spin-allowed only for the generation of the C_2 $C^1\Pi_g$ state, but spin-forbidden for the generation of the C_2 $d^3\Pi_g$ state. The sequential photodissociation path (Eq. 4.3) is spin-allowed for the generation of both C_2 C and d states.

Even for the generation of the C_2 C state, the H_2 elimination channel (Eq. 4.3) can be ruled out, based on my analysis of the DF spectra and the photofragment time-traces. First, given that the H_2 elimination path involves one fewer photon than the sequential path, the production of the C_2 C state (via H_2 elimination) is expected to be more efficient than the production of the d state (via sequential bond-breaking). However, as discussed in Section 4.3.1, I estimate that the total population in the d state is about four times the total population in the C state. In addition, in a concerted H_2 elimination process, the transition state should have a near-*cis* geometry (i.e. the two hydrogen atoms would be on the same side of the CC bond). The H_2 elimination process is likely more efficient for photodissociation from *cis* 3^16^1 than from *trans* 3^4, because the *cis* level has a significantly better Franck-Condon overlap with the elimination reaction path than the *trans* level. As a result, for the *cis* 3^16^1 level, the C_2 $C - A$ emission intensity should be greatly enhanced with respect to the $d - a$ emission, and the observed $(C - A)/(d - a)$ intensity ratio should be different for the *cis* 3^16^1 and the *trans* 3^4 levels (i.e. the ratio should be larger for the former). However, in our experiment, the $(C - A)/(d - a)$ intensity ratio appears to be identical for photodissociation from the *cis* 3^16^1 and *trans* 3^4 levels, as shown in Fig. 4-4a. Those two pieces of evidence strongly suggest that the observed C_2 C state is not generated via the H_2 elimination channel. The absence of the H_2 elimination channel in the two-photon energy region (11.7 eV) is also in agreement with the earlier VUV photodissociation study of acetylene [63], where the $C_2(C)+H_2$ elimination channel was only observed at VUV photon energy >12.98 eV (~2.6 eV higher than the thermodynamic threshold of the H_2 elimination process, see Table 4.4), consistent with a high potential energy barrier along the H_2 elimination pathway.

4.5.3 Summary of the dissociation mechanisms

Given that the H_2 elimination path is highly unlikely for the production of the C_2 C state, I conclude that both the C and d states of C_2 are generated entirely via the sequential dissociation path (Eq. 4.4). It also seems most likely that the intermediate $C_2H^{*'}$ species in Eq. 4.4 is the same species as the observed long-lived C_2H^* fragment. The mechanism of the one-color (212-220 nm), resonance-enhanced photodissociation

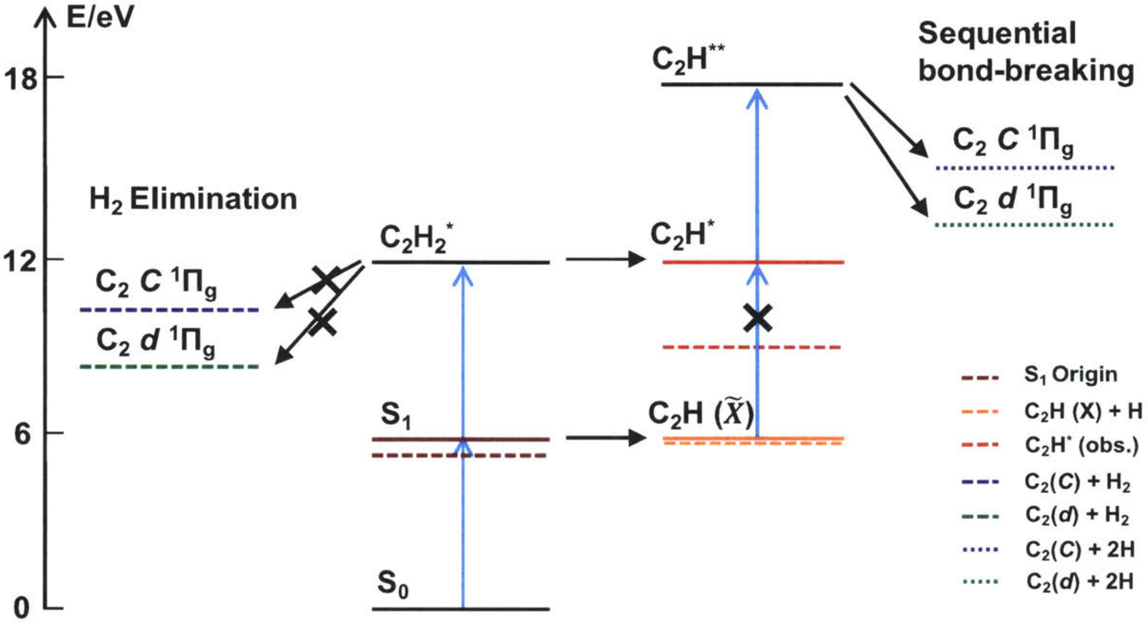

Figure 4-5: Mechanism of the one-color, resonance-enhanced photodissociation of acetylene. The UV-photon (blue arrows) has energy of ~5.85 eV, and the populated S_1 level is a predissociated level. Hydrogen atoms (in the sequential pathway) and the molecular H_2 fragment (in the H_2 elimination pathway) are omitted from the figure for simplicity. The pathways that have been ruled out based on my analysis are marked by crosses. The thermodynamic thresholds of various processes are indicated by dashed horizontal lines (see the legend). The threshold for the C_2H^* fragment corresponds to the lowest photon energy at which C_2H^* was observed in the VUV photodissociation study of acetylene [157].

of acetylene is summarized in Fig. 4-5, where competing processes (which have been ruled out and marked by an X) are also shown. The acetylene molecules are pumped by the UV excitation beam into an S_1 level. The same focused UV beam excites the S_1 molecule into the $\sim$90000 cm^{-1} energy region, where a fast dissociation channel into C_2H^*+H is known to exist [3, 21, 26, 92, 98–100, 162, 163]. The resulting electronically excited C_2H^* fragments are subsequently excited by another UV photon into an even higher-lying state, C_2H^{**}, which dissociates into the $d^3\Pi_g$ and $C^1\Pi_g$ states of C_2. The long-lived C_2H^* fragment fluoresces in the visible, while the C_2 C and d states fluoresce, respectively, in the near UV and in the green. From my analysis of the DF spectra and fluorescence time-traces (collision-free), I estimate the relative populations of the three fluorescing photofragments to be $C_2H^* : C_2(d) : C_2(C)$ = >40 : 4 : 1. The yield of C_2 fragment (C and d states) from the C_2H^* fragment appears to be different (by a factor of two) between the *trans* 3^4 and *cis* 3^16^1 levels (see Table 4.3). Given the distinctively different vibronic characters of the two S_1 levels, it is possible that the C_2H^* photofragments generated from the two S_1 levels have different (ro)vibrational distributions, which might be reflected in the slightly different C_2H^* emission patterns (Fig. 4-4b) from the two S_1 levels. The photodissociation efficiencies (to produce C_2 C and d states) from different (ro)vibrational states of C_2H^* may vary, which leads to the different yield of C_2 photofragments from the two intermediate S_1 levels.

While it is clear that photodissociation of S_1 acetylene proceeds via a two-step sequential C-H bond breaking mechanism, my analysis cannot determine the electronic identities of the long-lived C_2H^* species and the two intermediate states, $C_2H_2^*$ and C_2H^{**}. Assignment of the near-continuum C_2H^* long-lived emission has been investigated in earlier *ab initio* calculations. Work from Shih et al. [141] suggested that the C_2H^* fluorescence is the result of transitions from the lowest vibrational levels of the $3^2A'$ and $2^2A''$ states to the high-lying levels of $2\,^2A'$, $^2A'$, and $^2A''$ states (corresponding to the $\tilde{X}$ and $\tilde{A}$ states in linear geometry). However, in a more recent study, Boyé et. al. [21] assigned the emission as transitions from vibrationally-hot levels of the $\tilde{A}$ state to the $\tilde{X}$ state. In neither of the two studies, the observed lifetime $(3-6$

μs) [17, 21, 138] of the C_2H^* emission was reproduced (400 ns from Shih et al and 10 ns from Boyé et. al.). However, given that the long lifetime visible fluorescence signals are produced by photolysis of C_2H_2, C_2D_2, and C_2HBr, at a threshold energy of ~9.5 eV (which is ~1 eV lower than the thermodynamic threshold of $C_2H \rightarrow C_2$ (X) +H), it seems probable that the long-lived visible wavelength signal comes from C_2H.

Due to ambiguity regarding the identity of the C_2H^* fragment, it is not possible to deduce the nature of the intermediate $C_2H_2^*$ and C_2H^{**} states. The $C_2H_2^*$ state can be a rapidly dissociating acetylene valence or Rydberg state, or a state with mixed valence and Rydberg characters. The latter is a more likely case, given the strong Rydberg-valence interactions in the two-photon energy region of interest (11.5 eV) [92]. Transitions into the $C_2H_2^*$ state must be one-photon allowed from both S_1 conformer levels (*trans* 3^4 and *cis* 3^16^1), with similar transitions probabilities, given that photodissociation efficiencies via the two S_1 conformer levels are essentially the same (see Table 4.3). Without further guidance from *ab initio* calculations, I will not speculate further on the possible identity of $C_2H_2^*$.

The one-color (~220 nm), resonance-enhanced (S_1-S_0), multi-photon dissociation of acetylene studied in this chapter is qualitatively different from the widely-studied one-color photolysis of acetylene using a 193 nm ArF laser [5, 39, 40, 101, 124, 148, 167, 179]. The S_1 level (or more likely a group of S_1 levels), initially populated by the first 193 nm photon, dissociates rapidly into H+CCH ($\tilde{X}^2\Sigma_g^+$), and is not directly involved in the subsequent photodissociation process. The observed electronically excited C_2 (i.e. C and d states) and C_2H^* fragments result from excitation of the C_2H $\tilde{X}$-state fragments by the second 193 nm photon (i.e. the process given by Eqs. 4.2). In comparison, in one-color (~220nm), multi-photon dissociation of acetylene discussed in this chapter, S_1 acetylene molecules, which are populated by the first UV photon, are excited by the second (same-color) photon into a higher-lying acetylene electronic state near 11.7 eV before rapid dissociation takes place (i.e. the process given by Eq. 4.1). As mentioned in Section 4.5.1, some ambiguity remains about whether Eq. 4.1 is applicable to *predissociated* S_1 levels in the 47000 cm^{-1} region. However, for photodissociation via a *non-predissociated* S_1 acetylene level, this ambiguity does not exist.

4.5.4 Proposed experiments

With 193 nm ArF photolysis of acetylene, a wide range of C_2 electronic states have been observed (in addition to the C and d states) [39, 101, 148, 167]: $X^1\Sigma_g^+$, $A^1\Pi_u$, $B^1\Delta_g$, $B'^1\Sigma_g^+$, $a^3\Pi_u$, and $b^3\Sigma_g^1$. The $X^1\Sigma_g^+$ and $a^3\Pi_u$ states cannot be detected in our fluorescence-based experiment, because they are, respectively, the lowest state in the C_2 singlet and triplet manifolds. The $A^1\Pi_u$ state [148, 167], which was determined to be the most abundant species following 193 nm ArF photolysis, cannot be detected in our experiment, because the PMT used in this work is not sensitive at the C_2 $A - X$ emission region (near IR). In Chapters 5 and 6, I describe a new technique, based on frequency-modulation (FM) spectroscopy, which allows me to determine the population difference between the X and A states.

To determine which of the two processes given by Eqs. 4.1 and 4.2 is responsible for photodissociation via predissociated S_1 acetylene levels near 47000 cm^{-1}, a two-color pump-probe time-delay experiment (in a supersonic jet) is proposed. In the pump-probe experiment, a first pump laser beam (~212 nm) is used to populate a predissociated S_1 level near 47000 cm^{-1} (e.g. a *trans* 3^5 $K = 1$ rotational level). A second probe laser (delayed with respect to the pump), which is not resonant with any S_1-S_0 transition (in the ~220 nm region), is used to generate C_2H^* fragments, from either the S_1 molecules (according to Eq. 4.1) or the C_2H $\tilde{X}$-state fragments resulting from S_1 predissociation (according to Eqs. 4.2). The time-delay between the probe and pump beams can be changed from 0 to 100 ns. Given that the predissociation reaction time of S_1 levels near 47000 cm^{-1} is ~10 ns [158], if direct one-photon photodissociation of the S_1 level (i.e. $C_2H_2\,(S_1) + h\nu \rightarrow C_2H_2^* \rightarrow C_2H^* + H$) is the pathway by which C_2H^* is generated via a predissociated S_1 level, in a pump-probe time-delay experiment, the C_2H^* signals should only be observed when the pump and probe beams are essentially overlapped in time (or with <10 ns time-delay). If the process given by Eqs. 4.2 ($C_2H_2\,(S_1) \rightarrow C_2H\,(\tilde{X}^2\Sigma_g^+) + H$, $C_2H(\tilde{X}) + h\nu \rightarrow C_2H^*$)

is responsible for the generation of C_2H^* via a predissociated S_1 level, C_2H^* signals should still be observable with a long pump-probe delay, because the C_2H $\tilde{X}$-state fragments resulting from S_1 predissociation are long-lived. Assuming that both the pump and probe beams have beam diameter of 1 mm (and a molecular beam velocity of ~1500 m/s), the fly-out time of the C_2H $\tilde{X}$-state fragments should be >100 ns, which means the C_2H^* signals should be observable with a time-delay >100 ns, if the process given by Eqs. 4.2 occurs.

Given that the two-photon energy region of interest ($11.5-11.8$ eV) lies above the first ionization potential (IP) of acetylene (11.4 eV), two-photon ionization can compete against dissociation. The dissociation precursor $C_2H_2^*$ state, which is expected to have at least partial Rydberg-state character, can undergo rapid autoionization. It is not possible to determine from the current experiment which process (autoionization *vs.* dissociation) is more efficient in the $11.5-11.8$ eV region. It would be informative to carry out an experiment where one-color 1+1 REMPI and photofragment signals are collected simultaneously using multiple S_1 *trans*-bending levels, e.g. $\nu_3 = 0-5$. The two-photon energies accessed via resonance with the $\nu_3 = 0-3$ levels lie below the first IP, while those of $\nu_3 = 4-5$ lie slightly above the IP. The proposed experiment would likely be difficult, because it would be difficult to ensure that the REMPI signal arises exclusively from two-photon processes.

4.6 Conclusion

In this chapter, I present an analysis of the dispersed-fluorescence spectra (collected in a 3 torr flow cell) and the fluorescence time-traces (collected in the collision-free supersonic jet) of photofragments resulting from one-color ($212-220$ nm), resonance-enhanced (S_1-S_0), multi-photon dissociation of acetylene. Specifically, photodissociation via three individually selected intermediate S_1 levels, *trans* 3^4, *trans* 3^5, and *cis* $3^1 6^1$ ($K=1$, $J=6$, e-symmetry for all three levels), are studied in detail. In both DF spectra and the fluorescence time-traces, the C_2 Swan band ($d^3\Pi_g - a^3\Pi_u$) and C_2 Deslandres-d'Azambuja band ($C^1\Pi_g - A^1\Pi_u$) emissions are observed (in addition to acetylene S_1 LIF fluorescence in the $230-350$ nm region). The intensity ratios of the two C_2 emission bands are similar in the flow-cell (DF) and supersonic-jet (time-trace) experiments. In addition, long-lived emission (>3 μs) from an electronically highly-excited C_2H^* fragment is observed in the supersonic-jet condition (i.e. the signals are likely collisionally-quenched in the cell-condition).

Both C and d states of C_2 are generated with high rotational (the rotational population reaches a maximum broadly around $J \approx 27$) and vibrational ($v > 4$ levels are observed) excitation. The population ratios among the three observed fluorescing photofragments is estimated to be $C_2H^*:C_2(d):C_2(C) = {>}40 : 4 : 1$, although the photodissociation yields of the two C_2 fragments are observed to be slightly different (by a factor of two) between *trans* 3^4 and *cis* $3^1 6^1$ levels.

Based on my analysis of the flow cell DF spectra and the photofragment fluorescence signals obtained under the supersonic jet conditions, the mechanisms of the observed one-color ($212-220$ nm), resonance-enhanced (S_1-S_0) photodissociation of acetylene are discussed. The C_2H^* fragment results from one-photon dissociation from the S_1 acetylene level, and both C_2 C and d states are generated via a three-photon (from S_0) sequential C-H bond-breaking process. The long-lived C_2H^* photofragment fluoresces in the visible, while the C_2 C and d states fluoresce, respectively, in the near UV and in the green. Further information from high-level *ab initio* calculations are called for, in order to suggest vibronic assignments to various intermediate dissociation precursor states.

Chapter 5

Determination of the Sign of the Population Difference in a Two-level System by Frequency-modulation Spectroscopy

Abstract

In this chapter, I report the use of frequency-modulation (FM) spectroscopy to determine, from the *phase* of the FM signal, the sign of the population difference in a two-level system (i.e. whether the two-level system is inverted). I demonstrate that FM signals from an *inverted* I_2 $B - X$ system, prepared by a pulsed laser, have opposite phase with respect to signals from the Rb D_1-line absorption transition (i.e. a *non-inverted* system). This technique is applied in Chapter 6 to probe the $A - X$ transitions of the C_2 fragments, generated from one-color (~220 nm), resonance-enhanced (S_1-S_0), multi-photon dissociation of acetylene, with the goal of determing the relative abundance of the nascent C_2 A and X-state products.

The work described in this chapter was performed with Professor Zhenhui Du, who is a visiting scholar from Tianjin University, China. T. J. Erickson and C. L. Keenan also helped with the experiment.

5.1 Introduction

Frequency modulation (FM) spectroscopy, based on phase-sensitive heterodyne detection in a frequency window (typically up to a few GHz) outside of the laser amplitude noise spectrum, has been widely used for precision measurements, laser frequency stabilization, and sensitive detection of weak absorptions [61]. It has also been applied to measure transient species following photodissociation [61, 120, 121]. As far as I am aware, the technique has only been applied to study systems that are either thermalized (e.g. in trace-gas detection) or generated without population inversion (e.g. CN radials following 193 nm photolysis of NCCN [120]), with the exception of the work from Levenson et al., [95] where the frequency-modulated (FM-ed) laser is used to detect stimulated Raman gain of D_2, as a demonstration of the quantum-noise-limited performance of their FM setup. No comments are made in Levenson's work regarding the differences between FM signals in a gain (stimulated emission) *vs.* loss medium (absorption). Chemical processes, which involve large amount of excess energy (e.g. from a multi-photon dissociation), can give rise to population inversions between different electronic states. For example, following 193 nm ArF photolysis of acetylene [5, 101, 124, 148, 167], the C_2 $A^1\Pi_u$ state is known to be the most abundant C_2 species [5, 148]. The ratio of C_2 populations between the $A^1\Pi_u$ and $X^1\Sigma_g^+$ states was measured to be $19(3) : 1$.

In this chapter, I present a slightly modified application of FM spectroscopy (from its most conventional applications), which allows me to determine, from the *phase* of the FM signal, the sign of the population difference between two levels probed by the FM-ed laser. A λ-type excitation scheme for the I_2 $B - X$ transition, and a comparison against the Rb D_1-line transition (at ~795 nm), are used in a proof of principle experiment. In the I_2 experiment, the FM-ed laser beam is used to probe the inverted population between the pulsed-laser populated vibration-rotation level of the B state and the unpopulated vibrationally highly-excited level of the X state. As I will demonstrate both theoretically (Section 9.2) and experimentally (Section 5.4), FM signals from the inverted I_2 $B - X$ system have opposite phase with respect to signals from the Rb D$_1$-line absorption.[1] FM signals from a non-inverted system would have the same phase as the Rb absorption signals. In Chapter 6, the technique is applied to probe the $A-X$ transitions of the C$_2$ fragments, generated from one-color (~220 nm), resonance-enhanced at the one photon level (S$_1$-S$_0$), multi-photon dissociation of acetylene, with the goal of determining the nascent population difference between the C$_2$ A and X states.

5.2 Theory

The basic principle of FM spectroscopy is briefly discussed first, based on reviews of the topic in Refs [56, 61]. Using complex notation, the electric field of a laser beam at the optical carrier angular frequency, ω_c, is given by

$$E_1(t) = E_0 \exp(i\omega_c t). \tag{5.1}$$

The beam is passed through an electro-optic phase modulator (EOM) driven at angular frequency, ω_{rf} (referred to as the rf frequency). The electric field of the modulated beam is described by

$$\begin{aligned} E_2^F(t) &= E_0 \exp[i(\omega_c t + M \sin \omega_{rf} t)] \\ &= E_0 \sum_{n=-\infty}^{n=\infty} J_n(M) \exp[i(\omega_c + n\omega_{rf})t], \end{aligned} \tag{5.2}$$

where M is the modulation index and the J_n are Bessel functions of order n. The modulated beam has frequency components at sidebands, displaced by integer multiples of ω_{rf} above and below ω_c. With modulation index $M < 1$, the FM-ed beam can be described by a strong carrier at frequency ω_c and two weak sidebands at frequencies $\omega_c \pm \omega_{rf}$,

$$E(t) = E_0 \left\{ \frac{M}{2} \exp(i(\omega_c + \omega_{rf} t) + \exp(i\omega_c t) - \frac{M}{2} \exp(i(\omega_c - \omega_{rf} t) \right\}. \tag{5.3}$$

---

[1] Note that the Rb D$_1$-line is split into two well-resolved hyperfine components, as illustrated in Fig. 5-5b.

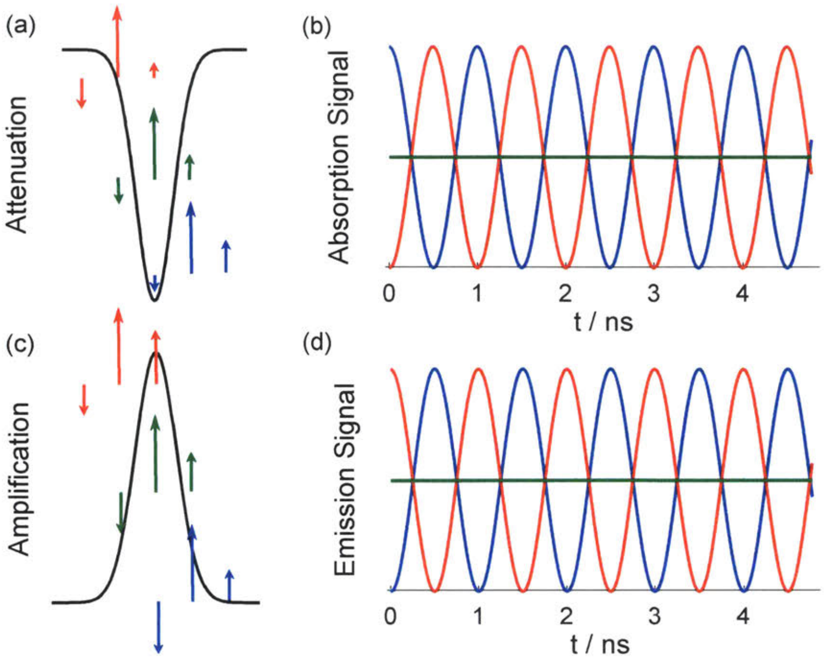

Figure 5-1: Evolution of the FM quadrature signals, as the FM carrier frequency is scanned through a transition line. In (a)-(d), the color green is used when the FM carrier frequency is on-resonance with the transition center frequency. The colors, red and blue, are used, respectively, for cases when the FM carrier frequency is red and blue-detuned for an equal amount. (a) Relative amplitudes of the two FM sidebands at three characteristic carrier frequencies in a loss medium (which attenuates the beam amplitudes). (b) FM quadrature (absorption) signal at the three carrier frequencies, color-coded accordingly. (a) Relative amplitudes of the two FM sidebands at three characteristic carrier frequencies in a gain medium (which amplifies the beam amplitudes) (b) FM quadrature (emission) signal at the three carrier frequencies, color-coded accordingly.

Note that the two sidebands have the same magnitude but are of opposite phase. In all of the experiments described in this chapter, the amplitudes of the two sidebands are approximately 25% of the amplitude of the main carrier peak. In a pure FM-ed beam, each first-order side-band beats against the carrier with a beat frequency ω_{rf}. The beats have the same amplitude and differ in phase by exactly 180°, thus resulting in no amplitude modulation, when the frequency of the beam is far off-resonance from the transition frequency (or when there is no sample present).

In a typical absorption experiment, as a beam passes through a sample, it experiences both intensity attenuation and phase-shift. The sample probed in an absorption experiment is referred to as a loss medium in the following discussions. The dimensionless frequency-dependent amplitude attenuation is given by $\delta_{\uparrow}(\omega)$, and the dimensionless frequency-dependent phase-shift is given by $\phi_{\uparrow}(\omega)$, where the subscript, $\uparrow$, is used to indicate that the initial state of the associated transition is *lower* in energy than the final state of the transition. For a two-level system, it can be shown [143] that both $\delta_{\uparrow}$ and $\phi_{\uparrow}$ are directly proportional to the *population difference* between the two states, $\Delta N = N_l - N_h$, where N_l and N_h are, respectively, the population in the lower and higher energy state. With a square-law light detector of band-width $>\omega_{rf}$, the transmitted beam intensity (excluding the *dc* component) becomes (assuming an optically-thin sample)

$$I_m(t) = I_0 \exp[-2\delta_{\uparrow}(\omega_c)] M[\Delta\delta_{\uparrow} \cos\omega_{rf}t + \Delta^2\phi_{\uparrow} \sin\omega_{rf}t], \tag{5.4}$$

where

$$\begin{aligned} \Delta\delta_{\uparrow} &= \delta_{\uparrow}(\omega_c - \omega_{rf}) - \delta_{\uparrow}(\omega_c + \omega_{rf}) \\ \Delta^2\phi_{\uparrow} &= \phi_{\uparrow}(\omega_c + \omega_{rf}) + \phi_{\uparrow}(\omega_c - \omega_{rf}) - 2\phi_{\uparrow}(\omega_c). \end{aligned} \tag{5.5}$$

As can be seen from Eqs. 5.4 and 5.5, the quadrature component $(\cos\omega_{rf}t)$ of the transmitted beam intensity is proportional to the difference in attenuation experienced by the upper and the lower sidebands, and the in-phase component $(\sin\omega_{rf}t)$ is proportional to the difference between the phase shift experienced by the carrier and the average of the phase shifts experienced by the sidebands. In Figs. 5-1a and 5-1b, I present a graphical illustration of the origin of the quadrature component signal, as the carrier frequency of the FM-ed beam is scanned through a resonant transition. When the carrier frequency is exactly on resonance with the transition center frequency (this case is color-coded green in Fig. 5-1a), the quadrature FM signal (color-coded green in Fig. 5-1b) is zero, because the two side-bands are equally attenuated. When the carrier frequency is slightly detuned, one of the sidebands is more strongly attenuated than the other, and a beat signal can be detected. However, the *phase* of the beat signal is exactly opposite for the red (color-coded red in Figs. 5-

1a and b) and blue (color-coded blue in Figs. 5-1a and b) detuned cases, because the amplitude of the quadrature signal is proportional to $\Delta\delta_\uparrow$. It can be seen from Eqs. 5.4 and 5.5 that there is a similar phase-flip between the red and blue-detuned cases for the in-phase FM signal. To summarize, in the FM absorption experiment, the differential attenuation and phase shift of the two sidebands caused by the sample leads to a detectable beat signal at the modulation frequency, ω_{rf}, and the beat signals at red-detuned and blue-detuned carrier frequencies are 180° out-of-phase with each other.

What happens to an FM-ed beam when it passes through an inverted gain medium (i.e. more population in the excited state than in the ground state)? The beam, instead of being attenuated, is amplified, due to stimulated emission from the initially inverted system. In addition, the beam experiences a frequency-dependent phase-shift. The frequency-dependent amplitude amplification is given by $\delta_\downarrow(\omega)$, and the frequency-dependent phase-shift is given by $\phi_\downarrow(\omega)$, where the subscript, $\downarrow$, is used to indicate that the initial state of the associated transition is *higher* in energy than the final state of the transition. The transmitted beam intensity through an inverted gain medium is given by an expression similar to Eq. 5.4, except that $\Delta\delta_\uparrow$ and $\Delta\phi_\uparrow$ are respectively replaced by

$$\begin{aligned}\Delta\delta_\downarrow &= \delta_\downarrow(\omega_c - \omega_{rf}) - \delta_\downarrow(\omega_c + \omega_{rf}) \\ \Delta^2\phi_\downarrow &= \phi_\downarrow(\omega_c + \omega_{rf}) + \phi_\downarrow(\omega_c - \omega_{rf}) - 2\phi_\downarrow(\omega_c),\end{aligned} \tag{5.6}$$

and the exponential pre-factor becomes $\exp[2\delta_\downarrow(\omega_c)]$. As in the absorption experiment, the differential amplification and phase shift of the two sidebands, as the beam passes through a gain medium, leads to a detectable beat signal at the modulation frequency, ω_{rf}. In addition, similar to $\delta_\uparrow$ and $\phi_\uparrow$ in a loss medium, both $\delta_\downarrow$ and $\phi_\downarrow$ in a gain medium are proportional to the *population difference* between the two levels, $\Delta N = N_l - N_h$ [143]. The signs of ΔN, however, are opposite for the two types of system, which means that near the transition center frequency, the signs of $\delta_\downarrow$ and $\phi_\downarrow$ are opposite to those of $\delta_\uparrow$ and $\phi_\uparrow$, respectively (see Figs. 1.25 and 1.26 of Ref [143]).

Consequently, for the same amount of detuning of the carrier frequency from the transition center frequency, the FM signal from a gain medium is 180° out of phase with respect to the FM signal from a loss medium. This is illustrated in Fig. 5-1, where beat signals resulting from beam amplification (Fig. 5-1d) are compared with those resulting from beam attenuation (Fig. 5-1b) for three different detuning cases. For simplicity, in the following discussions, the FM experiment on a gain medium (with population inversion) is referred to as a stimulated emission experiment.

The FM signals, given by Eqs. 5.4-5.6, can be demodulated into in-phase and quadrature components (with respect to the phase of the rf modulation reference), to generate a conventional FM spectrum. Around each transition center frequency, the in-phase (dispersion) and quadrature (absorption) signals from a loss medium (Fig. 5-2a) are expected to have the opposite phase (or sign) with respect to the in-phase (dispersion) and quadrature (stimulated emission) signals from a gain medium, respectively (Fig. 5-2b). I emphasize that in order to compare the demodulated spectra from an unknown system (for which I want to determine whether there is population inversion) with the demodulated spectra resulting from an absorption experiment, I need to demodulate the unknown spectrum with the same phase and frequency as I demodulate the absorption spectrum. As can be seen from the simulations in Fig. 5-2, the in-phase signal of a given transition is expected to have three zero-crossings, while the quadrature signal has only one zero-crossing.

The rf reference, which is used to drive the EOM, is typically used to demodulate the experimental FM signal (at the modulation rf frequency). However, the relative phases of the rf reference and FM signals are affected by various experimental factors, such as the length of the cables used to transfer the two signals. As a result, phase-corrections are applied to the rf reference, so that the in-phase and quadrature components can be separated in the resulting demodulated spectra. In this work, the phase-corrections to the rf reference signal for the in-phase and quadrature components are determined from the absorption experiment on the Rb D_1-line transitions, based on the simulation results in Fig. 5-2. A pair of phase-adjustments, ϕ_1 and $\phi_2 = \phi_1 + \pi/2$, are found, such that the corresponding demodulated signals have

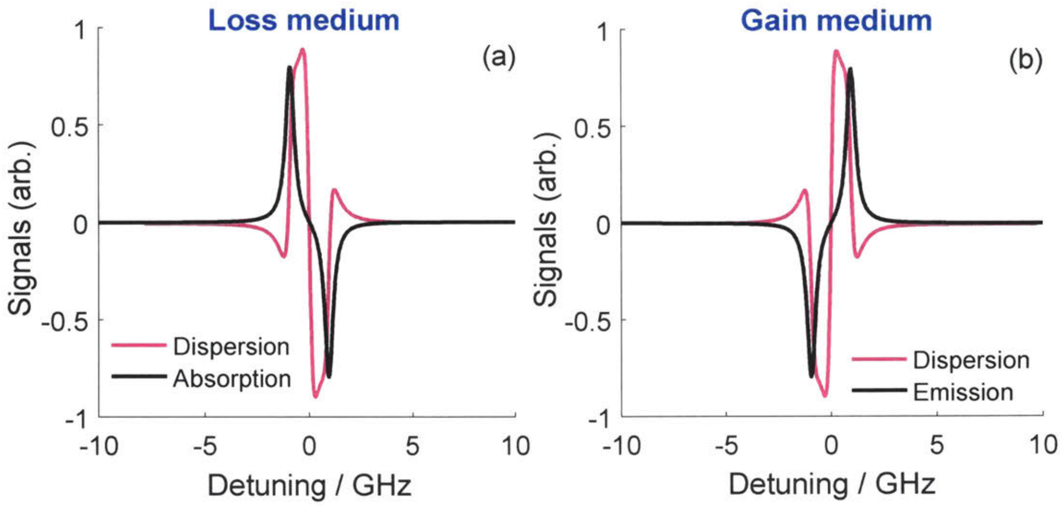

Figure 5-2: Simulated lineshapes of the in-phase and quadrature components of the demodulated FM signal. (a) A loss medium (absorption experiment) (b) A gain medium (stimulated emission experiment). In the simulation of both types of experiment, the transition has a Lorentzian lineshape with FWHM=0.5 GHz. The modulation rf signal is given by $\sin(\omega_{rf}t)$, where $\omega_{rf} = 2\pi \times 0.94$ GHz. In both panels (a) and (b), the in-phase and quadrature components are obtained, respectively, by demodulating the FM signal, given by Eqs. 5.4-5.6, with $\cos(\omega_{rf} + \pi/2)$ and $\cos(\omega_{rf})$.

three (i.e. in-phase component) and one zero-crossing (i.e. quadrature component), respectively. The same set of phase-adjustments (ϕ_1 and ϕ_2) is used to demodulate the time-domain FM signal from the I_2 $B \rightarrow X$ stimulated emission transitions. I emphasize that, for the purpose of determining the sign of the population difference between two levels probed by the FM-ed beam (by comparing the resulting spectra to the Rb absorption spectra), it is not necessary to demodulate the time-domain FM signals into pure in-phase and quadrature components. Both components have opposite phases in a gain *vs.* a loss medium (see Fig. 5-2), which means that an arbitrary linear combination of the two components is also of opposite phase in those two types of media.

5.3 Experimental Details

The experimental setup is summarized in Figs. 5-3 and 5-4. In describing the experimental setup, I will refer to the components in those two figures without indicating the manufacturer and model information. Detailed component information (and a brief discussion of its function, if necessary) is included in Section 5.3.3 for reference.

5.3.1 The FM setup

The FM setup used in this work differs from a conventional FM setup in both the generation of the FM-ed beam and the method of data collection. Other than those two differences, I use standard microwave and optical components (Fig. 5-3), and follow the standard procedures to set up the experiment. I emphasize that in order to minimize residual amplitude modulation (RAM), it is essential to insert a linear polarizer before the EOM to clean up the polarization of the incoming laser beam. In addition, I ensure that the beam enters any transmissive optical component in the setup (e.g. the cell) at an tilted incident angle to minimize accidental etalon effects.

Unlike the conventional FM setup, where the laser beam is modulated continuously (the *cw* mode), in this work, the laser beam is pulsed-frequency-modulated with a pulse duration of ~350 ns at a repetition rate of 10 Hz (illustrated at the top portion of Fig. 5-3). Specifically, the cw output of a voltage-controlled oscillator (with output frequency of ~940 MHz) passes through a fast switch, with <6 ns rise/fall time. The switch is controlled by a pulse generator. The pulsed rf modulation reference is used to modulate the output of a Ti-sapphire laser $(720 - 800$ nm). The frequency and the sideband characters of the FM-ed beam can be monitored by a high-finesse wavemeter. The amplitudes of the two sidebands are chosen to be ~25% that of the carrier. Note that due to the presence of a resonant cavity inside the EOM, the pulsed FM-ed beam has finite rise and ring-down times (discussed in Section 5.3.2). The rise and ring-down of the FM-ed beam poses no problems for the present experiment, because I can always select a time-region of the FM signal during which the FM-ed beam intensity is constant.

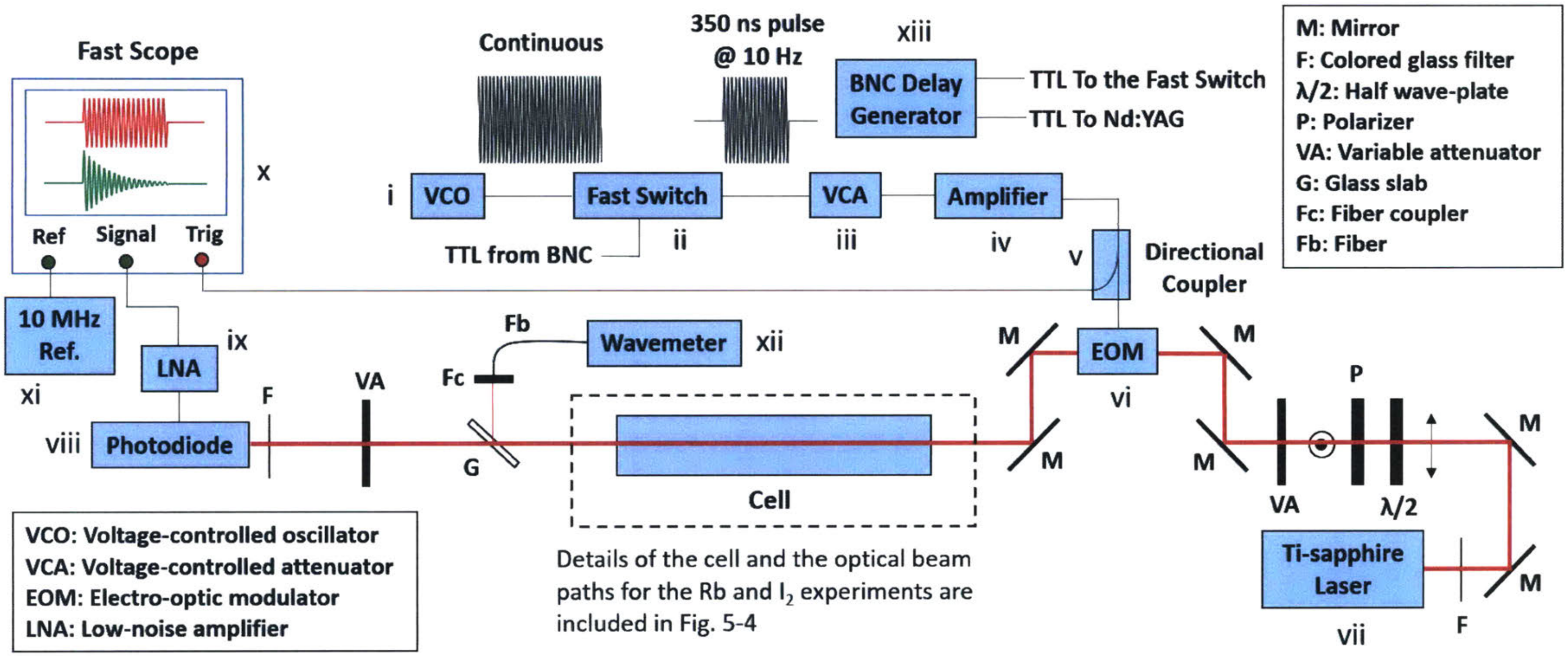

Figure 5-3: Schematic diagram of the FM setup. Detailed configuration of the cell and the optical beam path in the I_2 and Rb experiment are shown in Fig. 5-4. For a full list of parts (with manufacturer and model information), see Section 5.3.3.

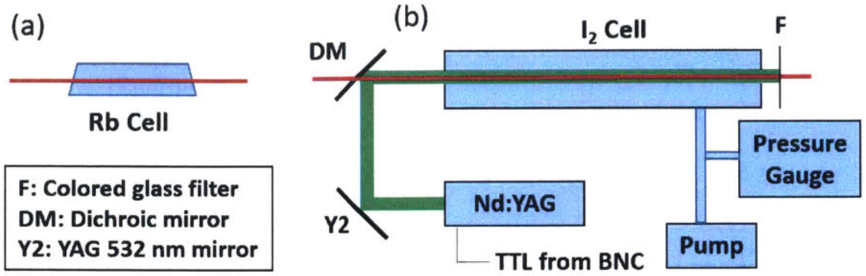

Figure 5-4: Detailed configuration of the cell and optical beam path used in the Rb (a) and I_2 (b) experiments.

In addition, in a conventional FM setup, the FM signal (at the *rf* modulation frequency) is demodulated by an I & Q demodulator (i.e. hard-ware demodulation), and the two *dc* output channels are monitored and averaged on an oscilloscope. In this work, time-domain FM signals (at 940 MHz) are collected and averaged directly on a fast oscilloscope, with maximum 20 Gs/s sampling rate (per channel) and clocked by a 10 MHz Rb reference. In all experiments described in this chapter, I use a 10 Gs/s sampling rate to increase the data acquisition efficiency. In order to average the rapidly-oscillating time-domain signals in a *phase-coherent* manner, it is necessary to use part of the *rf* modulation reference (split by a directional coupler) to trigger the fast scope (i.e. triggered by the steep turn-on of the *rf* reference). With such a triggering scheme, the time-domain signal can be averaged for >1000 shots without degradation of its phase-coherence. All of the data shown in this chapter are the result of 5 averages at each laser-frequency step.

Note that direct averaging of the 940 MHz FM signals cannot be achieved when the output of the pulse generator, used to trigger the fast switch, is also used to trigger the scope. This is because the time-jitter (rms=1 ns) between different output channels of the pulse generator is too large compared to the modulation period, ~1 ns. The *rf* modulation reference, recorded simultaneously with time-domain FM signal, also serves as phase-reference for the experiment. I observe that the relative phase between the *rf* modulation signal and the time-domain FM signal (i.e. from a Rb absorption experiment) remains unchanged for weeks. The stability of the relative phase is crucial, because determination of the sign of the population difference (between two

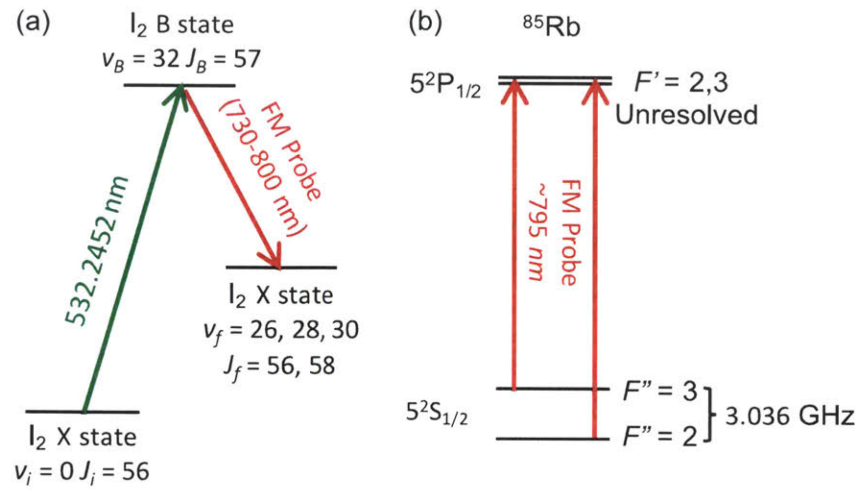

Figure 5-5: Level diagrams of (a) λ-type excitation scheme for an I_2 $B-X$ transition, and (b) ^{85}Rb $5^2P_{1/2} \leftarrow 5^2S_{1/2}$ transition.

levels) relies on the ability to draw meaningful a *phase* comparison between FM absorption signals and signals from a system with an unknown population difference. In this work, the rf modulation signal is also used as a direct input to demodulate the collected time-domain signals, thus generating the conventional FM spectra, as shown in Fig. 5-2.

5.3.2 Proof of principle experiments on the I_2 $B-X$ transition

A λ-type excitation scheme (i.e. SEP) of an I_2 $B-X$ transition (Fig. 5-5a), in combination with the Rb D_1-line absorption transition (Fig. 5-5b), is used to demonstrate the possibility of using the phase of the FM signal to determine the sign of the population difference between the upper and lower energy levels probed by the FM-ed beam.

In the I_2 experiment, the $J_B = 57$, $v_B = 32$ level of the I_2 B state is first populated by the second harmonic of the injection-seeded Nd:YAG laser, tuned to the Doppler line-center of the transition (532.2452 nm) [81]. A weak FM-ed beam is used to probe the population difference between the Nd:YAG-pumped B-state level and an unpopulated, vibrationally highly-excited X-state level ($J_f = 56$ or $J_f = 57$ of $v = 26$, 28, and 30 vibrational levels). Prior to the experiments, molecular constants from

Refs [94] (for the I_2 X state) and [145] (for the I_2 B state) are used to predict the frequencies of the relevant $B \rightarrow X$ transitions.

The 532 nm Nd:YAG laser beam (1.4 mJ/pulse) is unfocused (~0.75 cm in diameter) and overlaps spatially with the FM-ed beam (counter-propagating with respect to the Nd:YAG beam). Given that the FM-ed beam has a diameter of ~1 mm, the effective Nd:YAG pulse-energy is ~30 μJ/pulse. The $v_B = 32 \rightarrow v_f = 26, 28, 30$ transitions are probed, respectively, with 1.5 mW, 2 mW, and 4.5 mW of the FM-ed beam (measured when the beam is frequency-modulated in the *cw* mode). Different probe power is used for the three v_f levels, due to difference in their transition strengths. The I_2 cell is actively pumped by a mechanical pump during the experiment, and the pressure is held at ~200 mtorr, measured immediately after the cell. Note that without active pumping of the cell, the fluorescence lifetime of the I_2 B-state level (populated by the 532 nm pulsed laser) is collisionally-quenched to <10 ns, and the observed $B \rightarrow X$ stimulated emission signals are similarly short-lived. The fluorescence lifetime increases to ~200 ns, when the cell is actively pumped. (The I_2 B-state level is expected to have a lifetime of ~900 ns in collision-free conditions [25, 35].)

The phases of FM signals from the I_2 $B \rightarrow X$ stimulated emission transitions can be compared to those of the ^{85}Rb $5^2P_{1/2} \leftarrow 5^2S_{1/2}$ absorption transition near 795 nm. Based on information from Ref [152], two ^{85}Rb absorption lines are expected to be resolved due to the hyperfine splitting of the lower $5^2S_{1/2}$ level (~3 GHz). The hyperfine splitting of the upper $5^2P_{1/2}$ level (0.36 GHz) cannot be clearly resolved in the experiment, given an expected Doppler-broadened linewidth of 0.5 GHz.[2] For similar reasons, the hyperfine splittings of the I_2 $B - X$ transitions (split into >10 lines with <50 MHz average spacings) are too small to be resolved (at an expected 0.3 GHz Doppler linewidth). Aside from causing the observed lineshape to be slightly asymmetric, the presence of unresolved hyperfine structures does not affect the determination of the sign of the population differences between the two (zero-order) levels (i.e.

---

[2] The D_1 absorption transitions of the less abundant ^{87}Rb (27.8%) species can also be observed. The ^{87}Rb signals do not interfere significantly with the ^{85}Rb signals, because the two observed ^{87}Rb transtions (due to ~7 GHz hyperfine-splitting of the lower $5^2S_{1/2}$ [153]) are not overlapped in frequencies with the two ^{85}Rb transitions, and the ^{87}Rb signals are weaker by a factor of three compared to the ^{85}Rb signals, due to lower natural abundance of ^{87}Rb.

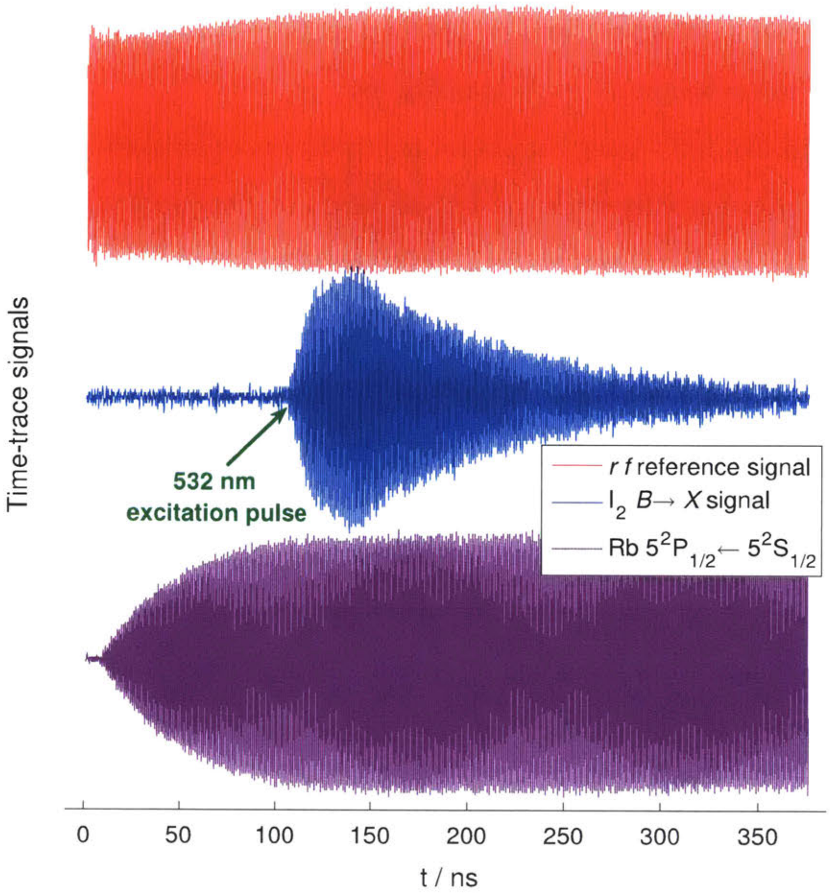

Figure 5-6: Examples of signals (at 940 MHz) collected directly by the fast oscilloscope. The fast rising-edge (not shown on the figure) of the pulsed rf modulation reference (red) is used as the trigger of the fast oscilloscope. The rf reference is simultaneously recorded along with the FM signal at each laser frequency step. The green arrow on the I_2 time-trace (blue) indicates the approximate time at which 532 nm $B-X$ excitation occurs.

neglecting hyperfine splittings) probed by the FM-ed beam. As the carrier-frequency of the FM-ed beam is scanned through the effective lineshape of the transition (with unresolved hyperfine splittings), the differential attenuation/amplification and phase shift of the two sidebands are expected to have qualitatively the same patterns as in an idealized two-level system (see Fig. 5-1).

Typical time-traces collected on the oscilloscope are shown in Fig. 5-6 (the rf reference signal is collected simultaneously for the I_2 or the Rb signal). The slow rise-time (>70 ns) of the Rb $5^2P_{1/2} \leftarrow 5^2S_{1/2}$ signal is due to the build-up time of the EOM cavity (i.e. it takes >70 ns for the intensity of the rf input into the EOM cavity to reach steady state). The Rb signal also has a ring-down time (i.e. the exponentially decaying signal after the *rf* reference is switched off) of similar duration (not shown in Fig. 5-6). Keeping in mind the finite build-up time of the FM-ed beam intensity, in the I_2 experiment the $B(v = 32) \leftarrow X(v = 0)$ transition (at 532 nm) is excited after the FM reaches the steady-state intensity.

5.3.3 Part list

i. Voltage-controlled oscillator (Mini Circuits, ZOS-1205)

ii. SPDT switch (Mini Circuits, ZYSWA-2-50DR), with rise/fall time of 6 ns

iii. Voltage variable attenuator (Mini Circuits, ZX73-2500-s+)

iv. High power amplifier (Mini Circuits, ZHL-1000-3W+)

v. Directional coupler (Mini Circuits ZEDC-15-2B)

vi. Electro-optic modulator (New Focus, 4421)

vii. Ti-sapphire laser (M Squared, Solstis) pumped by the 532 nm output of a diode-pumped solid-state laser (Lighthouse Photonics, Sprout G18)

viii. Amplified high speed photodetector (Newport, 818-BB-21A)

ix. Low noise amplifier (Mini Circuits, ZEL-0812LN), with bandwidth of 800-1200 MHz.

x. Digital storage oscilloscope (Tektronix, TDS6124C). A sampling rate of 10 Gs/s is used in all the experiments described in this chapter.

xi. Rubidium frequency standard (Stanford Research Systems, FS725)

xii. Wavelength Meter (HighFinesse, WS7)

xiii. Pulse/delay generator (Berkeley Nucleonics Corporation, Model 555)

Nd:YAG: Q-switched, injection-seeded Nd:YAG laser (Spectra-Physics, LAB-170).

Rb cell: Thorlabs, GC19075-RB

I_2 cell: Home-made cylindrical single-pass cell (30 cm in length) containing solid I_2 crystal.

Pressure gauge: Thermocouple gauge (Varian, Type 0531)

Pump: Rotary vane pump (Edwards, E2M1.5)

M: Broadband dielectric mirror (Thorlabs BB1-E02)

F: 630 nm long-pass filter (Newport, 20CGA-630)

$\lambda/2$: Zero-order half-wave plate (Thorlabs, WPH05M-780)

P: Glan-Laser calcite polarizer with 800 nm AR coating

VA: Continously variable metallic neutral density filters (Thorlabs, NDC-25C-2M)

G: 1" uncoated UV fused-silica slab (6 mm in thickness), used as a pick-up mirror of the 730 – 800 nm beam for wavelength (and FM sidebands) monitoring.

Fc: Fiber collimation package (Thorlabs, F240FC-780)

Fb: Multi-mode fiber (Thorlabs)

DM: Nd:YAG dichroic beamsplitter (Thorlabs, HBSY12). It reflects 532 nm and transmitts 730 – 800 nm laser beam.

Y2: Nd:YAG 2^{nd} harmonic mirror (Thorlabs, NB1-K12)

5.4 The I_2 $B \rightarrow X$ Transition

As discussed in Section 9.2, the phases of the time-domain FM signals from the ^{85}Rb $5^2P_{1/2} \leftarrow 5^2S_{1/2}$ absorption and I_2 $B \rightarrow X$ stimulated emission transitions are expected to be qualitatively different. In Fig. 5-7, the time-domain FM signals from the $5^2P_{1/2}(F' = 2,3) \leftarrow 5^2S_{1/2}(F'' = 3)$ upward transition are compared to the FM signals from the I_2 P(58) $B(v = 32) \rightarrow X(v = 26)$ downward transition. In Figs. 5-7a and 5-7b, the red and blue traces correspond, respectively, to the time-domain signals at carrier frequencies that are red and blue-detuned by the same amount (0.016 cm^{-1}) from the transition center frequency. Similar to the simulations in Fig 5-1, with equal detuning (i.e. comparing time-traces of the same color in Figs. 5-7a and 5-7b), FM signals from the *inverted* I_2 $B - X$ two-level system are observed to be 180° out-of-phase with respect to FM signals from the *non-inverted* ^{85}Rb $5^2P_{1/2} - 5^2S_{1/2}$ system.

Time-domain FM signals are also demodulated into in-phase and quadrature components, based on the strategy discussed at the end of Section 9.2. For the ^{85}Rb $5^2P_{1/2} \leftarrow 5^2S_{1/2}$ transitions, the in-phase and quadrature components correspond, respectively, to the absorption and dispersion signals. For the I_2 P(58) $B(v = 32) \rightarrow X(v = 26)$ transition, the two components correspond, respectively,

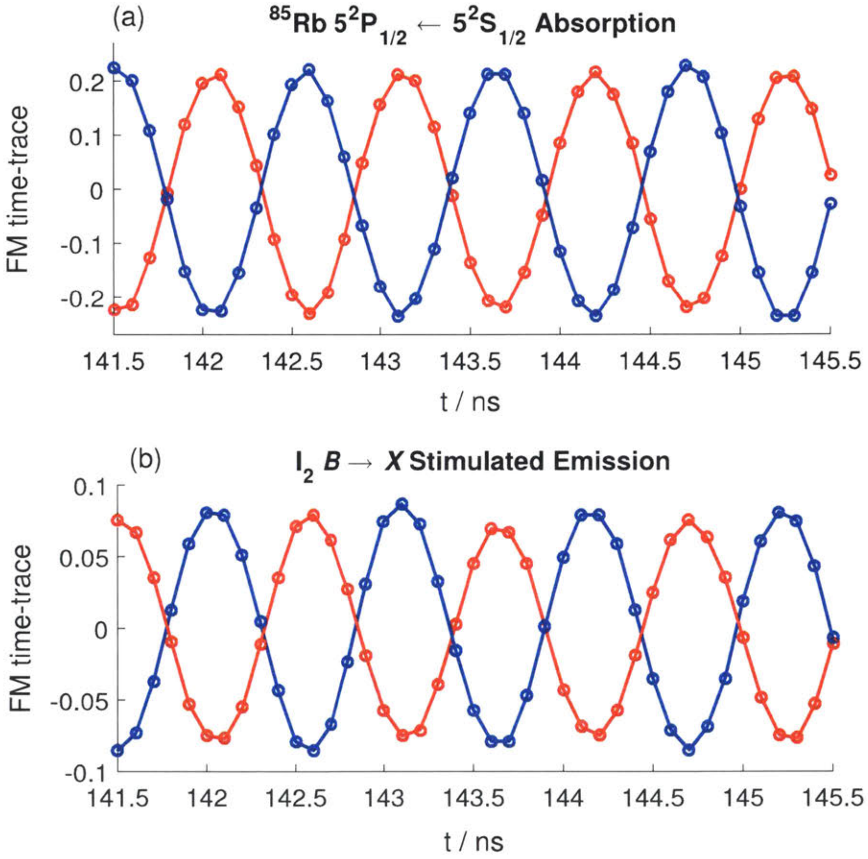

Figure 5-7: FM signals of (a) the observed ^{85}Rb $5^2\mathrm{P}_{1/2} \leftarrow 5^2\mathrm{S}_{1/2}$ transition, originating from the $F'' = 3$ hyperfine component of the $5^2\mathrm{S}_{1/2}$ state, and (b) the observed I_2 $B(v = 32, J = 57) \rightarrow X(v = 26, J = 58)$ transition. In each plot, the red and blue traces, correspond, respectively, to the FM signals collected at laser carrier frequencies that are red and blue-detuned by an equal amount, 0.016 cm^{-1}, from the transition center frequency.

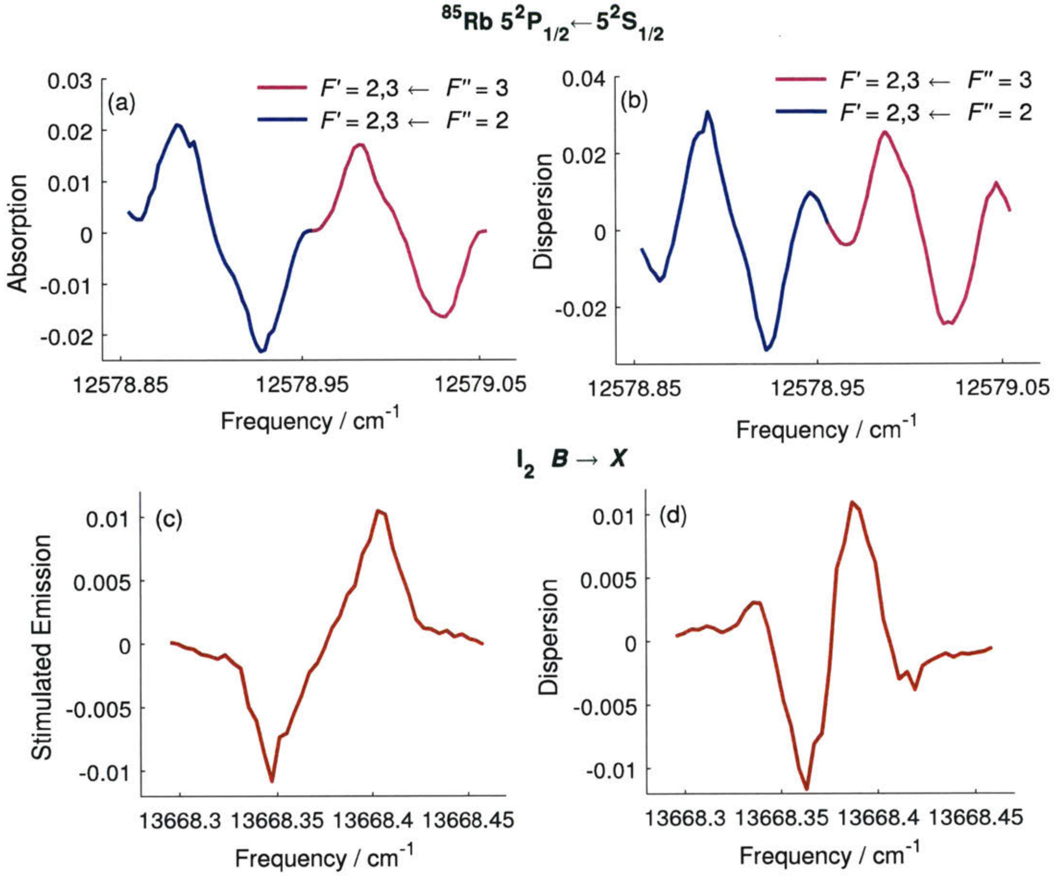

Figure 5-8: Demodulated spectra of the observed ^{85}Rb $5^2\mathrm{P}_{1/2} \leftarrow 5^2\mathrm{S}_{1/2}$ transitions (a and b) and the I_2 $B(v = 32, J = 57) \rightarrow X(v = 26, J = 58)$ transition (c and d). For the Rb transitions, two absorption lines are resolved, due to large hyperfine splitting of the lower $5^2\mathrm{S}_{1/2}$ state. [152] Hyperfine splittings of the I_2 $B - X$ transitions (split into >10 lines with <50 MHz average spacings) are too small to be resolved, given the Doppler-broadened linewidth (300 MHz).

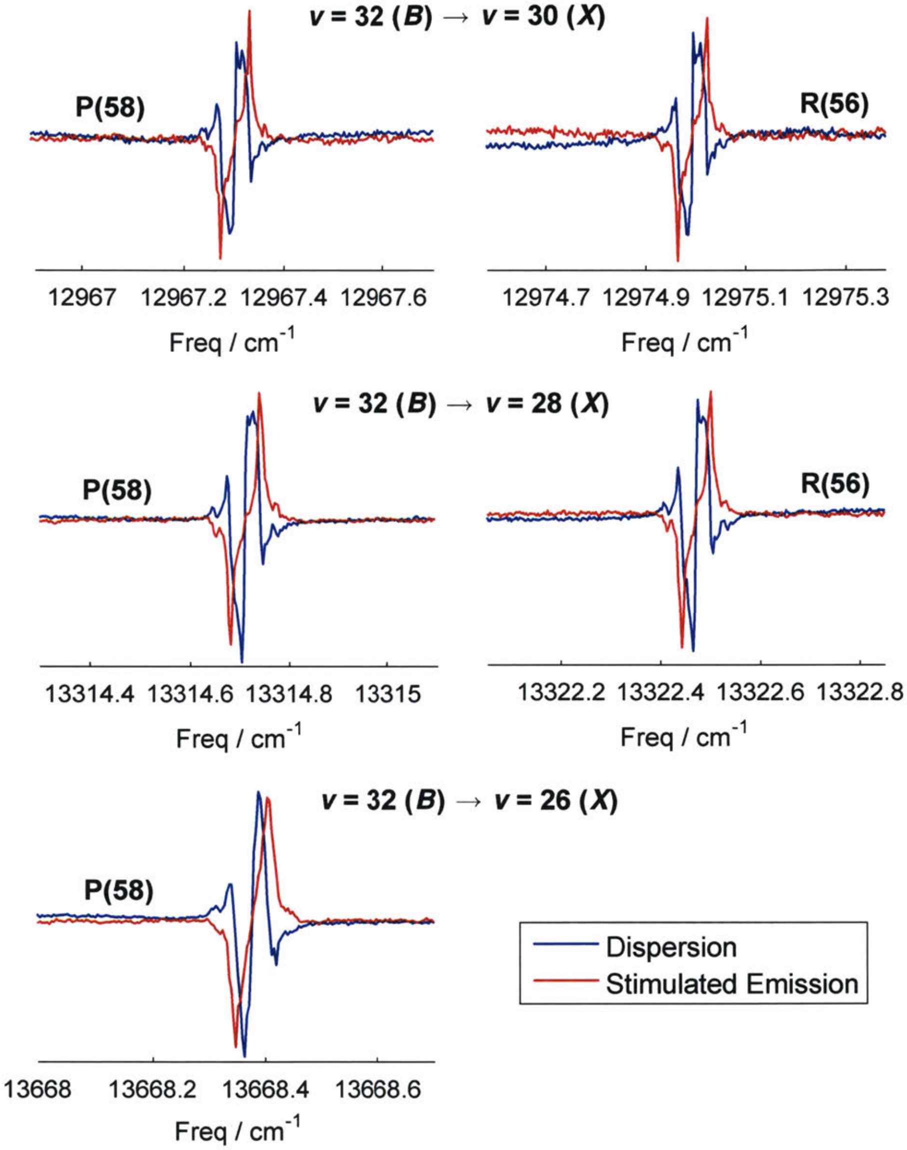

Figure 5-9: Demodulated spectra of all observed I_2 $B \rightarrow X$ transitions. Finer structures on the observed lineshape are due to unresolved hyperfine splittings.

Table 5.1: Measured frequencies of the observed $B \rightarrow X$ transitions of I_2. Numbers in parentheses are the predicted transition frequencies, calculated based on the I_2 molecular constants from Refs [94, 145]. Units are in cm^{-1}.

	P(58)	R(56)
32→30	12967.30	12975.00
	(12967.24)	(12974.95)
32→28	13314.71	13322.47
	(13314.67)	(13322.44)
32→26	13668.38	
	(13668.35)	

to the stimulated emission and dispersion signals. As discussed in Section 9.2, near the transition center frequency, both the in-phase and quadrature signals from the I_2 $B \rightarrow X$ transition are expected to have the opposite phase (or sign) with respect to those from the Rb $5^2P_{1/2} \leftarrow 5^2S_{1/2}$ transitions. This is confirmed in Fig. 5-8, where the absorption and dispersion components of the two observed ^{85}Rb D_1 transitions are shown in panels a and b, and the stimulated emission and dispersion components of the I_2 P(58) $B(v = 32) \rightarrow X(v = 26)$ transition are shown in panels c and d. In Fig. 5-9, demodulated spectra of multiple additional I_2 $B \rightarrow X$ transitions are shown. The general shapes (or phases) of both the dispersion and stimulated emission spectra for those transitions are the same, because the original FM signals are demodulated with the same set of phase corrections (ϕ_1 and ϕ_2, determined from the ^{85}Rb $5^2P_{1/2} \leftarrow 5^2S_{1/2}$ transition).

The observed $B \rightarrow X$ transition frequencies (taken as the frequencies at the zero-crossings of the stimulated emission spectra) are included in Table 5.1, together with predictions (in parentheses) based on the I_2 molecular constants from Refs [94, 145].

5.5 Conclusion

In this work, I demonstrate a modified application of FM spectroscopy, which allows me to determine the sign of the population difference between two levels probed by an FM-ed beam. FM signals from a stimulated emission experiment (e.g. the I_2

$B \rightarrow X$ transition) have been shown, both theoretically and experimentally, to be 180° out-of-phase with respect to FM signals from an absorption experiment (e.g. ^{85}Rb $5^2P_{1/2} \leftarrow 5^2S_{1/2}$ transition). The technique is applied in Chapter 6 to probe the C_2 fragments, generated via one-color (~220 nm), resonance-enhanced (S_1-S_0), multiphoton dissociation of acetylene. The goal is to determine the relative abundance of the C_2 A and X fragments.

Chapter 6

Determination of the Population Difference Between the C_2 $A^1\Pi_u$ and $X^1\Sigma_g^+$ States Following One-color (218 – 226 nm), Resonance-enhanced (S_1-S_0), Multi-photon Dissociation of Acetylene

Abstract

One-color (~220 nm), resonance-enhanced (S_1-S_0), multi-photon dissociation of acetylene gives rise to strong photofragment fluorescence signals in the visible and near UV regions. By dispersing the photofragment fluorescence (see Chapter 4), I demonstrate that the photolysis leads to significant C_2 populations in the $C^1\Pi_g$ and $d^3\Pi_g$ states. It is not known, from these experiments, whether the C_2 $A^1\Pi_u$ and $X^1\Sigma_g^+$ states are also populated. In this work, I determine the population difference between the $v = 2$ vibrational level of the C_2 A state and the $v = 0$ vibrational level of the C_2 X state, based a modified application of frequency-modulation (FM) spectroscopy, discussed in Chapter 5. The wavelength of the pulsed UV photolysis laser is tuned to each of the three individual acetylene S_1-S_0 transitions, which populate, respectively, the $K = 1$, $J = 8$, e-symmetry levels of the S_1 3^2 and 3^3 vibrational levels, and the $K = 1$, $J = 7$, f-symmetry level of the S_1 3^4 vibrational level. A weak FM probe is used to

measure six different Q-branch transitions ($J'' = 2, 8, 14, 20, 26,$ and 32) of the $(2-0)$ band of the C_2 $A - X$ transition, within 5 ns after the photolysis. By comparing the *phase* of th]e FM signal from the C_2 $A - X$ transitions with that from the Rb D_1-line absorption transitions, I determine that for all probed $A(v=2) - X(v=0)$ two-level systems, there is more population in the lower-energy X-state level. The production of the C_2 X state is likely an overall two-photon process. From each of the three acetylene S_1 vibrational levels populated by the first photon used in this work, the one-photon photodissociation cross-section, i.e. HCCH $(S_1)\xrightarrow{h\nu} C_2$ (X)+2H, appears to be similar.

The work described in this chapter was performed with Professor Zhenhui Du, who is a visiting scholar from Tianjin University, China.

6.1 Introduction

In Chapter 4, I present my identifications of the molecular transitions which give rise to the strong photofragment fluorescence signals, following one-color, resonance-enhanced (via the S_1 *trans*-conformer 3^4, 3^5 vibrational levels, and the S_1 *cis*-conformer 3^16^1 vibrational level), multi-photon dissociation of acetylene. The C_2 Swan ($d^3\Pi_g - a^3\Pi_u$) and Deslandres-d'Azambuja ($C^1\Pi_g - A^1\Pi_u$) emission bands are observed in the dispersed fluorescence (DF) spectra excited via all three S_1 vibrational levels. In a collision-free environment, long-lived (>3 μs) emission from electronically excited C_2H^* is also observed (the electronic transitions associated with this long-lived emission have not been assigned). The branching ratios for the formation of photofragments in C_2H^*, C_2 d, and C_2 C states are similar for the S_1 *trans* 3^4 and *cis* 3^16^1 vibrational levels, and the ratios, $C_2H^* : C_2(d) : C_2(C)$, are estimated to be >40 : 4 : 1. The two C_2 species are likely generated via a three-photon (from S_0 acetylene) sequential C-H bond-breaking process, while the C_2H^* fragments are most likely generated by a two-photon process.

All three photofragment transitions are observed in 193 nm ArF photolysis studies of acetylene [5, 101, 124, 148, 167]. Among all of the observed C_2 fragments in the 193 nm acetylene photolysis, the C_2 $A^1\Pi_u$ state is known to be the most abundant, e.g. the ratio between the $A^1\Pi_u$ and $X^1\Sigma_g^+$-state population is estimated to be 19(3) : 1 [5, 148]. Results from *ab initio* calculations by Cui et al. [39] confirm the observed population of the A state relative to other C_2 electronic states. However, the C_2 $A^1\Pi_u - X^1\Sigma_g^+$ Phillips band emission, which accounts for ~90% of the total integrated emission intensity following 193 nm photolysis of acetylene [101], is not observed in the photofragment DF spectra analyzed in Chapter 4. While transitions involving low-lying A-state vibrational levels ($v < 3$) are outside the operating range of the monochromator and photomultiplier tube (PMT) used in Chapter 4, a search for the $(4, 0)$ band of the C_2 $A - X$ transition in the 691 nm region shows no sign of the transitions. This, however, does not rule out the possibility that lower-lying vibrational levels of the A state ($v \leq 3$) are populated.

The goal of this work is to determine the population difference between C_2 A and X-state levels following one-color (~220 nm), resonance-enhanced (S_1-S_0), multiphoton dissociation of acetylene. Specifically, C_2 fragments (A or X state) generated via three non-predissociated S_1 $K = 1$ vibrational levels, 3^2 (226 nm), 3^3 (222 nm), and 3^4 (218 nm)[1], are probed, based on a slight modification of frequency-modulation (FM) spectroscopy, which allows me to determine, from the *phase* of the FM signals, the sign of the population difference in a two-level system probed by the FM beam (i.e. is the two-level system inverted?). In Chapter 5, a λ-type excitation scheme (i.e. stimulated emission pumping) of the I_2 $B - X$ transition, along with the Rb D_1-line transition, is used as a proof of principle demonstration of the technique. In the I_2 experiment, the FM laser beam is used to probe an inverted population between the pulsed-laser populated B-state level and the vibrationally highly-excited X-state level (i.e. $v = 28$, which is unpopulated at room temperature). FM signals from the inverted I_2 $B - X$ system are observed to be opposite in phase with respect to signals from the Rb D_1 absorption transitions. In contrast, FM signals from a two-level system that is not inverted (i.e. more population in the lower energy level) should have the same phase as signals from the Rb absorption transitions.

While the C_2 A state is significantly more populated than the X state following 193 nm photolysis, it is not immediately clear whether this will be true following

---

[1] The $K = 1$ level of the S_1 3^4 vibrational level lies ~200 cm^{-1} higher than the acetylene dissociation threshold [112]. However, as discussed in Section 4.4.3 of Chapter 4, the S_1 3^4 vibrational level is essentially non-predissociated, as evidenced by its long fluorescence lifetime (>200 ns).

photodissociation via the three S_1 vibrational levels used in this work. Assuming that the photodissociation proceeds exclusively via a sequential C-H bond-breaking process (instead of a concerted H_2 elimination pathway), for all three S_1-S_0 excitation energies, the C_2 $v = 0$ X-state fragments are energetically accessible with two photons, based on the experimental C-H bond dissociation energies of C_2H_2 [112] and C_2H [34]. Population of the C_2 A state requires three photons. Therefore, from an energetic point of view, production of the X-state fragments is favored over that of the A-state fragments. The $C_2(A$ or $X)+H_2$ elimination pathways, which are not observed in the vacuum ultraviolet (VUV) photolysis study of acetylene in the $8-12$ eV region (where the H_2 elimination processes would have been energetically accessible) [21, 26, 157], are assumed to be absent following 220 nm photolysis of acetylene studied in this work.[2]

Even though the production of the C_2 X state is favored energetically over that of the A state following the 220 nm photolysis of acetylene, the difference in the efficiencies of the dissociation process (i.e. bond-breaking process *after* photo-excitation is complete) which leads to the two C_2 states could also affect the *total* efficiency of the two photodissociation channels. This difference in the dissociation efficiency is used to explain the observed large population difference between the C_2 X and A states, following 193 nm ArF photolysis of acetylene [39]. Production of C_2 X and A states requires the same number of 193 nm photons (two). However, while the C_2 A state is produced after a *direct* barrierless adiabatic dissociation on the 4 $^2A'$ potential energy surface (PES) of C_2H (which is the most likely electronic state of C_2H initially populated by the second 193 nm photon), the molecule (C_2H) must undergo a sequence of internal conversions, $4\ ^2A' \rightarrow 3\ ^2A' \rightarrow 2\ ^2A' \rightarrow 1\ ^2A'$, before dissociation occurs. The direct adiabatic dissociation process is more efficient than the sequential internal-conversion-assisted dissociation process.[3] It is thus conceivable

---

[2] The concerted H_2 elimination pathway has been shown to be absent in the generation of the C_2 $C^1\Pi_g$ state following 220 nm photolysis of acetylene, discussed in Chapter 4.

[3] Note that the sequential internal-conversion-assisted dissociation process is referred to as non-adiabatic transitions in Ref [39], since a *jump* between adiabatic PES's is facilitated by non-adiabatic interactions among those surfaces. The jump between adiabatic PES's occurs near the avoided-crossings, where the electronic character of the (adiabatic) electronic states changes most rapidly, which induces non-adiabatic interactions.

that, following multi-photon (~220 nm) photolysis of acetylene studied in this work, the C_2 A state could have been generated with higher efficiency than the X state, if the dissociation process that leads to the A state is more efficient than the process that leads to the X state, despite the energetic argument (which affects the photo-excitation process which takes places *before* bond-breaking dissociation) mentioned earlier.

6.2 Experimental Details

6.2.1 The FM setup

The FM setup used in this work differs from a conventional FM setup in the generation of the FM beam and the method of the data collection, discussed in detail in Section 5.3. A brief description of the setup and the differences is provided here. The output of a Ti-sapphire laser (M Squared, Solstis), pumped by the 532 nm output of a diode pumped solid-state laser (Lighthouse Photonics, Sprout G18), is frequency-modulated by an electro-optic phase modulator (EOM) (New Focus, 4421), driven at ~1 GHz. However, instead of using a continuous 1 GHz modulation, by pulsing the radio-frequency (*rf*) modulation input into the EOM, the Ti-sapphire output is frequency-modulated with a duration of ~350 ns at a repetition rate of 20 Hz. Direct time-domain averaging of the FM signals, which are detected with an amplified high speed photodiode (Newport, 818-BB-21A) and collected on a fast oscilloscope (Tektronix, TDS6124C), can be achieved in this pulsed-modulation mode. Using the simultaneously recorded pulsed *rf* modulation input as the phase reference, time-domain FM signals (at ~1 GHz) can be demodulated to obtain the in-phase and quadrature signals (with empirical phase-adjustments of the *rf* modulation signal). The experimental setup is summarized in Fig. 5-3 of Chapter 5.

6.2.2 Probing the C_2 $A-X$ transitions

The C_2 fragments are generated by one-color (~220 nm), resonance-enhanced ($S_1 \leftarrow S_0$), multi-photon dissociation of acetylene (BOC, atomic absorption grade 2.6 99.6% purity). The frequency-doubled output (218-227 nm) of a pulsed dye laser (Sirah Cobra-Stretch, dual-grating with 3000 lines/mm), pumped by the third harmonic of a Q-switched, injection-seeded Nd:YAG laser (Spectra-Physics Pro-270), is focused by an $f = 80$ cm lens to beam waist at the center of a single-pass flow cell (40 cm in length). The use of a focusing lens with a long focal-length is intended to maximize the spatial overlap between the UV photolysis beam and the FM probe beam. The flow-rate inside the cell is controlled by a needle valve, and the cell pressure is maintained at 2 torr. The UV energy is ~300 μJ/pulse at the entrance port of the flow cell for all the experiments described here.

The wavelength of the UV beam is tuned to each of the three individual S_1-S_0 transitions which populate, respectively, the $K = 1$, $J = 8$, e-symmetry levels of the S_1 3^2 and 3^3 vibrational levels [174], and the $K = 1$, $J = 7$, f-symmetry level of the S_1 3^4 vibrational level [104, 169]. From each intermediate S_1 rovibrational level, the same UV beam photodissociates the molecule into C_2 fragments. The C_2 fragments from the one-color photolysis are probed by a counter-propagating FM beam (~1 mm in diameter). For C_2 detection involving resonance with the S_1 3^3 and 3^4 levels, a high-reflectance mirror for the Nd:YAG 5^{th} harmonic (CVI Laser Optics, Y5-1025-45) is used as the beam combiner. For C_2 detections via resonance with the S_1 3^2 level, a high-reflectance mirror at 225 nm is used. For experiments via all three intermediate S_1 levels, Q(2), Q(8), Q(14), Q(20), and Q(26) transitions of the $(2-0)$ band of the C_2 $A-X$ transition [33, 134] are used. For experiments involving the S_1 3^4 level, an additional Q(32) transition is probed. The FM beam power (measured in the *cw* modulation mode) is ~3.5 mW, ~5.5 mW and ~15 mW, respectively, for experiments involving S_1 3^4, 3^3, and 3^2 intermediate levels. The resulting FM signals can be normalized to the same power level for intensity comparison.

I emphasize that signal intensities are sensitive to laser-beam alignment (because the UV beam is focused), as well as to both the short term (i.e. shot-to-shot) and long term (i.e. hour-long) power (and frequency) fluctuation of the UV excitation laser. During the experiments, the UV power is monitored and is maintained at a relatively constant level (i.e. the average laser power decreases by <5% during experiments involving a single S_1 level). There is, however, some uncertainty about the quality of laser alignment throughout the experiments, because in order to probe each of the Q-branch transitions used in this work, the wavelength of the FM beam must be changed by ~20 nm. I do not believe that the beam alignment deteriorates noticeably when the FM laser wavelength is changed by this amount, based on the following observations. At the beginning of each set of experiments using a specific resonant S_1 level, I align and fine-tune the UV beam alignment with respect to the FM beam (mostly by adjusting the position of the focusing lens mounted on a translation stage) to optimize the strong Q(14) signal. No further adjustment of the UV laser beam is necessary in order to observe all of the other Q-branch transitions, and the amount of signal improvement is minor (<10%) even after I attempt to optimize those additional transitions (e.g. Q(26)).

To determine the sign of the population difference between the C_2 A and X-state levels probed by the FM beam, the phase of the FM signal from each C_2 $A-X$ transition must be compared with that of the ^{85}Rb $5^2P_{1/2} \leftarrow 5^2S_{1/2}$ transition (the D_1-line absorption) near 795 nm. A commercially available Rb cell (Thorlabs, GC19075-RB) is used, and the FM beam power is ~2.2 mW during the experiment. As already discussed in Chapter 5, two ^{85}Rb absorption lines are expected to be resolved due to the hyperfine splitting (3 GHz) of the lower $5^2S_{1/2}$ level [152]. The hyperfine splitting (0.36 GHz) of the upper $5^2P_{1/2}$ is too small to be clearly resolved in the current experimental setup. Transitions from the less abundant ^{87}Rb species (27.8%) do not interfere significantly with the ^{85}Rb transitions, due to large hyperfine splitting (7 GHz) of the ^{87}Rb $5^2P_{1/2}$ level and its smaller natural abundance (which leads to weaker signals) [153].

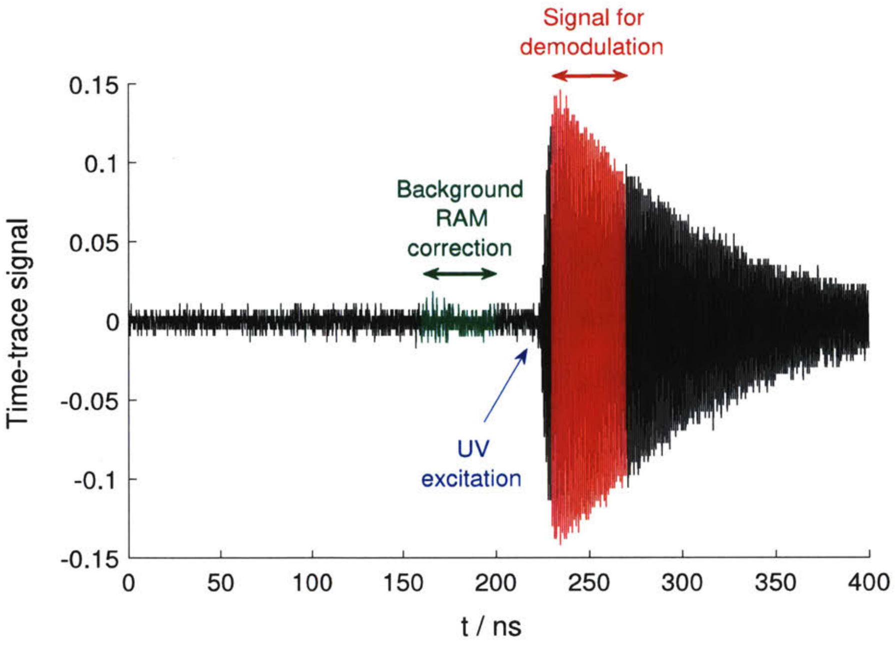

Figure 6-1: A typical time-trace of the observed C_2 $A(v=2)-X(v=0)$ transition. The FM signal oscillates at the rf modulation frequency (~1 GHz). The blue arrow indicates the (approximate) time at which the UV excitation occurs. The first 30 ns of the FM time-trace immediately after the UV excitation (color-coded red) is used to generate the demodulated spectrum. A portion of the FM time-trace (color-coded green) is used for background RAM correction.

6.3 The C_2 $A-X$ Transitions

6.3.1 Population in the C_2 A and X-state vibrational levels

A typical FM signal of the observed C_2 $A-X$ transitions, recorded directly on a fast oscilloscope, is displayed in Fig. 6-1. The time-domain signal has a laser-pulse limited rise-time of ~10 ns, followed by a decay with a time-constant of ~100 ns. In Figs. 6-2a and 6-2b, time-domain FM signals from the ^{85}Rb $5^2P_{1/2} \leftarrow 5^2S_{1/2}$ transition and the observed C_2 (populated via the S_1 3^4 level) $A(v=2)-X(v=0)$ Q(14) transition are compared. With equal detuning from the center frequency of the transition (i.e. comparing the time-traces of the same color in Figs. 6-2a and 6-2b), FM signals from the C_2 $A-X$ transition are observed to have the same phase as signals from the known absorbing ^{85}Rb $5^2P_{1/2} \leftarrow 5^2S_{1/2}$ system. This implies that there is more C_2 population in the $J=14$, $v=0$, X-state level than in the $J=14$, $v=2$, A-state

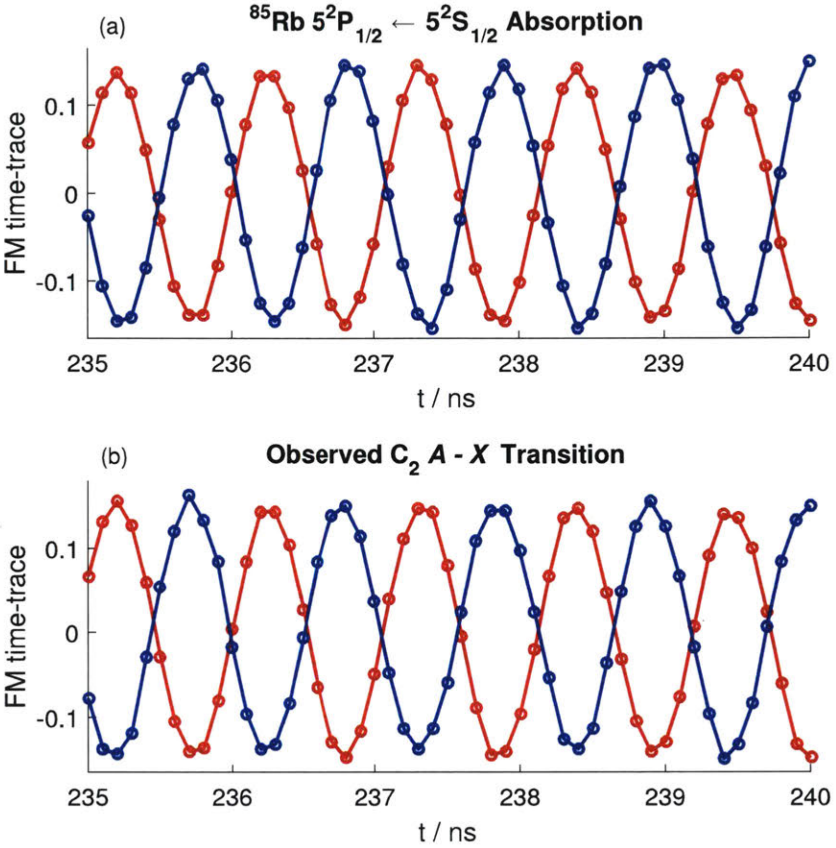

Figure 6-2: FM signals of the C_2 $A(v=2)-X(v=0)$, Q(14) transition, generated via resonance with the S_1 acetylene 3^4 vibrational level (a), and FM signals of the ^{85}Rb $5^2P_{1/2} \leftarrow 5^2S_{1/2}$ transition, excited from the $F''=2$ hyperfine component of the $5^2S_{1/2}$ state (b). In each plot, the red and blue traces, correspond, respectively, to the FM signals collected at laser carrier frequencies that are red and blue-detuned by an equal amount, 0.016 cm^{-1}, from the transition center frequency.

level. The same conclusions can be drawn for all of the $A(v=2)-X(v=0)$ two-level systems probed in this work.

The population differences between $A(v=2)$ and $X(v=0)$ levels are also reflected in the demodulated spectra (see Fig. 6-3). The demodulation procedure is based on the strategy outlined in Section 5.2. I emphasize that in order to compare the demodulated spectra of an observed C_2 $A-X$ transition with those of the Rb D_1-line absorption, the same set of phase-adjustments (to the rf signal), ϕ_1 and $\phi_2=\phi_1+\pi/2$, is used to produce the in-phase and quadrature components of the FM signal for both C_2 and Rb transitions. For all of the spectra in Fig. 6-3, at each frequency step of the

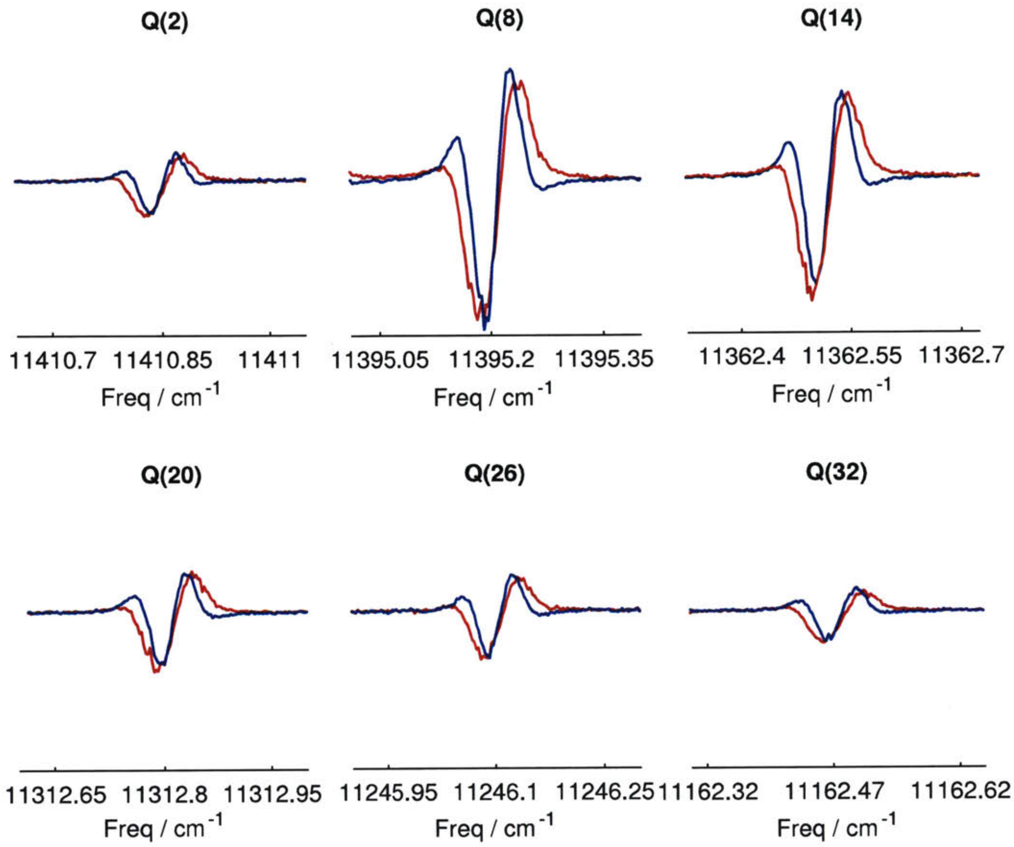

Figure 6-3: The demodulated spectra of the C_2 $A(v = 2) - X(v = 0)$ transitions, generated via the S_1 acetylene 3^4 vibrational level. In each plot, the blue and red spectra, correspond, respectively, to the in-phase (dispersion) and quadrature (absorption) component of the FM signal. The vertical scales are identical in each plot.

FM laser, the first 30 ns of the FM time trace immediately after the UV excitation (i.e. color-coded red in Fig. 6-1) is used, in order to minimize the effect of collisions on the nascent C_2 population distribution. In addition, due to the transient nature of the sample (i.e. generated by pulsed-laser photolysis), a portion of the FM time-trace (color-coded green in Fig. 6-1) before the UV excitation can be used for subtraction of background residual amplitude modulation (RAM). In Fig. 6-3, both the in-phase (blue) and quadrature (red) components of all observed C_2 $A(v = 2) - X(v = 0)$ transitions, excited via the S_1 acetylene 3^4 level, are shown, and they have the same phase with the in-phase (Fig. 6-4a) and quadrature (Fig. 6-4b) signals of each observed ^{85}Rb $5^2P_{1/2} \leftarrow 5^2S_{1/2}$ absorption line. Again, this indicates that none of the probed C_2 $A(v = 2) - X(v = 0)$ two-level systems are inverted. The same conclusions can

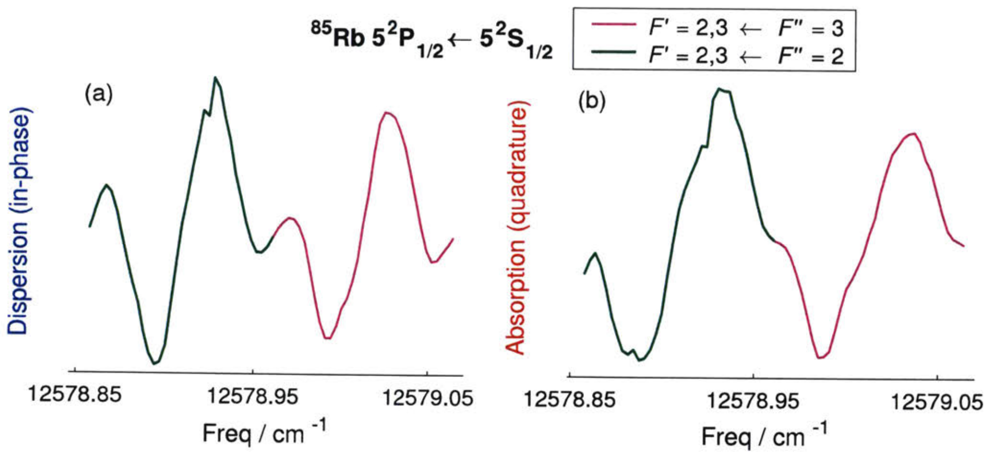

Figure 6-4: The demodulated spectra of the observed $5^2\mathrm{P}_{1/2} \leftarrow 5^2\mathrm{S}_{1/2}$ ^{85}Rb transitions. As mentioned in Section 6.2.2, two absorption lines (color-coded) are resolved, due to large hyperfine splitting of the $5^2\mathrm{S}_{1/2}$ level. For both of these well-resolved lines, the in-phase (dispersion) and quadrature (absorption) spectra are shown, respectively, in panels (a) and (b). The vertical axes of the in-phase and quadrature plots are color-coded, respectively, to match the colors in the corresponding plots in Fig. 6-3.

be drawn for all of the C_2 $A - X$ transitions, observed after photolysis via the S_1 acetylene 3^2 and 3^3 vibrational levels.

Note that the FM lineshape of all C_2 $A - X$ transitions (see, for example, those in Fig. 6-3) are slightly asymmetric, with the magnitude of the lower-frequency lobe systematically higher by ~20% than that of the higher-frequency lobe. I do not have a good explanation for the observed asymmetry. The asymmetry is not a result of background RAM, because the magnitude of RAM is small ($<5\%$) compared to that of the strong C_2 signals excited via the S_1 3^4 level (for which this asymmetry is still observed), and the asymmetry is not reduced even after I subtract the background RAM (using the method discussed in the previous paragraph). In addition, the asymmetry does not seem to result from systematic defects of the detection system, because all observed FM lineshapes of the I_2 and Rb transitions (see Figs. 5-9 and 6-4) appear to be nearly symmetric (despite the presence of unresolved hyperfine splittings). The presence of asymmetry cannot affect the conclusions regarding the *sign* of the population differences (i.e. whether there is population inversion) between the C_2 A and X-state levels, because the *sign* of the population differences is reflected

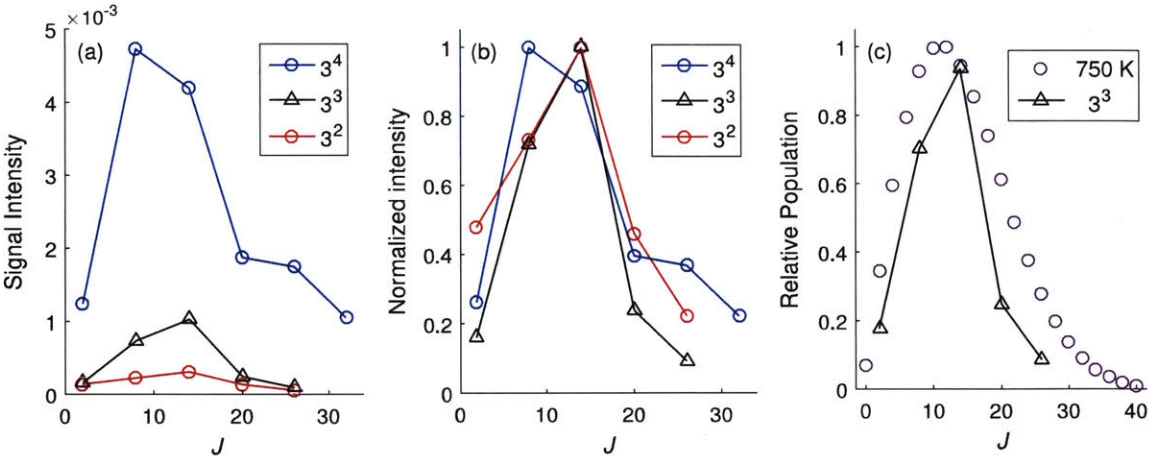

Figure 6-5: Observed intensities of various Q-branch transitions of the C_2 $A-X$ $(2,0)$ band. (a) The signal intensities are normalized to the same FM probe power (measured in the continuous modulation mode). (b) The relative intensities are normalized to the maximum intensity from each acetylene intermediate level. (c) Comparison of the intensities of C_2, generated via the 3^3 level, with a Boltzmann rotational distribution of 750 K.

in the *phase*, rather than in the magnitude, of the FM signal.

To summarize, from both the FM time-domain signals and the demodulated spectra, I reach the same conclusion that, for all of the C_2 $A(v=2)-X(v=0)$ two-level systems probed in this work, there is more population in the lower-energy X-state level. It is likely that this population relation applies to all other pairs of $A(v=2)-X(v=0)$ levels (not probed in the experiment). I emphasize that only the population differences are probed in the FM experiments. I cannot rule out the possibility that the $v=2$ level of the C_2 A state is populated, but with smaller *absolute* population than the X state. In addition, probing of the $(1,0)$ and $(0,0)$ bands of the C_2 $A-X$ transition, which would provide a more complete picture of the population differences in the C_2 $A-X$ system, cannot be carried out because the transition wavelengths [33, 134] are outside the operation range of the EOM.

6.3.2 The C_2 X-state population distribution

Signal intensities (from the first 30 ns of the FM time-trace) of the probed transitions contain information about the nascent C_2 population in the $v=0$ level of the X state.

In Fig 6-5a, the intensities of the observed C_2 $A-X$ transitions (normalized to the same FM probe power), resulting from resonance-enhanced photodissociation via all three S_1 acetylene vibrational levels, are shown. The ratio of the maximum C_2 $A-X$ signals from the three intermediate S_1 levels is $C_2(3^4 : 3^3 : 3^2) = 15 : 3 : 1$, which is similar to the observed relative intensities [75, 127, 173] of one-photon transitions into the three intermediate S_1 acetylene levels, $S_1 \leftarrow S_0(3^4 : 3^3 : 3^2) = 14 : 4 : 1$. This suggests that the photodissociation cross-sections of HCCH $(S_1) \xrightarrow{h\nu} C_2$ (X)+2H are similar for all three S_1 levels.

It is also evident in Fig. 6-5b that the C_2 rotational distributions, resulting from photodissociation of the three intermediate S_1 acetylene levels, are slightly different. The maximum J-population appears to be centered around $J = 8$ following photodissociation via S_1 3^4, but the maximum rotational population shifts towards higher J-levels ($J \approx 14$) for 3^3 and 3^2 levels. In addition, the C_2 X-state rotational population distribution for photodissociation via the three intermediate levels cannot be fitted to a Boltzmann distribution, as shown specifically for the C_2 X-state molecules generated via S_1 3^3. The widths of the observed X-state population distribution from the three S_1 vibrational levels, however, do not seem to follow a simple monotonic trend. I must emphasize that the observed rotational distributions are subject to experimental uncertainties, such as laser power fluctuations and issues with laser-alignment, which are discussed in Section 6.2.2. More systematic evaluations of those experimental uncertainties are needed in order to ensure that the observed rotational distributions are meaningful.

6.3.3 An estimate of the overall photodissociation efficiency

The efficiency of generating a single quantum state of C_2 (e.g. X-state $v = 0$, $J = 14$ level) from the $J = 7$ level of the S_0 vibrational ground state (the initial acetylene rovibrational level used in all experiments in this work) can be estimated by comparing the intensity of an observed C_2 $A-X$ transition with that of the ^{85}Rb D_1 transition. The estimate given in this section is based on the C_2 $A(v = 2) - X(v = 0)$ Q(14) transition generated via the S_1 acetylene 3^4 intermediate state. Using the known vapor pressure of Rb at room temperature (2×10^{-7} torr) [152], and given the length of the single-pass Rb cell (7.5 cm) and the diameter of the FM beam (~1 mm), I estimate that the observed ^{85}Rb D_1-line signal strength (see Fig. 6-2) corresponds to ~4.2×10^8 Rb atoms in the ground state. As is shown in Fig. 6-2, the observed peak intensity of the C_2 Q(14) transition is similar to that of the Rb transition. Considering the difference in the transition dipole moments between the Rb D_1-line (~ 8 Debye) [152] and the C_2 $A(v=2)-X(v=0)$ transition (~0.15 Debye) [28, 149] (and given that the FM laser beam intensities are similar for the two experiments), the C_2 $A(v=2) \leftarrow X(v=0)$ Q(14) absorption signal corresponds to a population difference of ~1.2×10^{12} molecules between the two C_2 levels (larger in the X state, as discussed in Section 6.3.1). The interaction volume of the UV and FM probe beams inside the cell is ~100 mm^3, estimated from the length of the single-pass cell (40 cm) and the approximate diameter of the focused UV beam (~1 mm) near the cell entrance (the UV beam has minimum beam-waist near the center of the cell). Given that the effective acetylene pressure is ~2 torr inside the cell at room temperature, the total number of $J = 7$ S_0 acetylene molecules inside the interaction volume is 7×10^{14}. If I assume that the population in the C_2 A state is negligible compared to that in the X state, which means that the estimated total number of C_2 molecules in the X-state $v = 0$, $J = 14$ level is ~1.2×10^{12}, I obtain an efficiency of ~0.2% in generating this specific X-state level from the $J = 7$ S_0 acetylene level. Given that the $J = 14$ level accounts for ~10% of the total $v = 0$ population (estimated from the observed rotational population distribution in Fig. 6-5), the total efficiency (i.e. including all J levels) of producing the C_2 X-state $v = 0$ level (via the S_1 3^4 level) is thus ~2%. This is a rather high efficiency, considering that a two-photon excitation process is needed to generate the X state, and that the initial S_1-S_0 pumping efficiency is not 100%. The Doppler line-width of the initial S_1-S_0 UV transition is ~0.11 cm^{-1}, which is significantly larger than the linewidth of the photolysis laser (0.03 cm^{-1}). The S_1-S_0 transition probability varies for different acetylene velocity groups, i.e. higher for molecules near the center of the Doppler-profile (to which the UV laser frequency is tuned) than those at the two wings of the profile. The photolysis efficiency is thus not uniform across all acetylene velocity groups, which further decreases the overall photolysis efficiency.

6.3.4 Photodissociation pathway

With all three acetylene S_1-S_0 excitation energies used in this work, the C_2 $v = 0$ X-state fragments are energetically accessible with two (same-color) photons, with excess energy (for the $J = 0$ level) of approximately 3000 cm^{-1}, 5000 cm^{-1}, and 7000 cm^{-1}, respectively, for the S_1 3^2, 3^3, and 3^4 levels. It is likely that the observed C_2 X-state levels are populated via one-color, two-photon excitation of acetylene, resonance-enhanced by the S_1-S_0 transition.

The C_2 X state has been previously observed in a two-photon 193 nm photodissociation study of acetylene [5, 148, 167]. However, the mechanism by which the observed C_2 X state is generated in my work is qualitatively different from that of the 193 nm photolysis. The S_1 levels initially populated by the 193 nm photon dissociate rapidly into C_2H ($\tilde{X}^2\Sigma^+$ and $\tilde{A}^2\Pi$)+H. As a consequence of fast dissociation, the S_1 level is not directly involved in the subsequent photodissociation process and the observed C_2 X-state populations are generated from the C_2H $\tilde{X}^2\Sigma_g^+$ molecules. Given that none of the three S_1 levels used in this work are predissociated, the production of the C_2 X state must result from *direct* photodissociation of the S_1 acetylene level. The S_1 acetylene is excited by a second photon to an electronically highly-excited acetylene state. Assuming a sequential bond-breaking process (instead of a concerted elimination of H_2), dissociation of the acetylene precursor state produces C_2H, which further dissociates, thus populating the C_2 X state.

While insufficient experimental information exists to suggest the electronic assignments of the dissociation precursor C_2H_2 and C_2H states, some of the characteristics of those states (in particular, those of the C_2H_2 dissociation precursor) can be determined from the current work. First, since the S_1 electronic state is an intermediate (with *ungerade* electronic symmetry) in the photodissociation process, the transition into the C_2H_2 precursor state (in the 11 eV energy region) must be one-photon allowed from the S_1 level. This excludes all of the known centro-symmetric *ungerade* singly-excited ($\pi_g^* \leftarrow \pi_u$) acetylene valence states. The electronic transition must be strong, given that the efficiency of the two-photon dissociation process is high, based on the estimate in Section 6.3.3. In addition, since the observed photodissociation cross-sections from all three S_1 vibrational levels (with varying quanta of the *trans*-bending vibrational excitation) are similar, the geometry, in particular the CCH bend angle, of the C_2H_2 precursor state, is probably not too different from that of the S_1 state.

Due to uncertainty in the electronic assignment of the C_2H_2 precursor, less can be inferred reliably about its dissociation product, electronically excited C_2H, which ultimately dissociates into the C_2 X state. Energetically, the C_2H state can only be one of the low-lying electronic states [39, 49, 141], $\tilde{X}^2\Sigma^+(1\ ^2A')$, $\tilde{A}^2\Pi(1\ ^2A''$ and $2\ ^2A')$, $2^2\Sigma^+(3\ ^2A')$, and $2^2\Pi(2\ ^2A''$ component only), where the electronic symmetries in parentheses are the symmetry-labels in the C_s point-group. As shown in Fig. 6-6, direct adiabatic dissociation (to produce the C_2 X state) can take place on both $1\ ^2A'$ and $2\ ^2A'$ PES's of C_2H, because the C_2 X state correlates to $1\ ^2A'$ and $2\ ^2A'$ states at different C-C bond lengths [39], i.e. $1\ ^2A' \rightarrow C_2(X)+H$ at short C-C bond length (e.g. R_{CC}=1.25 Å) and $2\ ^2A' \rightarrow C_2(X)+H$ at long C-C bond length (e.g. R_{CC}=1.4 Å). This change in the adiabatic correlation (as a function of C-C bond length) occurs because, while the $X^1\Sigma_g^+$ state is the lowest-energy C_2 state near the X-state equilibrium bond-length (1.243 Å) [72], the C_2 $a^3\Pi_u$ state becomes lower in energy than the X state at longer C-C bond-length (>1.35Å). There is, however, a significant dissociation barrier on the $2\ ^2A'$ PES, which might lower the efficiency of direct adiabatic dissociation on that surface. The dissociation barrier is a consequence of avoided-crossings between $2\ ^2A'$ and higher-lying $3\ ^2A'$ and $4\ ^2A'$ states. If the dissociation precursor C_2H belongs to the $3\ ^2A'$ electronic state, internal conversion (to either $1\ ^2A'$ or $2\ ^2A'$) is required. Due to symmetry constraints, the C_2 X state could not be generated from the C_2H $1\ ^2A''$ and $2\ ^2A''$ states (which would lead to production of the C_2 a state instead), unless there is an unusually strong Coriolis-type interaction between $^2A''$ and $^2A'$ electronic states.

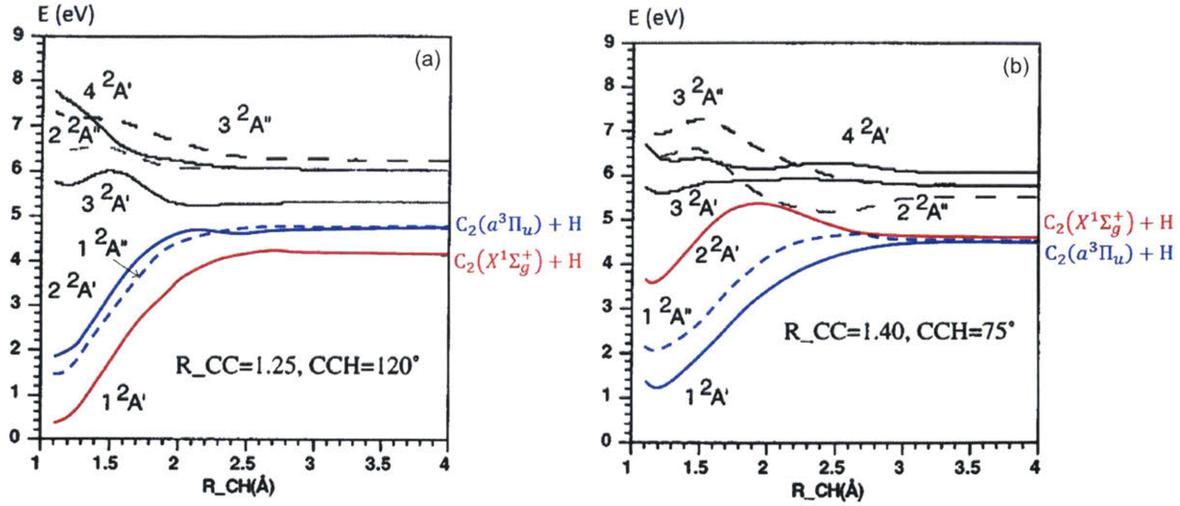

Figure 6-6: Potential energy curves calculated at 7-state-averaged CASSCF/D95(d,p) level—adapted from Ref [39]—for seven electronic states of C_2H in C_s symmetry, with C-C bond length and CCH bend angle fixed at two sets of values. Solid lines are for A' states, and dashed lines for A'' states. The adiabatic curves which correlate to the $C_2(a^3\Pi_u)$+H dissociation limit are color-coded blue, and the adiabatic curve which correlates to the $C_2(X^1\Sigma_g^+)$+H dissociation limit is color-coded red.

6.4 Conclusion

Based on a modified application of FM spectroscopy, I determine that for all of the probed $A(v = 2) - X(v = 0)$ two-level systems, the C_2 population is not inverted. The population in the lower energy X-state vibrational level is larger than that in the A-state level, following one-color, resonance-enhanced (via the S_1 3^2, 3^3, and 3^4 intermediate levels) photodissociation of acetylene. The production of the C_2 X state, in the 220 nm photolysis studied in this work, is likely a two-photon process for all three S_1 acetylene intermediate vibrational levels used in this work. The energetic advantage of the X-state dissociation channel (two photons) over the A-state channel (three photons) likely explains the observed relative efficiency of the two channels.

I have already shown in Chapter 4 that one-color (~220 nm), two-photon, resonance-enhanced (S_1-S_0) excitation of acetylene leads to production of long-lived electronically-excited C_2H^* fragments (which have a near-continuum emission spectrum in the >400 nm region). Therefore, for the resonance-enhanced photodissociation process of acetylene, I have now discovered two open dissociation channels in the 11 eV region: one that produces C_2 in the X state and the other that produces the long-lived C_2H^* species (which is the most abundant species among the three observed fluorescing photofragments, as discussed in Chapter 4). Unfortunately, it is difficult to estimate the relative efficiency of the two channels, because I do not have a reliable method to estimate the total population of the long-lived C_2H^* fragment based on the available spectroscopic data reported in Chapter 4. The long-lived C_2H^* molecules are only observed in photolysis experiments under the supersonic-jet conditions (collision-free), in which the photofragment fluorescence is not dispersed. As a result, I am unable to correct the observed C_2H^* signal intensity for the wavelength-dependent PMT quantum yield, which is $<2\%$ in spectral region (550 – 800 nm) where fluorescence from C_2H^* is expected to be strongest, based on previous VUV acetylene photolysis studies [21, 26, 157]. In order to have a reliable estimate of the total population of C_2H^*, I need a detection scheme which allows observations of all C_2H^* fluroescence signals.

The identity of the intermediate dissociation precursor states in the two two-photon photodissociation channels (C_2 X state and C_2H^*) is unknown, although certain characters of the precursor states can be deduced from the available spectroscopic information presented in this chapter and in Chapter 4. Further information from high-level *ab initio* calculations is needed.

Chapter 7

Laser-Induced Fluorescence Study of the S_1 State of Doubly-Substituted ^{13}C Acetylene and Harmonic Force Field Determination

Abstract

In the first half of this study, rotational and vibrational constants of six Franck-Condon bright vibrational levels of S_1 doubly-substituted ^{13}C acetylene are determined from laser-induced fluorescence spectra and an updated geometry of the *trans* conformer of S_1 acetylene is obtained. In the second half, we determine the quadratic force field of S_1 acetylene based on the harmonic frequencies of four isotopologues of acetylene. The effects of both diagonal and off-diagonal x_{ij} anharmonicities are removed from the input harmonic frequencies. Results from both experimental and theoretical studies of various isotopologues of acetylene (including those from the first half of this paper) are used to obtain a set of force constants that agrees well with *ab initio* calculations. Our set of force constants for S_1 acetylene is an improvement over previous work by Tobiason *et al.*, which did not include off-diagonal anharmonicities.

The results in this chapter have been published in the Journal of Physical Chemistry A [78].

7.1 Introduction

The study of the first electronically excited singlet (S_1) state of acetylene molecule dates back one hundred years, when Stark and Lipp [151] published the first absorption spectrum of gas-phase acetylene from 2200-1900 Å. The major breakthrough in the analysis of the spectrum occurred in the mid-1950's, when Ingold and King [75] and Innes [76] demonstrated that the excited electronic state observed in the absorption spectrum has a *trans*-bent structure (C_{2h} point group), in contrast to the linear structure of the electronic ground state. From the rotational selection rules, they identified the transition as a *c*-type $\tilde{A}^1A_u - \tilde{X}^1\Sigma_g^+$ transition. Since then, the vibrational structure of the *trans* conformer of S_1 $^{12}C_2H_2$ has been nearly completely characterized up to the energy of the transition state for *cis* ↔ *trans* isomerization, [12, 104, 106, 107, 111, 154, 155, 160, 168, 174] and all of the anharmonicity constants, x_{ij}, have been obtained (as summarized in ref [14]). Although most of the previous work on S_1 acetylene was performed on the naturally abundant $^{12}C_2H_2$ isotopologue, information from the other isotopologues of acetylene has provided important evidence for the vibrational assignments of S_1 $^{12}C_2H_2$. For example, using hydrogen-isotope shifts, Ingold and King [75] were able to identify both the *trans*-bending and the CC stretch modes of S_1 $^{12}C_2H_2$ from the stronger vibrational progressions observed in the absorption spectrum of the molecule. Recently from our group, ^{13}C isotope shifts have been used to assign the 46 175 cm^{-1} state to the S_1-*cis* electronic state of $^{12}C_2H_2$. [10?] In the course of obtaining those S_1 $^{13}C_2H_2$ spectra, with the initial goal of understanding the *cis* ↔ *trans* isomerization process, we also find ourselves in a position to be able to refine the molecular geometry, as well as the harmonic force field of S_1 acetylene, given this extra piece of isotopologue information together with information from studies of other isotopologues of acetylene.

In this paper, the laser induced fluorescence spectra of doubly-substituted ^{13}C acetylene are analyzed and the rotational constants and band-origins of six Franck-Condon bright states involving ν_2' (CC-stretch) and ν_3' (*trans*-bend) are determined, namely $n\nu_3'\,(n = 0 - 2)$ and $\nu_2' + n\nu_3'\,(n = 0 - 2)$ levels. Based on the rotational constants of various isotopologues of acetylene [73, 74, 174] (including those reported here), we are able to refine the geometry of the S_1 *trans* conformer of acetylene, derived previously by Huet *et al.* [73] We also obtain more accurate harmonic force constants for S_1 acetylene that are more complete than those derived from Tobiason's force field analysis [161]; to do this, we combine previous experimental [74, 155, 160, 168, 171, 174] as well as theoretical [14] studies of S_1 acetylene. The most significant contribution of our present work is the inclusion of *all* of the x_{ij} anharmonicities, both diagonal and off-diagonal, in the determination of the harmonic frequencies, in addition to the inclusion of the corrected ν_1 fundamental frequency of $^{12}C_2H_2$, [155] as well as two fundamental frequencies of $^{13}C_2H_2$, determined in this work. The refined geometry of S_1 acetylene determined here is used in the **GF** analysis to obtain the force constants. The force constants and molecular geometry obtained in this work are used to refine the calculation of S_1-S_0 Franck-Condon factors [127, 129, 132].

7.2 Methods

The laser-induced fluorescence studies were performed using a static gas cell containing 250 mTorr of $^{13}C_2H_2$ at room temperature. The output of a Lambda-Physik FL2002 dye laser, pumped by an XeCl excimer laser, and operating with Coumarin 440 or 450 dye, was frequency-doubled using a β-BBO crystal. The dye laser was equipped with an intracavity etalon. Approximately 1 mJ of tunable UV radiation was produced with a spectral width ≤ 0.05 cm^{-1}. The sample of $^{13}C_2H_2$ (MSD Isotopes, 98% pure) was subjected to several freeze-pump-thaw cycles for purification. Fluorescence in the cell was detected perpendicular to the laser propagation direction using a Hamamatsu R331 photomultiplier tube. Frequency calibration was performed by reference to the absorption spectrum of $^{130}Te_2$ using the undoubled frequency from the dye laser. The spectra were calibrated to an accuracy of ± 0.02 cm^{-1}. Details of the experiment can be found in Chapter 2 of Silva's PhD thesis [144].

PGOPHER [175] was used for the rotational fitting of the six vibrational levels listed in Table 7.1, where we follow the notation in ref [174]. All transitions to the levels listed in Table 7.1 are transitions from the $v'' = 0$ level of the ground electronic state of $^{13}C_2H_2$. Alternatively, V_n^m is sometimes used in this paper as a short-hand notation for a transition from n quanta of the *trans*-bending mode, ν_4'' of the ground electronic state (in this work, $n = 0$), to m quanta of the *trans*-bending mode, ν_3' in the excited state. Rotational constants of the electronic ground state of ^{13}C acetylene are taken from ref [45]. A brief introduction to the axis-switching effect, as well as the fitting procedure, is provided below.

The c-type rotational selection rule $K_a' - l'' = \pm 1$ for the S_1-S_0 electronic transition of acetylene normally prohibits transitions to $K_a' = 0$ and 2 levels from the $v'' = 0$ level of the ground electronic state, which has zero vibrational angular momentum, $l'' = 0$. For a near prolate top, the diagonal matrix elements of the rotational Hamiltonian are ($K \equiv K_a$ is unsigned and k is signed) [174]

$$\begin{aligned}\langle \nu Jk|H|\nu Jk\rangle = T_v + \frac{1}{2}(B+C)(J(J+1)-k^2) + Ak^2 \\ - D_J J^2(J+1)^2 - D_{JK}J(J+1)k^2 - D_K k^4, \quad (7.1)\end{aligned}$$

and the off-diagonal matrix elements are given by

$$\langle \nu Jk \pm 2|H|\nu Jk\rangle = \frac{1}{4}(B-C)\sqrt{(J^2-(k\pm 1)^2)((J+1)^2-(k\pm 1)^2)}. \quad (7.2)$$

As a result, only B, C, and D_J can be determined from a $\Pi - \Sigma$ ($K' = 1 \leftarrow l'' = 0$ transition) sub-band, since one needs at least two K' values to determine the A constant. However, because of the large change of geometry upon excitation to the S_1 state, $K_a' - l'' = 0, \pm 2$ transitions (among others) can be weakly allowed. [69] This so-called axis-switching effect can be understood if one realizes that the molecular wave function normally used is expressed in terms of a molecule-fixed coordinate system instead of a space-fixed coordinate system. [69] In other words, the coordinate system rotates as the geometry of the molecule changes. However, in the derivation of the usual rotational selection rules, a fixed coordinate system is assumed. Consequently, the simple selection rule no longer holds when the molecule undergoes a large geometry change, as occurs in the $\tilde{A} - \tilde{X}$ transition of acetylene.

For each vibrational level, rotational constants B and C, D_J, and the $T_v{+}Ak^2$ term of the electronically excited S_1 state of $^{13}C_2H_2$ are first determined by assigning the rotational lines of the $\Pi - \Sigma$ subband. This subband is much stronger than the axis-switching subbands. Axis-switching lines from the weaker $\Sigma{-}\Sigma$ transition can then be picked out by noticing that the axis-switching $Q(J)$ line near $J = 20$ should lie close to the normal $\Pi{-}\Sigma$ $Q(J{+}1)$ line. This prediction is made based on the observed location of the axis-switching lines in the rotational structure of $^{12}C_2H_2$, the spectrum of which is expected to be similar to that of $^{13}C_2H_2$, due to the small relative mass difference between ^{13}C and ^{12}C and consequently small difference (expected to be within a few percent) in the rotational constants between the two isotopologues. This is indeed found to be true and in general, the positions of the $\Sigma - \Sigma$ axis-switching Q lines can be easily located. Note that the weak axis-switching $\Sigma{-}\Sigma$ subband is red-shifted with respect to the strong $\Pi - \Sigma$ transitions. In addition, for axis-switching transitions in acetylene, the intensities scale approximately as $J^3\exp[-B''J(J+1)hc/k_BT]$, whereas the normal rotational intensities scale as $J\exp[-B''J(J+1)hc/k_BT]$ (where B'' is the ground electronic state rotational constant). [69] As a result, the strongest part of the relatively weak $\Sigma - \Sigma$ axis-switching branch avoids being buried under stronger $\Pi - \Sigma$ Q-branch lines, which reach their maximum intensity at around $J'' = 8$ in our experimental conditions. Unfortunately, only Q-type transitions are allowed for a $\Sigma - \Sigma$ band because of the parity selection rule, thus we are not able to confirm our assignments using combination differences between the P and R branches. Despite that, in general the observed progressions of axis-switching Q lines fit satisfactorily. In contrast, P, Q, and R transitions are all allowed for the axis-switching $\Delta - \Sigma$ subbands. However, the intensities of these transitions are only about half that of the $\Sigma - \Sigma$ subband, [69] and the $\Delta - \Sigma$ subband is severely overlapped by the R-head of the $\Pi - \Sigma$ band. As a result, no attempts are made to assign the $\Delta - \Sigma$ transitions, except for the V_0^0 and V_0^1 bands, mainly due to the fact that those bands were sampled only by relatively short scans and only a few $\Sigma - \Sigma$ Q lines can be assigned. For those two bands, a progression of Q and/or P branch lines of the $\Delta - \Sigma$ transition can still be observed (the R-branch region was not recorded). After assigning the axis-switching transitions, the A rotational constant can be determined for all observed vibrational levels. Additional D_{JK} and D_K parameters are included only if they significantly improve the fit and are determined with reasonable uncertainties. Note that the inclusion of those two constants causes only small changes in the other fitted constants. The results of the fit are listed in Table 7.1, and line assignments are provided in Appendix A.2. The overall root-mean-square (rms) error of the fit is good, given that the spectra are calibrated to an accuracy of approximately ± 0.02 cm^{-1}. Note that we did not fit the axis-switching angle, θ_T, which characterizes the geometry change of acetylene during the $\tilde{A} - \tilde{X}$ transition and thus determines the intensity of axis-switching lines with respect to normal transition lines. Instead, for each vibrational transition, θ_T is set to a value between 2° and 3°, typical for the $\tilde{A} - \tilde{X}$ transition of acetylene, [69] such that the observed relative intensities of the rotational lines match approximately with the fit.

From the rotational constants of the six vibrational levels of $^{13}C_2H_2$, we determine the rovibrational parameters, which reflect the vibrational dependence of rotational constants; from the band origins of the six levels, we also obtain the harmonic frequencies, ω_i, and anharmonicities, x_{ij}, of the normal modes ν_2' and ν_3' of S_1 $^{13}C_2H_2$. The geometry of the S_1 *trans* conformer of acetylene can be obtained by fitting the values of the principal moments of inertia of $^{13}C_2H_2$, $^{12}C_2H_2$, and $^{12}C_2D_2$, derived from their respective rotational constants, to the calculated values based on bond length and bond angle. From all available harmonic frequencies of four isotopologues of acetylene ($^{12}C_2HD$ and the previously mentioned three isotopologues), we then apply the standard **GF** analysis to obtain quadratic force constants of the S_1 *trans* conformer of acetylene. Details of the analysis can be found in the relevant sections below. MATLAB built-in function *lscov* is used for the least-square fitting of the rovibrational parameters and the vibrational constants; *lsqnonlin* is used for the nonlinear least-square fitting for the determination of molecular geometry, as well as in the **GF** analysis. Note that a weighted fit based on the uncertainties of the data values is used throughout this work.

Table 7.1: Rotational and vibrational constants for the observed vibrational levels of S_1 $^{13}C_2H_2$. Units are all in cm^{-1}. Constants left blank were not included in the fit. Numbers in the parentheses are $\pm 1\sigma$ uncertainties.

Constants	$0\nu_3'$	ν_3'	$2\nu_3'$	ν_2'	$\nu_2' + \nu_3'$	$\nu_2' + 2\nu_3'$
T_v	42214.49(1)	43250.06(1)	44268.55(1)	43551.43(1)	44586.99(1)	45605.17(3)
A	12.783(13)	13.692(7)	14.811(7)	12.661(9)	13.513(8)	14.340(26)
B	1.0592(1)	1.0610(1)	1.06178(3)	1.0513(1)	1.05223(4)	1.0514(1)
C	0.9750(1)	0.9717(1)	0.96861(3)	0.9679(1)	0.96416(4)	0.9609(1)
$D_J \times 10^6$	2.30(7)	2.44(7)	1.98(4)	2.6(1)	2.04(4)	2.00(2)
$D_{JK} \times 10^5$		9(2)		7(1)	5(3)	28(9)
D_K	0.004(3)		0.013(2)			
rms error	0.021	0.026	0.016	0.017	0.015	0.024

Table 7.2: Rovibrational parameters of the S_1 *trans* conformer of $^{13}C_2H_2$. Units are all in cm^{-1}. Numbers in the parentheses are $\pm 1\sigma$ uncertainties.

$A_e = 12.44(15)$	$B_e = 1.064(1)$	$C_e = 0.9806(3)$
$\alpha_2^A = 0.23(9)$	$\alpha_2^B = 0.0088(6)$	$\alpha_2^C = 0.0075(2)$
$\alpha_3^A = -0.96(6)$	$\alpha_3^B = -0.0009(4)$	$\alpha_3^C = 0.0034(1)$

7.3 Rotational and Vibrational Analysis

As can be seen from Table 7.1, the A and C rotational constants depend linearly on the number of quanta in ν_3', with the largest changes occurring in the values of the A constant. This is consistent with the fact that as the *trans*-bending ν_3' levels are excited, the molecule becomes quasi-linear, with a rapidly increasing A rotational constant. [174] It should be noted that the values of the B constant deviate from the expected linear trend, in particular for the ν_3' progression involving one quantum of ν_2'. This might be caused by Fermi resonances or some J-dependent Coriolis-type perturbation. A similar effect has been observed in $^{12}C_2H_2$ [174] and $^{12}C_2D_2$ [74].

The rovibrational parameters can be determined from the rotational constants by the relation

$$\Re_v = \Re_e - \alpha_2^{\Re}(v_2 + \frac{1}{2}) - \alpha_3^{\Re}(v_3 + \frac{1}{2}), \tag{7.3}$$

where $\Re$ can be either A, B, or C, and v_2 and v_3 stand for the number of quanta of those two modes in each vibrational level. The results are presented in Table 7.2. The $\Re_e$ obtained here can only be considered effective values, since not all of the α's can be determined from the available data. Note that the rovibrational parameters for the A and B rotational constants are not as well-determined as those for the C rotational constant. This can be explained by the fact that the A rotational constants determined for each vibrational level have larger uncertainties associated with them, because of the smaller number of axis-switching lines observed than normal $\Pi - \Sigma$ lines. The larger uncertainties on the rovibrational parameters for the B constant are caused by the deviation from the linear trend discussed earlier.

With the inclusion of the new $^{13}C_2H_2$ rotational constants, the geometrical param-

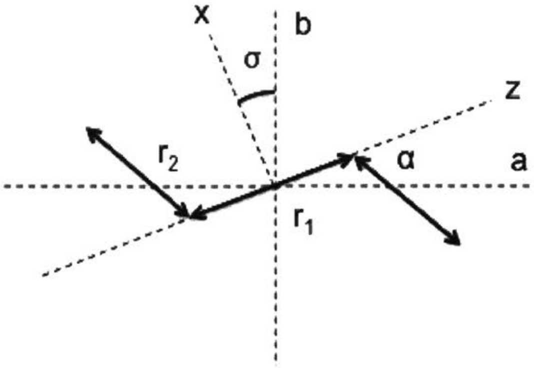

Figure 7-1: Geometry of *trans* acetylene (adapted from ref [73]). r_1 and r_2 are the r_{CC} and r_{CH} bond lengths respectively. α is the supplement to $\angle CCH$ ($\alpha = 180° - \angle CCH$). σ is the angle between the principal axis system and the body-fixed x, y, z-coordinate system, with the y-axis being out of plane. Note that α is used in our calculation, for consistency with the notation used by ref [73].

eters of the *trans* conformer of S_1 acetylene can be updated. Assuming the validity of the Born-Oppenheimer approximation, the equilibrium structure of a molecule should be isotope-independent. For *trans* S_1 acetylene, the principal moments of inertia are given by the expressions [73]

$$\frac{1}{2}I_0^A = \frac{r_1^2}{4}(m_1 + m_2)\sin^2\sigma + m_2 r_2^2 \sin^2(\sigma - \alpha) + m_2 r_1 r_2 \sin(\sigma - \alpha)\sin\sigma \tag{7.4}$$

$$\frac{1}{2}I_0^C = \frac{r_1^2}{4}(m_1 + m_2) + m_2 r_2^2 + m_2 r_1 r_2 \cos\alpha \tag{7.5}$$

$$\tan 2\sigma = \frac{m_2 r_2^2 \sin 2\alpha + m_2 r_1 r_2 \sin\alpha}{\frac{1}{4}(m_1 + m_2) r_1^2 + m_2 r_2^2 \cos 2\alpha + m_2 r_1 r_2 \cos\alpha}, \tag{7.6}$$

where m_1 and m_2 are the masses of the appropriate isotopes of carbon and hydrogen atoms, respectively. In this study, geometrical parameters are fitted to I_a and I_c of $^{12}\mathrm{C}_2\mathrm{H}_2$, [174] $^{12}\mathrm{C}_2\mathrm{D}_2$, [73, 74] [1] and $^{13}\mathrm{C}_2\mathrm{H}_2$. The rotational constants from the ground

---

[1] In this work, we use A_0 and C_0 of S_1 $\mathrm{C}_2\mathrm{D}_2$ as reported in ref [73]. Note that in ref [73], the extended ν_3' progression ($v_3' = 1 - 5$) observed in ref [74] was used to extrapolate the A and C rotational constants of S_1 $\mathrm{C}_2\mathrm{D}_2$ to the ground vibrational state. The uncertainties of the two extrapolated values, however, were not reported. In this work, the uncertainty on A_0 is estimated to be 0.1 cm^{-1} and that on C_0 to be 0.0004 cm^{-1}, by extrapolating the relevant values reported in ref [74] to the ground vibrational state from the $v_3' = 2 - 5$ progression. We were unable to locate the relevant values for the $v_3' = 1$ level, so the estimated uncertainties on A_0 and C_0 might be a little larger than their actual uncertainties. We choose to use the values of A_0 and C_0 as reported in ref [73], instead of those obtained from our extrapolation, because with the inclusion of

vibrational state are used, instead of equilibrium rotational constants, primarily because not all of the α_i parameters are known for all three isotopologues. It should be noted that attempts have been made to include I_b in the fit as well. However, the fit residuals become larger when I_b is included, possibly due to the presence of a positive inertial defect, observed to be $\triangle^\circ = I_c - I_a - I_b \approx 0.06\,\mathrm{u}\,\mathrm{\AA}^2$ for all three isotopologues.[2] Since a planar geometry is assumed in Eq.(7.4)-(7.6) (and thus $I_c = I_a + I_b$), the fit gets worse when all three moments of inertia are simultaneously fitted. The observed inertial defect, which occurs mainly due to the vibrational motion of the molecule, is consistent with the typical value for the ground vibrational state of a "well-behaved" planar molecule. [91] Here, the inertial defect is effectively set to be zero during the structural determination. From the fit, we obtain

$$r_{CC} = 1.374(1)\,\mathrm{\AA} \quad r_{CH} = 1.098(1)\,\mathrm{\AA} \quad \angle CCH = 122.80(7)^\circ.$$

The updated structure is not very different from the result obtained by Huet *et al.* [73] The most noticeable change is a slight increase (+0.32°) in the CCH bond angle. However, compared to the previous result, [73] our geometrical parameters are more accurate and precise, because we not only include one additional set of isotopologue information ($^{13}C_2H_2$ from this work), but we also obtain smaller fit residuals.

From the band origins of the six vibrational levels, harmonic frequencies and anharmonicities can be obtained. However, as no global fit is possible, the results should be treated with care, especially for the harmonic frequencies and T_e (which does not include the zero-point energy) in Eq. (7.7). The six levels are fitted to the model

$$\begin{aligned} G(v_2, v_3) = T_e + (\omega_2 + 2x_{22})(v_2 + 1/2) + \omega_3(v_3 + 1/2) + x_{33}(v_3 + 1/2)^2 \\ + x_{23}(v_2 + 1/2)(v_3 + 1/2). \quad (7.7) \end{aligned}$$

It should be mentioned that the x_{22} term itself cannot be fitted in our model, because

---

the additional $v_3' = 1$ level, the extrapolated values of A_0 and C_0 are expected to be more accurately determined. Our values also differ by <0.1% from the values reported in ref [73], and using a slightly larger uncertainties should have negligible effects on the fitting process.

[2] "u" is the unified atomic unit and 1 Å = 10^{-10} m.

Table 7.3: Vibrational parameters of the S_1 *trans* conformer of $^{13}C_2H_2$. Units are all in cm^{-1}. Numbers in the parentheses are $\pm 1\sigma$ uncertainties.

T_e	41021.7(2)
$\omega_2 + 2x_{22}$	1337.1(2)
ω_3	1052.9(2)
x_{33}	-8.60(8)
x_{23}	-0.15(10)

we need at least one additional level with $v_2 \geq 2$ to determine its value. As a result, in Eq. (7.7), we have (ω_2+2x_{22}), which is fitted as a single term. The result is shown in Table 7.3. Note that we follow the convention in spectroscopy that the harmonic frequencies listed have units of cm^{-1}, even though strictly speaking, cm^{-1} is a unit of wavenumber. This convention is followed throughout this paper. It should be re-emphasized that the "harmonic frequencies" obtained here are not genuine harmonic frequencies, since no global fit is possible. Thus, the treatment introduced in the next section is still necessary to obtain more accurate harmonic frequencies. The values of x_{23} and x_{33}, however, are accurate.

7.4 Harmonic Force-Field Determination

With the inclusion of several updated fundamental frequencies, notably ν_1 of $^{12}C_2H_2$ [155] and ν_2 and ν_3 of $^{13}C_2H_2$ from the present work, as well as a complete set of $^{12}C_2H_2$ x_{ij} anharmonicities, [12, 14, 107, 154, 155, 160] a new harmonic force-field analysis of S_1 acetylene, based on a larger and more accurate set of harmonic frequencies, can now be completed. In the harmonic force field analysis of Tobiason *et al.*, [161] only the diagonal anharmoncities, x_{ii}, were included and all of the off-diagonal x_{ij} were neglected. However, recent work on S_1 $^{12}C_2H_2$, both experimental and *ab initio*, has shown that several off-diagonal anharmonicities are much larger than, or at least comparable to, the diagonal ones, most notably $x_{15} = -158.57$ cm^{-1} and $x_{36} = -33.45$ cm^{-1} (ref [14]). An almost complete list of anharmonicities of S_1 $^{12}C_2H_2$ can be found in ref [14], which does not include two newly obtained values: $x_{56} = -8.98\,cm^{-1}$ and

$x_{45} = -16.81\,\mathrm{cm}^{-1}$ (ref [9]). Only those x_{ij} associated with ν_1' and ν_5' have not been experimentally determined because doing so would require observation of very high-lying vibrational levels. However, given the excellent agreement of the *ab initio* fundamental frequencies of those two modes with the experimental values, [14] we use the *ab initio* values of x_{11}, x_{55}, and x_{15} in our calculation of harmonic frequencies. Anharmonicity constants for the other isotopologues of S_1 acetylene are very sparsely available and most of them are not very well-determined. An empirical relation [65] is used instead to infer those values from $^{12}\mathrm{C}_2\mathrm{H}_2$ anharmonicities

$$x_{ik}^* = \frac{\omega_i^* \omega_k^*}{\omega_i \omega_k} x_{ik}, \tag{7.8}$$

where an asterisk indicates the corresponding value for an isotopologue. Since the relation involves ratios of harmonic frequencies, but not all of them are available for various isotopologues (only those of $^{12}\mathrm{C}_2\mathrm{H}_2$ can be determined), *ab initio* harmonic frequencies are used to obtain the anharmonicities of the other isotopologues. *Ab initio* harmonic frequencies of the isotopologues are generated based on the results of ref [14] and [10]. The harmonic frequencies are related to the fundamental frequencies and the anharmonicities via the relation

$$\omega_i = \nu_i - 2x_{ii} - \frac{1}{2}\sum_{k \neq i} x_{ik} \tag{7.9}$$

where ν_i is an observed fundamental frequency (e.g. the difference between the band origin of v_i=1 and v_i=0), while harmonic frequencies are related to the second derivative of the potential energy surface along a normal mode direction. For harmonic force constant calculations, harmonic frequencies must be used, and the values we obtain are listed in Table 7.4.

As can be seen, due to the inclusion of off-diagonal x_{ij} anharmonicities (all of them are negative) in Eq. (7.9), harmonic frequencies obtained in this work are at least 10 cm^{-1} higher than the ones used by Tobiason *et al.*, [161] with our ω_5 value of $^{12}\mathrm{C}_2\mathrm{H}_2$ almost 120 cm^{-1} higher than the value previously used. [161] Most of our

Table 7.4: Experimental, *ab initio*, and fit harmonic frequencies. Units are all in cm^{-1}.

		Ab initio ω	Exp. ω[a]	Fit ω[b]	Exp. ν[c]	Fit ν[d]
$^{12}C_2H_2$	1	3053.5	3052.1	3052.2	2880.1 [155]	2880.1
	2	1424.6	1420.9	1421.0	1386.9 [174]	1387.0
	3	1106.1	1098.0	1098.1	1047.6 [174]	1047.7
	4	757.9	787.7	787.7	764.9 [168]	764.9
	5	3033.4	3032.4	3031.1	2857.4 [160]	2856.1
	6	780.6	801.6	800.8	768.3 [168]	767.5
$^{12}C_2D_2$	1	2262.6	2303.5*	2262.3	2209.2 [74]	2168.0
	2	1385.1	1335.3*	1378.0	1305.8 [74]	1348.5
	3	877.8	875.5	874.0	845.3 [74]	843.8
	4	556.5		578.4		564.6
	5	2227.2		2225.6		2130.6
	6	573.2		588.0		568.7
$^{12}C_2HD$	1	3043.6		3041.8		2893.5
	2	1403.7	1399.0	1398.2	1367.4 [171]	1366.6
	3	1026.1	1021.8	1022.7	980.8 [171]	981.7
	4	664.8		691.0		672.4
	5	2245.2		2244.2		2131.3
	6	644.4	660.5	659.5	635.7 [171]	634.7
$^{13}C_2H_2$	1	3043.7		3042.3		2871.4
	2	1372.4	1368.9	1369.5	1336.9	1337.6
	3	1093.5	1085.1	1085.0	1035.6	1035.5
	4	755.6		785.4		763.0
	5	3024.4		3022.0		2848.2
	6	778.3		798.4		765.5

[a] Harmonic frequencies obtained via Eq. (7.9). Numbers in asterisks are not included in the **GF** analysis.

[b] Predicted harmonic frequencies based on the force constants obtained in the **GF** analysis.

[c] Observed fundamental frequencies.

[d] Predicted fundamental frequencies based on values in column Fit ω and the experimental anharmonicities.

Table 7.5: Teller-Redlich product rule ratio for mode 1, 2 and 3. The number in the parenthesis is $\pm 1\sigma$ uncertainty.

	Calc. [a]	*Ab initio* [b]	Exp.
$^{12}C_2H_2/^{12}C_2D_2$	1.748	1.749	1.768(13) [c]
$^{12}C_2H_2/^{13}C_2H_2$	1.054	1.054	

[a] Calculated value of the RHS of Eq. (7.10).
[b] Ratio of products of *ab initio* harmonic frequencies by using the LHS of Eq. (7.10).
[c] Ratio of products of experimental harmonic frequencies of $^{12}C_2H_2$ and $^{12}C_2D_2$ listed in Table 7.4.

harmonic frequencies, even those of the other isotopologues, agree excellently with *ab initio* harmonic frequencies. This justifies the use of the empirical relation Eq. (7.8).

The discrepancies for mode 4 and mode 6 can mostly be explained by the choice of coordinate system. [14] In the VPT2 calculations, a rectilinear coordinate system is used, which tends to yield more accurate results for stretching modes and less accurate ones for bending and especially torsional modes. [14] When a curvilinear system is used, a much better agreement with the experiment can be achieved for those two modes. It should be noted that the agreement with the *ab initio* ω_1 and ω_2 for $^{12}C_2D_2$ is significantly poorer than for other harmonic frequencies. This casts doubt on the accuracy of the fundamental frequencies of the two modes, [74] since the stretching mode should be very accurately determined in the *ab initio* calculation, as is the case for other isotopologues. Using the Teller-Redlich product rule, [65] which relates the product of the harmonic frequencies of a given symmetry of two different isotopologues to the mass and geometrical structure of the molecule, we have for modes 1, 2, and 3 of $^{12}C_2H_2$ and $^{12}C_2D_2$

$$\frac{\omega_1\omega_2\omega_3}{\omega_1^*\omega_2^*\omega_3^*} = \frac{m_H^* m_C^*}{m_H m_C}\sqrt{\frac{I_c}{I_c^*}}, \tag{7.10}$$

where an asterisk indicates the relevant value for an isotopologue. This product rule, which holds rigorously within the Born-Oppenheimer approximation, [65] can

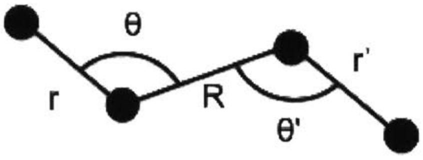

Figure 7-2: Internal coordinates of the S_1 *trans* conformer of acetylene. Note that the torsional coordinate, τ, is not shown, being out of plane.

be used to check whether the harmonic frequencies of $^{12}C_2D_2$ listed in Table 7.4 are correct (assuming those of $^{12}C_2H_2$ are accurate, given good agreement with the *ab initio* values), by comparing the ratio of products of experimentally-determined harmonic frequencies with the RHS of Eq. (7.10). The product rule can also be used to confirm the accuracy of the *ab initio* harmonic frequencies of $^{12}C_2H_2$, $^{13}C_2H_2$, and $^{12}C_2D_2$ by performing similar comparisons. Note that Eq. (7.10) does not apply to $^{12}C_2HD$, because it has a lower symmetry (C_s point group). The results are shown in Table 7.5. It is evident that *ab initio* calculation essentially yields the same ratio as the one calculated from the RHS of Eq. (7.10), but the agreement with experimental harmonic frequencies is worse for $^{12}C_2D_2$. In comparison, if we use the experimental ω_2 and ω_3 values of $^{13}C_2H_2$ and the calculated ratio from the RHS of Eq. (7.10) to extrapolate to its ω_1 value, we get ω_1=3043(19) cm^{-1}, which is very close to the *ab initio* value. Furthermore, in the original paper on $^{12}C_2D_2$, the ν_2 fundamental was not directly observed; the ν_2 fundamental frequency seems to be determined from a combination band with ν_1, and the position of the ν_1 fundamental also might not be securely determined. Considering all of these difficulties, the ν_1 and ν_2 fundamentals of $^{12}C_2D_2$ are not included in the harmonic force-field fit. In fact, inclusion of the two corresponding $^{12}C_2D_2$ harmonic frequencies makes the fit residual much larger than otherwise. The assignment of the ν_3 fundamental [74] of $^{12}C_2D_2$ should be secure, since a long progression of this Franck-Condon active mode was observed in the study.

Using the experimental harmonic frequencies listed in Table 7.4, harmonic force constants of the *trans* conformer of the S_1 state of acetylene can be determined by the **GF** matrix method. This is a well-developed method to obtain harmonic force constants, and has been discussed in great detail in ref [178]. Here, only a brief theoretical background is provided. In the internal coordinate system, harmonic frequencies can be obtained from the secular equation

$$| \mathbf{F} - \mathbf{G}^{-1}\lambda | = 0, \tag{7.11}$$

where **F** is the force constant matrix expressed in internal coordinates, $\mathbf{G}^{-1}$ is the inverse of the matrix **G**, which contains geometrical and mass information of the molecule, and the λ are proportional to the squares of the harmonic frequencies ($\lambda = 4\pi\omega^2$). The internal coordinates of acetylene are shown in Fig. 7-2. Details of obtaining the **G** matrix, as well as the specific form of the **F** matrix, can be found in the Supplemental Information. Note that the elements of **G** are isotope-dependent and thus different for each isotopologue, but **F** is not isotope-dependent within the Born-Oppenheimer approximation. The square-roots of the eigenvalues of each **GF** matrix are fitted to the experimental harmonic frequencies listed in Table 7.4. An uncertainty of 2 cm^{-1} is estimated for all $^{12}\mathrm{C}_2\mathrm{H}_2$ harmonic frequencies to account for the inclusion of either *ab initio* anharmonicities (x_{11}, x_{55}, and x_{15}) or two less well-determined anharmonicities, x_{36} and x_{34}, in the calculation of $^{12}\mathrm{C}_2\mathrm{H}_2$ harmonic frequencies.[3] An uncertainty of 5 cm^{-1} is estimated for the harmonic frequencies of the other three isotopologues, since an empirical relation (Eq. 7.8) is used to obtain the anharmonicities for those three isotopologues.

To increase the accuracy of the fit, we also fit to the observed a-axis Coriolis constant $\xi_{46}^{a} = 0.707 \pm 0.006$. [168] Details of obtaining ξ_{46}^{a} from the **GF** procedure are described in the literature. [103, 161, 166]

We encounter fitting problems similar to the ones noted by Tobiason *et al.* [161] When we try to fit all ten parameters, large relative uncertainties are found in F_{rR} and $\mathrm{F}_{r'\theta}$, as well as in $\mathrm{F}_{rr'}$. The first two were constrained to be zero in ref [161]. Indeed, those three force constants are much smaller than the others, as obtained from the *ab initio* calculation. [14] We also tried constraining the first two parameters to

---

[3] An uncertainty of 2 cm^{-1} is used for the harmonic frequency of mode 2 as well, even though its harmonic frequency can certainly be determined to a better precision, given that all the relevant anharmonicities of mode 2 were experimentally available and were well-determined.

Table 7.6: Force constants of the *trans* conformer of S_1 acetylene. Numbers in the parentheses are $\pm 1\sigma$ uncertainties.

[a]	Constrain I [b]	Constrain II [c]	*Ab initio* [14]	Tobiason [161]
F_{rr}	5.07(1)	5.055(5)	5.08	4.78(3)
F_{rR}	0.089(18)	0	0.086	0
$F_{rr'}$	0.043(8)	0.029(6)	0.041	0.138(25)
$F_{r\theta}$	0.219(47)	0.188(43)	0.212	0.188(40)
$F_{r'\theta}$	0.032(6)	0	0.031	0
F_{RR}	7.71(2)	7.74(2)	7.75	7.63(2)
$F_{R\theta}$	0.434(50)	0.434(49)	0.417	0.583(21)
$F_{\theta\theta}$	0.545(6)	0.543(6)	0.536	0.541(4)
$F_{\theta\theta'}$	0.114(6)	0.112(6)	0.128	0.127(4)
$F_{\tau\tau}$	0.145(1)	0.145(1)	0.136	0.137(4)
rms [d]	0.7	1.1		9.0

[a] Units of the force constants are: mdyn/Å for F_{rr}, F_{RR}, F_{rR}, and $F_{rr'}$; mdyn×Å for $F_{\theta\theta}$, $F_{\theta\theta'}$, and $F_{\tau\tau}$; and mdyn for $F_{r\theta}$, $F_{r'\theta}$, and $F_{R\theta}$. Note that 1 mdyn $= 1\times10^{-8}$ N.
[b] Constrain F_{rR} and $F_{r'\theta}$ to have their *ab initio* ratios with respect to $F_{r'\theta}$.
[c] Constrain F_{rR} and $F_{r'\theta}$ to be zero.
[d] Root-mean-square of the fit residuals, (Exp. ω −Fit ω).

be zero, and reasonable parameter uncertainties are obtained. In addition, given the accuracy of the *ab initio* calculation, we also tried constraining F_{rR} and $F_{rr'}$ to have their *ab initio* ratio with respect to $F_{r'\theta}$. The results are presented in Table 7.6. The fitted harmonic frequencies (Fit ω) shown in Table 7.4 are based on the ratio-constrained set (values from the column Constrain I in Table 7.6).

As can be seen, both approaches give similar force constants, with the ratio-constrained set matching almost perfectly with the *ab initio* results. We are also able to obtain much smaller root-mean-square values of the fit residuals[4] than Tobiason *et al.* [161]. Our force constants give accurate Coriolis constants, [168] $\xi_{46}^{a} = 0.707_3$

---

[4] Note that for both approaches, the reduced chi-square, $\chi_\nu^2 \approx 0.1 < 1$, which indicates that we have overestimated the uncertainties on the experimental harmonic frequencies. [18] Using another set of uncertainties that optimizes χ_ν^2 slightly changes the values of the force constants, with the greatest change occurring for $F_{r\theta}$ and $F_{R\theta}$, which have large uncertainties associated with them, but all of the values fall within one standard deviation of the force constants listed in Table 7.6.

and $\xi_{46}^{b} = -0.706_9$, which obey the sum rule [174]

$$(\xi_{46}^{a})^2 + (\xi_{46}^{b})^2 = 1. \tag{7.12}$$

In addition, using our force constants as well as our updated molecular geometry, we are able to derive the equilibrium quartic centrifugal distortion constant of S_1 $^{12}C_2H_2$, $D_J^e = 2.37 \times 10^{-6}$ cm^{-1} (based on the ratio-constrained set in Table 7.6). Note that $D_J^0 = 2.3(1) \times 10^{-6}$ cm^{-1} for the vibrational ground state of S_1 $^{12}C_2H_2$ [174] and the value of D_J^e is in general expected to be close that of D_J^0. [50, 59] Details of calculating D_J^e from the harmonic force constants can be found in the literature. [50, 59]

We want to re-emphasize that we have made several important improvements over Tobiason's previous work [161] on the accuracy of the input harmonic frequencies to the **GF** analysis. We remove the effects of both diagonal and off-diagonal x_{ij} anharmonicities in the determination of harmonic frequencies of four different isotopologues of acetylene, and we are able to obtain a set of harmonic frequencies that agrees well with *ab initio* calculations. Due to large values of several off-diagonal x_{ij} anharmonicities, which were neglected in Tobiason's previous study, [161] our harmonic frequencies are quite different from those that Tobiason *et al.* used in their analysis. In addition, we have included three additional harmonic frequencies in our **GF** analysis, and abandoned two questionable harmonic frequencies of $^{12}C_2D_2$, which were used in Tobiason's analysis. [161] The inclusion of those two harmonic frequencies might be the source of a much larger rms of the fit residuals in their work than in the present work.

In terms of the harmonic force constants that we obtain, one of the most obvious and easily understandable changes in our force constants compared with Tobiason's force constants [161] is an increase in F_{rr}, as the harmonic frequency of the CH asymmetric stretching mode, ν_5', of $^{12}C_2H_2$ used in this work is significantly larger. A similar argument applies to the torsional force constant. Using our harmonic force constants, both the harmonic and fundamental frequencies can be predicted for all six vibrational modes of all isotopologues (see Table 7.4). As can be seen, for the vibrational modes included in our **GF** calculation, the predicted harmonic and fundamental frequencies agree excellently with the experimental values; for those not included as inputs to the **GF** analysis (e.g. ω_1 and ω_5 of $^{13}C_2H_2$), their predicted harmonic frequencies also agree well with the *ab initio* values. The agreement is worse for ω_4 and ω_6, for the reason discussed earlier regarding the choice of coordinate system in the *ab initio* calculation. Based on our discussion earlier, it is also not surprising that the predicted fundamental frequencies of ν_1' and ν_2' of $^{12}C_2D_2$ are quite different from the values proposed in ref [74].

Considering all the improvements we have made in terms of the accuracy of the input harmonic frequencies, as well as excellent agreement of our force constants and predicted harmonic and fundamental frequencies with *ab initio* and/or experimental results, our set of force constants should be more accurate and reliable than Tobiason's previous result. [161]

7.5 Conclusion

We have assigned and fit the rotational and vibrational structures of six Franck-Condon bright vibrational levels of doubly-substituted ^{13}C acetylene. Rovibrational parameters, as well as harmonic frequencies and anharmonicities, associated with ν_2' and ν_3' of $^{13}C_2H_2$, are determined. We then derived a refined geometry of the *trans* conformer of S_1 acetylene, based on the rotational constants of $^{12}C_2H_2$ [174], $^{12}C_2D_2$ [74], as well as those of $^{13}C_2H_2$ from this work. By allowing for the effects of both the diagonal and off-diagonal x_{ij} anharmonicities, we obtain harmonic frequencies of four isotopologues (the aforementioned three isotopologues and $^{12}C_2HD$) of S_1 acetylene, which agree well with *ab initio* calculations. The **GF** matrix method is then applied to obtain harmonic force constants of S_1 acetylene, which also agree well with the calculations and experimental data. This updated set of harmonic force constants is used, together with our new molecular geometry, to refine the S_1-S_0 Franck-Condon calculation.

Chapter 8

The Rotation-Vibration Structure of the SO_2 $\tilde{C}^1B_2$ State Explained by a New Internal Coordinate Force Field

Abstract

A new quartic force field for the SO_2 $\tilde{C}^1B_2$ state has been derived, based on high resolution data from $S^{16}O_2$ and $S^{18}O_2$. Included are nine b_2 symmetry vibrational levels of $S^{16}O_2$ reported in the first paper of this series [G. B. Park, J. Jiang, C. A. Saladrigas, and R. W. Field, J. Chem. Phys. **144**. 144311 (2016)]. Many of the experimental observables not included in the fit, such as the Franck-Condon intensities and the Coriolis-perturbed effective C rotational constants of highly anharmonic $\tilde{C}$ state vibrational levels, are well reproduced using our force field. Because the two stretching modes of the $\tilde{C}$ state are strongly coupled via Fermi-133 interaction, the vibrational structure of the $\tilde{C}$ state is analyzed in a Fermi-system basis set, constructed explicitly in this work via *partial diagonalization* of the vibrational Hamiltonian. The physical significance of the Fermi-system basis is discussed in terms of semiclassical dynamics, based on study of Fermi-resonance systems by Kellman and coworkers [M. E. Kellman and L. Xiao, J. Chem. Phys. **93**, 5821 (1990)]. By diagonalizing the vibrational Hamiltonian in the Fermi-system basis, the vibrational characters of all vibrational levels can be determined unambiguously. It is shown that the bending mode cannot be treated separately from the coupled stretching modes, particularly at vibrational energies of more than 2000 cm^{-1}. Based on our force field, the structure of the Coriolis interactions in the $\tilde{C}$ state of SO_2 is also discussed. We identify the origin of the alternating patterns in the effective C rotational constants of levels in the vibrational progressions of the symmetry-breaking mode, ν_β (which correlates with the antisymmetric stretching mode in our assignment scheme).

The results in this chapter have been published in the Journal of Chemical Physics [79].

8.1 Introduction

Pioneering work by Hoy and Brand [22, 70], based on earlier analysis by Coon and coworkers [36, 80], established the presence of a double-well structure in the anti-symmetric stretching coordinate on the potential energy surface (PES) of the SO_2 $\tilde{C}^1B_2$ state. That is, the minimum geometry of the $\tilde{C}$ state has nonequivalent S-O bond lengths. A strong Fermi interaction between the symmetric and anti-symmetric stretching modes was inferred from the anomalously intense transition into the first overtone of the anti-symmetric stretching mode. Using a reduced-dimension model that excludes terms containing q_2, Hoy and Brand [70] derived an internal coordinate force field of the $\tilde{C}$ state.

The presence of a double well in the q_3 coordinate and a strong Fermi interaction between ν_1 and ν_3 was validated in subsequent studies of the $\tilde{C}$ state [20, 51, 62, 83, 118, 136, 139, 181, 182]. In a series of papers published in the late 90's [139, 182], Yamanouchi et al. experimentally determined an additional 33 vibrational term values of a_1 vibrational symmetry levels [182]. Normal-mode assignments were given for some of the observed levels in their first paper [182], although those assignments were later found to be inaccurate, given the large Fermi interactions. In the second paper [139], Sako et al. inspected the shapes of the $\tilde{C}$ state vibrational wavefunctions (obtained from the derived normal-mode force field) in the $q_1 - q_3$ plane after integrating the 3D wavefunctions along the q_2 coordinate. The nodal patterns of the integrated wavefunctions were found to be characteristic of Fermi resonance systems [85–87, 97, 180]. The vibrational levels were assigned by a generalized vibrational assignment scheme, based on visual inspection of the nodal patterns. In Sako's work, the stretch-bend interactions were assumed to be less important than the stretch-stretch interactions for the $\tilde{C}$ state vibrational levels (and their assignments), and the effects from the stretch-bend interactions were effectively averaged out after the 3D wavefunctions were integrated along q_2. However, given that some of the derived stretch-bend interaction constants have non-negligible magnitudes (e.g. $\phi_{233} = -44\ \mathrm{cm}^{-1}$) [139], the assumption of near-complete separability of ν_2 from the other two strongly interacting modes is expected to break down for levels with higher quanta of excitation, although Sako et al. did not discuss when and how the breakdown occurs.

In addition to extensive anharmonic interactions, the majority of the $\tilde{\mathrm{C}}$ state vibrational levels exhibit c-axis Coriolis perturbations [22, 62, 70, 131, 182]. Since the effects of Coriolis interactions are sensitive to the energy spacings between levels, a double-well structure on the PES, which gives rise to vibrational level-staggerings, is expected to cause staggering-related anomalies in the rotational structure of the $\tilde{\mathrm{C}}$ state, especially in the vibrational levels that involve the symmetry-breaking mode. However, rotational information for levels with odd quanta of excitation in the symmetry-breaking mode had not been available until our recent direct observations of b_2 vibrational symmetry levels, reported in the first paper of this series [131] and in Ref [133]. With those crucial pieces of information on the rotational structure of the $\tilde{\mathrm{C}}$ state, we can now validate and interpret the rotational anomalies caused by the double-well structure on the PES. However, correct identification and detailed understanding of the anomalies require knowledge of the molecular force field.

With direct high resolution measurements of the first eight b_2 symmetry vibrational levels [131], and an additional b_2 level at 2754 cm^{-1} [133], we can now determine a more physical and accurate force field for the SO_2 $\tilde{\mathrm{C}}^1\mathrm{B}_2$ state. The accuracy of Hoy and Brand's force field is limited by the reduced-dimension nature of their fit, and the fact that the ν_3 fundamental level, the position of which was estimated from the inferred position of the (0,1,1) level [70], was the only b_2 symmetry level included in the fit. Somewhat fortuitously, their estimated ν_3 fundamental frequency was extremely accurate [131]. Yamanouchi et al. [139, 182] extended Hoy and Brand's Hamiltonian to three-dimensions. However, all the parameters associated with the double-well structure were fixed to the values derived from the Hoy and Brand 2D fit, and no b_2 symmetry levels were included in the fit. In addition, none of the available rotational and isotopologue information was used as inputs to the fit.

In this paper, we derive an internal coordinate force field of the $\tilde{\mathrm{C}}$ state of

SO_2, which incorporates vibrational and rotational information of two isotopologues, $^{32}S^{16}O_2$ and $^{32}S^{18}O_2$. Our methods for calculating and fitting rovibrational information of the $\tilde{C}$ state of SO_2, e.g. vibrational band-origins, rotational constants, and Coriolis matrix elements, are described in Section 8.2. In Section 8.3, we present the result from a reduced-dimension fit, similar to the fit model developed by Hoy and Brand [70]. The reduced-dimension model provides insight into the unique effects of stretch-stretch Fermi resonance on the vibrational dynamics in the $\tilde{C}$ state. A scheme for assigning the 2D wavefunctions of the $\tilde{C}$ state is also discussed, based on semiclassical work by Kellman and coworkers [85–87, 97, 180]. In Section 8.4, our 3D internal coordinate force field is reported. We demonstrate the accuracy and predictive power of our 3D force field by comparing the values of the experimental observables that are not directly used as inputs to our fit to the calculated values from our force field. In particular, the Franck-Condon intensities and the strongly perturbed effective C rotational constants of highly anharmonic $\tilde{C}$ state vibrational levels are well reproduced. A two-step diagonalization procedure of the vibrational Hamiltonian is developed in Section 8.4.1. The two-step diagonalization allows assignments and characterization of an unprecedented number of $\tilde{C}$ state vibrational levels in a new Fermi-system basis (the Kellman basis), constructed explicitly in this work via partial diagonalization of the Hamiltonian. We investigate the breakdown of the separability of ν_2 from the other two strongly Fermi-interacting modes for levels >2000 cm^{-1} above the $\tilde{C}$ state zero-point level. Based on our force field, the structure of the Coriolis interactions in the $\tilde{C}$ state is discussed in Section 8.4.4. We are able to identify and explain the alternating patterns in the effective C rotational constants for levels in the vibrational progressions of the symmetry-breaking mode.

8.2 Methods

A vibrational Hamiltonian of the following form is used to fit the vibrational band origins of the SO_2 $\tilde{\mathrm{C}}$ state:

$$\begin{aligned}
H/hc = {} & \frac{1}{2}\omega_1(q_1^2+p_1^2)+\frac{1}{2}\omega_2(q_2^2+p_2^2)+\frac{1}{2}\omega_3(q_3^2+p_3^2) \\
& +\frac{1}{6}\phi_{111}q_1^3+\frac{1}{2}\phi_{112}q_1^2q_2+\frac{1}{2}\phi_{122}q_1q_2^2+\frac{1}{2}\phi_{133}q_1q_3^2+\frac{1}{2}\phi_{233}q_2q_3^2+\frac{1}{6}\phi_{222}q_2^3 \\
& +\frac{1}{24}\phi_{1111}q_1^4+\frac{1}{4}\phi_{1122}q_1^2q_2^2+\frac{1}{4}\phi_{1133}q_1^2q_3^2+\frac{1}{24}\phi_{2222}q_2^4+\frac{1}{4}\phi_{2233}q_2^2q_3^2+\frac{1}{24}\phi_{3333}q_3^4 \\
& +\frac{1}{6}\phi_{1222}q_1q_2^3+\frac{1}{6}\phi_{1112}q_1^3q_2+\frac{1}{2}\phi_{1233}q_1q_2q_3^2+C_1\exp(\text{-}C_2q_3^2), \qquad (8.1)
\end{aligned}$$

where

$$C_1 = \frac{b\exp(\rho)}{\exp(\rho)-\rho-1}, \qquad (8.2)$$

$$C_2 = \omega_3[\exp(\rho)-\rho-1]/2b, \qquad (8.3)$$

and the q's and p's are dimensionless normal-mode coordinates and the conjugate momenta, respectively. Eq. (8.1) is an expansion around C_{2v} geometry through quartic terms of the pure vibrational part of the molecular Hamiltonian, with a Gaussian hump in the antisymmetric stretch q_3 direction to account for non-equivalent S-O bond-lengths. The Gaussian hump in the PES is defined by three parameters, b, ω_3, and ρ [36]. The parameter, b, characterizes the height of the barrier along the q_3 direction (with $q_1 = q_2 = 0$), and the parameter, ρ, gives information about the curvatures at the two minima of the PES along q_3. More detailed discussions regarding the parameters involved in the Gaussian hump can be found in Ref [36]. Through quartic terms, there are a total of eighteen normal-mode force constants. The eigenvalues and eigenvectors of the vibrational Hamiltonian are obtained from diagonalization of the Hamiltonian in the normal-mode basis. Details regarding the construction of the Hamiltonian matrices are given in Appendix B.1.

Since normal-mode coordinates depend on the atomic masses, the normal-mode force constants, ω's and ϕ's, are isotopologue-dependent [126]. However, the observed vibrational levels of both $^{32}S^{16}O_2$ and $^{32}S^{18}O_2$ can be fit using *one* set of isotopologue-independent internal force constants (the superscript on ^{32}S will be dropped from here on). A transformation from normal-mode force constants to internal force constants is employed. This nonlinear transformation was worked out by Hoy, Mills, and Strey [71], and is summarized in Ref [126]. We therefore omit discussion of details of the transformation.

Given that the q_3 coordinate is in a symmetry species of its own, the isotope dependence of the two remaining parameters defining the Gaussian hump, b and ρ, can be determined by considering the 1D cross-section of the PES at $q_1 = q_2 = 0$. We constrain b, which characterizes the barrier height along this cross-section, to be isotopologue-independent. The saddle point energy, C_1, should also remain unchanged with isotopic substitution, so we also constrain ρ to be isotopologue-independent.

Another benefit of using internal force constants is that they enable us to calculate and incorporate rotational information – such as the rotational constants, centrifugal distortion coefficients, and Coriolis matrix elements – into the fit. However, the very strong q_3 anharmonicity and the large Fermi-133 resonance interaction necessitate a special treatment of the rotational information. We have adopted Hoy and Brand's treatment of the quartic centrifugal distortion constants for the zero-point vibrational level of both isotopologues [70]. The treatments of the rotational constants and the Coriolis matrix elements are summarized below, with additional information included in the Supplementary Material (see Appendix B.3).

The rotational constant, $\mathcal{R}_v$, of a vibrational level of the $\tilde{\mathrm{C}}$ state of SO_2 is calculated by

$$\mathcal{R}_v = \sum_n c_{n,v}^2 \mathcal{R}_n, \tag{8.4}$$

where $\mathcal{R}_n$ is the rotational constant of a normal-mode basis state, and $c_{n,v}$ is the coefficient of that basis state in the eigenvector that results from diagonalizing the Hamiltonian (Eq. (8.1)). Note that the symbol, $\mathcal{R}$, is used to generalize the notations for A, B, and C rotational constants. The rotational constant of a normal-mode basis state is given by the conventional expression

$$\mathcal{R}_n = \mathcal{R}_e - \sum_i \alpha_i^{\mathcal{R}}(v_i + 1/2), \tag{8.5}$$

where $\mathcal{R}_e$ is the rotational constant at the equilibrium geometry, v_i is the number of quanta in a specific normal-mode, and α_i is the rotation-vibration constant for that mode. The rotation-vibration constants are functions of the cubic normal-mode force constants. Some of the rotation-vibration constants also contain information about the Coriolis interactions in the molecule. For those reasons, the experimentally derived $\alpha_i^{\mathcal{R}}$ constants provide constraints on the derived force field. The general forms of rotation-vibration constants (see Supplementary Material) are derived by Mills via perturbation theory [109, 110]. Specific forms applicable to SO_2 are also available in Ref [114]. One advantage provided by Eq. (8.4) is that the rotational constants of a vibrational eigenstate can be calculated independent of the vibrational assignment of the eigenstate, which can be ambiguous due to anharmonic interactions, even in our assignment scheme discussed in Section 8.4.1. The effects from the double-well and the resonant interactions on the rotational constants of a vibrational eigenstate are contained in the basis state expansion coefficients of the eigenstate.

In the $\tilde{\mathrm{C}}$ state of SO_2, the C rotational constants are strongly perturbed by c-axis Coriolis interactions [22, 62, 70, 182]. The A and B rotational constants, however, are unaffected by Coriolis interactions up to second-order of perturbation theory. In cases where non-degenerate perturbation theory is valid, Coriolis contributions to rotational constants can be included in the α_i parameter, and Eq. (8.4) can be used to calculate rotational constants of the perturbed levels. However, this approach fails for all of the C rotational constants of the $\tilde{\mathrm{C}}$ state of SO_2 (even those which are not severely perturbed by Coriolis interactions), due to the presence of the double-well on the PES. Using second-order perturbation theory, the Coriolis contributions (C_{Cor}) to the C constant of a vibrational level of the $\tilde{\mathrm{C}}$ state must instead be calculated by the general expression

$$C_{Cor} = \sum_{v'} \langle v| h |v'\rangle \langle v'| h |v\rangle / (E_v - E_{v'}), \tag{8.6}$$

where

$$h = 2C_e\zeta_{23}^c \left[\sqrt{\frac{\omega_3}{\omega_2}} q_2 p_3 - \sqrt{\frac{\omega_2}{\omega_3}} q_3 p_2 \right] . \tag{8.7}$$

In Eq. (8.6), the eigenvalues and eigenvectors of the vibrational Hamiltonian in Eq. (8.1) are used for both $|v\rangle$ and the intermediate state $|v'\rangle$'s. The operator, h, defined in Eq. (8.7), is part of the Coriolis term, hJ_c, in the molecular Hamiltonian [109]. If we exclude the Coriolis contributions to the rotation-vibration constants, the rotational constants calculated using Eqs. (8.4)-(8.5) correspond to the Coriolis-deperturbed rotational constants from the experiments. The perturbed value of the C rotational constant of a vibrational level, C_p, is then the sum of the deperturbed C constant, C_{dp}, and C_{Cor}, or $C_p = C_{dp} + C_{Cor}$.

In our fit, the A and B constants of the three fundamental levels, as well as those of the zero-point vibrational level, are included. This helps to ensure a physical determination of both the equilibrium geometry and the cubic force parameters. The experimental C constants are used to validate the goodness of our internal coordinate force field by comparing their values to the C constants calculated from our force field.

Coriolis matrix elements between a_1 and b_2 symmetry vibrational levels of the $\tilde{\mathrm{C}}$ state of SO_2 derived from fits to the observed energy levels [131] are not included directly in the fit. However, the Coriolis matrix elements can be calculated using the derived force field and the calculated values may be compared to the experimentally derived values. The Coriolis matrix element, t_1, between vibrational eigenstates $|v\rangle$ and $|v'\rangle$ is defined as

$$t_1 \equiv \frac{1}{2} \langle v| h |v'\rangle . \tag{8.8}$$

The eigenvectors, $|v\rangle$ and $|v'\rangle$, are calculated from the force field. In this work, Coriolis interactions between modes ν_1 and ν_3 are neglected, since the ν_1 and ν_3 frequencies are very different, and ζ_{13}^c is about three times smaller than ζ_{23}^c.

To summarize our fit procedure, internal force constants through quartic terms expanded about the C_{2v} geometry are used as parameters in our force field fit of the $\tilde{C}$ state of SO_2. From those parameters, we derive the isotopologue-specific normal-mode force constants used in Eq. (8.1) for both $S^{16}O_2$ and $S^{18}O_2$. The Hamiltonian (Eq. (8.1)) for each isotopologue is diagonalized to obtain eigenvalues and eigenvectors. The eigenvalues are fit to the observed vibrational band origins. The isotope shift of the zero-point level between the two isotopologues is also calculated and fitted to observed value. From the internal coordinate force field and the equilibrium geometry, we derive the rotational constants of each vibrational eigenstate, using Eqs. (8.4)-(8.5). The derived A and B rotational constants of the fundamental levels, and those of the zero-point vibrational level, are fitted to the experimental values for both isotopologues. All five quartic centrifugal distortion coefficients of the zero-point vibrational level for each isotopologue are also calculated from the internal force field and included in the fit. A nonlinear least-square fit is carried out to derive the internal coordinate force constants.

Because we include vibrational and rotational information of two isotopologues, the number of data in our fit far exceeds that of all previous force field fits on the $\tilde{C}$ state of SO_2 [139, 181, 182]. We have therefore chosen to use 23 fit parameters (one of which is constrained), compared with 17 in Yamanouchi's normal-mode force constants fit. [139][1]

To validate our internal coordinate force field, the C rotational constants and Coriolis matrix elements are calculated from the force field. The calculated values are compared to the experimentally determined values. In addition, Franck-Condon factors between the $\tilde{X}$ state zero-point vibrational level and the $\tilde{C}$ state vibrational levels are calculated. The vibrational overlap integrals with the harmonic basis states of the $\tilde{C}$ state are calculated by the method of Sharp and Rosenstock [140], using the $\tilde{X}$ state geometry and quadratic force field parameters from Ref [110]. Anharmonic Franck-Condon factors for the $\tilde{C}$ state vibrational eigenstates are then calculated from

---

[1] Note that there are 15 parameters in total in their vibrational Hamiltonian. For their Franck-Condon calculation, they also need equilibrium geometry, which are presumably obtained from Hoy and Brand's 2D fit. This means effectively, they are using 17 parameters in their fit and calculation.

Table 8.1: Internal force constants of the $\tilde{\mathrm{C}}$ state of SO_2 obtained from a two-dimensional fit, and normal-mode force constants of $S^{16}O_2$. Internal and normal-mode force constants derived by Hoy and Brand [70] are included for comparison. All normal-mode force constants have units of cm^{-1}. The mdyn-Å unit system is used for the internal force constants, e.g. $[f_{rr}]$=mdyn/Å, $[f_{r\theta}]$=mdyn, $[f_{rrr}]$=mdyn/$\mathrm{Å}^2$, etc., where 1 mdyn=10^{-8} N and 1 Å=10^{-10} m.

Internal	This work	H&B	Normal	This work	H&B
f_{rr}	4.1623(859)	4.1736	ω_1	929.57	935.2
$f_{rr'}$	1.8138(1022)	1.9128	ω_3	635.32	623.3
$f_{r\theta}$	0.215(177)	0.3746	ϕ_{111}	-274.65	-322.5
$f_{\theta\theta}$	1.1203(144)	1.1616	ϕ_{133}	-283.85	-305.8
f_{rrr}	-32.698(1281)	-36.261	ϕ_{3333}	98.44	122.4
$f_{rrr'}$	-4.988(928)	-7.015	ϕ_{1133}	59.28	72.0
$f_{rr\theta}$	-2.784(1332)	-3.340	ϕ_{1111}	27.54	32.2
$f_{rr'\theta}$	-0.301(662)	-0.918	ω_2	377.17	384.9
$f_{r\theta\theta}$	-3.467(1008)	-3.593	ϕ_{122}	-33.11	-29.9
$f_{\theta\theta\theta}$	-3.306(466)	-3.755	ϕ_{112}	-29.31	-38.5
f_{rrrr}	138.26(745)	165.66	ϕ_{222}	-78.86	-79.6
			ϕ_{233}	-49.80	-44.4
b/cm^{-1}	102.86(439)	117.5			
ρ	0.3485(197)	0.4			
θ_e/deg.	103.80(3)	103.75			
r_e/Å	1.5557(3)	1.5525			

the harmonic basis expansion coefficients.

8.3 Reduced-dimension fit

Before we present the results from a complete 3D fit using Eq. (8.1), we first discuss the result obtained from a 2D fit model (excluding ν_2 bending) originally developed by Hoy and Brand for the $\tilde{\mathrm{C}}$ state of SO_2 [70]. We follow their treatment, but we also include isotopologue information and rotational constants, as described in Section 8.2. The reason for the success of a reduced-dimension 2D fit model is that, although the ν_1 and ν_3 modes interact strongly, the ν_2 mode remains approximately isolated below 2000 cm^{-1} [22, 70, 182]. The fit result is presented in Table 8.1, along with the Hoy and Brand result [70]. The force field (from a 2D fit) derived in this work

Table 8.2: Experimental (Obs.) and calculated (Cal.) vibrational term energies of states included in the 2D fit. For both isotopologues, the energy of the zero-point level has been subtracted from each term value. The observed [62] and calculated isotope shift between the zero-point vibrational levels of the $\tilde{\mathrm{C}}$ state of $S^{16}O_2$ and $S^{18}O_2$ are -26.3 cm^{-1} and -28.0 cm^{-1}, respectively. The asterisks indicate a mixing of wavefunctions between those of the nearest neighbor energy levels. The notations used in the vibrational assignments are explained in Section 8.3.1. Units in cm^{-1}.

	Assig.	Obs.	Cal.		Assig.	Obs.	Cal.
$S^{16}O_2$	$(0,0,0)_r$	0	0	$S^{16}O_2$	$(0,0,1)_r$	212.6	212.3
a_1 sym.	$(0,0,2)_r$	561.2	560.7	b_2 sym.	$(0,0,3)_r$	890.9	891.1
	$(1,0,0)_l$	960.0	960.5		$(1,0,1)_l$	1261.4	1262.2
	$(0,0,4)_r$	1245.4	1247.4		$(0,0,5)_r$	1595.8	1596.9
	$(1,0,2)_r$	1653.7	1650.8		$(1,0,3)_r$		1996.7
	$(2,0,0)_l$*	1917.5	1916.7		$(0,0,7)_r$*		2315.2
	$(0,0,6)_r$*	1964.9	1963.7		$(2,0,1)_l$*		2338.7
	$(1,0,4)_r$		2371.7		$(1,0,5)_r$		2729.4
	$(0,0,8)_r$*	2680.3	2680.0				
	$(2,0,2)_r$*		2727.7				
	$(3,0,0)_l$	2920.6	2921.9				
$S^{18}O_2$	$(0,0,2)_r$	535.1	534.7	$S^{18}O_2$	$(0,0,1)_r$		200.4
a_1 sym.	$(1,0,0)_l$	920.9^a	921.1	b_2 sym.	$(0,0,3)_r$		852.2
	$(1,0,2)_r$	1582.3^a	1580.5		$(1,0,1)_l$		1206.4
	$(2,0,0)_l$*	1840.0^a	1838.0		$(0,0,5)_r$		1531.6
	$(0,0,6)_l$*	1880.2^a	1884.8				
	$(3,0,0)_l$	2798.4^a	2799.6				

[a] Low resolution measurement [70].

is qualitatively similar to the one obtained by Hoy and Brand [70]. Also listed are normal-mode force constants of $S^{16}O_2$ derived from the internal coordinate force field. The measured and calculated vibrational term values are included in Table 8.2. The quantum numbers and the subscript, r or l, used in our vibrational assignments in Table 8.2, are related to the nodal patterns and the general shapes of the vibrational wavefunctions respectively, which are explained in detail in Section 8.3.1.

Table 8.3 shows the C_s equilibrium bond lengths obtained from our internal coordinate force field of the $\tilde{\mathrm{C}}$ state of SO_2. The barrier on the PES is relatively low, but it is sufficient to produce a significant depression of the antisymmetric stretch fundamental frequency. The ν_3 fundamental frequency, which is usually the highest

Table 8.3: C_s equilibrium geometry of the $\tilde{C}$ state of SO_2.

	This work	H&B [70]
$r_1/\text{Å}$	1.642	1.639
$r_2/\text{Å}$	1.494	1.491

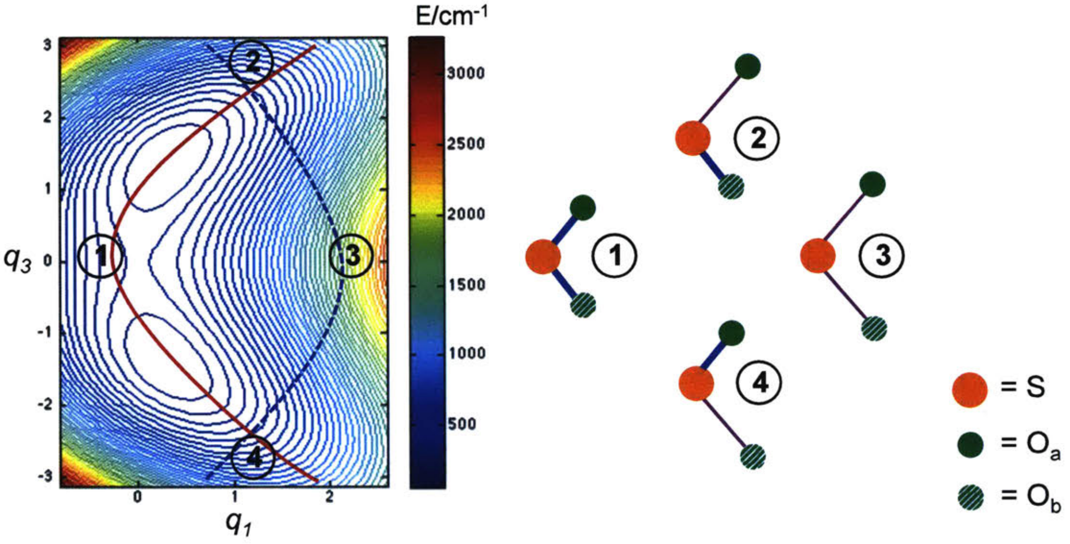

Figure 8-1: Two-dimensional potential energy surface obtained from the 2D fit, along with the approximate geometries of the molecule at four different points on the PES. The two oxygen atoms are labelled and color-coded differently for clarity in the text. The red solid curve and the blue dashed curve on the PES are related to the nodal patterns of the wavefunctions, discussed in detail in Section 8.3.1.

among the three fundamental frequencies of symmetric triatomic molecules, is the lowest in the $\tilde{C}$ state of SO_2. The parameter, ρ, characterizes the curvatures at the two minima of the PES. The bottoms of the two wells on the PES would be nearly parabolic if $\rho = 1.5$ (in the absence of cubic and higher-order anharmonicities) [36]. For $\rho < 1.5$, which is true for the $\tilde{C}$ state of SO_2 (see Table 8.1), starting from a minimum of the PES and moving along q_3, the potential should rise more steeply in the direction away from the barrier than in the direction towards the barrier. This is indeed the case for the $\tilde{C}$ state, as can be seen from the PES in Fig. 8-1.

8.3.1 Fermi Resonance in the $\tilde{\mathrm{C}}$ state of SO_2 and Vibrational Assignments

Due to the presence of a Gaussian hump along the q_3 coordinate, the antisymmetric stretch is grossly anharmonic and is poorly described by the harmonic basis set used to construct the vibrational Hamiltonian. Therefore, we use a set of *anharmonic* basis states, $|v_1, v_2, v_3\rangle_{\mathrm{a}}$, obtained from a first-order perturbation theory treatment of the vibrational Hamiltonian, where all terms other than the harmonic oscillator terms are treated as perturbations. Below 1000 cm^{-1}, the energies of the anharmonic states, i.e. the diagonal matrix elements of the vibrational Hamiltonian, are much closer to the observed eigenenergies than the energies of the harmonic basis states. For example, the energy of the *anharmonic* $|0, 0, 1\rangle_{\mathrm{ah}}$ basis state (317 cm^{-1}) is much closer than that of the *harmonic* basis state $|0, 0, 1\rangle$ (635 cm^{-1}) to the observed ν_3 eigenenergy (212 cm^{-1}).

Due to the depression of the ν_3 frequency, the $|0, 0, 2\rangle_{\mathrm{a}}$ energy is close to that of the $|1, 0, 0\rangle_{\mathrm{a}}$ state, with an energy separation of 200 cm^{-1}. Given the large ϕ_{133} constant (-284 cm^{-1}), anti-symmetric and symmetric stretching modes are mixed via Fermi resonance. This strong mixing was first noted by Hoy and Brand [22, 70], and recognized by others in more recent studies [20, 62, 139, 181, 182]. A large ϕ_{133} force constant is not unusual in symmetric triatomic molecules. Consider, for example, values for the ground electronic state of H_2O (-1785 cm^{-1}) [110], or SO_2 (-319 cm^{-1}) [114]. However, strong Fermi interaction between symmetric and antisymmetric triatomic stretching modes is unusual, because the harmonic stretching frequencies are not typically in 1:2 resonance.

The effects of Fermi resonance on the semiclassical dynamics of molecules have been studied by Kellman and coworkers [85–87, 97, 180]. The standard procedure of labeling vibrational levels by normal-mode quantum numbers is inadequate and misleading for Fermi resonance systems. Kellman and coworkers provide an alternative assignment scheme based on the semiclassical dynamics [87, 180]. An especially important feature of Kellman's assignment scheme is that one can make semiclassical vibrational assignments based on the nodal patterns of the wavefunction. This is particularly useful in the $\tilde{C}$ state of SO_2, because clear nodal patterns persist in many of the wavefunctions (available from Discrete Variable Representation calculations (DVR)), despite the fact that strong anharmonic effects prevent assignment of a dominant harmonic basis state, even at low vibrational energy. In Fig. 8-2, some of the a_1 vibrational symmetry wavefunctions of $S^{16}O_2$ obtained from our 2D fit are plotted, with assignments from Kellman's scheme discussed below. Additional discussion on the semiclassical dynamics of the $\tilde{C}$ state of SO_2 can be found in Appendix B.2.

The shapes of the wavefunctions in Fig. 8-2 are distorted from the shapes of normal-mode wavefunctions. Some of the wavefunction shapes are curved so that the nodal patterns extend along the red solid curve shown in Fig. 8-1, while others extend along the blue dashed curve, perpendicular to the red curve. Wavefunctions with nodes organized along the red curve are given an 'r' subscript in their assignment (indicating the wavefunctions "open to the right"), e.g. $(0, 0, 6)_r$, while those with nodes organized along the blue curve are given an 'l' subscript (indicating the wavefunctions "open to the left"), e.g. $(3, 0, 0)_l$.

The three quantum numbers used in our assignment scheme, (v_α, v_2, v_β), are related to the nodal pattern of the wavefunctions. The second number, v_2, gives the number of bending quanta, which are uncoupled from stretching quanta in our 2D model. All vibrational levels displayed in this section and used in the 2D fit have $v_2 = 0$. The first and last quantum numbers describe the nodal pattern of the wavefunction in the 2D stretching plane. Using the wavefunction of the assigned $(2,0,4)_r$ state in Fig. 8-2 as an example, the first number, v_α, refers to the number of parallel red solid nodal curves that one can draw on the wavefunction, and the third number, v_β, is the number of blue dashed nodal lines, that cross the red solid nodal curves. The ν_α mode, with a_1 vibrational symmetry, correlates to the symmetric stretching mode, ν_1, in the normal mode basis, and the ν_β mode, with b_2 vibrational symmetry, correlates to the anti-symmetric stretching mode, ν_3.

Using our assignment scheme, the wavefunctions can be grouped according to the polyad number, $P = v_\alpha + \frac{1}{2}v_\beta$. There are $(P + 1)$ levels that belong to a given

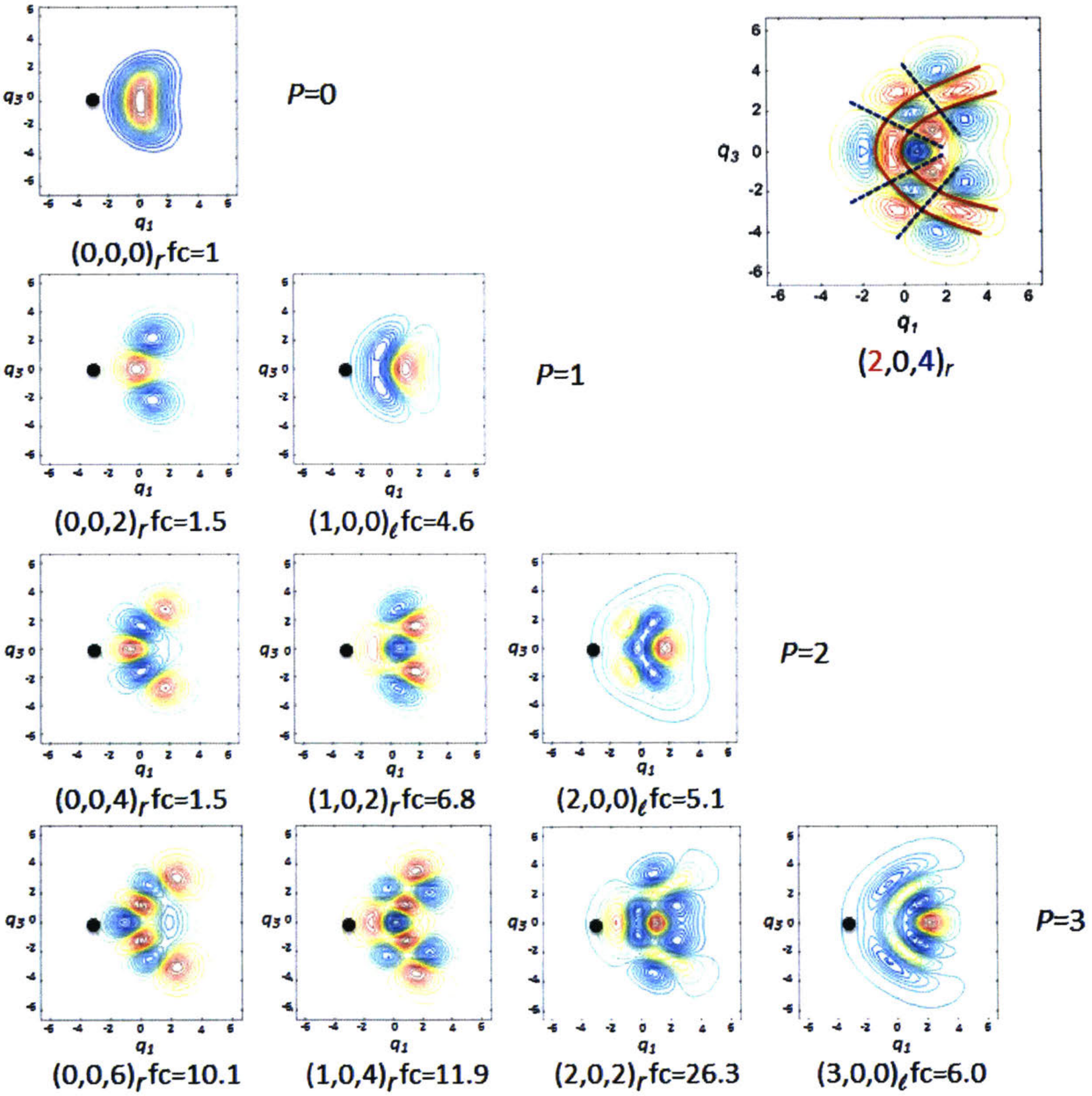

$(0,0,0)_r$fc=1

$(0,0,2)_r$fc=1.5 $(1,0,0)_\ell$fc=4.6

$(0,0,4)_r$fc=1.5 $(1,0,2)_r$fc=6.8 $(2,0,0)_\ell$fc=5.1

$(0,0,6)_r$fc=10.1 $(1,0,4)_r$fc=11.9 $(2,0,2)_r$fc=26.3 $(3,0,0)_\ell$fc=6.0

$(2,0,4)_r$

Figure 8-2: a_1 vibrational symmetry wavefunctions of $S^{16}O_2$ from the 2D fit. The semiclassical assignment (in parentheses) is given below each wavefunction, along with the calculated relative Franck-Condon factor (fc) for a transition from the zero-point level of the SO_2 $\tilde{X}$ state. The black dot on each figure is the approximate (center) location of the zero-point wavefunction of the $S^{16}O_2$ $\tilde{X}$ state. The vibrational wavefunction of the $(2,0,4)_r$ state in the P=4 polyad is plotted separately to illustrate how nodes in the eigenstates determine the $(v_\alpha, 0, v_\beta)_r$ assignments. Within a given polyad (designated by polyad number, $P = v_\alpha + \frac{1}{2}v_\beta$), the energy increases for sub-figures from left to right.

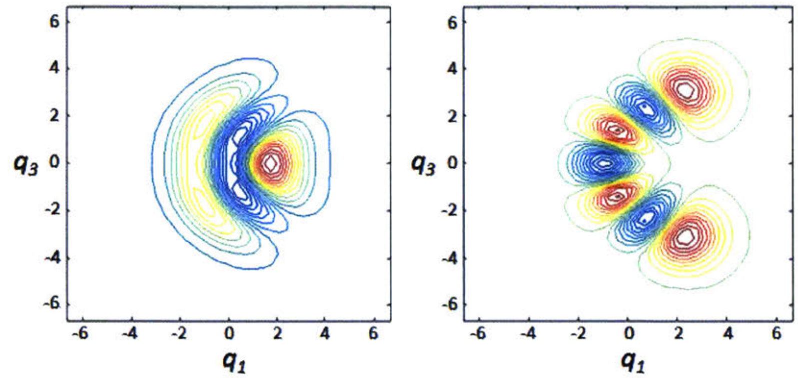

Figure 8-3: Linear combinations of the $(2,0,0)_l$ and $(0,0,6)_r$ eigenstate wavefunctions (as in Fig. 8-2). The wavefunction on the left results from $0.93\,(2,0,0)_l - 0.37\,(0,0,6)_r$ and the one on the right comes from $0.37\,(2,0,0)_l + 0.93\,(0,0,6)_r$.

polyad with polyad number P. A polyad consists of a group of systematically near-degenerate interacting zero-order states. For example, the three levels with polyad number $P = 2$ result predominantly from three strongly anharmonically interacting zero-order wavefunctions $|0,0,4\rangle_{\rm a}$, $|1,0,2\rangle_{\rm a}$, and $|2,0,0\rangle_{\rm a}$.

The polyad number P is not strictly conserved in the $\tilde{\rm C}$ state of SO_2. Note that the $(2,0,0)_l$ and $(0,0,6)_r$ wavefunctions in Fig. 8-2 appear to deviate from the expected shape of Kellman's Fermi resonance wavefunctions (e.g. there should not be a local maximum at $q_1 = 0, q_3 = 0$ for the $(2,0,0)_l$ wavefunction). However, if one takes a specific linear combination of $(2,0,0)_l$ and $(0,0,6)_r$ wavefunctions (see Fig. 8-3), the zero-order wavefunctions are restored, which indicates an interaction between the zero-order basis states. The ϕ_{1133} term, which has a magnitude of 60 cm^{-1}, is primarily responsible for the interaction. This Darling-Dennison interaction breaks the strict conservation of the polyad number, P. Similar interaction occurs between the zero-order $(2,0,2)_r$ and $(0,0,8)_r$ states (not shown in Fig. 8-2). The inter-polyad interaction that we see here is *not* an artifact of the 2D nature of the fit, since it is observed in the wavefunctions obtained from the 3D fit as well (Section 8.4.1).

The peculiar shapes of the wavefunctions in Fig. 8-2 have their origins in the shape of the PES. The PES has a kidney-bean shape (Fig. 8-1), as a result of the large Fermi ϕ_{133} term. In the absence of strong Fermi-133 interaction, a double-well structure in the q_3 direction will cause a staggered energy pattern in the *normal-mode* $(0, 0, v_3)$ progression. The Fermi-133 resonance mixes the normal-modes to create Kellman-type modes, but the nodal coordinate along which the $(0, 0, v_\beta)_r$ Kellman-type progression is organized–the red solid curve in Fig. 8-1–also passes through both minima of the PES. As a result, levels in the $(0, 0, v_\beta)_r$ progression, which extends along the new nodal coordinate, also exhibit staggering from the double-well minimum. The staggered energy pattern is obvious in Fig. 1 of the third paper of this series [130].

8.3.2 Effects of Fermi Resonance on the Dynamics of $\tilde{C}$ state of SO_2

The r- and l-type wavefunctions encode two different types of classical motions. As illustrated in Fig. 8-1, molecules with the r-type motion pass through the C_{2v} geometry with a shorter S-O bond length (see configuration ①) than those with the l-type motion (see ③). In the pure r-type motion, starting from ②, where the S-O_a bond is stretched while the other bond is at approximately the bond length of the C_{2v} configuration ① (R_1), S-O_a contracts to R_1. Then, while the S-O_a bond remains at the bond length of ①, the S-O_b bond elongates until the molecule reaches configuration ④. S-O_a continues to stay at R_1, and S-O_b contracts back to R_1. The molecule then returns to ② by locally stretching the S-O_a bond. The motion repeats itself. In the pure l-type motion, starting from ②, where the S-O_b bond is contracted while the other bond is at approximately the bond-length of C_{2v} configuration ③ (R_3), S-O_b stretches to R_3. Then, while the S-O_b bond remains at R_3, the S-O_a bond contracts until the molecule reaches configuration ④. S-O_b remains at R_3, while S-O_a contracts back to R_3. The molecule then returns to ② by locally contracting the S-O_b bond. The motion then repeats itself. We emphasize that the semiclassical motion that results from the Fermi-133 resonance in the $\tilde{C}$ state is similar to but qualitatively different from the local stretching motion caused by the Darling-Dennison resonance at high excitation, e.g. in water.

Sako et al. [139] first noted this behavior of the wavefunctions for the $\tilde{C}$ state of SO_2, although they did not give an explicit interpretation of the semiclassical motions encoded in the wavefunctions. In the same work [139], it was noted that above the predissociation threshold, r-type levels dissociate more rapidly than l-type levels. They argue that the r-type wavefunctions, with intensity along the S-O dissociation coordinate, have better overlap with the dissociation continuum of the ground electronic surface, while the l-type wavefunctions have less overlap with the ground state continuum. The level-dependence of the predissociation rates of the $\tilde{C}$ state vibrational levels can also be understood in light of the semiclassical motions encoded in the wavefunctions. In the r-type motion, the stretching momentum is always localized in the S-O bond that is instantaneously longer, whereas the momentum is localized in the instantaneously shorter S-O bond in the l-type motion. As a result, vibrational levels with r-type semiclassical motion couple better to the reaction coordinate, while those with 'l'-type motion waste their energy by visiting configuration ③ in Fig. 8-1.

8.3.3 Franck-Condon Factors of the SO_2 $\tilde{C}$-$\tilde{X}$ transition

Also given in Fig. 8-2 are calculated relative Franck-Condon factors (fc) from the zero-point level of the $\tilde{X}$ state of SO_2. The ground electronic state of SO_2 has a shorter equilibrium S-O bond length than the $\tilde{C}$ state. As a result, the symmetric stretching mode is Franck-Condon active. Ordinarily, one would not expect Franck-Condon activity in the antisymmetric stretching mode of a symmetric triatomic molecule. However, as shown in Fig. 8-2, for polyads with $P > 1$, the highest energy member of the polyad, which correlates with a pure symmetric stretching zero-order state, does not have the largest Franck-Condon factor. The Franck-Condon intensities migrate toward lower polyad members as the polyad number increases, in agreement with the trend observed experimentally [182]. This can be understood in terms of the effect of the Fermi-133 resonance on the shapes of the wavefunctions. The black dot on each subfigure in Fig. 8-2 indicates the approximate center location (at $q_1 = -3.2$) of the $\tilde{X}$ state zero-point level wavefunction in the q_1-q_3 plane. Below 3000 cm^{-1}, the highest energy states of a given polyad all have l-type wavefunctions, which open up toward the negative q_1 direction and have almost no intensity at the Franck-Condon point, while lower members of a given polyad are r-type, which are curved toward the Franck-Condon active area. As a result, the highest member loses its Franck-Condon activity, while lower members gain significant intensity.

8.4 Three-dimensional fit

The internal coordinate force field obtained from our 3D fit is presented in Table 8.4, along with the normal-mode force constants derived for $S^{16}O_2$, for comparison with values derived by Yamanouchi [139]. In our 3D fit, despite inclusion of rotational and isotopologue information, all three parameters that characterize the Gaussian hump in Eq. (8.2) and (8.3), b, ω_3 (which in our internal coordinate force field is determined by f_{rr} and $f_{rr'}$), and ρ are strongly correlated (>0.95 correlation parameters among them). To break this correlation, additional b_2 vibrational symmetry levels, especially the $(0,0,1)_r$ levels of different isotopologues, must be measured and included in the fit. In the absence of those isotopologue data, we have fixed the value of ρ to 0.35, which is the value we obtained from our two-dimensional fit. The value of ρ was better determined in the 2D fit, due to constraints made to obtain the force field (although we cannot guarantee the accuracy of ρ obtained from the 2D fit). By constraining the value of ρ, the correlation among B, f_{rr}, and $f_{rr'}$ is much reduced (<0.5). We must emphasize that the uncertainties of the fit parameters listed in Table 8.4 are only statistical uncertainties of the fit, which do not take into account correlation effects. The actual uncertainties in some of the parameters might realistically be 5 to 10 times larger [110]. Information from other isotopologues would certainly reduce correlation. Alternatively, high-level quantum calculations might provide better constraints on some of the fit parameters, which would allow us to obtain a more physical and accurate internal coordinate force field fit. In Tables 8.5-8.10, the measured and calculated values of the observables from our 3D calculation are listed.

For all of the vibrational term values included in the fit, the difference between experiment and fit is less than 1.9 cm^{-1} and the rms error is 0.9 cm^{-1}. The observed

Table 8.4: Internal force constants of the $\tilde{\text{C}}$ state of SO_2 obtained from a three-dimensional fit, along with normal-mode force constants of $S^{16}O_2$. Normal-mode force constants derived by Yamanouchi [139] are included for comparison. All of the normal-mode force constants have units of cm^{-1}. Internal force constants are given in the mdyn-Å unit system.

Internal	This work	Normal	This work	Yamanouchi [139]
f_{rr}	3.9326(353)	ω_1	938.03	942.6
$f_{rr'}$	2.0185(476)	ω_2	392.28	389.13
$f_{r\theta}$	0.093(58)	ω_3	573.56	589.6
$f_{\theta\theta}$	1.2250(97)	ϕ_{111}	-283.72	-306.0
f_{rrr}	-32.080(1044)	ϕ_{133}	-300.21	-288.6
$f_{rrr'}$	-5.763(924)	ϕ_{112}	-46.143	-22.16
$f_{rr\theta}$	-1.702(432)	ϕ_{122}	0.381	16.26
$f_{rr'\theta}$	-0.354(176)	ϕ_{222}	-85.375	-65.538
$f_{r\theta\theta}$	-2.156(217)	ϕ_{233}	-48.584	-43.48
$f_{\theta\theta\theta}$	-3.521(64)	ϕ_{1111}	57.321	33.12
f_{rrrr}	149.89(1049)	ϕ_{1133}	52.237	53.52
$f_{rrrr'}$	-4.226(8783)	ϕ_{3333}	223.05	177.36
$f_{rrr'r'}$	29.60(1034)	ϕ_{1122}	-0.458	-21.52
$f_{rr\theta\theta}$	12.21(226)	ϕ_{2222}	8.276	
$f_{rr'\theta\theta}$	7.26(210)	ϕ_{2233}	-8.827	
$f_{\theta\theta\theta\theta}$	9.88(169)	ϕ_{1222}	8.110	
$f_{rrr\theta}$	5.78(379)	ϕ_{1112}	0.086	
$f_{rrr'\theta}$	-5.15(478)	ϕ_{1233}	10.294	
$f_{r\theta\theta\theta}$	3.90(272)			
b/cm^{-1}	90.39(180)			117.5[a]
ρ	0.35[b]			0.4[a]
θ_e/deg.	103.80(2)			103.75[a]
r_e/Å	1.5557(3)			1.5525[a]

[a] Constrained to the 2D fit value of Ref [70].

[b] Constrained.

level at 2224.9 cm^{-1} [182] is not included in our fit. Based on the energy, the only possible assignment is $(0,6,0)_r$, which, according to our derived force field, is predicted at 2208 cm^{-1} (see Table 8.5). However, the 2224.9 cm^{-1} level seems unlikely to correspond to the $(0,6,0)_r$ state. The A rotational constant of $(0,6,0)_r$ is predicted to be around 1.27 cm^{-1}, given the large positive α_2^a constant (0.02 cm^{-1}). The experimentally derived A rotational constant of the 2224.9 cm^{-1} level is, however, only 1.1226(159) cm^{-1} [182], which is significantly smaller than *any* of the A constants of the $\tilde{\mathrm{C}}$ state of SO_2. In addition, the observed and calculated trend in the Franck-Condon factors suggests that the $(0,6,0)_r$ level should be too weak to be observed in the spectrum. Using our force field, it is also clear that the 2224.9 cm^{-1} level is not due to a hot-band transition; nor can it be a level from $^{34}SO_2$, which has about 5% natural abundance. We believe that the 2224.9 cm^{-1} level may be an interloper from another electronic state that borrows transition intensity from the $\tilde{\mathrm{C}}$-state. Further characterizations of this level (e.g. fluorescence lifetime and magnetic field response measurements) are necessary to confirm its identity. Considering all the uncertainties pertaining to this level, we have excluded it from our fit model.

For the rotational constants included in the fit (Table 8.7), the calculated values fall within (or very close to) the 2σ uncertainties of the experimentally derived values, except for the A and B constants of the $(1,0,0)_l$ level of $S^{16}O_2$. The $(1,0,0)_l$ level is Coriolis-coupled to the close-lying $(0,2,1)_r$. Due to lack of high-J data points for $(0,2,1)_r$, which are crucial to deperturbation of the Coriolis interactions, the derived rotational constants of $(1,0,0)_l$ [131], especially the B and C constants, are likely not fully deperturbed. In addition, the total error (0.073 cm^{-1}) of the fit to the Coriolis-interacting tetrad containing $(1,0,0)_l$ and $(0,2,1)_r$ is significantly larger than the calibration error (0.02 cm^{-1}), and not all parameters are fit simultaneously. Therefore, the real uncertainties on the derived rotational constants of $(1,0,0)_l$ can be significantly larger than the the statistical uncertainties. Overall, the fit to the centrifugal distortion coefficients given in Table 8.9 is quite good, although some of the centrifugal distortion coefficients included in the fit (e.g. Δ_K of both isotopologues) fall outside of the 3σ uncertainties of the experimentally derived values [62].

Table 8.5: Experimental (Obs.) and calculated (Cal.) vibrational term energies of a_1 symmetry states of $S^{16}O_2$, along with their vibrational assignments. The energy of the $\tilde{C}$-state origin has been subtracted from each term value. Unless otherwise stated, the experimental term values are from Ref [182]. Units in cm^{-1}. Levels are labeled according to the degree of perturbation in the Kellman basis (explained in Section 8.4.1). Levels with a single Kellman basis state coefficient greater than 0.9 are considered minimally perturbed (no label); '$*$' indicates a coefficient of 0.8-0.9; '†' indicates a coefficient of 0.7-0.8; '‡' indicates coefficients <0.7 (no nominal assignment possible). Superscript numbers after the assignments indicate eigenstates that result from the same set of interacting Kellman basis states, e.g. $(0,2,4)_r$ and $(0,0,6)_r$ interact to yield the eigenstates at 1958 cm^{-1} and 1965 cm^{-1} (both with superscript 1).

Assig.	**Obs.**	**Cal.**	**Assig.**	**Obs.**	**Cal.**	**Assig.**	**Obs.**	**Cal.**
$(0,0,0)_r$	0	0	$(0,2,4)_r{*}^1$		1958.2	$(0,0,8)_r$	2680.3	2681.2
$(0,1,0)_r$	377.5	377.3	$(0,0,6)_r{*}^1$	1964.9	1965.4	$\ddagger^8$		2729.3
$(0,0,2)_r$	561.2	561.2	$(1,1,2)_r$	2018.9	2019.8	$(0,6,2)_r\dagger^6$		2739.5
$(0,2,0)_r$	751.5	751.0	$(0,4,2)_r{*}^2$		2024.8	$\ddagger^8$	2743.0[a,c]	2744.7
$(0,1,2)_r$	932.0	930.9	$(1,3,0)_l$	2084.3	2084.6	$\ddagger^8$	2762.1	2763.6
$(1,0,0)_l$	960.0	960.8	$(0,6,0)_r{*}^3$		2207.3	$(1,5,0)_l$		2817.5
$(0,3,0)_r$	1122.0	1121.1	$(2,1,0)_l$	2285.3	2284.4	$(0,8,0)_r{*}$		2910.1
$(0,0,4)_r$	1245.4	1246.6	$(0,3,4)_r\dagger^4$	2308.7	2310.0	$(3,0,0)_l$	2920.6	2921.5
$(0,2,2)_r$	1300.0	1298.1	$(0,1,6)_r\dagger^4$	2321.8	2320.8	$\ddagger$	3118.6[a]	3119.8
$(1,1,0)_l$	1337.9	1338.5	$(1,2,2)_r{*}^5$	2370[a,b]	2378.3	$(1,0,6)_r\dagger$	3136.4[a]	3141.0
$(0,4,0)_r$		1487.2	$(0,5,2)_r{*}^3$		2383.8	$(3,1,0)_l$	3281.8[a]	3283.9
$(0,1,4)_r$	1604.3	1604.9	$(1,0,4)_r{*}^5$	2394.3	2393.8	$\ddagger$	3494.8[a]	3500.4
$(1,0,2)_r$	1653.7	1653.9	$(1,4,0)_l$	2452.6	2452.8	$(2,0,4)_r$	3526.0[a]	3528.8
$(0,3,2)_r$		1662.8	$(0,7,0)_r{*}^6$		2560.9	$(3,2,0)_l$	3640.5[a]	3643.9
$(1,2,0)_l$	1712.7	1713.1	$\ddagger^7$	2644.3	2643.7	$(3,0,2)_r$	3763.9[a]	3762.3
$(0,5,0)_r{}^2$		1849.3	$\ddagger^7$	2663.5	2662.8	$\ddagger$	3887.7[a]	3898.5
$(2,0,0)_l$	1917.5	1916.3	$\ddagger^7$		2673.4	$(3,3,0)_l$	3996.8[a]	4001.2

[a] Not included in the fit.

[b] Low resolution measurement [51].

[c] MODR result [133].

Table 8.6: Experimental (Obs.) and calculated (Cal.) vibrational term energies of b_2 symmetry levels of $S^{16}O_2$, as well as both a_1 and b_2 levels of $S^{18}O_2$. The energy of the zero-point level has been subtracted from each term value. The observed [62] and calculated isotope shift between the zero-point vibrational levels of the $\tilde{C}$ state of $S^{16}O_2$ and $S^{18}O_2$ are -26.3 cm ^{1} and -27.7 cm^{-1}, respectively. See the caption of Table 8.5 and Section 8.4.1 for details regarding the meaning of the notations in the assignments.

	Assg.	Obs.	Cal.		Assig.	Obs.	Cal.
$S^{16}O_2$	$(0,0,1)_r$	212.6	212.8	$S^{18}O_2$	$(0,1,0)_r$	359.5	359.6
b_2 sym.	$(0,1,1)_r$	582.2	583.2	a_1 sym.	$(0,0,2)_r$	535.1	534.5
	$(0,0,3)_r$	891.0	891.1		$(0,2,0)_r$	715.2^{a}	715.9
	$(0,2,1)_r$	949.1	950.4		$(1,0,0)_l$	920.9^{a}	922.3
	$(0,1,3)_r*^1$	1252.3	1251.8		$(1,0,2)_r$	1582.3^{ab}	1581.9
	$(1,0,1)_l*^1$	1261.3	1259.7		$(2,0,0)_l$	1840.0^{ab}	1838.3
	$(0,3,1)_r$	1313.2	1314.3		$(0,0,6)_r$	1880.2^{ab}	1882.6
	$(0,0,5)_r$	1595.8	1595.5		$(3,0,0)_l$	2798.4^{ab}	2798.7
	$(0,2,3)_r*^2$		1612.0	b_2 sym.	$(0,0,1)_r$		200.6
	$(1,1,1)_l*^2$		1628.4		$(0,1,1)_r$		553.8
	$(1,0,5)_r$	2754.7	2752.8				

^{a} Based on low resolution band-head measurement.
^{b} Not included in the fit.

The treatments of the centrifugal distortion coefficients used in this work follow the treatments developed by Hoy and Brand [70], which take into account the effect of the double-well on the centrifugal distortion coeffcients, but neglect other smaller anharmonic effects. This is likely the source of discrepancies between the observed and calculated values of some of the centrifugal distortion coefficients.

Table 8.7: Experimental and calculated rotational constants of $S^{16}O_2$. The experimentally derived rotational constants are given below the calculated values. Numbers below the vibrational assignments are the vibrational energy of that level. Values in bold face are included in our fit. Units in cm^{-1}. 2σ uncertainties are given for experimentally derived rotational constants. The meanings of C_{dp}, C_{Cor}, and C_p are defined in Section 8.2.

Assig.	A	B	C_{dp}	C_{Cor}	C_p
$(0,0,0)_r$	1.1505	0.3475	0.2658	0.0000	0.2658
0	**1.1505(1)**	**0.3475(1)**			0.2654(1)
$(0,0,1)_r$	1.1466	0.3447	0.2631	-0.0015	0.2616
213	**1.1474(16)**	**0.3444(5)**			0.2614(4)
$(0,1,0)_r$	1.1705	0.3460	0.2650	0.0013	0.2663
378	**1.1705(1)**	**0.3459(1)**			0.2658(1)
$(0,0,2)_r$	1.1447	0.3427	0.2614	-0.0168	0.2445
561	1.1443(4)	0.3429(1)	0.2615(1)		0.2457(1)
$(0,1,1)_r$	1.1672	0.3432	0.2623	0.0136	0.2759
582	1.1695(11)	0.3382(2)	0.2596(4)		0.2743(7)
$(0,2,0)_r$	1.1905	0.3443	0.2641	0.0025	0.2666
752	1.1914(1)	0.3443(1)			0.2657(1)
$(0,0,3)_r$	1.1424	0.3403	0.2594	-0.0105	0.2488
891	1.1432(19)	0.3405(5)	0.2595(10)		0.2498(4)
$(0,1,2)_r$	1.1659	0.3413	0.2607	-0.0290	0.2317
932	1.1627(3)	0.3359(3)	0.2574(5)		0.242(4)

Continued on next page

Table 8.7– *continued from previous page*

Assig.	A	B	C_{dp}	C_{Cor}	C_p
$(0,2,1)_r$	1.1877	0.3416	0.2615	0.0334	0.2949
949	1.1908(17)	0.3430(6)	0.2625(13)		0.2906(6)
$(1,0,0)_l$	1.1485	0.3444	0.2637	0.0008	0.2645
961	**1.1480(2)**	**0.3456(1)**	0.2643(2)		0.266(16)
$(0,3,0)_r$	1.211	0.3426	0.2632	0.0034	0.2666
1122	1.209(12)	0.3419(24)			0.2650(21)
$(0,0,4)_r$	1.1412	0.3383	0.2578	-0.0856	0.1722
1245	1.1389(16)	0.3398(5)	0.2586(9)		0.2008(18)
$(0,1,3)_r$	1.1581	0.3395	0.2592	0.0655	0.3246
1252	1.1670(30)	0.3404(6)	0.2601(11)		0.2926(20)
$(1,0,1)_l$	1.1488	0.3404	0.2597	-0.0031	0.2566
1261	1.1462(12)	0.3420(3)			0.2558(2)
$(0,2,2)_r$	1.187	0.3399	0.2601	-0.0530	0.2071
1300	1.1861(98)	0.3365(11)	0.2580(22)		0.2069(23)
$(0,3,1)_r$	1.2084	0.3400	0.2607	0.0643	0.3250
1313	1.2140(25)	0.3390(9)	0.2604(17)		0.3188(14)
$(1,1,0)_l$	1.169	0.3428	0.2628	0.0047	0.2675
1338	1.182(26)	0.3433(24)			0.2685(10)
$(0,0,5)_r$	1.1414	0.3361	0.2561	-0.0425	0.2137
1596	1.1399(27)	0.3384(8)	0.2574(17)		0.2128(10)
$(0,1,4)_r$	1.163	0.3368	0.2571	-0.1147	0.1444
1604	1.161(26)	0.3400(25)	0.2588(50)		0.1795(11)
$(0,2,3)_r$	1.1815	0.3377	0.2582	0.1269	0.3851
1612 [a]	1.1879[b]	0.3388[b]	0.2600[b]		

[a] Not directly observed. Band-origin calculated from the fit.

[b] Constrained in the rotational fit [131].

Table 8.8: Observed [62] and calculated rotational constants of $S^{18}O_2$. 2σ Uncertainties are given for the experimentally derived values.

Assig.	A	B	C
$(0,0,0)_r$	1.0862	0.3089	0.2396
	1.0863(2)	0.3089(1)	0.2392(1)[a]
$(0,1,0)_r$	1.1039	0.3076	0.2399
	1.1038(1)	0.3077(1)	0.2391(1)[a]

[a] Not included in the fit.

Table 8.9: Observed [62] and calculated quartic centrifugal distortion coefficients for the zero-point levels of $S^{16}O_2$ and $S^{18}O_2$, using Watson's A reduction in the I^r representation. 3σ uncertainties are given for the experimentally derived values. Units in cm^{-1}.

	$S^{16}O_2$		$S^{18}O_2$	
	Obs.	Cal.	Obs.	Cal.
$10^7\Delta_J$	4.98(77)	4.44	4.07(11)	3.55
$10^7\Delta_{JK}$	129.2(60)	136.0	113.7(23)	115.8
$10^7\Delta_K$	73.8(103)	55.8	75.0(125)	55.7
$10^7\delta_J$	1.60(52)	1.53	1.40(9)	1.18
$10^7\delta_K$	84.0(26)	92.8	78.4(30)	79.1

As in the 2D fit, the C_s equilibrium geometry is determined (Table 8.11). The C_s geometry agrees well with *ab initio* values [118]. Recall that we constrained only the barrier height, b, and the shape parameter, ρ, to be isotopologue-independent. Even though we did not constrain the isotopologue independence of the absolute minimum geometry, the calculated minimum geometries given in Table 8.11 for $S^{16}O_2$ and $S^{18}O_2$ agree well with each other, which attests to the isotopologue independence of the PES. Note that the barrier height derived from our 3D fit differs by more than 10% from the 2D value (compare the values of b in Table 8.1 and 8.4). Without the ability to vary the shape parameter, ρ, the value of which is highly correlated with the barrier height, it is difficult to evaluate the accuracy of our derived barrier height.

Experimental observables not included in the fit are well reproduced using our force field (see Tables 8.5, 8.7, and 8.10). For the nine vibrational levels in the 3000-4000 cm^{-1} region, which we do not include in our fit, the rms error between

Table 8.10: Calculated and experimentally-determined [131] c-axis Coriolis matrix elements, t_1 (in cm^{-1} units). The harmonic predictions (reproduced from Table X of Ref [131]) are also listed for comparison. Values in parentheses are the 2σ uncertainty of the final significant digitis.

	Expt.	Cal.	Harmonic
$(0,1,1)_r$-$(0,0,2)_r$	0.2978(7)	0.3040	0.3819
$(0,0,3)_r$-$(0,1,2)_r$	0.3250(89)	0.3216	0.4677
$(0,2,1)_r$-$(0,1,2)_r$	0.3532(44)	0.4357	0.5401
$(0,1,3)_r$-$(0,0,4)_r$	0.3463(14)	0.3211	0.5401
$(0,1,3)_r$-$(0,2,2)_r$	0.4528(99)	0.3961	0.6614
$(0,3,1)_r$-$(0,2,2)_r$	0.4764(42)	0.5373	0.6614
$(0,0,5)_r$-$(0,1,4)_r$	0.2957(35)	0.3134	0.6038
$(0,2,3)_r$-$(0,1,4)_r$	0.5187(75)	0.5161	0.7638

Table 8.11: C_s equilibrium geometry obtained in the 3D fit. The number in parentheses after the θ value reflects the difference between the derived value of θ at the minima of the PES of the two isotopologues used in this study. The geometry derived from our 2D fit is reproduced here for comparison.

	3D fit	*ab initio* [118]	2D fit
$r_1/\text{Å}$	1.639	1.633	1.642
$r_2/\text{Å}$	1.494	1.488	1.494
θ/deg	103.95(1)	103.3	103.80

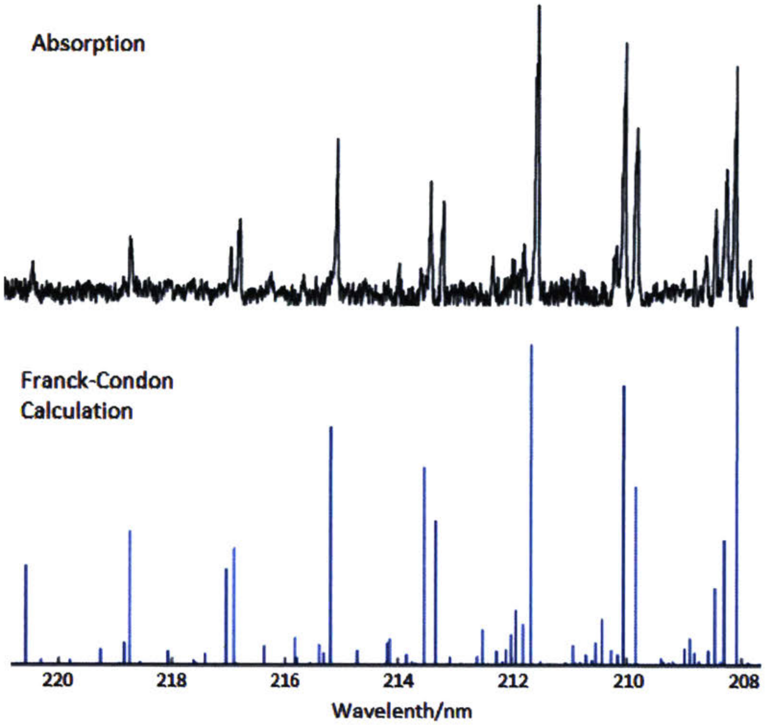

Figure 8-4: Comparison of anharmonic Franck-Condon factors, calculated from the internal coordinate force field, with the low-resolution absorption spectrum (jet-cooled condition) in the 208-221 nm region. The experimental spectrum is adapted and reproduced with permission from Chem. Phys. Lett. **294**, 571 (1998). Copyright 1998 Elsevier. Even though none of the levels in the region with wavelength shorter than 220 nm are included directly in our fit, the calculated Franck-Condon intensities in this energy region agree well with the observed intensity pattern.

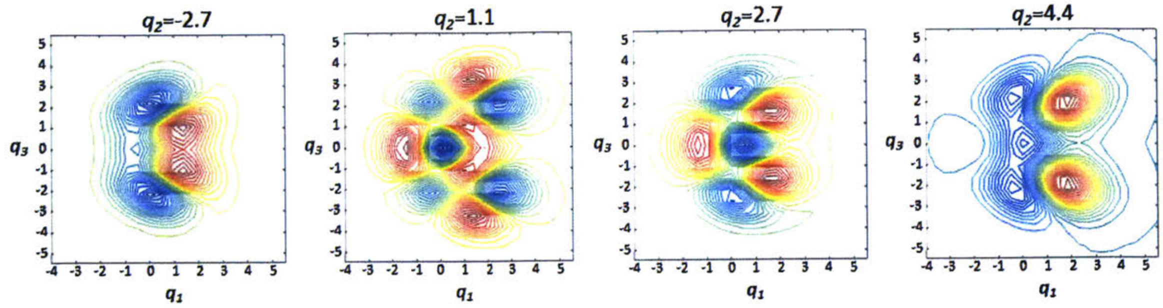

Figure 8-5: Projections of the wavefunction of the 2394 cm^{-1} state onto the q_1–q_3 plane at different values of q_2. The wavefunction is obtained directly from DVR calculations, using the force constants derived from the 3D fit.

the calculated and the observed terms is 5 cm^{-1} (rms=3.5 cm^{-1}, if we exclude the 3887.7 cm^{-1} level). The Franck-Condon factors calculated from our force field also agree well with the observed intensity pattern in the absorption [52, 137, 139] and LIF [182] spectra. As shown in Fig. 8-4, despite the fact that we have not input to the fit any of the vibrational term energies of levels with transition wavelength shorter than 220 nm (corresponding to levels >3000 cm^{-1} above the $\tilde{\text{C}}$ state zero-point level), the calculated Franck-Condon intensities in this energy region agree well with the observed intensity patterns. The rotational constants that are not included in the fit (Table 8.7) and the Coriolis matrix elements between highly anharmonic $\tilde{\text{C}}$ state vibrational levels (Table 8.10) are also well reproduced from our force field (see detailed discussions in Section 8.4.4).

8.4.1 Vibrational Assignment Scheme

How are the eigenstates from the 3D fit assigned? In the 2D case, Kellman-type vibrational assignments can be made easily based on visual inspection of the wavefunction, but visual assignment of the three-dimensional eigenstates is more challenging. Figure 8-5 illustrates the projections of the wavefunction of the 2394 cm^{-1} state onto the q_1–q_3 plane at different values of q_2. If the ν_2 bending mode is rigorously separable from the stretching modes, the projection of the wavefunction should be independent of the value of q_2 (although the relative amplitude of each projection will depend on q_2, e.g. it will be small when the value of q_2 is near a node of the wavefunction along

q_2 direction). This is, however, obviously not the case, as can be seen in Fig. 8-5. Depending on which projection of the wavefunction we choose to look at, different Kellman-type vibrational assignments can be made. If we only consider basis states that are close in energy to the observed eigenstate, at $q_2 = 1.1$, the wavefunction could be assigned as $(1,0,4)_r$, which is predicted by our 2D model to occur at 2372 cm^{-1}. However, at q_2=2.7, the nodal pattern of the projection suggests v_α=1 and v_β=2, consistent with an assignment $(1,2,2)_r$. The eigenstate in Fig. 8-5 most likely contains contributions from both Kellman-type basis states. Therefore, we conclude that the separability of ν_2 is not rigorous above 2000 cm^{-1}, and assignment schemes based on visual inspection of the 3D wavefunctions will be impractical.

To quantify the contributions from different Kellman-type basis states to each vibrational eigenstate, we transform our complete normal-mode Hamiltonian defined in Eq. (8.1) into a Hamiltonian in a new Kellman basis. The new basis takes into account the two most prominent vibrational features of the $\tilde{\mathrm{C}}$ state, i.e. strong interactions between ν_1 and ν_3 and a double-well in the q_3 coordinate. The bending mode ν_2 is completely separable from the two stretching modes in the Kellman basis. In this work, the Kellman basis states are constructed via *partial diagonalization* of the original normal-mode Hamiltonian. Specifically, all the terms in Table 8.4 that involve interaction between ν_2 and the other two modes are set to zero (e.g. ϕ_{233}, ϕ_{122}, ϕ_{2233} etc.), which results in a new Hamiltonian, H_t. A basis transformation, V_t, between the harmonic basis states and our Kellman basis states is obtained by diagonalizing H_t. The transformed Hamiltonian in the Kellman basis, H_K, is given by

$$H_K = V_t^{-1} H V_t, \tag{8.9}$$

where H is the original Hamiltonian expressed in the harmonic basis. The ϕ_{222} and ϕ_{2222} terms are not set to zero in H_t, thus the intra-mode anharmonicity in ν_2 is partially accounted for in our new basis set. Since ν_2 is rigorously uncoupled from the other modes in this basis, we can easily assign *definite* quantum numbers, $(v_\alpha, v_2, v_\beta)_{l/r}$, similarly defined as in Section 8.3.1, to the new basis states by visual inspection of each basis state wavefunction. Projections of the Kellman basis state wavefunctions onto the q_1–q_3 plane are qualitatively similar to those shown in Fig. 8-2, and the quantum number, v_2, is obtained by counting the number of nodes along the q_2 coordinate. By diagonalizing the transformed Hamiltonian, we obtain the composition of each eigenstate as a linear combination of Kellman basis states.

Using this two-step diagonalization method, the 2394 cm^{-1} state has the following basis composition

$$\begin{aligned}|2394\ \mathrm{cm}^{-1}\rangle = &\{0.8|\mathbf{1,0,4}\rangle_{\mathbf{r}} + 0.2\,|1,1,4\rangle_r\}\\ &- \{-0.05\,|1,1,2\rangle_r + 0.4|\mathbf{1,2,2}\rangle_{\mathbf{r}} + 0.2\,|1,3,2\rangle_r\}\\ &+ 0.2\,|0,1,6\rangle_r + 0.1\,|2,1,0\rangle_l + \cdots \end{aligned} \tag{8.10}$$

Equation (8.10) shows that the 2394 cm^{-1} state consists primarily of the Kellman $|1,0,4\rangle_r$ state, with an additional contribution from $|1,2,2\rangle_r$, in agreement with the result of visual deperturbation described earlier. Throughout this work, we use quantum numbers enclosed in parentheses, i.e. $(v_\alpha, v_2, v_\beta)_{r/l}$, to denote the vibrational assignment of an eigenstate (based on the dominant vibrational character of the state), and we reserve kets, i.e. $|v_\alpha, v_2, v_\beta\rangle_{r/l}$, to denote basis states. Occasionally, as in Eq. (8.10), kets with the vibrational term energy of the state are also used to describe eigenstates. The presence of the $|1,1,4\rangle_r$ and $|1,3,2\rangle_r$ basis states in the composition of the 2394 cm^{-1} eigenstate indicates large *intra-mode* anharmonicity in ν_2. Recall that *intra-mode* anharmonicity in ν_2 has already been partially accounted for in our Kellman basis by the inclusion of ϕ_{222} and ϕ_{2222} terms in H_t. However, additional contributions to ν_2 anharmonicity arise from other terms omitted from H_t, such as ϕ_{112}, ϕ_{233}, etc. The basis states enclosed within each pair of curly brackets in Eq. (8.10) can be considered collectively as an *anharmonic* Kellman state, (e.g. $0.8\,|1,0,4\rangle_r + 0.2\,|1,1,4\rangle_r$ as an *anharmonic* $|1,0,4\rangle_r$ state, which we label as $\mathcal{A}\,|1,0,4\rangle_r$, and $-0.05\,|1,1,2\rangle_r + 0.4\,|1,2,2\rangle_r + 0.2\,|1,3,2\rangle_r$ as $\mathcal{A}\,|1,2,2\rangle_r$), just as a Morse-oscillator eigenstate can be expressed as a linear combination of normal-mode basis states. Therefore, the 2394 cm^{-1} state is largely a linear combination of anharmonic $\mathcal{A}\,|1,0,4\rangle_r$ and $\mathcal{A}\,|1,2,2\rangle_r$ states, with some small contributions from two other states from the second line of Eq. (8.10). The projections of $\mathcal{A}\,|1,0,4\rangle_r$ onto the q_1-q_3 plane clearly remain unchanged from those of the original Kellman $|1,0,4\rangle_r$ basis, since they only involve contributions from progressions in ν_2. In addition, for $\mathcal{A}\,|1,0,4\rangle_r$, the original Kellman basis states within each pair of curly brackets have the correct relative phases and magnitudes such that the number of nodes along the q_2 direction is zero, despite contribution from $|1,1,4\rangle_r$. This can be verified by inspecting the wavefunction of the *anharmonic* state. A similar argument applies to $\mathcal{A}\,|1,2,2\rangle_r$. Thus, in $\mathcal{A}\,|v_\alpha, v_2, v_\beta\rangle_r$, v_2 should be taken as an *anharmonic* quantum number, while the meanings of v_α and v_β remain unchanged from those of the original Kellman basis. *Intra-mode* anharmonicity becomes larger for states with more quanta of excitation in ν_2 (compare the partitioning of states in the first and second pair of curly brackets in Eq. (8.10)). This is not surprising given that the size of the ϕ_{112} and ϕ_{233} matrix elements, which connect different Kellman basis states that differ by one quantum of ν_2, increase as the quantum number increases.

We must also point out that for the 2394 cm^{-1} state, the direct interaction matrix element between the $|1,0,4\rangle_r$ and $|1,2,2\rangle_r$ states in the transformed Hamiltonian is small (1 cm^{-1}) compared to the energy difference of the two basis states ($\sim$13 cm^{-1}). This means, in order to obtain the mixing coefficients in Eq. (8.10), there must be an additional strong indirect interaction path between the $|1,0,4\rangle_r$ and $|1,2,2\rangle_r$ states. In fact, $|1,1,4\rangle_r$ and $|1,3,2\rangle_r$ states act as the dominant intermediate states of the indirect coupling. For example, anharmonicity in ν_2 connects $|1,0,4\rangle_r$ with $|1,1,4\rangle_r$. The matrix element between $|1,1,4\rangle_r$ and $|1,2,2\rangle_r$, 44 cm^{-1}, has appreciable magnitude. As a result, the $|1,0,4\rangle_r$ and $|1,2,2\rangle_r$ states interact indirectly via $|1,1,4\rangle_r$ and similarly via $|1,3,2\rangle_r$, or to put it in another way, the anharmonic $\mathcal{A}\,|1,0,4\rangle_r$ and $\mathcal{A}\,|1,2,2\rangle_r$ states, which have a larger effective matrix element, interact directly to give rise to the eigenstate at 2394 cm^{-1}.

Figure 8-6 displays the basis state distributions of the eigenstate at 2394 cm^{-1} in both normal-mode and Kellman-mode representations. In the normal-mode representation shown on the left, basis states within each color-coded cluster belong to one

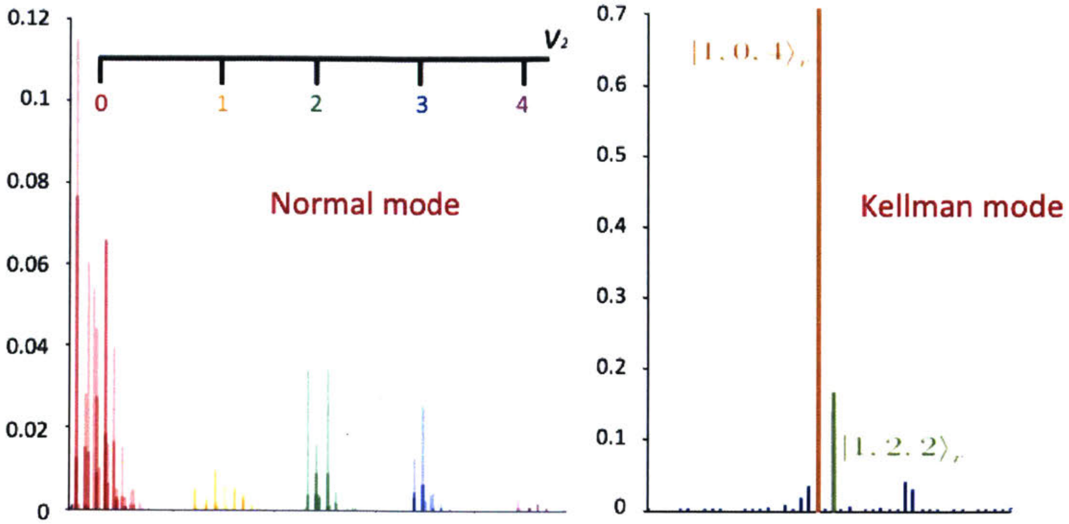

Figure 8-6: Basis state distribution of the eigenstate at 2394 cm^{-1} in normal-mode (left panel) and Kellman-mode (right panel) representations. The vertical axis represents the squares of the coefficient of a specific basis state. (See text for an explanation of the ordering of states in the normal-mode representations.)

value of v_2 (color-coded accordingly), and within each cluster, basis states are ordered according to quantum number v_1 followed by v_3. That means the first cluster contains harmonic basis states with $v_2 = 0$ arranged in the order of $(|0,0,0\rangle, |0,0,2\rangle ...)$, $(|1,0,0\rangle, |1,0,2\rangle ...)$, $(|2,0,0\rangle, |2,0,2\rangle ...)$. It is clear that the eigenstate character is more broadly distributed among basis states in the normal-mode representation than in the Kellman-mode representation. While it is impossible to identify a dominant basis state in the normal-mode representation, using the Kellman-mode representation, we are immediately able to identify the presence of two dominant basis states in the composition of the eigenstate.

In Ref [139], the vibrational eigenstates of the $\tilde{\mathrm{C}}$ state were assigned based on visual inspection of the nodal patterns of the integrated 3D vibrational wavefunctions in the $q_1 - q_3$ plane. The effects from the stretch-bend couplings were averaged over q_2 in their assignment scheme. The 2394 cm^{-1} state was assigned as a pure Kellman-type $(1,0,4)_r$ state (translated into our notation). While this assignment is nominally correct, our analysis clearly shows that the 2394 cm^{-1} state also has appreciable $|1,2,2\rangle_r$ character. Vibrational assignment based on visual inspection

Table 8.12: Estimated vibrational term energies and Franck-Condon factors (fc), relative to the (0,0) transition, for three states near 2750 cm^{-1}, calculated from the 2D internal force field.

Assig.	$\mathrm{E/cm}^{-1}$	fc
$(2,0,2)_r$	2728	26
$(1,1,4)_r$	2750	41
$(1,3,2)_r$	2785	10

of the integrated wavefunction is flawed due to anharmonic interactions involving ν_2. In contrast, we must emphasize that the vibrational character of each eigenstate can be unambiguously identified in our work from the eigenstate composition of the transformed Hamiltonian in the Kellman basis.

8.4.2 Franck-Condon Interference Effects

Our 2D internal force field, discussed in Section 8.3, provides the first evidence of Franck-Condon interference effects in the $\tilde{\mathrm{C}}$ state of SO_2. Before presenting a more quantitative demonstration of the interference effects based on our 3D force field, we first give a brief discussion of the result from our 2D model. Using a constant ω_2 frequency of 378 cm^{-1}, our 2D force field predicts three states, $(1,1,4)_r$, $(2,0,2)_r$ and $(1,3,2)_r$, near 2750 cm^{-1}, based on the calculated vibrational term energies of the corresponding states with $v_2 = 0$ in Table 8.2, e.g. $(1,0,2)_r$ is predicted at 1651 cm^{-1}, which puts $(1,3,2)_r$ at 2785 cm^{-1}. Given the calculated Franck-Condon intensities into the three corresponding $v_2 = 0$ levels from the 2D force field (see Fig. 8-2) and the observed $(0, v_2, 0)$ Franck-Condon progression [52, 137, 182], relative Franck-Condon factors can be estimated for $(1,1,4)_r$, $(2,0,2)_r$ and $(1,3,2)_r$. As can be seen from Table 8.12, all of the three close-lying levels obtained from the model have large Franck-Condon factors. However, there is only one strong transtion observed in this energy region at 2762 cm^{-1} [182]. Our Franck-Condon calculation, based on our 3D force field, also predicts only one strong transition in this energy region, along with two other much weaker transitions. Therefore, there must be interactions among the three Kellman-type levels. The interactions are capable of mixing levels that have different quanta of excitation in ν_2, and they are sufficiently strong to cause nearly complete annihilation of the Franck-Condon intensities to two of the three states.

Using our transformed Hamiltonian in the Kellman basis, the interference effect can be analyzed in more detail based on our 3D internal force field. The three eigenstates of interest have the following Kellman basis composition:

$$\begin{aligned}
|2729\ \mathrm{cm}^{-1}\rangle = {} & \{-0.2|1,0,4\rangle_r + 0.5|\mathbf{1},\mathbf{1},\mathbf{4}\rangle_{\mathbf{r}} + 0.3|1,2,4\rangle_r\} \\
& + \{0.4|\mathbf{2},\mathbf{0},\mathbf{2}\rangle_{\mathbf{r}} + 0.1|2,1,2\rangle_r\} \\
& - \{-0.3\,|1,2,2\rangle_r + 0.4|\mathbf{1},\mathbf{3},\mathbf{2}\rangle_{\mathbf{r}} + 0.2\,|1,4,2\rangle\} + \cdots \\
|2744\ \mathrm{cm}^{-1}\rangle = {} & \{-0.06\,|1,0,4\rangle_r + 0.2|\mathbf{1},\mathbf{1},\mathbf{4}\rangle_{\mathbf{r}} + 0.01|1,2,4\rangle_r\} \\
& + \{0.6|\mathbf{2},\mathbf{0},\mathbf{2}\rangle_{\mathbf{r}} + 0.2\,|2,1,2\rangle_r\} \\
& + \{-0.2\,|1,2,2\rangle_r + 0.5|\mathbf{1},\mathbf{3},\mathbf{2}\rangle_{\mathbf{r}} + 0.3\,|1,4,2\rangle\} + \cdots \\
|2762\ \mathrm{cm}^{-1}\rangle = {} & \{-0.2\,|1,0,4\rangle_r + 0.6|\mathbf{1},\mathbf{1},\mathbf{4}\rangle_{\mathbf{r}} + 0.2\,|1,2,4\rangle_r\} \\
& - \{0.6|\mathbf{2},\mathbf{0},\mathbf{2}\rangle_{\mathbf{r}} + 0.1|2,1,2\rangle_r\} \\
& + \{-0.02|1,2,2\rangle_r + 0.3|\mathbf{1},\mathbf{3},\mathbf{2}\rangle_{\mathbf{r}} + 0.2|1,4,2\rangle_r\} + \cdots
\end{aligned} \tag{8.11}$$

As in Eq. (8.10), basis states enclosed in each pair of curly brackets can be considered collectively as an *anharmonic* state. The anharmonic $\mathcal{A}\,|1,1,4\rangle_r$, $\mathcal{A}\,|2,0,2\rangle_r$, and $\mathcal{A}\,|1,3,2\rangle_r$ states account for about 90% of the total composition of the three eigenstates in Eq. (8.11). Note that basis states in each pair of curly brackets have consistent relative phases and approximately consistent amplitudes such that the *anharmonic* ν_2 quantum number is meaningful. Given that the 2762 cm^{-1} state predominantly consists of Kellman basis states with $v_2 = 0$ or 1, the widely-adopted assignment of the 2762 cm^{-1} state as a normal-mode (1,3,2) level [20, 181, 182], based on an apparent $(1, n, 2)$ progression, is *incorrect*, even when we interpret the assignment as Kellman $(1,3,2)_r$.

To demonstrate the interference effect on the Franck-Condon intensities of the three eigenstates in Eq. (8.11), we consider only the three anharmonic states, $\mathcal{A}\,|1,1,4\rangle_r$,

Table 8.13: Franck-Condon factors, relative to that of the (0,0) transition, calculated from the three-state interaction model described in the text. The contributions from each *anharmonic* Kellman state to the vibrational overlap integral of the three eigenstate wavefunctions with the $\tilde{X}$ state zero-point level are calculated using the three-state model, and the results are listed in columns 2-4. Vibrational overlap integrals and Franck-Condon factors of the three 'eigenstates' in the three-state interaction model are then calculated and listed respectively in the overlap and fc_{model} column. Franck-Condon factors for the actual eigenstates calculated from a full 3D calculation are listed in the fc column for comparison. Note that, experimentally, transitions into the 2762 cm^{-1} level are about 200-300 times stronger than transitions into the 2743 cm^{-1} level (see Fig. 5 in Ref [133]). The 2730 cm^{-1} level has not been experimentally observed.

	$\mathcal{A}\|1,1,4\rangle_r$	$\mathcal{A}\|2,0,2\rangle_r$	$\mathcal{A}\|1,3,2\rangle_r$	overlap	fc_{model}	fc
$\|2730\ \text{cm}^{-1}\rangle$	3.1	-2.1	-0.8	0.2	0.04	0.5
$\|2743\ \text{cm}^{-1}\rangle$	-0.4	3.4	-1.6	1.4	1.9	0.4
$\|2762\ \text{cm}^{-1}\rangle$	3.3	2.6	1.2	7.1	50	82

$\mathcal{A}|2,0,2\rangle_r$, and $\mathcal{A}|1,3,2\rangle_r$. The contribution from each anharmonic Kellman state to the vibrational overlap integral of an eigenstate in Eq. (8.11) with the $\tilde{X}$ state zero-point wavefunction is calculated, using the basis transformation matrix, V_t, in Eq. (8.9). Franck-Condon factors for each 'eigenstate' in the three-state interaction model can then be calculated and these are summarized in Table 8.13. Our three-state model indeed reproduces the experimental observation that there is only one strong transition at 2762 cm^{-1}. Vibrational overlap integrals of the three anharmonic states combine constructively for the 2762 cm^{-1} eigenstate, but almost perfectly cancel for the other two eigenstates. This causes near-annihilation of Franck-Condon intensity in two of the three states and an enhancement for the third state. Such Franck-Condon interference effects are prevalent for vibrational levels above 2500 cm^{-1}. This indicates a serious breakdown of the assumption of separability of the bending motion from the other two strongly interacting motions, especially for states above 2500 cm^{-1}. The Kellman basis states are no longer sufficient to describe the dynamics in this energy region. Interference effects like these suggest the emergence of a new class of zero-order state. Decoding the new dynamics poses an interesting challenge for future work. In Tables 8.5 and 8.6, we label the eigenstates according to the degree of interaction in the Kellman basis. For some of the levels, no vibrational assignment can be given, since none of the *anharmonic* Kellman basis states has greater than 50% of the character of the eigenstate.

8.4.3 Rotational Information and Vibrational Assignments

Many of our vibrational assignments are confirmed by the magnitude of the experimental rotational constants, especially the A rotational constants. The A constant increases by $\sim$0.02 cm^{-1} per quantum of excitation of the bending mode, compared to $\sim$0.003 cm^{-1} for ν_1 and ν_3. Thus, the number of quanta in ν_2 can be estimated qualitatively from $v_2 \approx (A_v - A_0)/(0.02\text{ cm}^{-1})$, where A_0=1.1505 cm^{-1} is the A constant of the $\tilde{\text{C}}$ state $(0,0,0)_r$ level. Here, we demonstrate the use of rotational information to provide an additional check on the vibrational assignment of the 2762 cm^{-1} level, which is discussed in Section 8.4.2.

The level at 2762 cm^{-1} is rotationally perturbed by strong c-axis Coriolis interactions with nearby b_2 vibrational levels, leading to large uncertainties in the effective rotational constants. For example, the effective A constant of the 2762 cm^{-1} level is 1.186 ± 0.044 cm^{-1} (2σ uncertainty). This uncertainty is sufficiently large that it precludes determination of the number of quanta of excitation in ν_2. Recently, we implemented a coherence-converted population transfer in a sensitive, background-free scheme for millimeter-wave optical double resonance (CCPT-MODR) [133, 165] to probe the vibrational levels near the 2762 cm^{-1} state, including one dark b_2 symmetry level, which borrows intensity via the Coriolis interaction. We assigned 16 rotational levels of the dark b_2 symmetry level (as well as many additional rotational levels of the 2762 cm^{-1} state and 4 rotational levels of an a_1 symmetry level at 2743 cm^{-1}). This allowed us to deperturb the Coriolis interactions among the three observed vibrational states. The deperturbed A rotational constant of the 2762 cm^{-1} level is 1.169(7) cm^{-1}, which indicates that this level effectively has approximately one quantum of excitation in ν_2, in agreement with our analysis in Section 8.4.2 indicating that the 2762 cm^{-1} level is predominatly a linear combination of $\mathcal{A}\left|1,1,4\right\rangle_r$ and $\mathcal{A}\left|2,0,2\right\rangle_r$, with a smaller contribution from $\mathcal{A}\left|1,3,2\right\rangle_r$. The magnitude of the newly derived A constant helps us to rule out the original vibrational assignment of this state as (1,3,2) [20, 181, 182], which should have an A constant close to 1.20 cm^{-1}.

We can compare the rotational constants of the three states studied in the CCPT-MODR experiments to our calculated rotational constants (see Table 8.14). Note that the three states are labeled according to the notations used in our CCPT-MODR paper on the $\tilde{\mathrm{C}}$ state [133], where the label 'B' is given for the Franck-Condon bright state at 2762 cm^{-1} and 'P' for the two Franck-Condon dark perturbing eigenstates. The subscripts indicate the vibrational symmetry of the levels. The calculated A constant for the 2762 cm^{-1} ($\mathrm{B}_{\mathrm{a}_1}$) level in Table VII falls very close to the 2σ uncertainty of the experimentally derived value, which supports the accuracy of our eigenstate expansion. The experimental and calculated A constants for the 2753 cm^{-1} ($\mathrm{P}_{\mathrm{b}_2}$) level suggest v_2=0, consistent with the vibrational assignment $(1,0,5)_r$.

Note that only the first eight b_2 vibrational symmetry levels have been experimentally observed in the IR-UV double resonance experiment [131]. This means that there is a large energy gap between the last observed b_2 level at 1595 cm^{-1} and this level at 2753 cm^{-1}. However, we believe that we match the eigenstate correctly because, according to our calculation, there are only four b_2 symmetry levels between 2700 cm^{-1} and 2800 cm^{-1}, and only one of these has no excitation in ν_2. The other three levels have at least two quanta in ν_2. Using this eigenstate assignment, the calculated Coriolis matrix element, t_1, between the $\mathrm{B}_{\mathrm{a}_1}$ and $\mathrm{P}_{\mathrm{b}_2}$ levels in Table 8.14 agrees with the experimental value. The assignment of the other a_1 level at 2743 cm^{-1} is less certain, given that there are two calculated a_1 levels in the small energy region, 2740–2745 cm^{-1}. In addition, only four rotational term energies belonging to this level have been observed [133], resulting in large uncertainty in its molecular constants. However, the $\mathrm{P}_{\mathrm{a}_1}$ level most likely corresponds to the calculated level at 2744.5 cm^{-1} in Table 8.5 because, using this assignment, the calculated value of the Coriolis matrix element is in better agreement with the experimental value. In addition, the experimental A rotational constant of the $\mathrm{P}_{\mathrm{a}_1}$ level, although not precisely determined, indicates moderate excitation in ν_2, allowing us to rule out the $(0,6,2)_r$

Table 8.14: Calculated (A_c) and experimentally derived (A_o) rotational A constants and Coriolis matrix elements of three states near 2762 cm^{-1} observed in MODR study. For convenience, each state is given the label assigned in Ref [133].

E/cm^{-1}	Assig.	A_o/cm^{-1} [132]	A_c/cm^{-1}
B_{a_1} 2762		1.169(7)	1.159
P_{b_2} 2753	$(1,0,5)_r$	1.1410(10)	1.1388
P_{a_1} 2743		1.09(10)	1.18
	Exp./cm^{-1}	Cal./cm^{-1}	
$t_1(B_{a_1}, P_{b_2})$	0.43(4)	0.45	
$t_1(P_{b_2}, P_{a_1})$	0.15(4)	0.19	

level predicted at 2741 cm^{-1} (Table 8.5), which has substantial excitation in ν_2. However, due to ambiguity in eigenstate assignment for the observed state at 2743 cm^{-1}, the observed P_{a_1} level in Table 8.14 is not included in our fit.

Above 3000 cm^{-1}, very few vibrational levels of the $\tilde{C}$ state have been observed in the high-resolution LIF study from Yamanouchi et al. [182], because of predissociation. Moreover, vibrational level density in the 3000–4000 cm^{-1} region is twice that between 2000–3000 cm^{-1}. However, we believe that the vibrational assignments that are listed for the nine observed levels between 3000–4000 cm^{-1} (Table 8.5) are correct, because the assigned v_2 quantum numbers of those levels are consistent with the magnitudes of the experimental A rotational constants. We emphasize that the assignment scheme developed in this work provides unambiguous vibrational assignments to an unprecedented number of the $\tilde{C}$ state levels, all consistent with available rotational information.

8.4.4 The Coriolis Effects in the $\tilde{C}$ state of SO_2

As recognized in earlier studies of the SO_2 $\tilde{C}$ state [22, 62, 70, 182], the C rotational constants are severely perturbed by c-axis Coriolis interactions between ν_2 and ν_3 (more precisely, ν_β, due to Fermi-133 resonance). However, accurate deperturbation had been impossible until the recent direct observation of b_2 vibrational levels [131, 133]. In this section, we present level-specific Coriolis interaction strengths derived from our force field, and we analyze how the double-well structure of the PES leads to specific diagnostic patterns of Coriolis interactions in the $\tilde{\mathrm{C}}$ state.

First, we discuss the calculated rotational constants in Table 8.7, in particular the C rotational constants. The Coriolis contributions to the values of the Coriolis-*perturbed* C rotational constants are listed in the C_{Cor} column of Table 8.7. It is obvious that Coriolis contributions are significant (in some cases, 50% contribution) to the values of the C constants of the majority of vibrational levels. In addition, the sign of the Coriolis contribution indicates the relative locations of the interacting states [62, 70, 182]. A positive (negative) Coriolis contribution to the C constant indicates that an interacting level lies below (above) the level of interest. The calculated C_p constants agree well with the experimentally derived ones, except in the case of a few close-lying Coriolis-interacting pairs of levels. For example, the calculated C constants for the $(0,0,4)_r$, and $(0,1,3)_r$ levels, whose vibrational origins are separated by only 7 cm^{-1}, differ from the experimentally derived values by 0.03 cm^{-1}. Note that the Coriolis contribution to the C constants of these strongly perturbed levels is about 30–40%. It is not surprising that our nondegenerate perturbation treatment of the Coriolis interactions (Eq. (8.6)) fails for those close-lying levels.

The calculated A, B, and C_{dp} rotational constants, and the Coriolis matrix elements between vibrational levels calculated from Eq. (8.8) (Table 8.10), can be compared directly with deperturbed rotational constants and Coriolis matrix elements reported in the first paper of this series [131]. For some levels, deperturbed C constants are not available from the experiment, because the Coriolis-interacting states are distant in energy and Coriolis deperturbation is not possible without observations of high-J levels. The agreement between the experiment and our calculation is good for most cases, considering that it is unclear whether the experimentally derived values are fully deperturbed. (Due to lack of high-J data points for most of the observed vibrational levels, approximations must be made in the Coriolis fit [131], in order to reduce correlations among the fit parameters. However, the general agreement between the experimental and calculated values supports the validity of these approximations.) As can be seen in Table 8.10, the calculated and experimental Coriolis matrix elements are both smaller than the harmonic predictions by ~20-50%. In the first part of this series [131], this decrease in the effective Coriolis interactions is explained in terms of anharmonic effects (Fermi-133 and Darling-Dennison-1133). Our calculated Coriolis matrix elements, which explicitly take into account anharmonic effects in the $\tilde{C}$ state vibrational levels, successfully reproduce this decrease in the effective Coriolis interactions due to anharmonic interactions.

Just as Fermi-133 resonance is unusual in symmetric triatomic molecules, strong Coriolis mixing between the bending (ν_2) and antisymmetric stretching (ν_3) modes is also unusual, because the ν_2 and ν_3 modes are not typically close in frequency. These resonances occur in the $\tilde{C}$ state of SO_2 because the double-well dramatically depresses the effective ν_3 frequency. To demonstrate the structure of Coriolis interactions in the $\tilde{C}$ state of SO_2, the rotationless Coriolis mixing angles between the two states in question, defined as $|\frac{t_1}{\Delta E}|$, where ΔE is the energy difference between the band-origins of the two states, are displayed in Fig. 8-7. The mixing angles, which measure the extent of Coriolis interactions, are taken to be positive and are color-coded in Fig. 8-7. In the absence of indirect higher-order interaction, a_1 vibrational symmetry levels interact only with b_2 symmetry levels via Coriolis interaction.

In Fig. 8-7, Coriolis-interacting states are grouped together to indicate that they form a Coriolis polyad (designated by a polyad label, P_n, where $n = v_2 + v_\beta$). Vibrational levels within each Coriolis polyad interact strongly, while inter-polyad interactions are much weaker. Note that even if our assignments are based on Kellman's semiclassical assignment scheme, the selection rule for Coriolis interactions appears to be very similar in form to the harmonic selection rule. In the harmonic case, when ν_2 and ν_3 have similar frequencies, $(0, v_2, v_3-1)$ and $(0, v_2+1, v_3)$ are a pair of Coriolis interacting states, while in our assignment scheme, $(0, v_2, v_\beta - 1)_r$ and $(0, v_2 + 1, v_\beta)_r$ are strongly Coriolis interacting (when $v_\beta > 1$). For levels that lie below 1600 cm^{-1} in the $\tilde{C}$ state, where *all* of the a_1 and b_2 symmetry levels have been experimentally observed, this selection rule seems to be obeyed and the Coriolis polyads are formed based on this selection rule, as is schematically displayed in Fig. 8-7.

Note that the mixing-angles of pairs of levels in the P_1-P_5 polyads in Fig. 8-

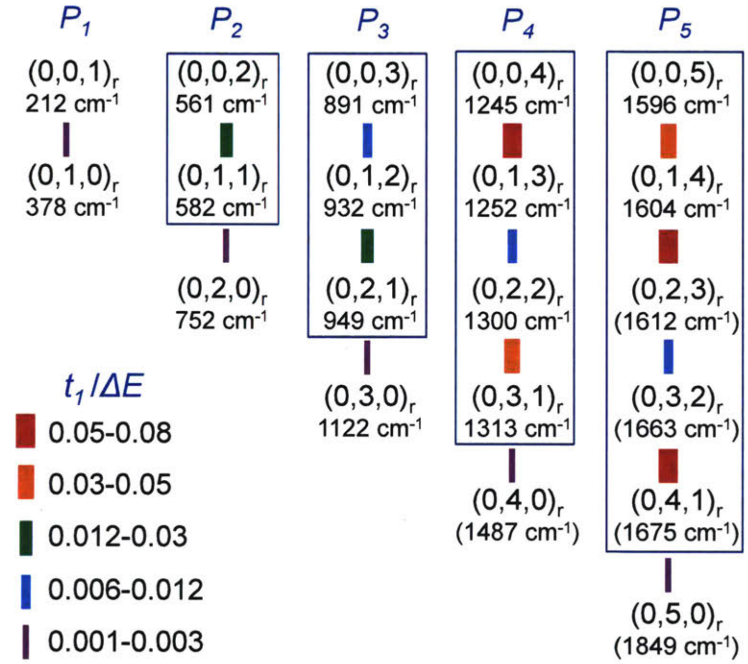

Figure 8-7: Formation of Coriolis polyads. Note that energies of the vibrational states increase from left to right and from top to bottom. The lines between different pairs of states are drawn with different color and width, in order to depict the magnitude of the rotationless Coriolis mixing angle. Strongly interacting states forming a polyad (designated by the polyad number, P_n) are grouped together. The calculated vibrational term energies are used for levels not observed experimentally and are enclosed in parentheses.

7 seem to develop an alternating pattern, e.g. the mixing angle of the $(0, v_2, v_\beta)$-$(0, v_2+1, v_\beta-1)$ pair does not increase monotonically as v_β increases, and the mixing angle between the a_1 and b_2 symmetry levels within a P_n polyad oscillates as one moves down the P_n column in Fig. 8-7. As is evident from Table 8.10, both the experiment and the calculation based on our force field show that the Coriolis matrix elements, t_1, are similar in this energy region. *Thus, the variation in the mixing angles in Fig. 8-7 is mostly due to the variation of the energy difference between the two states in question.* The alternating pattern in the Coriolis mixing angle is in fact a manifestation of the effects of the double-well on the PES on the rotational structure of the molecule.

To see how the double-well structure leads to the alternating pattern, we define the effective ν_β frequency of the $(0, v_2, v_\beta)_r$ level as the energy difference between the $(0, v_2, v_\beta)_r$ and $(0, v_2, v_\beta+1)_r$ levels. Similarly, the effective ν_2 frequency of $(0, v_2, v_\beta)_r$ is the energy difference between $(0, v_2, v_\beta)_r$ and $(0, v_2+1, v_\beta)_r$. The effective ν_2 frequency is approximately a constant ($\sim$ 377 cm^{-1}). Due to the double-well structure of the PES, the magnitude of the effective ν_β frequency alternates as a function of v_β, as can be seen in Fig. 8-8. The effective ν_β frequency of $(0, v_2, v_\beta)_r$ is larger than that of $(0, v_2', v_\beta+1)_r$ if v_β is odd, and it is smaller than that of $(0, v_2', v_\beta+1)_r$ if v_β is even. Given this alternating pattern in the effective ν_β frequency, the alternations in the mixing angles down each of the P_2-P_5 polyad columns in Fig. 8-7 can be explained. Similar arguments are applicable to the oscillating patterns across each row in Fig. 8-7. As shown here, the staggering in the vibrational energy spacings results in an alternation in the degree of Coriolis interactions between levels in the P_1-P_5 polyads.

8.4.5 The Zigzag Patterns in the C Rotational Constants

The alternating patterns in the Coriolis mixing angles shown in Fig. 8-7 are manifest as zigzag patterns in the C_p rotational constants (the Coriolis-perturbed C rotational constants). In Fig. 8-9, values of the experimental effective C_p constants [131, 182] of levels in the $(0, 0, v_\beta)$ and $(0, 1, v_\beta)$ progressions are plotted as a function of v_β.

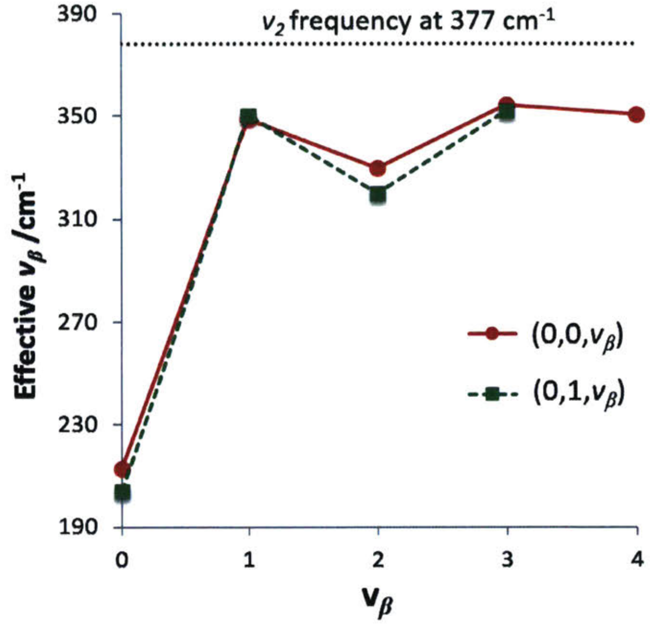

Figure 8-8: The effective ν_β frequency in the $(0, 0, v_\beta)$ and $(0, 1, v_\beta)$ progressions. The dotted line at the top of the figure shows the approximate magnitude of the v_2 frequency.

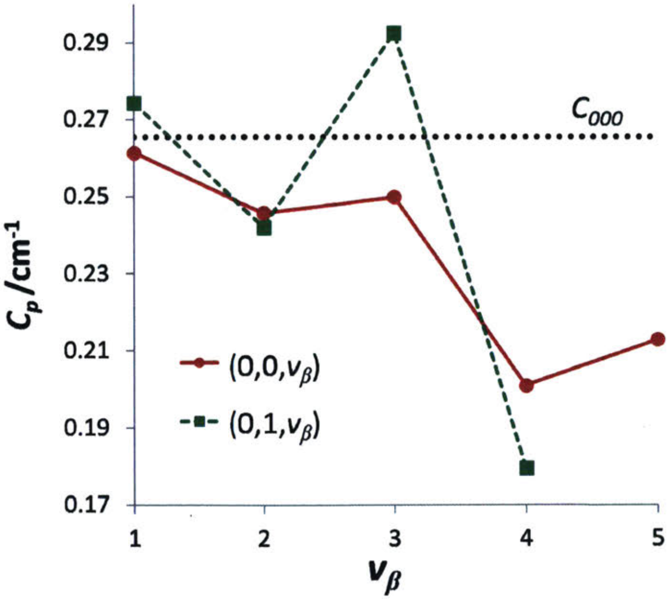

Figure 8-9: Values of the experimental *perturbed* C rotational constants [131, 182] of levels in the $(0, 0, v_\beta)$ and $(0, 1, v_\beta)$ progressions, with $v_\beta > 1$. The dashed line indicates the value of the C constant of the zero-point level, C_{000}=0.2654 cm^{-1}.

It is evident that the C_p rotational constants in both progressions follow a zigzag trend. The C constant of the zero-point level (C_{000}) is used as a reference for the C_p constants in Fig. 8-9. Given that the Coriolis contribution to the C constants outweighs the corrections from other contributions by an order of magnitude (with the exception of the $(0,0,1)_r$ level), the deviation of the C_p constant of a specific vibrational level from C_{000} gives information about the mixing angle between that level and its Coriolis-interacting levels.

The C_p rotational constants of levels in the $(0,0,v_\beta)$ progression ($v_\beta \leq 5$) are all smaller than C_{000}, since all of the Coriolis-interacting partners of those levels lie higher in energy. The zigzag pattern arises from oscillations in the magnitudes of the Coriolis mixing angles between the $(0,0,v_\beta)$ an $(0,1,v_\beta - 1)$ levels as v_β increases (see Fig. 8-7). Note that the deviations of the C_p constants from C_{000} match the trend in the mixing angles between the $(0,0,v_\beta)$ and $(0,1,v_\beta - 1)$ levels in Fig. 8-7, i.e. a larger mixing angle leads to a larger deviation. The C_p rotational constants of levels in the $(0,1,v_\beta)$ progression ($v_\beta \leq 4$) oscillate around the value of C_{000}, because levels in this progression are affected by two competing Coriolis interactions with $(0,0,v_\beta + 1)$ and $(0,2,v_\beta - 1)$ levels. The two resulting mixing angles are not equal and their relative magnitudes alternate as v_β increases (see Fig. 8-7). Consequently, the C_p constants of levels in the $(0,1,v_\beta)$ progression ($v_\beta \leq 4$) oscillate around the value of C_{000}, as v_β increases.

We believe that a zigzag trend in the rotational constants of levels in a vibrational progression is a signature of a double-well on the PES. Similar observations have been made in other molecular systems with a small barrier on the PES [29, 47, 48], although in other molecules, the rotational constants that exhibit the zigzag pattern are not strongly perturbed by Coriolis interactions, so the deviations of those rotational constants from the usual linear trend is about two or three orders of magnitude smaller than in the C rotational constants of the $\tilde{\mathrm{C}}$ state of SO_2. Thus, Coriolis interactions amplify the effect of a double-well structure on the rotational constants.

8.5 Conclusion

In this work, an internal coordinate force field through quartic terms for the SO_2 $\tilde{C}^1B_2$ state has been derived. The force field fit incorporates vibrational and rotational information from two isotopologues of SO_2 ($S^{16}O_2$ and $S^{18}O_2$), and, in particular, it includes nine recently measured b_2 symmetry levels of $S^{16}O_2$ [131, 133] . The good agreement between the experimental and calculated values of observables, many of which are not directly included in the fit, indicates that the force field is physical and accurate. In particular, the Franck-Condon intensities and the Coriolis-perturbed effective C rotational constants of highly anharmonic $\tilde{C}$ state vibrational levels are well reproduced using our force field. The force field, together with our recent direct observations of b_2 vibrational symmetry levels [131, 133], add crucial pieces of information to our understanding of the SO_2 $\tilde{C}^1B_2$ system. Key aspects of the dynamics predicted by the new force field are analyzed.

The assumption of the separability of ν_2 from the other two strongly Fermi-interacting modes breaks down for levels that lie >2000 cm^{-1} above the $\tilde{C}$ state zero-point level. Franck-Condon interference effects, due to interactions among states that have different numbers of quanta of excitation in ν_2, are found to be prevalent among the $\tilde{C}$ state vibrational levels above 2500 cm^{-1}. The presence of interference effects in this energy region invalidates vibrational assignment based on apparent ν_2 progressions. However, using a two-step diagonalization procedure of the vibrational Hamiltonian, an unprecedented number of $\tilde{C}$ state vibrational levels can now be assigned. The vibrational levels are characterized in the Kellman basis, constructed explicitly via partial diagonalization of the Hamiltonian. Decoding the new classes of dynamics exhibited by levels above 2500 cm^{-1}, which are highly mixed even in the Kellman basis, poses an interesting challenge for future work.

The Coriolis interactions in the $\tilde{C}$ state are modeled in this work using second-order non-degenerate perturbation theory. Most importantly, we identify a rotational signature indicating the presence of the double-well structure of the PES. The anomalies in the C rotational constants result from the staggering in the vibrational energy spacings, due to the double-well structure.

Chapter 9

Two-state Interaction Model of the C_2 $C^1\Pi_g$ State

Abstract

The rotation-vibration structure of the C_2 $C^1\Pi_g$ state is modeled as results of homogenous interaction between two electronic configurations: $1\sigma_g^2 1\sigma_u^2 2\sigma_g^2 2\sigma_u^1 1\pi_{ux}^2 1\pi_{uy}^1 3\sigma_g^2$ and $1\sigma_g^2 1\sigma_u^2 2\sigma_g^2 2\sigma_u^2 1\pi_{ux}^1 1\pi_{uy}^1 3\sigma_g^1 1\pi_{gx}^1$. By fitting to the experimental C-state term values of both ${}^{12}C_2$ and ${}^{13}C_2$ isotopogues (specifically, J=1, 5, 10, 15, 20 levels of the observed vibrational states), we obtain a fit model which quantitatively reproduces all of the key C-state rotation-vibration features, i.e. rapid and early convergence in the vibrational energy spacings and rotational constants, and curvatures in the $\Delta_2 F(J)/(J+1/2)$ *vs.* $(J+1/2)^2$ plots. The model Hamiltonian is diagonalized in both adiabatic and diabatic rovibronic basis sets. We show that the adiabatic basis is a better representation of the C_2 $C^1\Pi_g$ system.

9.1 Introduction

The Deslandres-d'Azambujia band system ($C^1\Pi_g - A^1\Pi_u$) of the C_2 molecules were first discovered more than a century ago from the condensed discharge of CO and CO_2 [44]. Since then, observations of the $C^1\Pi_g - A^1\Pi_u$ emissions have been made in the lab in different experimental conditions, from shock-heating [37] and discharge [2, 46, 67, 108, 135] of various carbon-containing sources (e.g. acetylene), to three-photon laser dissociation of acetylene, using 193 nm ArF excimer laser [101, 167]. The three-photon dissociation process of acetylene has also been shown to be resonantly enhanced by the S_1-S_0 acetylene transition [79]. In most of the photochemical and thermal processes where the $C^1\Pi_g - A^1\Pi_u$ transitions are observed, the Swan band emissions ($d^3\pi_g - a^3\pi_u$) are also typically present. This is expected, because both the upper and lower states of the two band systems have similar electronic configurations (differing only in their spin alignments) [8, 27, 28, 115, 147], and that $C^1\Pi_g$ and its triplet counterpart, $d^3\pi_g$, are similar in energy (differing by < 2 eV) [72].

Early spectroscopic analyses of the Deslandres-d'Azambujia band system [46, 67, 89] revealed that the vibrational energy spacings in the $C^1\Pi_g$ state decrease rapidly, and the rotational constants follow a similar trend. An extrapolation by Herzberg et. al. [67] led to a dissociation limit at 35900 cm^{-1} above the lower $A^1\Pi_u$ state (the absolute position which was not known at that time). Almost immediately after the publication of Herzberg's analysis, Gero and Schmid [57] questioned the validity of Herzberg's result, on the basis that rotational levels belonging to the $C^1\Pi_g$ state could be observed several thousands wavenumber higher in energy than the extrapolated dissociation energy. It was suggested that the presence of extensive homogenous perturbations in the $C^1\Pi_g$ state could be the origin of the fast and early convergence. The observation of a new vibrational level of $C^1\Pi_g$ by Phillips [135] seemed to support the hypothesis of Gero and Schmid, although the arguments of Phillips were based on an incorrect vibrational assignment of the level (which was tentatively assigned as $v = 7$, instead of $v = 8$, as our work suggests). With various accurate measurements of the dissociation energy of C_2 [23, 90], and knowledge of absolute energies of its low-lying singlet and triplet states [6, 7], it became obvious that the extrapolated dissociation energy of C_2 from the $C^1\Pi_g$ state by Herzberg was $\sim$0.8 eV lower than the correct value. Ballik and Ramsay [8], drawing analogy to the C_2 $d^3\pi_g$ state, hypothesized the presence of an avoided crossing between $C^1\Pi_g$ and a higher-lying $^1\Pi_g$ state. In the absence of the avoided-crossing, the two zero-order $^1\Pi_g$ states were assumed to dissociate, respectively, into $C(^1D)+C(^1D)$ and $C(^3P)+C(^3P)$ fragment limits of C_2. However, as in the analysis of Gero and Schmid [57], no quantitative treatment of the interactions was provided.

In the work by Messerle and Krauss [108], rotational perturbations were observed in the $v = 3-8$ levels of the $C^1\Pi_g$ state at relatively high rotational quantum number ($J > 20$). The vibrational level origins and rotational constants of the perturbing levels were derived, and the perturbers were assigned as the lowest six vibrational levels of a nearby $^1\Pi_g$ state (denoted by the label, C', in their work), responsible for the peculiar vibration and rotation structure of the $C^1\Pi_g$ state. However, as we discuss in detail in Section 9.6, the analysis of Messerle and Krauss was based on incorrect interpretations of curvatures in the observed $\Delta_2F(J)/(J+1/2)$ *vs.* $(J+1/2)^2$ plot (where $\Delta_2F(J) = F(J+1)-F(J-1)$ is the upper state combination difference of the Deslandres-d'Azambujia band system). To our knowledge, errors in the analysis of Messerle and Krauss have not been properly recognized in the literature, and the incorrectly assigned transition between the $C'^1\Pi_g$ perturber state and the $A^1\Pi_u$ state is sometimes referred as the Messerle and Krauss band system of C_2.

Detailed spectroscopic investigations of the C_2 Deslandres-D'Azambujia band system largely came to an end after 1970s. However, as we have pointed out, there remain a few unresolved problems regarding the upper electronic state of the band. More recent *ab initio* calculations [27, 28, 147] confirm the hypothesis of Ballik and Ramsay [8]. The $C^1\Pi_g$ state consists primarily of the same two electronic configurations that make up the $d^3\pi_g$ state (see details in Section 9.2), and that the interaction between the two configurations is strongest at an internuclear distance of ~1.5 Å. However, none of the previous studies (both spectroscopic and *ab initio*) have treated the two-state interaction model directly, which, we believe, is the key to fully understand the rotation-vibration structure of the C_2 $C^1\Pi_g$ state. In addition, the two-state interaction model provides a framework for more accurate determinations of the transition probabilities between C and A state rovibrational levels. This is important in quantitative modelings of the C_2 $C^1\Pi_g$ emissions, resulting from various photochemical and/or thermal processes. Note that, throughout this work, the term, $C^1\Pi_g$, is used to label the upper electronic state of the C_2 Deslandres-D'Azambujia band, even though the electronic state is more accurately described as a $^1\Pi_g$ coupled system.

9.2 Theory

The rotation-vibration structure in the upper electronic state of the Deslandres-D'Azambujia band system is modeled as results of homogenous interactions between two close-lying single-configuration diabatic ${}^1\Pi_g$-symmetry electronic states: $1\sigma_g^2 1\sigma_u^2 2\sigma_g^2 2\sigma_u^1 1\pi_{ux}^2 1\pi_{uy}^1 3\sigma_g^2$ (labeled as state d_1, with corresponding Φ_1^d electronic wavefunction) and $1\sigma_g^2 1\sigma_u^2 2\sigma_g^2 2\sigma_u^2 1\pi_{ux}^1 1\pi_{uy}^1 3\sigma_g^1 1\pi_{gx}^1$ (labeled as state d_2, with corresponding Φ_2^d electronic wavefunction). The letter, d, in both the state labels and the wavefunctions, indicates diabatic wavefunctions. Both diabatic states are assumed to be bound. *Ab initio* calculations of the $C^1\Pi_g$ state [28, 88, 147] suggest an additional contribution from a third electronic configuration. In this work, interactions from other states with either of the two diabatic states are assumed to be negligible. From *ab initio* calculations [28, 116, 147], it is clear that the minimum of the d_1 state is lower in energy than that of the d_2 state. The triplet counterpart of the d_1 state (i.e. having the same electron configuration as the singlet d_1, but with parallel spin alignment for the two unpaired electrons) is also known to have a shorter equilibrium bond length than the triplet d_2 state [8, 27, 28, 72, 116, 147]. In the singlet system studied in this work, the d_1 state is assumed to lie lower in energy and have a shorter equilibrium bond length than d_2.

The two single-configuration diabatic states are orthnormal, and they differ by two electron-orbitals. As a result, both diagonal (due to the normalization condition) [96] and off-diagonal (due to the assumed electron configurations of the two states) [142] matrix elements of the $\frac{\partial}{\partial R}$ operator (where R is the internuclear distance) are zero for the two states, that is,

$$\left\langle \Phi_i^d \left| \frac{\partial}{\partial R} \right| \Phi_j^d \right\rangle_r = 0 \text{ for both } i = j \text{ and } i \neq j, \tag{9.1}$$

with the integration carried over the electronic coordinates, r. It must be emphasized that vanishing off-diagonal matrix element of the $\frac{\partial}{\partial R}$ operator is the usual requirement of diabatic states [55, 93, 96, 102, 142, 146]. The two single-configuration states in this work automatically fulfill such requirement. The importance Eq. (9.1) will be discussed in Section 9.2.1 and 9.2.2.

Single-configuration diabatic states are, generally, not eigenstates of the electronic Hamiltonian, $H^{el} = T_e + V_e(r, R)$, where T_e is the electron kinetic energy and V_e is the electrostatic potential energy for the nuclei and electrons. The two diabatic states interact to form adiabatic electronic states, which are eigenstates of H^{el}, via a two-by-two matrix [93],

$$\begin{pmatrix} E_1^d(R) & H_{12}^e(R) \\ H_{12}^e(R) & E_2^d(R) \end{pmatrix}, \tag{9.2}$$

where $E_i^d = \langle \Phi_i^d | H^{el} | \Phi_i^d \rangle_r$ and $H_{12}^{el} = \langle \Phi_1^d | H^{el} | \Phi_2^d \rangle_r$. The diagonal terms of the matrix, E_1^d and E_2^d, are the *crossing* Born-Oppenheimer (BO) diabatic potential curves. Both curves are assumed to have the functional form of a Morse potential,

$$T_e + D_e[1 - e^{-\beta(R-R_e)}]^2, \tag{9.3}$$

where T_e, D_e, β, and R_e are the usual Morse potential parameters, characterizing, respectively, the minimum energy, depth, curvature, and equilibrium bond distance of the potential. Furthermore, the d_1 and d_2 states are assumed to dissociate, respectively, into C(^{1}D)+C(^{1}D) and C(^{3}P)+C(^{3}P) limits. In this work, experimental dissociation energies [72, 84], 71396 cm^{-1} for the C(^{1}D)+C(^{1}D) limit, and 51011 cm^{-1} for the C(^{3}P)+C(^{3}P) limit [1], are used for the two diabatic BO potential curves in Eq. (9.3). The d_2 state is expected to have a relatively shallow well, given that the electronic origin of the $C^1\Pi_g$ state is at ~34000 cm^{-1}, and that the minimum of the d_2 curve is expected to be higher than that of d_1.

Since the two diabatic states have single-configurations, the electronic coupling matrix element, $H_{12}^e(R)$, is expected to depend only weakly on R [93]. In this work, H_{12}^e is assumed to be a constant. The eigenvalues of the two-by-two matrix, E_1^a and E_2^a, are the *non-crossing* BO adiabatic potential curves (the superscript, a, indicates adiabatic wave functions). The adiabatic states are related to the diabatic states by

---

[1] The energy of the C(^{3}P)+C(^{3}P) fragment limit is taken as the sum of the experimental D_0^0 value (6.21 eV) of the ^{12}C$_2$ $X^1\Sigma_g^+$ state [72], and the energy of the zero-point level of the ^{12}C$_2$ X state, calculated from the molecular constants listed in Ref [72].

a unitary transformation

$$\begin{aligned}\Phi_1^a(r,R) &= \alpha(R)\Phi_1^d(r,R) + \beta(R)\Phi_2^d(r,R)\\ \Phi_2^a(r,R) &= \beta(R)\Phi_1^d(r,R) - \alpha(R)\Phi_2^d(r,R).\end{aligned} \tag{9.4}$$

The two adiabatic electronic wavefunctions are properly normalized with respect to the electronic coordinates (i.e. $\alpha^2 + \beta^2 = 1$). The upper adiabatic state (higher in energy at all values of R) is labeled as a_1 (with corresponding wavefunction Φ_1^a) and the lower one labeled as a_2 (with corresponding wavefunction Φ_2^a). The R-dependence in the mixing coefficients of the adiabatic wave functions originates largely from the R-dependence in the energy separation between the two BO diabatic potential curves.

Both diabatic and adiabatic electronic states are obtained within the framework of BO approximation, which neglects the effect of the nuclear kinetic energy operator,

$$T^N = -\frac{\hbar^2}{2\mu}\left[\frac{\partial^2}{\partial R^2} + \frac{2}{R}\frac{\partial}{\partial R}\right] + \frac{\hbar^2}{2\mu R^2}[J(J+1) - \Omega^2], \tag{9.5}$$

on the electronic wavefunctions. In Eq. (9.5), μ is the nuclear reduced mass of the molecule, and Ω is the projection of the total angular momentum, J, on the internuclear axis. Since the electronic states involved have $^1\Pi$-symmetry, $\Omega^2 = 1$ and $J \geq 1$ (integer values) [24, 93]. Effects from nuclear spin statistics (which lead to missing levels, but no level shifts) and Λ-type doubling (which causes small splittings between e and f symmetry rotational levels within one vibrational state) are not included in the calculations. The diagonal contributions of T^N can be incorporated directly into the BO potential curves in either diabatic or adiabatic representation by [24, 93]

$$\begin{aligned}V_i(R,J) &= E_i + \langle\Phi_i| T^N |\Phi_i\rangle_r\\ &= E_i - \frac{\hbar^2}{2\mu}\left[\langle\Phi_i|\frac{\partial^2}{\partial R^2}|\Phi_i\rangle_r + \frac{2}{R}\langle\Phi_i|\frac{\partial}{\partial R}|\Phi_i\rangle_r\right] + \frac{\hbar^2}{2\mu R^2}[J(J+1)-1]\\ &= E_i - \frac{\hbar^2}{2\mu}\langle\Phi_i|\frac{\partial^2}{\partial R^2}|\Phi_i\rangle_r + \frac{\hbar^2}{2\mu R^2}[J(J+1)-1],\end{aligned} \tag{9.6}$$

where E_i and Φ_i are, respectively, the BO potential curve and electronic wavefunction of state i in one representation. In Eq. (9.6), the diagonal matrix element of $\frac{\partial}{\partial R}$ vanishes in both adiabatic and diabatic bases, because both basis wavefunctions are properly normalized with respect to r [96]. The new potential curve, V_i, depending on the nature of the BO electronic wavefunctions used in Eq. (9.6), can be interpreted as the effective PEC of state i in that particular representation. The PECs given by Eq. (9.6) are sometimes referred to as the "the best possible potential curves" beyond BO approximation [24]. For simplicity, adiabatic or diabatic PEC is used, respectively, to refer to the effective PEC in either adiabatic or diabatic representation in Eq. (9.6).

We must emphasize that the rovibrational levels of neither the diabatic nor the adiabatic PEC exactly represent the observed levels. Interaction matrix elements among zero-order levels must be added to reproduce the observed levels. Zero-order levels in both representations can interact via the T^N operator, due to R-dependence in the electronic wavefunctions. The resulting off-diagonal matrix element between the $|v_1, J\rangle$ level of V_1 and the $|v_2, J\rangle$ level of V_2 is given by [93]

$$\begin{aligned} H_{1,v_1,J;2,v_2,J}(\text{cm}^{-1}) = & \frac{-16.8576}{\mu(\text{amu})} \langle \xi_{v_1} J| \langle \Phi_1| \frac{\partial^2}{\partial R^2} |\Phi_2\rangle_r (\text{Å}^{-2}) |\xi_{v_2} J\rangle_R \\ & \frac{-33.7152}{\mu(\text{amu})} \langle \xi_{v_1} J| \langle \Phi_1| \frac{\partial}{\partial R} |\Phi_2\rangle_r (\text{Å}^{-1}) \left|\left(\frac{d}{dR}\xi_{v_2}\right) J\right\rangle_R (\text{Å}^{-1}), \end{aligned} \tag{9.7}$$

where $|\xi_{v_i}\rangle$ is a vibrational wavefunction from V_i, normalized with respect to dR (instead of $R^2 dR$). Equation (9.7) is applicable in both adiabatic and diabatic representations. Furthermore, because diabatic electronic states are not eigenstates of the electronic Hamiltonian, H^{el}, diabatic levels from the two diabatic electronic states also interact via H^{el} (see Section 9.2.2). Treatments of each individual matrix elements in Eqs. (9.6)-(9.7) are subjects of the following two sections. In particular, we focus on the approximations that are made in our calculations. Numerical details of the calculations can be found in Appendix C.1.

9.2.1 Adiabatic representation

Since the adiabatic electronic states, obtained by diagonalizing Eq. (9.2), are assumed to be eigenstates of the electronic Hamiltonian, rovibrational levels of the two adiabatic electronic states interact only via the T^N operator. As can be seen from Eqs. (9.6) and (9.7), both diagonal and off-diagonal matrix elements involve matrix elements of the derivative operators ($\frac{\partial^2}{\partial R^2}$ and $\frac{\partial}{\partial R}$), which act on the adiabatic electronic wavefunction (see in Eq. (9.4)) via R-dependence in the diabatic basis wavefunctions and that in the mixing coefficients (α and β). For example, the diagonal matrix element, $\langle \Phi_1^a | \frac{\partial^2}{\partial R^2} | \Phi_1^a \rangle_r$, is given by

$$\begin{aligned}
\langle \Phi_1^a | \frac{\partial^2}{\partial R^2} | \Phi_1^a \rangle_r &= \langle\, \alpha(R)\Phi_1^d(r,R) + \beta(R)\Phi_2^d(r,R) \,|\, \frac{\partial^2}{\partial R^2} \,|\, \alpha(R)\Phi_1^d(r,R) + \beta(R)\Phi_2^d(r,R) \,\rangle_r \\
&= \left\langle \alpha\Phi_1^d + \beta\Phi_2^d \,\middle|\, \alpha''\Phi_1^d + 2\alpha'\Phi_1^{d\prime} + \alpha\Phi_1^{d\prime\prime} + \beta''\Phi_2^d + 2\beta'\Phi_2^{d\prime} + \beta\Phi_2^{d\prime\prime} \right\rangle_r \\
&= \alpha\alpha'' + \beta\beta'' + \alpha^2 \left\langle \Phi_1^d \mid \Phi_1^{d\prime\prime} \right\rangle_r + \beta^2 \left\langle \Phi_2^d \mid \Phi_2^{d\prime\prime} \right\rangle_r + 2\alpha\beta \left\langle \Phi_1^d \mid \Phi_2^{d\prime\prime} \right\rangle_r \\
&\approx \alpha\alpha'' + \beta\beta'',
\end{aligned} \tag{9.8}$$

where single and double prime indicate, respectively, the first and second derivative of the preceding function with respect to R. Relationships given by Eq. (9.1) are used to obtain the third line in Eq. (9.8). Without high-level *ab initio* calculations, it is not possible to obtain physically meaningful R-dependent expressions for the matrix elements of the second-derivative operator for the diabatic states, such as $\left\langle \Phi_1^d \mid \Phi_1^{d\prime\prime} \right\rangle_r$ [24]. However, as pointed by Lewis and Hougen [96], and demonstrated in Appendix C.2 of the current work, contributions from the second-order derivative matrix elements are expected to be at least an order of magnitude smaller than the $\alpha\alpha'' + \beta\beta''$ term. From those reasons, we assume that

$$\langle \Phi_i^d | \frac{\partial^2}{\partial R^2} | \Phi_j^d \rangle_r = 0 \text{ for both } i = j \text{ and } i \neq j, \tag{9.9}$$

throughout our calculations in either adiabatic or diabatic representation (discussed in Section 9.2.2). Other matrix elements relevant to the adiabatic representations are listed below without further proof:

$$\langle \Phi_1^a | \frac{\partial}{\partial R} | \Phi_2^a \rangle_r = \alpha\beta' - \beta\alpha' \tag{9.10}$$

$$\langle \Phi_1^a | \frac{\partial^2}{\partial R^2} | \Phi_2^a \rangle_r \approx \alpha\beta'' - \beta\alpha'' \tag{9.11}$$

With the above relationships and the zero-order rovibrational levels in both the upper and lower adiabatic PECs, eigenvalues of the full molecular Hamiltonian, $H^{mol} = H^{el} + T^N$, can be obtained.

9.2.2 Diabatic representation

Given Eq. (9.1) and the approximations in Eq. (9.9), both diagonal and off-diagonal matrix elements of the T^N operator vanish in the diabatic basis. However, since diabatic states are not eigenstates of H^{el}, electronic coupling between zero-order diabatic levels from each diabatic electronic state exists, and it is given by [93]

$$\begin{aligned} H_{1,v_1,J;2,v_2,J} &= \langle \Phi_1^d \xi_{v_1}^d J | \, H_{12}^{el} \, | \Phi_2^d \xi_{v_2}^d J \rangle_r \\ &= H_e \left\langle \xi_{v_1}^d J | \xi_{v_2}^d J \right\rangle_R , \end{aligned} \tag{9.12}$$

where $|\Phi_i^d \xi_{v_i}^d J\rangle$ is a rovibrational level from the diabatic electronic state, i, and $H_{12}^{el} = H_e$ is assumed to be a constant. Note that $\left\langle \xi_{v_1}^d J | \xi_{v_2}^d J \right\rangle_R$ is the vibrational overlap integral between two vibrational wavefunctions with total angular momentum, J. Therefore, the diabatic states are coupled by electrostatic interactions, instead of nuclear motions. As we have seen from Section 9.2.1, the exact opposite is true for the adiabatic states.

9.3 Details of the Fit

The full molecular Hamiltonian, expressed in the adiabatic basis, is diagonalized, and the eigenvalues are fitted to the experimental values. Our fit model involves a total of seven parameters: three for each diabatic BO Morse potentials and H_e. Recent *ab* *initio* work by Sorensen and England [147] provides a reasonable initial guess of the values of those fit parameters. In this work, J=1, 5, 10, 15, 20 levels are calculated for both $^{12}C_2$ and $^{13}C_2$. Since experimentally observed term values are subject to Λ-type doubling and nuclear-spin statistics, both of which are not accounted for in our model, term values obtained from an effective rotational fit to the observed levels for each vibrational levels are used as inputs to the fit. The effective term values, $F_v(J)$, are given by

$$F_v(J) = T_v + B_v[J(J+1) - 1] - D_v[J(J+1) - 1]^2, \tag{9.13}$$

where T_v, B_v, and D_v are, respectively, the origin, rotational constant, and centrifugal distortion constant, of the vibrational level, v. The number, 1, in the parentheses after $J(J+1)$ reflects the electronic angular momentum of the state (see discussion of Eq. (9.5)). The experimental term values used in the fit are considered the average values of the two Λ-components. Deviations of the average term values from the observed values are small (typically < 0.5 cm^{-1} for $J \leq 20$). For $^{12}C_2$, we assume that all the levels reported in Refs [46, 108] belong to the homogenously-coupled system studied in this work. The nine reported vibrational levels are assumed to be the lowest nine vibrational levels of the coupled system. The $v = 0 - 3$ levels of the $^{13}C_2$ $C^1\Pi_g$ state have also been experimentally observed [2]. However, there are slight uncertainties in the term values of those levels, because the $X^1\Sigma_g^+$ state of $^{13}C_2$ have not been experimentally observed (although $v = 0$ and 1 levels of the $^{13}C_2$ $A^1\Pi_u$ state have been observed [1, 2]). Isotopic relations [66] are used to obtain vibrational term energies of the $^{13}C_2$ X state, based on the molecular constants of $^{12}C_2$ [72]. Isotopic relations are expected to be quite accurate in reproducing the actual $^{13}C_2$ vibrational term energies [66]. In our fit, slightly smaller weights are placed on the $^{13}C_2$ C-state term energies (2/3 of the weight of $^{12}C_2$ term energies).

The seven parameters obtained from the fit (in the adiabatic representation) are then used as inputs to calculate $J = 1 - 50$ rotational levels of $^{12}C_2$, in both adiabatic and diabatic representations. The results are expected to the same in the two

Table 9.1: Molecular parameters of the $C^1\Pi_g$ coupled system of C_2, obtained from a fit using the adiabatic representation. Note that, the dissociation limits of both diabatic states, given by $T_e + D_e$, are fixed to the experimental values. Numbers in the parantheses are 1σ uncertainties of last digits.

diabatic state	$T_e\,/\,\mathrm{cm}^{-1}$	$D_e\,/\,\mathrm{cm}^{-1}$	$\beta\,/\,\text{Å}^{-1}$	$R_e\,/\,\text{Å}$
d_1	36,846.1(28)	34550.3(28)	2.9397(18)	1.2444(4)
d_2	45,539.7(668)	5471.3(668)	3.5090(327)	1.5839(33)
$H_e\,/\,\mathrm{cm}^{-1}$	3451.0(605)			

representations (within numerical errors of the calculations). The T_v, B_v, and D_v constants are derived, by Eq. (9.13), for each vibrational state from the calculated term energies. Those values can be compared to the experimental effective constants used to generate inputs to the fit. Unfortunately, in most of the earlier work on the $C^1\Pi_g$ state, where effective rotational and centrigual constants of the first nine vibrational levels were reported [46, 67, 108, 135], the uncertainties on those derived constants were not included. To have meaningful comparisons between our fit and the experiments, we re-derive those constants with fit uncertainties, using the available observed experimental term values. [2] The $J = 1 - 20$ term values are included in the fit (beyond which experimental values are not available for most vibrational levels). The rederived values are not significantly different from the reported values.

9.4 Fit Results

The result of the fit, obtained in the adiabatic representation, is listed in Table 9.1. The corresponding diabatic and adiabatic PEC's are shown in Fig 9-1. As expected (see Section 9.2), the minimum of the d_1 state is lower than that of d_2. The equilibrium bond lengths of the two states are also similar to the experimental bond lengths of their respective triplet counterpart states [72], $R_e = 1.266$ Å for the triplet counterpart

---

[2] The experimental values of the $v = 7$ level were not tabulated in Ref [108]. As a result, values of the B_v and D_v constants of $v = 7$ derived in Ref [108] are used directly, and the average fit uncertainty of each constant from all the other re-fitted levels in this work is taken as the fit uncertainty for the $v = 7$ level.

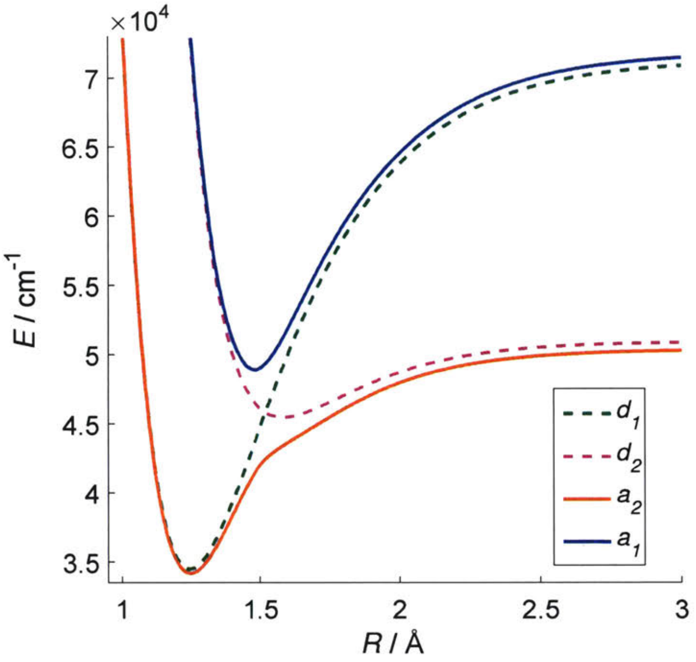

Figure 9-1: Diabatic PECs (dashed lines) and the resulting effective adiabatic PECs (solid lines).

of d_1, and $R_e = 1.535$ Å for the triplet counterpart of d_2.[3] With a total of sixty-five fitted energy levels, the average fit residual is $\sim$2.3 cm^{-1}. To further demonstrate the quality of the fit, the T_v, B_v, and D_v constants of the $^{12}C_2$ isotopologues levels are derived from the calculations, using fit parameters in Table 9.1, and they are compared with the corresponding experimental values (Fig. 9-2). The quality of the fit is equally good for the $^{13}C_2$ levels, which are not shown for simplicity. In this work, vibrational levels are labeled according to their energy-rank in the two-state coupled system, i.e. the i^{th} lowest energy vibrational eigenlevel is labeled as the $v = i - 1$ level. Quantitative agreements between the experiments and our fit demonstrate the validity of our two-state interaction model.

However, there still seems to some small systematic discrepancy between the experimental and calculated B_v rotational constants, i.e. the calculation overestimates B_v at low v, and underestimates B_v at high v (Fig. 9-2c). It is not immediately clear,

---

[3] Strictly speaking, the quoted triplet equilibrium bond lengths correspond to the experimental equilibrium bond lengths of the $d^3\pi_g$ and $e^3\pi_g$ states, both of which are results of mixing between the triplet d_1 and d_2 states. However, as shown in Fig. 5 of Ref [8], the deperturbed diabatic equilibrium bond lengths are expected to be close to those of the $d^3\pi_g$ and $e^3\pi_g$ states.

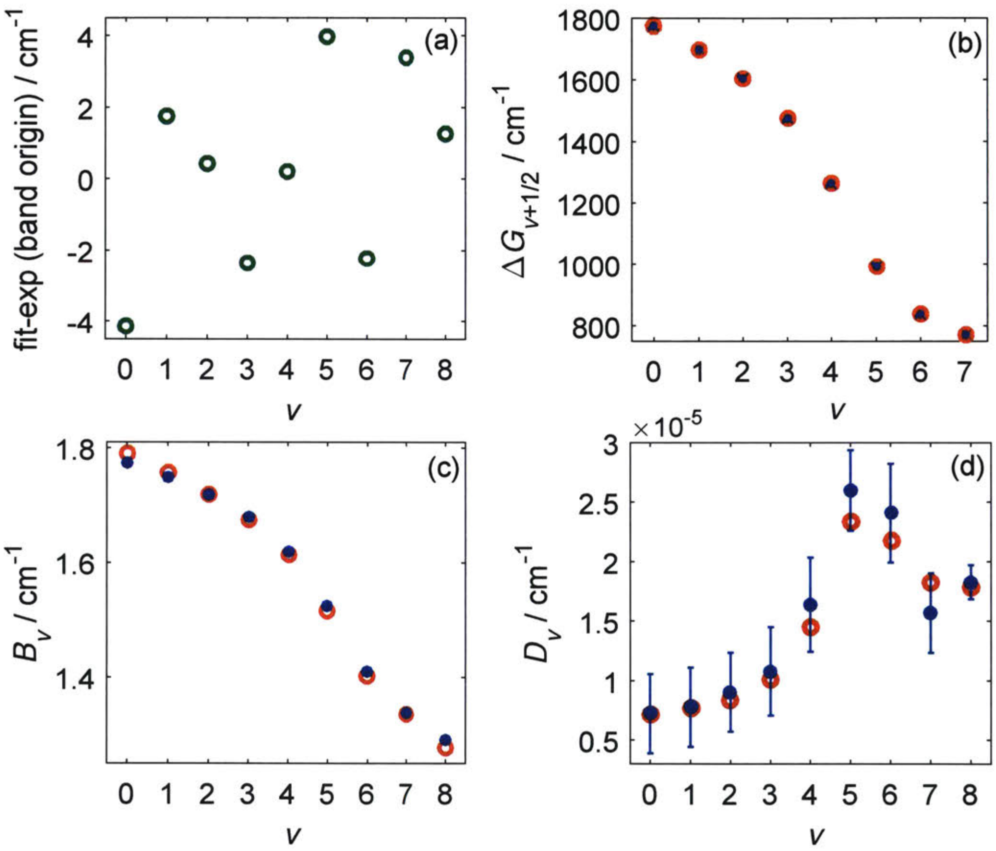

Figure 9-2: Comparison of the fit and the experiments. The blue filled circles are the experimental values, and the orange empty circles are from the calculations. (a) Residuals in the band-origin. (b) Vibrational energy spacings. (c) Rotational constants. (d) Centrifugal distortion constants. The errors bars in (d) are 2σ uncertainties of the experimental values. The error bars are too small to be shown in (b) and (c).

which of the approximations that we have made in our fit model contributes the most to the discrepancy, although we suspect that the systematic error possibly reflects the limit of the two-state interaction model, i.e. contribution from a third electronic configuration can be important at large R, as suggested by *ab initio* studies of the C_2 $C^1\Pi_g$ state [27, 28, 147]. A successful fitting to a three-state interaction model requires observations (which are not currently available) of higher-lying levels which sample the region of crossing between the third electronic configuration and d_1.

9.5 Adiabatic vs. Diabatic Representation

Using fit parameters obtained in the adiabatic representation, eigenvalues of the full molecular Hamiltonian are also calculated in the diabatic representation. The calculated eigenvalues from the two representations agree with each other (within numerical errors of the calculations), as shown in Appendix C.3. In this work, rovibrational levels obtained directly from the effective PECs of a given representation are taken as the zero-order levels of that representation. A specific representation is considered better, if energy differences between the zero-order levels and the eigenlevels of the full molecular Hamiltonian are smaller for the system studied. As shown in Fig. 9-3, it is obvious that for the C_2 system studied in this work, the adiabatic representation is a much better representation than the diabatic representation. In the diabatic representation, even the lowest energy vibrational level is significantly perturbed by higher-lying d_2 levels (see Fig. 9-3c). Given that the magnitude of the electrostatic interaction parameter, H_e, is greater than the C-state vibrational frequency, and that the two diabatic curves cross at relatively low energy region of d_1 (around the energy of the d_1 $v = 6$ level), electrostatic interactions strongly perturb the entire set of vibrational levels of both diabatic electronic states. In fact, for $v > 5$ vibrational levels, the eigenstates are highly mixed in the diabatic representation, and it is not possible to pick out dominant diabatic basis states for those eigenstates. In comparison, the lowest nine vibrational levels are minimally perturbed in the adiabatic representation (Fig. 9-3b).

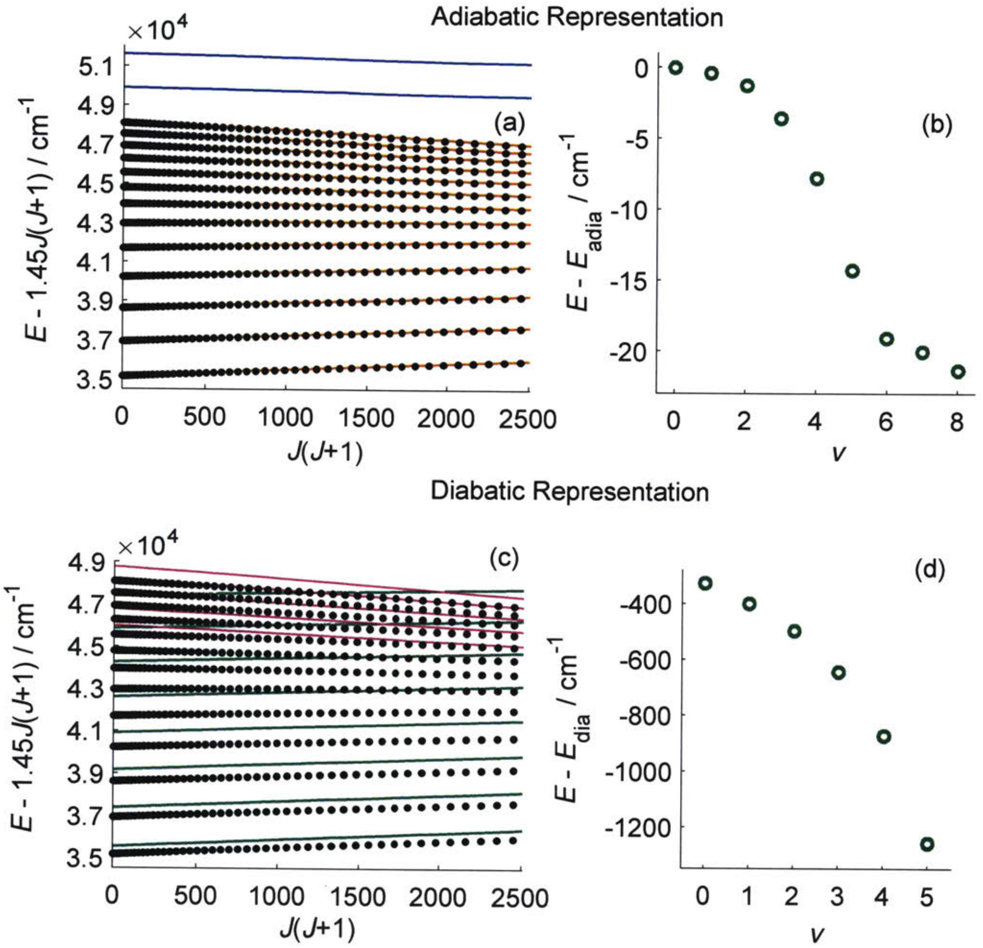

Figure 9-3: Comparisons between adiabatic and diabatic representations for the C_2 $C^1\Pi_g$ state. (a) Eigenvalues of the full molecular Hamiltonian (black filled circles), along with positions of zero-order adiabatic rovibrational levels of a_1 (blue) and a_2 (orange). (b) Difference in energy between the dominant zero-order adiabatic rovibrational basis state and eigenlevel at $J = 1$ of $v = 0 - 8$. (c) Eigenvalues of the full molecular Hamiltonian (black filled circles), along with positions of zero-order diabatic rovibrational levels of d_1 (green) and d_2 (magenta). (d) Difference in energy between the dominant zero-order diabatic rovibrational basis state and eigenlevel at $J = 1$ of $v = 0 - 5$. Reduced term values are used in (a) and (c). For simplicity, only low-lying vibrational levels are shown in (a) and (c), i.e. zero-order a_2 levels with $v > 12$ are not shown in (a).

Given that each observed C-state levels consists predominantly of a single a_2 rovibrational basis state, many of the observed C-state rotation-vibration features can be understood from the shape of the a_2 PEC (Fig 9-1). The $d_1 - d_2$ electrostatic interaction results in a hump on the a_2 PEC at $R \approx 1.5\,\text{Å}$, which lies well below the energy of the first dissociation limit of C_2. The hump mimics the situation in which the molecule approaches the dissociation limit, and consequently leads to rapid and early convergence of the vibrational energy spacings and rotational constants.

9.6 Curvatures in the $\Delta_2F(J)$ Plot

The combination difference, $\Delta_2F(J)$, can be used to graphically determine the B_v and D_v rotational constants of a vibrational level. For a non-rigid rotor given by Eq. (9.13),

$$\Delta_2F(J)/(J+1/2) = (4B_v + 2D_v) - 8D_v(J+1/2)^2. \tag{9.14}$$

By plotting $\Delta_2F(J)/(J+1/2)$ against $(J+1/2)^2$ (referred as the $\Delta_2F(J)$ plot), one obtains a straight line slightly inclined towards the horizontal axis [66]. D_v can be determined from the slope of the plot, and B_v from the vertical-intercept, $4B_v + 2D_v$. [4] Higher-order corrections to Eq. (9.13) (e.g. $H_v[J(J+1)]^3$) are not excepted to significantly alter the $\Delta_2F(J)$ plot, given that H_v is typically 5-6 orders of magnitude smaller than D_v. Significant deviations from a straight line in the $\Delta_2F(J)$ plot are indications of perturbations, which were observed in the $\Delta_2F(J)$ plots of $v = 3-8$ levels of the C_2 $C^1\Pi_g$ state, as shown specifically for the observed $v = 5$ level in Fig. 9-4 (reproduced from Ref [108]).

In the work of Messerle and Krauss [108], the first part of the $\Delta_2F(J)$ plot in Fig. 9-4 (prior to the location of an apparent change of slope at around $J = 35$) was assigned *exclusively* to the C-state $v = 5$ level, and the later part *exclusively* to the perturbing C'-state $v = 2$ level. The assigned C-state level has different rotational

---

[4] Equation (9.14) differs slightly from the usual expression of $\Delta_2F(J)/(J+1/2) = (4B_v - 6D_v) - 8D_v(J+1/2)^2$, which is strictly valid only for a $^1\Sigma$ state. The numbers, 1, in the rotational term expression of a $^1\Pi$ state, given by Eq. (9.13), lead to the slight modification.

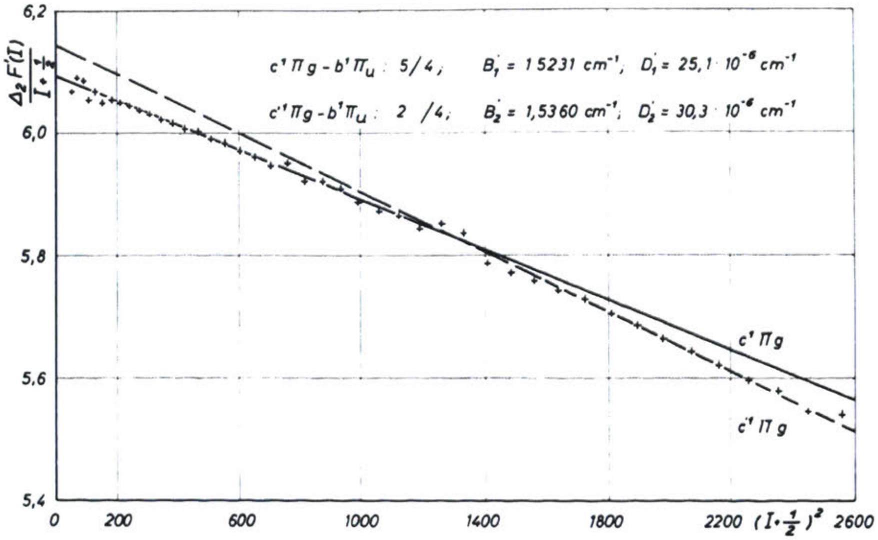

Figure 9-4: The $\Delta_2 F(J)$ plot for the $v = 5$ level of $C^1\Pi_g$, reproduced with permission from Ref [108]. The figure demonstrates the deperturbation method that Messerle and Krauss used to derive the vibrational level origins and rotational constants of the assigned $C''^1\Pi_g$ levels. The crosses in the figure indicate experimental values. The solid line is used for the zero-order $C^1\Pi_g$ levels, and the dashed line for the zero-order perturbing $C''^1\Pi_g$ levels. Note that the letter, I, was used in the figure as the rotational quantum number, which is denoted by the letter, J, in this work.

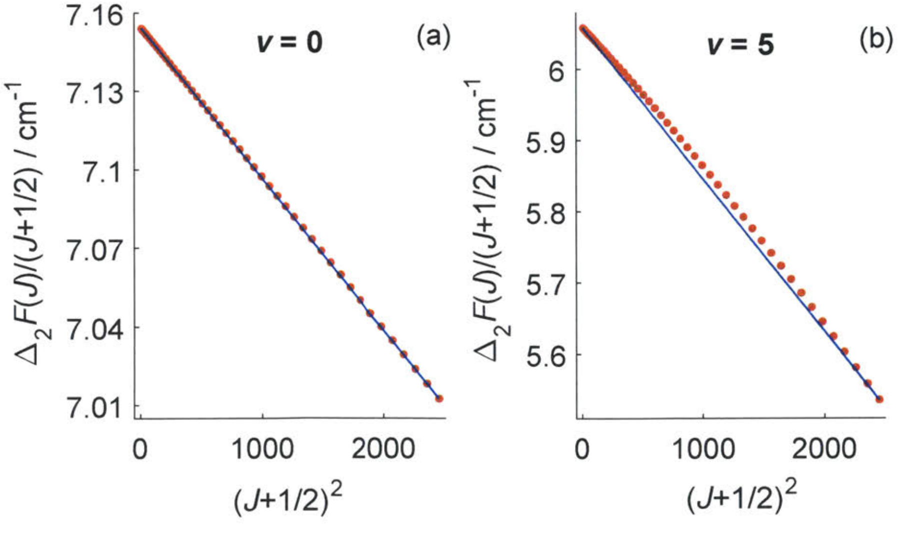

Figure 9-5: Calculated $\Delta_2 F(J)$ plots (orange dots) for the C-state $v = 0$ and 5 levels of $^{12}C_2$. The first and last data points in (a) and (b) are connected by a straight line (blue) to assist visualization of the curvatures.

constants than the perturbing C'-state level, because the two parts in the $\Delta_2 F(J)$ plot have different slopes and vertical-intercepts (extrapolation was needed to determine the vertical-intercept of the latter half of the plot). However, these assignments lead to an unphysical situation where the vibronic characters of the observed rotational levels change abruptly at the crossing point ($J = 35$) of the two interacting vibrational states, which, for some reason, did *not* result in an avoided-crossing. In addition, each of the C-state $v = 3 - 8$ levels interacts only locally with one closest-lying C'-state level ($v = 0 - 5$), i.e. the C-state $v = n$ level is perturbed only by the C'-state $v = n - 3$ level (where $n \geq 3$), and the two interacting levels typically lie within 10 cm^{-1} of each other. In order for the interaction to remain local, each pair of $C - C'$ level interactions must be small. However, small local interactions are not expected to result in large and extensive perturbations, as observed in the C-state (e.g. rapid and early convergence in the vibrational energy spacings, well below the dissociation limit).

We believe that the analysis of Messerle and Krauss was based on incorrect interpretations of the observed $\Delta_2 F(J)$ plots, which are well reproduced from our fit model (Fig. 9-5). For $v = 0 - 2$ levels, where no obvious perturbations were observed experimentally, the calculated $\Delta_2 F(J)$ plot (shown explicitly for the $v = 0$ level in Fig. 9-5a) is close to a straight line. For higher-lying levels, where apparent changes of slopes were observed in the experimental $\Delta_2 F(J)$ plots, the calculated $\Delta_2 F(J)$ plot (shown explicitly for the $v = 5$ level in Fig. 9-5b, which can be compared to Fig. 9-4) is curved. We must point out that there is not a clear and definitive turning point in each of the calculated $\Delta_2 F(J)$ plot. A clear separation of the observed $\Delta_2 F(J)$ plot into two distinct sections in Ref [108] was most likely an artifact of limited resolution and finite accuracy of the experimental measurements, i.e. the curved $\Delta_2 F(J)$ plot was interpreted as having two different slopes. Curvatures in the $\Delta_2 F(J)$ plot correspond to an apparent change in the value of B_v and D_v as a function of J, which was the basis of the deperturbation method in Ref [108].

Features in the $\Delta_2 F(J)$ plots can be understood in the diabatic representation, based on perturbation theory. For example, the zero-order d_1 $v = 5$ level ($v_1^d = 5$,

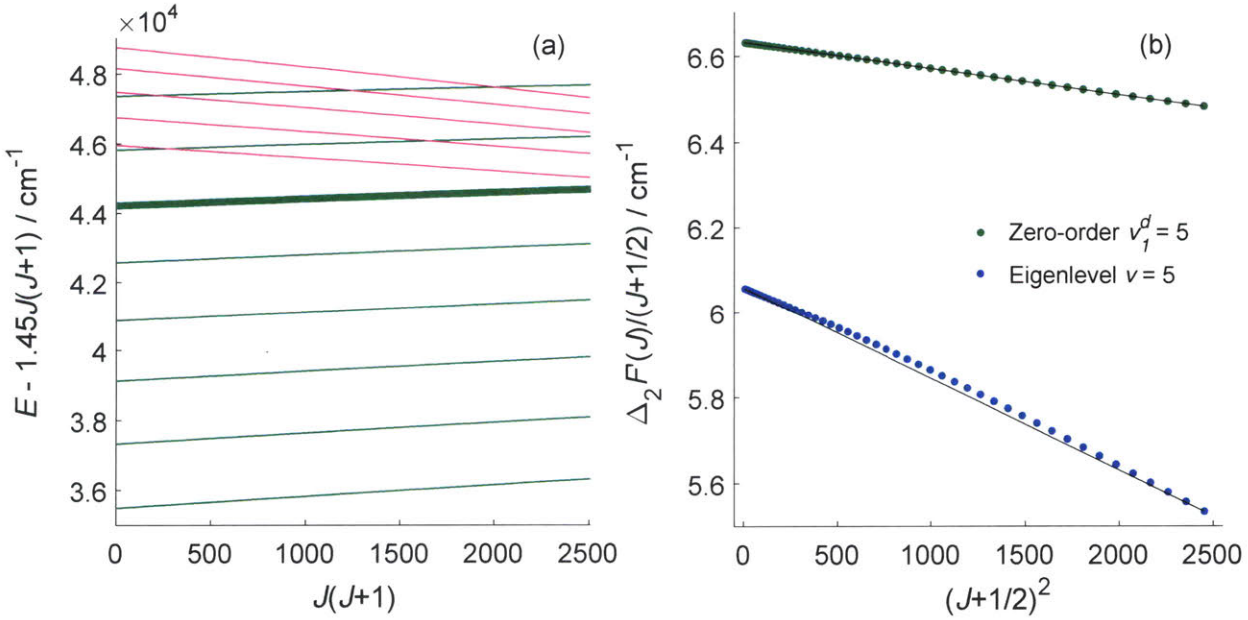

Figure 9-6: Origins of curvatures in the $\Delta_2 F'(J)$ plot. (a) Zero-order rovibrational levels (reduced term values) from the two diabatic states. The green and magenta lines indicate the locations of zero-order levels of the d_1 and d_2 state, respectively. The v_1^d=5 level is highlighted in bold. (b) Plots of $\Delta_2 F(J)/(J+1/2)$ against $(J+1/2)^2$ for the $v=5$ eigenlevel and the zero-order v_1^d=5 level.

highlighted in bold in Fig. 9-6a), which is the dominant basis state for the observed $v = 5$ level, has no curvature in its $\Delta_2 F(J)$ plot (Fig. 9-6b). All of the d_2 perturbing levels of $v_1^d = 5$ are *higher* in energy, and they also have much *smaller* B rotational constants than $v_1^d = 5$. The energy separations between $v_1^d = 5$ and its perturbers decrease as J increases. Consequently, higher J levels of $v_1^d = 5$ are pushed down in energy more than the lower J levels. The overall B rotational constant (related to the vertical intercept of the $\Delta_2 F(J)$ plot) of the observed $v = 5$ level becomes smaller than that of $v_1^d = 5$, and the $\Delta_2 F(J)$ plot of the observed $v = 5$ level is curved.

9.7 Conclusion

In this work, the rotation-vibration structure of the C_2 $C^1\Pi_g$ state is modeled as results of interactions between two diabatic electronic states. Our fit model successfully reproduces the experimental C-state rovibrational levels of $^{12}C_2$ and $^{13}C_2$, using both adiabatic and diabatic representations. We are able to show that, for the C_2 system studied in this work, the energies of the zero-order adiabatic basis states are much closer to the energies of the observed eigenstates, compared to the diabatic basis states.

The peculiar rotation-vibration features of the C_2 C-state can be understood in our two-state interaction model. The rapid and premature convergence in the vibrational energy spacings and rotational constants are both related to a hump on the lower adiabatic PEC, which lies well below the energy of the lowest C_2 dissociation limit. The hump is a direct result of electrostatic interactions between the two crossing diabatic electronic states. Curvatures in the $\Delta_2 F(J)$ plot, which were interpreted incorrectly by Messerle and Krauss [108], are reproduced in our calculations. A physical interpretation of those curvatures is provided in this work, based on perturbation theory in the diabatic representation.

The small systematic discrepancy in reproducing the observed C-state B_v rotational constants from our fit model might be an indication of the limit of our two-state model. As suggested by recent *ab initio* calculations of Sorensen and England [147] (see Fig. 3 of their work), strong interactions between d_1 and a third electronic configuration result in a hump on the a_1 PEC, similar to the one on the lower a_2 PEC. The hump on the a_1 PEC occurs at around $3000 - 4000$ cm^{-1} above the minimum of the a_1 state, which means that vibrational energy spacings of the a_1 vibrational levels converge even more rapidly than those of the a_2 levels (and the level spacings are expected to increase above the hump, before decreasing again as the molecule approaches the second C_2 dissociation limit). The a_1 rovibrational levels are also expected to be predissociated (given small but finite interactions with the surrounding a_2 continuum levels). Fluorescence quantum yield from those levels are expected to be low, which renders those states undetectable using fluorescence-based detection scheme. (In the discussions above, it is assumed that non-adiabatic couplings among the three adiabatic electronic states (in the three-state interaction picture) are small, which means that the a_1 and a_2 rovibrational levels are nearly the eigenstates of the system.)

We believe that our model provides a framework for more accurate determinations of the transition probabilities between $C^1\Pi_g$ and $A^1\Pi_u$ state rovibrational levels. It is well known that strong electrostatic interactions between two electronic configurations lead to significant R-dependent transition dipole moment between two adiabatic electronic states, as have been shown specifically for the C_2 $C - A$ transition in Ref [28]. However, given J-dependence in the diabatic interactions (as discussed in Section 9.6), the transition probabilities are also expected to be J-dependent, especially for $v > 2$ levels. Accurate determinations of the $C - A$ rovibrational transition probabilities are important in quantitative modelings of the $C - A$ emission spectrum of C_2, especially when the $C^1\Pi_g$ C_2 molecules are generated with high rotational and vibrational excitations [79, 101, 167]. High-level quantum chemical calculations of the electronic transition dipole moments are also required, between the A-state and each of the two electronic configurations of the C-state.

Appendix A

Laser-Induced Fluorescence Study of the S_1 State of Doubly-Substituted ^{13}C Acetylene and Harmonic Force Field Determination

A.1 The G and F matrix

The **G** matrix can be determined from

$$\mathbf{G} = \mathbf{B}\mathbf{m}^{-1}\mathbf{B}^T, \tag{A.1}$$

where **B** transforms Cartesian displacement coordinates (x, y, z-coordinate system defined in Fig. 7-1) to internal coordinates and $\mathbf{m}^{-1}$ is a diagonal inverse mass matrix. The **B** matrix, which is the same for all four isotopologues, is given by

$$\mathbf{B} = \begin{array}{|cccccccccccc|c}
\mathbf{H}_{1,y} & \mathbf{H}_{1,x} & \mathbf{H}_{1,z} & \mathbf{C}_{1,y} & \mathbf{C}_{1,x} & \mathbf{C}_{1,z} & \mathbf{C}_{2,y} & \mathbf{C}_{2,x} & \mathbf{C}_{2,z} & \mathbf{H}_{2,y} & \mathbf{H}_{2,x} & \mathbf{H}_{2,z} & \\
\hline
0 & \sin\theta & \cos\theta & 0 & -\sin\theta & -\cos\theta & 0 & 0 & 0 & 0 & 0 & 0 & \boldsymbol{r} \\
0 & 0 & 0 & 0 & 0 & -1 & 0 & 0 & 1 & 0 & 0 & 0 & \boldsymbol{R} \\
0 & 0 & 0 & 0 & 0 & 0 & 0 & \sin\theta & \cos\theta & 0 & -\sin\theta & -\cos\theta & \boldsymbol{r'} \\
0 & \frac{\cos\theta}{r_2} & \frac{-\sin\theta}{r_2} & 0 & -Q & \frac{\sin\theta}{r_2} & 0 & -\frac{1}{r_1} & 0 & 0 & 0 & 0 & \boldsymbol{\theta} \\
0 & 0 & 0 & 0 & \frac{1}{r_1} & 0 & 0 & Q & -\frac{\sin\theta}{r_2} & 0 & -\frac{\cos\theta}{r_2} & \frac{\sin\theta}{r_2} & \boldsymbol{\theta'} \\
\frac{1}{r_2\sin\theta} & 0 & 0 & \frac{-1}{r_2\sin\theta} & 0 & 0 & \frac{-1}{r_2\sin\theta} & 0 & 0 & \frac{1}{r_2\sin\theta} & 0 & 0 & \boldsymbol{\tau}
\end{array}$$

where $Q = \frac{\cos\theta}{r_2} - \frac{1}{r_1}$. r_1 and r_2 are as defined in Fig. 7-1, and $\theta = \angle CCH$. Each row of **B** corresponds to the transformation from the Cartesian displacement coordinates to the specific internal coordinate labeled in the last column. The **G** matrix can also be directly obtained from a purely geometrical point of view described in [178]. Our refined geometry of the S_1 *trans* conformer of acetylene is used in the determination of the **G** matrix for each isotopologue.The **F** matrix that should be used with the **G** matrix obtained from the **B** matrix above has the form:

$$\mathbf{F} = \begin{pmatrix} F_{rr} & F_{rR} & F_{rr'} & F_{r\theta} & F_{r\theta'} & 0 \\ F_{rR} & F_{RR} & F_{rR} & F_{R\theta} & F_{R\theta} & 0 \\ F_{rr'} & F_{rR} & F_{rr} & F_{r\theta'} & F_{r\theta} & 0 \\ F_{r\theta} & F_{R\theta} & F_{r\theta'} & F_{\theta\theta} & F_{\theta\theta'} & 0 \\ F_{r\theta'} & F_{R\theta} & F_{r\theta} & F_{\theta\theta'} & F_{\theta\theta} & 0 \\ 0 & 0 & 0 & 0 & 0 & F_{\tau\tau} \end{pmatrix}$$

There are no coupling terms between the torsional coordinate and the other internal coordinates, because only the torsional coordinate includes an out-of-plane motion. For the same reason, the **G** matrix is also block-diagonalized into an 1×1 ω_4 block and a 5×5 block.

Note that to obtain the Coriolis constant, ξ_{46}^{a}, from the **GF** procedure described in ref [161], the **B** matrix above needs to be transformed into the principal axis form. Also, there is a typo in Eq. (4) of ref [161]. The summation should be from $i = 1 - 4$, since there are only four atoms in acetylene, and the superscript should specify principal axes a, b, and c.

A.2 Rotational Line Assignments of $\tilde{A}-\tilde{X}$ transition of $^{13}C_2H_2$.

Table A.1: Rotational Line Assignments for V_0^0.

		$\Pi-\Sigma$		$\Sigma-\Sigma$	$\Delta-\Sigma$		$\Pi-\Sigma$
J	P	Q	R	Q	Q	J	R
0			42228.32			21	42232.70
1		42225.99	42230.27			22	
2	42221.59	42225.51	42231.98			23	42228.88
3	42219.06	42224.81	42233.55			24	42226.59
4	42216.33	42223.87[a]	42235.02	42212.45			
5	42213.43	42222.56	42236.33[a]	42211.41			
6	42210.41	42221.03	42237.35	42210.16			
7	42207.18	42219.30	42238.25	42208.66			
8	42203.79	42217.33	42239.00				
9		42215.05	42239.58	42205.10			
10		42212.64		42203.00			
11		42209.85					
12		42206.88					
13		42203.60					
14					42240.61		
15			42239.50		42237.73		
16			42238.82		42234.69		
17			42237.99		42231.48		
18			42237.01		42228.10		
19					42224.63		
20			42234.35				

[a] Not included in the fit because of large residuals (~0.1 cm^{-1}).

Table A.2: Rotational Line Assignments for V_0^1.

	$\Pi-\Sigma$			$\Sigma-\Sigma$	$\Delta-\Sigma$			$\Pi-\Sigma$
J	P	Q	R	Q	P	Q	J	R
0			43264.79				22	43267.54
1		43262.50	43266.72				23	43265.46
2	43258.07	43262.02	43268.49				24	43263.20
3	43255.56	43261.22	43270.03				25	43260.73
4	43252.81	43260.19	43271.46	43247.95			26	
5	43249.95	43258.94	43272.77	[a]			27	43255.13
6	43246.86	43257.44	43273.89	43245.67			28	
7	43243.70	43255.71	43274.77	43244.26			29	43248.46
8	43240.30	43253.64	43275.52	43242.49				
9		43251.38	43276.08	43240.60	43273.15			
10		43248.83			43268.97			
11		43246.04			[a]			
12		43243.00			[a]			
13		43239.72			[a]			
14					43250.46			
15					43245.27			
16			43275.42		43239.89			
17			43274.58			43270.43		
18			43273.61			43267.08		
19			43272.34			43263.47		
20			43270.90			43259.80		
21			43269.29			43255.97		

[a] Blended into a stronger peak nearby.

Table A.3: Rotational Line Assignments for V_0^2.

	$\Pi - \Sigma$			$\Sigma - \Sigma$		$\Pi - \Sigma$		$\Sigma - \Sigma$
J	P	Q	R	Q	J	R	Q	Q
0			44284.40		21	44289.01	44222.28	44216.28
1		44282.08	44286.33		22	44287.16	44216.48	44210.93
2	44277.69	44281.57	44288.09		23	44285.16	44210.39	44205.28
3	44275.14	44280.80	44289.63		24		44204.00	44199.33
4	44272.38	44279.78	44291.07		25		44197.34	44193.07
5	44269.53	44278.48	44292.35		26		44190.39	44186.50
6	44266.46	44276.96	44293.49	44264.17	27		44183.15	44179.62
7	44263.26	44275.17	44294.40		28			44172.43
8	44259.88	44273.11		44260.93				
9	44256.33	44270.82						
10	44252.63	44268.23		44256.84				
11	44248.75	44265.40		44254.42				
12	44244.69	[a]		44251.80				
13	44240.48	44258.94		44248.89				
14	44236.09	[a]		44245.76				
15	44231.52	44251.41		44242.36				
16	44226.77	44247.22		44238.70				
17	44221.84	44242.79		44234.78				
18	44216.74	44238.08	44293.24	44230.55				
19	44211.45	44233.10	44291.98	44226.10				
20	44205.97	44227.84	44290.55	44221.32				

[a] Doubling of lines observed, possibly due to perturbation. Q(12): 44262.26 and 44262.33; Q(14): 44255.24 and 44255.33.

Table A.4: Rotational Line Assignments for $2_0^1 V_0^0$.

	$\Pi-\Sigma$			$\Sigma-\Sigma$		$\Pi-\Sigma$
J	P	Q	R	Q	J	R
0			43565.15		21	43565.53
1		43562.83	43567.07		22	43563.35
2	43558.43	43562.33	43568.72		23	43560.89
3	435555.83	43561.52	43570.24			
4	43553.06	43560.42	43571.62			
5	43550.09	43559.14	43572.79	43548.13		
6	43546.97	43557.57	43573.73			
7	43543.66	43555.72	43574.46 [a]	43545.25		
8	43540.15	43553.63	43575.18	43543.43		
9	43536.51	43551.25		43541.34		
10	43532.62	43548.61				
11	43528.57	43545.70				
12	43524.36	43542.52		43533.81		
13	43519.94	43539.07	43575.45	43530.75		
14	43515.37	43535.38	43574.87	43527.48		
15	43510.52	43531.34		43523.93		
16	43505.54		43573.25	43520.10		
17		43522.52	43572.15	43515.99		
18		43517.70	43570.80	43511.60		
19		43512.60		43506.90		
20		43507.20	43567.51	43501.95		

[a] Not included in the fit because of large residuals ($\sim$0.1 cm^{-1}).

Table A.5: Rotational Line Assignments for $2_0^1V_0^1$.

	$\Pi-\Sigma$			$\Sigma-\Sigma$
J	P	Q	R	Q
0			44601.55	
1		44599.20	44603.42	
2	44594.84	44598.69	44605.13	
3	44592.20	44597.91	44606.66	
4	44589.47	44596.86	44608.00	
5	44586.48	44595.51	44609.16	
6	44583.37	44593.85	44610.14	44582.26
7	44580.05	44591.98	44610.94	44580.69
8	44576.54	44589.87	44611.54	44578.89
9	44572.87	44587.43	44611.99	44576.81
10	44569.03	44584.76		44574.49
11	44564.98	44581.76		44571.94
12	44560.74	44578.57		
13	44556.33	44575.02	44611.81	44566.07
14	44551.71	44571.23		
15	44546.92	44567.17	44610.58	44559.12
16	44541.91	44562.80	44609.66	44555.26
17		44558.17	44608.54	44551.10
18	44531.35	44553.28	44607.21	44546.66
19	44525.76	44548.07	44605.66	
20	44519.95	44542.56	44603.90	
21			44601.95	44531.54
22		44530.73	44599.72	44525.90
23		44524.36	44597.35	
24		44517.72	44594.67	44513.63
25		44510.75		44507.08
26		44503.52		
27		44495.97		44492.97

Table A.6: Rotational Line Assignments for $2^1_0 V^2_0$.

	$\Pi - \Sigma$			$\Sigma - \Sigma$
J	P	Q	R	Q
0			45620.55	
1		45618.23	45622.43	
2	45613.85	45617.67	45624.10	
3	45611.20	45616.87	45625.63	
4	45608.48	45615.81	45626.95	
5	45605.46	45614.42	45628.09	
6	45602.32	45612.72	45629.10	
7	45599.00	45610.83	45629.89	
8	45595.47	45608.66	45630.45	
9	45591.79	45606.16		
10	45587.91	45603.46		45592.47
11	45583.83	45600.38		
12	45579.56	45597.12		45586.98
13	45575.08	45593.53		
14	45570.44	45589.68		45580.50
15	45565.58	45585.49		45576.87
16	45560.49	45581.06		45572.86
17	45555.26	45576.33		45568.67
18	45549.80	45571.32		45564.18
19		45566.01		45559.32
20		45560.43		45554.22
21		45554.48		45548.79
22		45548.31		45543.06

Appendix B

The Rotation-Vibration Structure of the SO_2 $\tilde{C}^1B_2$ State Explained by a New Internal Coordinate Force Field

B.1 Construction of the Matrix Hamiltonian

Given a set of normal-mode force constants and the three parameters that describe a hump on the PES, a harmonic oscillator basis is used to construct a Hamiltonian matrix for each isotopologue (in our study, $S^{16}O_2$ and $S^{18}O_2$. The (rotationless) vibrational Hamiltonian matrix, as given in Eq. (8.1), is block-diagonalized into a_1 and a b_2 symmetry blocks. For the purpose of fitting to the observed energy levels, a dimension of around 1800 basis states for each symmetry block is found to be sufficient for convergence of the eigenvalues. Harmonic oscillator basis states that have diagonal matrix elements smaller than 21,000 cm^{-1} are included in the matrix. However, basis states with more than 22 quanta in ν_2 are excluded from the matrix because they are found to be unnecessary for eigenvalue convergence. Each Hamiltonian matrix (two for each isotopologue) is then diagonalized to obtain both eigenvalues and eigenvectors. Note that the matrix size necessary for eigenvalue convergence is large, despite the fact that only the lowest 60 eigenstates of each Hamiltonian are studied in the current work. The large size of the basis set is required because the harmonic basis set is not the most physical or efficient representation of the the $\tilde{C}$ state molecular system, primarily due to the presence of the double well structure of the PES.

B.2 Semiclassical Interpretations of the Wavefunctions

Based on visual inspection of the wavefunction shapes, the polyads of interest in Fig. 8-2 seem to exhibit semiclassical dynamics that correspond to the dynamics in the Zone III on the catastrophe map used in Kellman's work [87, 180]. The wavefunction of the highest member of each polyad for the $\tilde{C}$ state of SO_2 (see Fig. 8-2) resembles the wavefunction assigned as $[0,14]_{\mathrm{IIIbc}}$ in the first subfigure of Fig. B-1 (albeit with opposite pointing direction), while wavefunctions of the lower members of each polyad in Fig. 8-2 resemble the rest of the wavefunctions in Fig. B-1. Therefore, the lower members of each Fermi polyad in the $\tilde{C}$ state undergo what Kellman calls a resonance collective motion. The wavefunctions of those levels open up *completely* in the positive q_1 direction. The highest member of each polyad, $(v_\alpha, 0, 0)_l$, is a mixture of normal-mode and resonance collective mode states. The wavefunction of each highest-energy polyad level has contributions both from resonant collective motions, with the wavefunction opening up in the negative q_1 direction, and from normal-modes, which prevents the wavefunction from *completely* opening up, in contrast to the shapes of the wavefunctions of the lower polyad members.

Note that the majority of states within a given polyad in Zone III lie in region a of the classical polyad phase sphere (hence the subscripts 'IIIa' in the assignments of those states in Fig. B-1), where semiclassical trajectories of levels in this region correspond to a resonant collective mode. In the molecular systems Kellman has studied [87], the $[0,14]_{\mathrm{IIIbc}}$ level in Fig. B-1 spans both regions b and c. Trajectories in region b correspond to a different resonant collective mode (the wavefunction opens up in the direction opposite to the first resonant collective mode), while trajectories

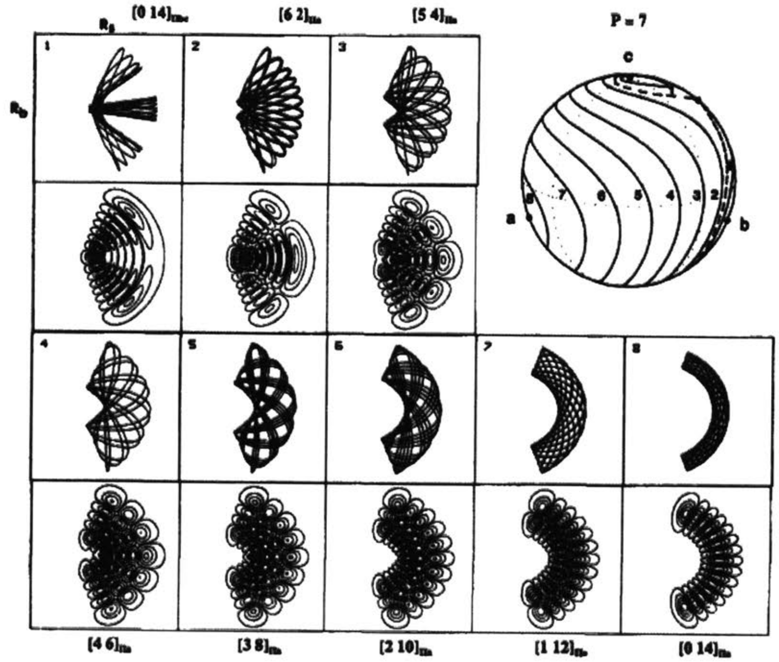

Figure B-1: Semiclassical dynamics in Zone III of Kellman's catastrophe map. Reproduced with permission from J. Chem. Phys. **93**, 5821 (1990). Copyright 1990 American Institute of Physics. Note that there are typographical errors in the assignments given in this figure. All of the 'II' in the subscripts of the assignment labels should be replaced by 'III'.

in region c correspond to normal stretching mode motion. As a result, the $[0,14]_{\text{IIIbc}}$ wavefunction has characters of both resonant collective mode and normal-mode wavefunctions.

We emphasize that, while we are using Kellman's assignment scheme, our notations are slightly different. First, in Kellman's notation, the subscripts indicate both the zone on the catastrophe map in which the polyad lies and the region on the polyad phase sphere where the level in question is located. In our notation, this semiclassical information is not included; instead, we give an r or l label, which indicates the direction in which the wavefunction opens. Our intention is to help the reader visualize the shape of the wavefunction. Second, our notations for the assignments of the highest member of the polyad differ from Kellman's choice. In his notation, the level we assign as $(3,0,0)_l$ would be $(0,0,6)_{\text{IIIbc}}$. Aside from the difference in the subscripts just discussed, the definitions of our quantum numbers differ from those used by Kellman [87]. In Kellman's choice, the quantum numbers for levels that span both regions b and c are defined with respect to the fixed point b in the polyad phase sphere shown in Fig. 8-2 [87], while in our choice, the quantum numbers for the same state are defined with respect to the normal-mode fixed point c, which, in the specific case of the $\tilde{\text{C}}$ state of SO_2, the fixed point c corresponds to the symmetric stretching normal-mode. Those two notations should be equally valid, since trajectories in regions b and c are degenerate, as long as one keeps in mind that semiclassically, the $(v_\alpha, 0, 0)_l$ state is a mixture of states in both regions b and c.

B.3 Supplementary Information

B.3.1 Treatment of the rotational constants

Rotational constants of molecules are typically linear functions of vibrational quantum numbers (see Eq. (5) of the paper). The proportionality factors, which are the rotation-vibration constants, are given by[23,24]

$$-\alpha_r^B = \frac{2B_e^2}{\omega_r}\left[\sum_{\xi}\frac{3(a_r^{b\xi})^2}{4I_\xi} + \sum_s (\zeta_{r,s}^b)^2\frac{3\omega_r^2+\omega_s^2}{\omega_r^2-\omega_s^2} + \pi\left(\frac{c}{h}\right)^{1/2}\sum_s \phi_{rrs}a_s^{bb}\left(\frac{\omega_r}{\omega_s^{3/2}}\right)\right], \tag{S1}$$

where $a_r^{\xi\xi'} = \frac{\partial I_{\xi\xi'}}{\partial q_r}$ and $\zeta_{r,s}^b$ is the Coriolis constant. The first contribution to Eq. (S1) comes from the mean square displacement of nuclei as a result of vibration, the second contribution is due to Coriolis interaction, and the last one is related to cubic anharmonicities of the PES.

However, it is not sufficient to use Eq. (5) alone to calculate the rotational constants of a vibrational level when resonant interactions occur among different modes of the molecule. As pointed out by earlier studies on the $\tilde{\text{C}}$ state of SO_2,[1,2,5–7] resonant interactions are pervasive in the $\tilde{\text{C}}$ state. The effects of resonant interactions on the rotational constants have been treated by Morino et al.[34] by taking a weighted linear combination of the rotational constants of the interacting levels, where the rotational constants of each level is derived using Eq. (5), and the weights are the squared coefficients of each interacting basis state in the vibrational eigenstate. In addition, for a molecule with a shallow double-well on its PES, the rotational constants are known to follow irregular patterns along the progression of the symmetry-breaking vibrational mode.[31–33] The irregular patterns could be reproduced by taking a vibration-average of the rotational Hamiltonian along the symmetry-breaking mode, but in the treatments of Refs [29, 47, 48], the effects from other sources of anharmonicities were neglected. In order to take into account both extreme anharmonicity in ν_3 and the resonant interactions in the $\tilde{\text{C}}$ state of SO_2, it is necessary to use Eq. (4) to calculate the rotational constants of a vibrational level of the $\tilde{\text{C}}$ state.

B.3.2 The Coriolis contributions to the effective C rotational constants

Using second-order perturbation theory, the correction to the rotational energy of a vibrational level, $|v\rangle$, due to the Coriolis interaction term in the molecular Hamiltonian, is given by the general expression of Eq. (6). This energy correction is sensitive to the energy differences between the levels v and v', where $\langle v| h_{21} |v'\rangle \neq 0$. For the ν_2 fundamental level of the $\tilde{\mathrm{C}}$ state of SO_2, for example, the largest contribution to the correction of its rotational energy comes from the interaction of the ν_2 fundamental level with the ν_3 fundamental. In the limit of a harmonic PES, where the Coriolis contribution (second term) in Eq. (S1) is derived, the energy difference between the two levels is simply given by $\omega_2 - \omega_3$. Anharmonicity spoils the goodness of using $\omega_2 - \omega_3$ as the energy difference between the two levels (as well as the validity of using harmonic oscillator basis states to evaluate the matrix element of the h operator defined in Eq. (7)). The effects from anharmonicity can be taken into account by using the weighted linear combination approach given in Eq. (4). This approach works for both A and B rotational constants of the $\tilde{\mathrm{C}}$ state of SO_2. However, for rotational constants that are perturbed by Coriolis interactions (such as the C rotational constants of the $\tilde{\mathrm{C}}$ state), this approach fails when the relative magnitude of the *harmonic* frequencies (ω) differ from that of the *fundamental* frequencies (ν), which occurs in the $\tilde{\mathrm{C}}$ state of SO_2 due to the presence of the double-well in the q_3 direction on the PES. Note that for the *harmonic* frequencies derived from our force field, $\omega_2 < \omega_3$, which would result in a positive Coriolis contribution to the value of α_2^C according to Eq. (S1). However, for the actual observed *fundamental* frequencies, $\nu_2 > \nu_3$, and the Coriolis contribution should actually be negative. To correctly calculate the Coriolis contributions to the C rotational constants of the $\tilde{\mathrm{C}}$ state, it is necessary to use the general expression given by Eq. (6) in Section II, where the actual vibrational eigenenergies and eigenvectors are used. The relative magnitudes of the harmonic frequencies are irrelevant in deriving both the first and third terms in Eq. (S1). This is the reason that, for the $\tilde{\mathrm{C}}$ state of SO_2, it is still valid to use the rotation-vibration constants associated with the A and B rotational constants in Eq. (4)-(5), despite the presence of a double well on the PES.

Appendix C

Two-state Interaction Model of the C_2 $C^1\Pi_g$ State

C.1 Numerical Details of the Calculations

Eigenvalues and normalized eigenvectors of Eq. (9.2) are obtained by numerically diagonalizing the matrix, at an evenly-spaced grid of R values, $0.8\,\text{Å} \leq R \leq 7\,\text{Å}$, with $\Delta R = 0.005\,\text{Å}$. From the effective PECs, zero-order rovibrational energies and wavefunctions are obtained numerically from Discrete Variable Representation (DVR) calculations. The vibrational wavefunctions are normalized, and the first inner lobe of the wavefunctions is taken to be positive. Depending on the representation, interaction matrix elements among the zero-order levels can be calculated accordingly (Section 9.2.1 or 9.2.2). In the adiabatic representation, methods of first and second symmetric derivative are used to numerically evaluate, respectively, the first and second derivative of the coefficients of the eigenvectors of the normalized eigenvectors of Eq. (9.2) with respect to R.

Given a shallow d_2 potential well, continuum levels of the d_2 state are relevant in our calculations. In this work, a steep wall is positioned at the upper $R = 7\,\text{Å}$ limit, which effectively discretizes the continuum. In the diabatic representation, a total of 50 vibrational states from the d_1 state and 500 states from d_2 are included in the calculation. In the adiabatic representation, a total of 250 vibrational states from the

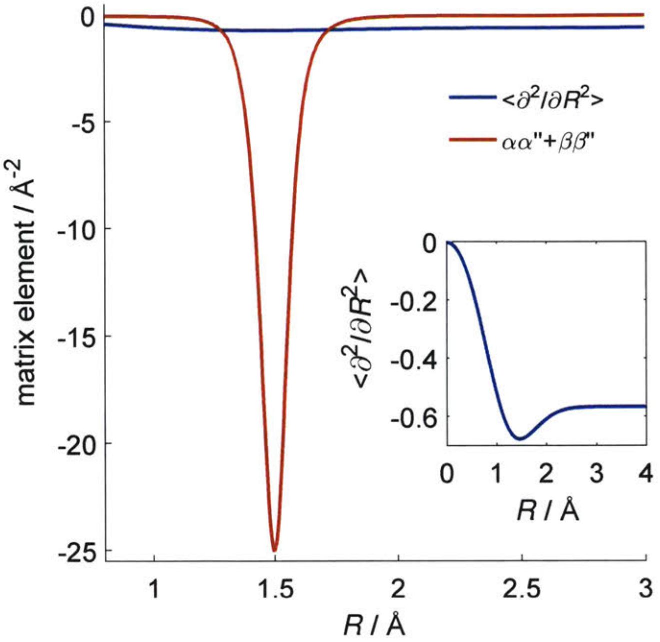

Figure C-1: Comparison of the $\alpha\alpha'' + \beta\beta''$ term with the diagonal matrix element of $\frac{\partial^2}{\partial R^2}$, approximated by Eq. (C.2). The inset provides an zoomed-in view of the $\frac{\partial^2}{\partial R^2}$ diagonal matrix element.

lower a_2 state and 30 states from the higher a_1 state are used. The vast majority of d_2 and a_2 states are the "discretized" continuum states. The final results are found to converge well, in both representations, with respect to the number of bound and quasi-continuum states, and the range of R used in the calculations. For example, for a given level included in the fit, the difference is $\ll 1\,\text{cm}^{-1}$ between calculation carried out with $R_{max} = 7\,\text{Å}$ and calculation with $R_{max} = 14\,\text{Å}$. Note that the number of d_2 states needed for convergence is much larger than that of a_2 states. This difference in the number of required basis states in the two representations is due to the fact that the adiabatic representation is a better representation of the $^1\Pi_g$ system of C_2 than the diabatic representation, as we show in Section 9.5.

C.2 The Order of Magnitudes of $\langle\Phi_i^d|\frac{\partial^2}{\partial R^2}|\Phi_j^d\rangle_r$

Lewis and Hougen [96] demonstrated that the matrix element, $\langle\Phi_i^d|\frac{\partial^2}{\partial R^2}|\Phi_j^d\rangle_r$ is on the order of magnitude of $1\,\text{Å}^{-2}$, which corresponds to an overall contribution of ~2-3

cm^{-1} to the system. In their work, the diabatic electronic wavefunctions were approximated as Gaussian orbitals which are centered on the nuclei as R changes. A similar (but slightly different) form of diabatic wavefunctions is used in this work, and the resulting $\langle\Phi_i^d|\,\frac{\partial^2}{\partial R^2}\,|\Phi_j^d\rangle_r$ matrix elements are compared to the remaining $\alpha\alpha''+\beta\beta''$ term in Eq. (9.8). The approximated one-dimensional diabatic electronic wavefunction is given by

$$|\Phi^d\rangle = \frac{1}{\sqrt{C}}\left[e^{-a^2(z-R/2)^2} + e^{-a^2(z+R/2)^2}\right], \tag{C.1}$$

where the parameter, a, characterizes the size of each atomic orbital, z is the electron coordinate along R, and $C = \frac{\sqrt{2\pi}}{a}(1+e^{-\frac{1}{2}a^2R^2})$. The diabatic wavefunction is properly normalized with respect to z. The two Gaussian functions in Eq. (C.1) approximate the two atomic orbitals centered at the nuclei. Given that the typical diameter of an atom (taken as positions at which the density of the electronic wavefunction decreases to $1/e$ of the maximum) is on the order of 1 Å, the typical value of the a parameter is $\sim 1.5\,\text{Å}^{-1}$. The diagonal matrix element of the $\frac{\partial^2}{\partial R^2}$ operator is thus approximated by

$$\langle\Phi^d|\,\frac{\partial^2}{\partial R^2}\,|\Phi^d\rangle_r = -\frac{a^2(-1+e^{a^2R^2}+a^2e^{a^2R^2/2}R^2)}{4(1+e^{a^2R^2/2})^2} \sim -\frac{a^2}{4}, \tag{C.2}$$

which is on the order of $0.1 - 1\ \text{Å}^{-2}$, in agreement with the result of Lewis and Hougen [96]. The off-digonal matrix element is expected to have a similar order of magnitude as the diagonal. In Fig. C-1, the magnitude of the $\alpha\alpha''+\beta\beta''$ term (obtained from the fit) is compared with that of Eq. (C.2). The diabatic $\frac{\partial^2}{\partial R^2}$ matrix element is about two orders of magnitude smaller than the $\alpha\alpha''+\beta\beta''$ term. In terms of overall contributions to the energies of the system (by multiplying each term with $\frac{\hbar^2}{2\mu}$, see Eq. (9.6)), the former contribution is ~1-2 cm^{-1}, and the latter ~50-100 cm^{-1}. In the diabatic representation, the contribution of the $\frac{\partial^2}{\partial R^2}$ matrix element is also negligible, considering that the electronic coupling factor is >1000 cm^{-1}. This justifies the approximations given by (9.9), which is applied consistently throughout the calculations in both representations.

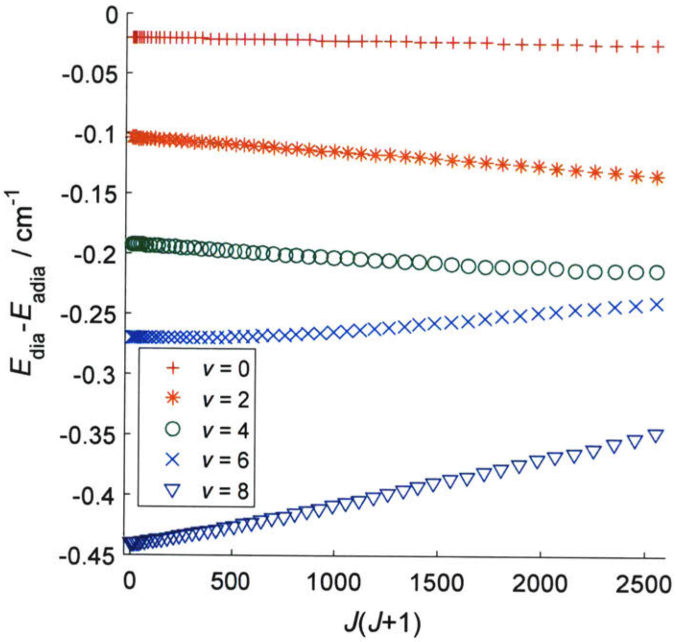

Figure C-2: Difference in the calculated energy levels using the adiabatic (E_{adia}) and diabatic (E_{dia}) representations.

C.3 Agreements between Calculations from the Adiabatic and Diabatic Representations

The eigenvalues of the full molecular Hamiltonian should be the same regardless of representation used in the calculations. For the lowest nine vibrational levels of the C_2 system, as can be seen from Fig. C-2, calculations based on the two representations agree with each other within 0.5 cm^{-1}, much less than the average fit residuals (2.3 cm^{-1}). An increase in the R-grid density ($\Delta R = 0.005\,\text{Å} \rightarrow \Delta R = 0.0025\,\text{Å}$) leads to a better agreement ($\sim$50% reduction in the discrepancy) between calculations from the two representations. This suggests that numerical errors are likely responsible for the discrepancy. Calculations in the adiabatic representation, which involve numerical first and second derivatives (Eqs. (9.6)-(9.8), and (9.10)-(9.11)), are more subject to the numerical errors, while calculations in the diabatic representation are found to converge well with respect to ΔR. In Fig. C-3, the difference in one of the diagonal adiabatic matrix elements, $\frac{\hbar^2}{2\mu}\left\langle\Phi_2^a\right|\frac{\partial^2}{\partial R^2}\left|\Phi_2^a\right\rangle_r$, is shown, between calculations with

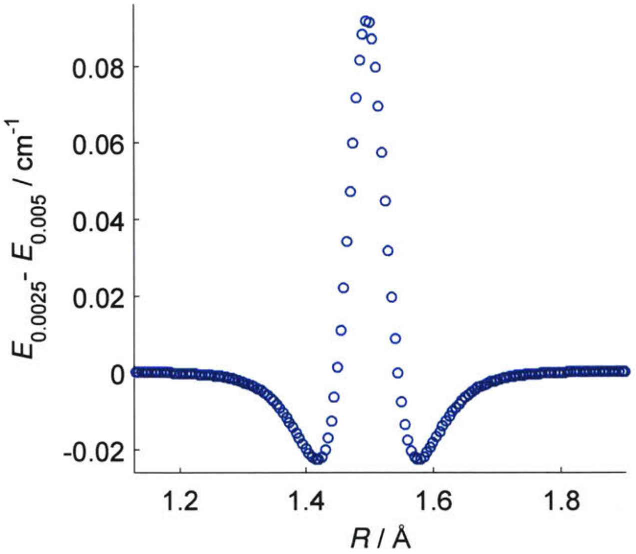

Figure C-3: Difference in $\frac{\hbar^2}{2\mu}\left\langle\Phi_2^a\right|\frac{\partial^2}{\partial R^2}\left|\Phi_2^a\right\rangle_r$ between calculations with $\Delta R = 0.0025\,\text{Å}$ ($E_{0.0025}$) and $\Delta R = 0.005\,\text{Å}$ ($E_{0.005}$), at common R values.

$\Delta R = 0.0025\,\text{Å}$ and $\Delta R = 0.005\,\text{Å}$. As the R-grid density is doubled, the diagonal contribution increases by $\sim$0.1 cm^{-1}, which is approximately the amount of improvement in agreement ($\sim$0.2 cm^{-1}) between calculations from the two representations for a specific level. In this work, $\Delta R = 0.005\,\text{Å}$ is used as a compromise between convergence and efficiency of calculation (and fit).

Bibliography

[1] C. Amiot and J. Verges. Fourier spectroscopy of the $C^{12}C^{13}$ and $^{13}C_2$ Phillips system. *Astronomy and Astrophysics Supplement Series*, 51:257–265, 1983.

[2] A. Antić-Jovanović, V. Bojović, D.S. Pesić, B.R. Vujisić, D. Rakotoarijimy, and S. Weniger. Study of isotopic $^{13}C_2$ bands of the Deslandres-d'Azambuja system. *Journal of Molecular Spectroscopy*, 110(1):86–92, 1985.

[3] M.N.R. Ashfold, B. Tutcher, B. Yang, Z.K. Jin, and S.L. Anderson. *Gerade* Rydberg states of acetylene studied by multiphoton ionization and photoelectron spectroscopy. *The Journal of Chemical Physics*, 87(9):5105–5115, 1987.

[4] David P. Baldwin, Mark A. Buntine, and David W. Chandler. Photodissociation of acetylene: Determination of D_0^0(HCC-H) by photofragment imaging. *The Journal of Chemical Physics*, 93(9):6578–6584, 1990.

[5] B.A. Balko, J. Zhang, and Yuan-Tseh Lee. 193 nm photodissociation of acetylene. *The Journal of Chemical Physics*, 94(12):7958–7966, 1991.

[6] E.A. Ballik and D.A. Ramsay. Infrared emission spectra from a carbon furnace. *The Journal of Chemical Physics*, 29(6):1418–1419, 1958.

[7] E.A. Ballik and D.A. Ramsay. Ground state of the C_2 molecule. *The Journal of Chemical Physics*, 31(4):1128–1128, 1959.

[8] E.A. Ballik and D.A. Ramsay. An extension of the Phillips system of C_2 and a survey of C_2 states. *The Astrophysical Journal*, 137:84, 1963.

[9] Joshua H. Baraban. *Spectroscopic Signatures of Isomerization.* PhD thesis, Massachusetts Institute of Technology, 2013.

[10] Joshua H. Baraban, Annelise R. Beck, Adam H. Steeves, John F. Stanton, and Robert W. Field. Reduced dimension discrete variable representation study of cis–trans isomerization in the S_1 state of C_2H_2. *The Journal of Chemical Physics*, 134(24):244311, 2011.

[11] Joshua H. Baraban, P. Bryan Changala, Georg Ch. Mellau, John F. Stanton, Anthony J. Merer, and Robert W. Field. Spectroscopic characterization of isomerization transition states. *Science*, 350(6266):1338–1342, 2015.

[12] Joshua H. Baraban, P. Bryan Changala, Anthony J. Merer, Adam H. Steeves, Hans A. Bechtel, and Robert W. Field. The $\tilde{\mathrm{A}}^1\mathrm{A}_u$ state of acetylene: ungerade vibrational levels in the region 45,800-46,550 cm^{-1}. *Molecular Physics*, 110(21-22):2707–2723, 2012.

[13] Joshua H. Baraban, Devin A. Matthews, and John F. Stanton. Communication: An accurate calculation of the S_1 $\mathrm{C}_2\mathrm{H}_2$ cis-trans isomerization barrier height. *The Journal of Chemical Physics*, 144(11):111102, 2016.

[14] Joshua H. Baraban, J.F. Stanton, A.J. Merer, and Robert W. Field. Anharmonic force fields of cis-and trans-S_1 $\mathrm{C}_2\mathrm{H}_2$. *Molecular Physics*, 110(21-22):2725–2733, 2012.

[15] A.P. Baronavski and J.R. McDonald. Multiphoton vacuum ultraviolet laser dissociation of $\mathrm{CH}_3\mathrm{Br}$—Analysis of chemiluminescent products. *Chemical Physics Letters*, 56(2):369–372, 1978.

[16] W. Bauer, K.H. Becker, M. Bielefeld, and R. Meuser. Lifetime measurements on electronically excited C_2 $(A^1\Pi_u)$ and C_2 $(d^3\Pi_g)$ by laser-induced fluorescence. *Chemical Physics Letters*, 123(1-2):33–36, 1986.

[17] K.H. Becker, D. Haaks, and M. Schürgers. Fluorescence by the vacuum-UV photolysis of acetylene. *Zeitschrift für Naturforschung A*, 26(10):1770–1771, 1971.

[18] P.R. Bevington and D.K. Robinson. *Data Reduction and Error Analysis for the Physical Sciences.* McGraw-Hill: New York, 2003.

[19] Kyle L. Bittinger, Wilton L. Virgo, and Robert W. Field. Spectral signatures of inter-system crossing mediated by energetically distant doorway levels: Examples from the acetylene S_1 state. *The Journal of Physical Chemistry A*, 115(43):11921–11943, 2011.

[20] Ota Bludský, Petr Nachtigall, Jan Hrušák, and Per Jensen. The calculation of the vibrational states of SO_2 in the $\tilde{\mathrm{C}}^1\mathrm{B}_2$ electronic state up to the SO $(^3\Sigma^-)$+O$(^3\mathrm{P})$ dissociation limit. *Chemical Physics Letters*, 318(6):607–613, 2000.

[21] S. Boyé, A. Campos, S. Douin, C. Fellows, D. Gauyacq, N. Shafizadeh, Ph. Halvick, and M. Boggio-Pasqua. Visible emission from the vibrationally hot $\mathrm{C}_2\mathrm{H}$ radical following vacuum-ultraviolet photolysis of acetylene: Experiment and theory. *The Journal of Chemical Physics*, 116(20):8843–8855, 2002.

[22] J.C.D. Brand, P.H. Chiu, A.R. Hoy, and H.D. Bist. Sulfur dioxide: Rotational constants and asymmetric structure of the $\tilde{\mathrm{C}}^1\mathrm{B}_2$ state. *Journal of Molecular Spectroscopy*, 60(1):43–56, 1976.

[23] Leo Brewer, W.T. Hicks, and O.H. Krikorian. Heat of sublimation and dissociation energy of gaseous C_2. *The Journal of Chemical Physics*, 36(1):182–188, 1962.

[24] P.R. Bunker. The electronic isotope shift in diatomic molecules and the partial breakdown of the Born-Oppenheimer approximation. *Journal of Molecular Spectroscopy*, 28(4):422–443, 1968.

[25] Robert L. Byer, R.L. Herbst, H. Kildal, and M.D. Levenson. Optically pumped molecular iodine vapor-phase laser. *Applied Physics Letters*, 20(11):463–466, 1972.

[26] A. Campos, S. Boye, Ph. Brechignac, S. Douin, C. Fellows, N. Shafizadeh, and D. Gauyacq. Vacuum-ultraviolet photodissociation of C_2H_2 via Rydberg states: A study of the fluorescent pathways. *Chemical Physics Letters*, 314(1):91–100, 1999.

[27] Cary F. Chabalowski, Robert J. Buenker, and Sigrid D. Peyerimhoff. Theoretical study of the electronic transition moments for the $d^3\Pi_g$-$a^3\Pi_u$ (Swan) and $e^3\Pi_g$-$a^3\Pi_u$ (Fox-Herzberg) bands in C_2. *Chemical Physics Letters*, 83(3):441–448, 1981.

[28] Cary F. Chabalowski, Sigrid D. Peyerimhoff, and Robert J. Buenker. The Ballik-Ramsay, Mulliken, Deslandres-d'Azambuja and Phillips systems in C_2: a theoretical study of their electronic transition moments. *Chemical Physics*, 81(1):57–72, 1983.

[29] Sunney I. Chan, John Zinn, Jose Fernandez, and William D. Gwinn. Trimethylene oxide. I. Microwave spectrum, dipole moment, and double minimum vibration. *The Journal of Chemical Physics*, 33(6):1643–1655, 1960.

[30] P. Bryan Changala. Reduced dimension rovibrational variational calculations of the S_1 state of C_2H_2. I. Methodology and implementation. *The Journal of Chemical Physics*, 140(2):024312, 2014.

[31] P. Bryan Changala, Joshua H. Baraban, Anthony J. Merer, and Robert W. Field. Probing cis-trans isomerization in the S_1 state of C_2H_2 via H-atom action and hot band-pumped IR-UV double resonance spectroscopies. *The Journal of Chemical Physics*, 143(8):084310, 2015.

[32] P. Bryan Changala, Joshua H. Baraban, John F. Stanton, Anthony J. Merer, and Robert W. Field. Reduced dimension rovibrational variational calculations of the S_1 state of C_2H_2. II. The S_1 rovibrational manifold and the effects of isomerization. *The Journal of Chemical Physics*, 140(2):024313, 2014.

[33] J. Chauville, J.P. Maillard, and A.W. Mantz. The infrared part of the C_2 Phillips system (2.3-0.9 μm). *Journal of Molecular Spectroscopy*, 68(3):399–411, 1977.

[34] Whe-Yi Chiang and Yen-Chu Hsu. Fluorescence lifetimes and predissociation processes in the $\tilde{B}^2A'$ state of CCH. *The Journal of Chemical Physics*, 112(17):7394–7399, 2000.

[35] Ara Chutjian, John K Link, and Leo Brewer. Measurement of lifetimes and quenching cross sections of the B state of I_2. *The Journal of Chemical Physics*, 46(7):2666–2675, 1967.

[36] J.B. Coon, N.W. Naugle, and R.D. McKenzie. The investigation of double-minimum potentials in molecules. *Journal of Molecular Spectroscopy*, 20(2):107–129, 1966.

[37] David M. Cooper and Ralph W. Nicholls. Absolute measurements of the electronic transition moments of seven band systems of the C_2 molecule. *Journal of Quantitative Spectroscopy and Radiative Transfer*, 15:139–150, 1975.

[38] Qiang Cui and Keiji Morokuma. Ab initio MO studies on the photodissociation of C_2H_2 from the S_1 (^1A_u) state. II. Mechanism involving triplet states. *Chemical Physics Letters*, 272(5-6):319–327, 1997.

[39] Qiang Cui and Keiji Morokuma. Ab initio molecular orbital studies on the structure, energies, and photodissociation of the electronic excited states of C_2H. *The Journal of Chemical Physics*, 108(2):626–636, 1998.

[40] Qiang Cui, Keiji Morokuma, and John F. Stanton. Ab initio MO studies on the photodissociation of C_2H_2 from the S_1 (^1A_u) state. Non-adiabatic effects and S-T interaction. *Chemical Physics Letters*, 263(1-2):46–53, 1996.

[41] L. Curtis, B. Engman, and P. Erman. High resolution lifetime studies of the $d^3\Pi_g$, $C^1\Pi_g$ and $D^1\Sigma_u^+$ states in C_2 with applications to estimates of the solar carbon abundance. *Physica Scripta*, 13(5):270, 1976.

[42] Mattijs de Groot, Robert W. Field, and Wybren J. Buma. Interference in acetylene intersystem crossing acts as the molecular analog of Young's double-slit experiment. *Proceedings of the National Academy of Sciences*, 106(8):2510–2514, 2009.

[43] Wolfang Demtröder. *Laser Spectroscopy Vol. 2: Experimental Techniques*. Springer-Verlag Berlin Heidelberg, 2008.

[44] H. Deslandres and L. d'Azambuja. Variations des spectres de bandes du carbone avec la pression, et nouveaux spectres de bandes du carbone. *Comptes Rendus*, 140:917, 1905.

[45] G. Di Lonardo, P. Ferracuti, L. Fusina, E. Venuti, and J.W.C. Johns. Vibration-rotation spectra of ^{13}C containing acetylene. *Journal of Molecular Spectroscopy*, 161:466–486, 1993.

[46] G.H. Dieke and W. Lochte-Holtgreven. Über einige Banden des Kohlenstoffimoleküls. *Zeitschrift für Physik*, 62(11-12):767–794, 1930.

[47] J.A. Duckett, Alan G. Robiette, and I.M. Mills. The two-dimensional anharmonic oscillator: The microwave spectrum of silyl isocyanate, SiH_3NCO. *Journal of Molecular Spectroscopy*, 62(1):34–52, 1976.

[48] J.A. Duckett, Alan G. Robiette, and I.M. Mills. The two-dimensional anharmonic oscillator: Vibration-rotation constants of fulminic acid, HCNO. *Journal of Molecular Spectroscopy*, 62(1):19–33, 1976.

[49] Denis Duflot, J-M. Robbe, and J-P. Flament. Ab initio potential energy surfaces for $C_2H \rightarrow C_2+$ H photodissociation. *The Journal of Chemical Physics*, 100(2):1236–1246, 1994.

[50] J.L. Duncan. Force-constant calculations in molecules. In R. F. Barrow, D. A. Long, and D. J. Millen, editors, *Molecular Spectroscopy Volume 3 Specialist Periodical Reports*, chapter 2, pages 104–157. The Chemical Society: London, 1984.

[51] T. Ebata, O. Nakazawa, and M. Ito. Rovibrational dependences of the predissociation in the $\tilde{C}^1B_2$ state of SO_2. *Chemical Physics Letters*, 143(1):31–37, 1988.

[52] D.E. Freeman, K. Yoshino, J.R. Esmond, and W.H. Parkinson. High resolution absorption cross section measurements of SO_2 at 213 K in the wavelength region 172-240 nm. *Planetary and Space Science*, 32(9):1125–1134, 1984.

[53] Michael J. Frost. Energy transfer in the 3_1, $2_14_15_1$ Fermi-resonant states of acetylene. I. Rotational energy transfer. *The Journal of Chemical Physics*, 98(11):8572–8579, 1993.

[54] Michael J. Frost and Ian W.M. Smith. Energy transfer in the 3_1, $2_14_15_1$ Fermi Resonant states of acetylene. 2. Vibrational energy transfer. *The Journal of Physical Chemistry*, 99(4):1094–1100, 1995.

[55] C. Galloy and J.C. Lorquet. Nonadiabatic interaction in unimolecular decay. III. Selection and propensity rules for polyatomic molecules. *The Journal of Chemical Physics*, 67(10):4672–4680, 1977.

[56] Manfred Gehrtz, Edward A. Whittaker, and Gary C. Bjorklund. Quantum-limited laser frequency-modulation spectroscopy. *Journal of the Optical Society of America B*, 2(9):1510–1526, 1985.

[57] L. Gerö and R.F. Schmid. On perturbations causing apparent convergence in the C_2 spectrum. *Physical Review*, 62(1-2):82, 1942.

[58] Y. Gontier and M. Trahin. On the multiphoton absorption in atomic hydrogen. *Physics Letters A*, 36(6):463–464, 1971.

[59] W. Gordy and R.L. Cook. *Microwave Molecular Spectra.* John Wiley & Sons: New York, 1984.

[60] Akimitsu Haijima, Masaaki Fujii, and Mitsuo Ito. Predissociation of the acetylene $\tilde{A}^1A_u$ state and its mechanism. *The Journal of Chemical Physics*, 92(2):959–968, 1990.

[61] Gregory E. Hall and Simon W. North. Transient laser frequency modulation spectroscopy. *Annual Review of Physical Chemistry*, 51(1):243–274, 2000.

[62] Karl-Eliv Johann Hallin. *Some Aspects of the Electronic Spectra of Small triatomic molecules.* PhD thesis, The University of British Columbia, 1977.

[63] J.C. Han, Chao Ye, Masako Suto, and L.C. Lee. Fluorescence from photoexcitation of C_2H_2 at 50-106 nm. *The Journal of Chemical Physics*, 90(8):4000–4007, 1989.

[64] Nobuhisa Hashimoto and Toshinori Suzuki. Energy and state dependence in the quenching and predissociation of C_2H_2. *The Journal of Chemical Physics*, 104(15):6070–6073, 1996.

[65] G. Herzberg. *Molecular Spectra and Molecular Structure II. Infrared and Raman Spectra of Polyatomic Molecules.* Van Nostrand Reinhold: New York, 1945.

[66] G. Herzberg. *Molecular Spectra and Molecular Structure: Spectra of Diatomic Molecules.* Van Nostrand, New York, 1950.

[67] G. Herzberg and R.B. Sutton. Tail bands of the Deslandres-d'Azambuja system of the C_2 molecule. *Canadian Journal of Research*, 18(4):74–82, 1940.

[68] Jon T. Hougen and Anthony J. Merer. Extended permutation-inversion groups for simultaneous treatment of the rovibronic states of trans-acetylene, cis-acetylene, and vinylidene. *Journal of Molecular Spectroscopy*, 267(1):200–221, 2011.

[69] J.T. Hougen and J.K.G. Watson. Anomalous rotational line intensities in electronic transitions of polyatomic molecules: Axis-switching. *Canadian Journal of Physics*, 43(2):298–320, 1965.

[70] A.R. Hoy and J.C.D. Brand. Asymmetric structure and force field of the $^1B_2(^1A')$ state of sulphur dioxide. *Molecular Physics*, 36(5):1409–1420, 1978.

[71] A.R. Hoy, I.M. Mills, and G. Strey. Anharmonic force constant calculations. *Molecular Physics*, 24(6):1265–1290, 1972.

[72] Klaus-Peter Huber and G. Herzberg. *Molecular spectra and molecular structure: IV. Constants of diatomic molecules.* Van Nostrand Reinhold Company, 1979.

[73] T.R. Huet, Michel Godefroid, and Michel Herman. The $\tilde{A}$ electronic state of acetylene: Geometry and axis-switching effects. *Journal of Molecular Spectroscopy*, 144(1):32–44, 1990.

[74] T.R. Huet and Michel Herman. The $\tilde{A}$-$\tilde{X}$ band system of C_2D_2: Vibration-rotation constants for the $\tilde{A}^1A_u$ state. *Journal of Molecular Spectroscopy*, 137(2):396–419, 1989.

[75] C.K. Ingold and G.W. King. Excited states of acetylene. Part I-V. *Journal of the Chemical Society*, pages 2702–2755, 1953.

[76] K. Keith Innes. Analysis of the near ultraviolet absorption spectrum of acetylene. *The Journal of Chemical Physics*, 22(5):863–876, 1954.

[77] K.K. Innes. SO_2: Origins of unequal bond lengths in the $\tilde{C}^1B_2$ electronic state. *Journal of Molecular Spectroscopy*, 120(1):1–4, 1986.

[78] Jun Jiang, Joshua H. Baraban, G. Barratt Park, Michelle L. Clark, and Robert W. Field. Laser-induced fluorescence study of the S_1 state of doubly-substituted ^{13}C acetylene and harmonic force field determination. *The Journal of Physical Chemistry A*, 117(50):13696–13703, 2013.

[79] Jun Jiang, G. Barratt Park, and Robert W. Field. The rotation-vibration structure of the SO_2 $\tilde{C}^1B_2$ state explained by a new internal coordinate force field. *The Journal of Chemical Physics*, 144(14):144312, 2016.

[80] V.T. Jones and J.B. Coon. The ultraviolet spectrum of SO_2 in matrix isolation and the vibrational structure of the 2348 Å system. *Journal of Molecular Spectroscopy*, 47(1):45–54, 1973.

[81] Peter A. Jungner, Steve Swartz, Mark Eickhoff, Jun Ye, J.L. Hall, and S. Waltman. Absolute frequency of the molecular iodine transition R(56)32-0 near 532 nm. *IEEE Transactions on Instrumentation and Measurement*, 44(2):151–154, 1995.

[82] Wolf Ekkehard Kammer. Ab initio SCF and CI calculations of linear and bent acetylene. *Chemical Physics Letters*, 6(5):529–532, 1970.

[83] Hideki Katagiri, Tokuei Sako, Akiyoshi Hishikawa, Takeki Yazaki, Ken Onda, Kaoru Yamanouchi, and Kouichi Yoshino. Experimental and theoretical exploration of photodissociation of SO_2 via the $\tilde{C}^1B_2$ state: Identification of the dissociation pathway. *Journal of Molecular Structure*, 413:589–614, 1997.

[84] Victor Kaufman and John F. Ward. Measurement and calculation of Cu II, Ge II, Si II, and C I vacuum-ultraviolet lines. *Journal of the Optical Society of America*, 56(11):1591–1597, 1966.

[85] Michael E. Kellman and Eric D. Lynch. Fermi resonance phase space structure from experimental spectra. *The Journal of Chemical Physics*, 85(12):7216–7223, 1986.

[86] Michael E. Kellman and Eric D. Lynch. Semiclassical phase space evolution of Fermi resonance spectra. *The Journal of Chemical Physics*, 88(4):2205–2215, 1988.

[87] Michael E. Kellman and Lin Xiao. New assignment of Fermi resonance spectra. *The Journal of Chemical Physics*, 93(8):5821–5825, 1990.

[88] K. Kirby and B. Liu. The valence states of C_2: a configuration interaction study. *The Journal of Chemical Physics*, 70(2):893–900, 1979.

[89] H. Kopfermann and H. Schweitzer. Über ein Bandensystem des zweiatomigen Kohledampfes. *Zeitschrift für Physik*, 61(1-2):87–94, 1930.

[90] J. Kordis and K.A. Gingerich. Gaseous phosphorus compounds. IX. Mass spectrometric studies of equilibria in the carbon-phosphorus system. *The Journal of Chemical Physics*, 58(11):5058–5066, 1973.

[91] H.W. Kroto. *Molecular Rotation Spectroscopy*. Wiley: New York, 1975.

[92] Fabrice Laruelle, Séverine Boyé-Péronne, Dolores Gauyacq, and Jacques Liévin. Revisiting Mulliken's concepts about Rydberg states and Rydberg-Valence interactions from large-scale ab initio calculations on the acetylene molecule. *The Journal of Physical Chemistry A*, 113(47):13210–13220, 2009.

[93] Helene Lefebvre-Brion and Robert W. Field. *The Spectra and Dynamics of Diatomic Molecules: Revised and Enlarged Edition*. Elsevier Academic Press, 2004.

[94] Robert J. LeRoy. Molecular constants and internuclear potential of ground-state molecular iodine. *The Journal of Chemical Physics*, 52(5):2683–2689, 1970.

[95] M.D. Levenson, W.E. Moerner, and D.E. Horne. FM spectroscopy detection of stimulated Raman gain. *Optics Letters*, 8(2):108–110, 1983.

[96] J.K. Lewis and J.T. Hougen. Avoided crossings in bound potential-energy curves of diatomic molecules: Derivation and analysis of the vibrational Hamiltonian. *The Journal of Chemical Physics*, 48(12):5329–5336, 1968.

[97] Zhiming Li, Lin Xiao, and Michael E. Kellman. Phase space bifurcation structure and the generalized local-to-normal transition in resonantly coupled vibrations. *The Journal of Chemical Physics*, 92(4):2251–2268, 1990.

[98] Jacques Lievin. Ab initio characterization of the $\tilde{C}'^1A_g$ state of the acetylene molecule. *Journal of Molecular Spectroscopy*, 156(1):123–146, 1992.

[99] James K. Lundberg, Yongqin Chen, Jean-Paul Pique, and Robert W. Field. Ultraviolet-optical double-resonance study of the predissociated $\tilde{C}'^1A_g$ state of acetylene. *Journal of Molecular Spectroscopy*, 156(1):104–122, 1992.

[100] James K. Lundberg, David M. Jonas, Bhavani Rajaram, Yongqin Chen, and Robert W. Field. Rotationally resolved ultraviolet-ultraviolet double resonance study of the nonplanar $\tilde{E}$ state of acetylene. *The Journal of Chemical Physics*, 97(10):7180–7196, 1992.

[101] J.R. McDonald, A.P. Baronavski, and V.M. Donnelly. Multiphoton-vacuum-ultraviolet laser photodissociation of acetylene: Emission from electronically excited fragments. *Chemical Physics*, 33(2):161–170, 1978.

[102] C. Alden Mead and Donald G. Truhlar. Conditions for the definition of a strictly diabatic electronic basis for molecular systems. *The Journal of Chemical Physics*, 77(12):6090–6098, 1982.

[103] Janet Hawkins Meal and S.R. Polo. Vibration-rotation interaction in polyatomic molecules. II. The determination of Coriolis coupling coefficients. *The Journal of Chemical Physics*, 24(6):1126–1133, 1956.

[104] Anthony J. Merer, Zicheng Duan, Robert W. Field, and James K.G. Watson. Perturbations in the $4\nu_3$ level of the $\tilde{\mathrm{A}}^1\mathrm{A}_u$ state of acetylene, $\mathrm{C_2H_2}$. *Canadian Journal of Physics*, 87(5):437–441, 2009.

[105] Anthony J. Merer, Adam H. Steeves, Joshua H. Baraban, Hans A. Bechtel, and Robert W. Field. Cis-trans isomerization in the $\mathrm{S_1}$ state of acetylene: Identification of cis-well vibrational levels. *The Journal of Chemical Physics*, 134(24):244310, 2011.

[106] Anthony J. Merer, Nami Yamakita, Soji Tsuchiya, John F. Stanton, Zicheng Duan, and Robert W. Field. New vibrational assignments in the $\tilde{\mathrm{A}}^1\mathrm{A}_u$-$^1\Sigma_g^+$ electronic transition of acetylene, $\mathrm{C_2H_2}$: the ν_1' frequency. *Molecular Physics*, 101(4-5):663–673, 2003.

[107] Anthony J. Merer, Nami Yamakita, Soji Tsuchiya, Adam H. Steeves, Hans A. Bechtel, and Robert W. Field. Darling-Dennison resonance and Coriolis coupling in the bending overtones of the $\tilde{\mathrm{A}}^1\mathrm{A}_u$ state of acetylene, $\mathrm{C_2H_2}$. *The Journal of Chemical Physics*, 129(5):054304, 2008.

[108] G. Messerle and L. Krauss. Ein neues $c'^1\pi_g - b^1\pi_u$-Bandensystem des $\mathrm{C_2}$-Moleküls. *Zeitschrift für Naturforschung*, 22 a:2015–2023, 1967.

[109] Ian M. Mills. Vibration-rotation structure in asymmetric- and symmetric-top molecules. In K. Narahari Rao and C. Weldon Mathews, editors, *Molecular Spectroscopy*, pages 115 – 140. Academic Press, 1972.

[110] I.M. Mills. Harmonic and anharmonic force field calculations. In R.N. Dixon, editor, *Theoretical Chemistry*, volume 1, pages 110–159. The Royal Society of Chemistry, 1974.

[111] Miwako Mizoguchi, Nami Yamakita, Soji Tsuchiya, Atsushi Iwasaki, Kennosuke Hoshina, and Kaoru Yamanouchi. IR-UV double resonance spectroscopy of acetylene in the $\tilde{A}^1A_u$ $n\nu_3' + \nu_4'$ and $n\nu_3' + \nu_6'$ ($n = 2, 3$) *ungerade* vibrational states. *The Journal of Physical Chemistry A*, 104(45):10212–10219, 2000.

[112] David H. Mordaunt and Michael N.R. Ashfold. Near ultraviolet photolysis of C_2H_2: A precise determination of D_0 (HCC-H). *The Journal of Chemical Physics*, 101(3):2630–2631, 1994.

[113] David H. Mordaunt, Michael N.R. Ashfold, Richard N. Dixon, Peter Löffler, Ludger Schnieder, and Karl H. Welge. Near threshold photodissociation of acetylene. *The Journal of Chemical Physics*, 108(2):519–526, 1998.

[114] Yonezo Morino, Yoshikazu Kikuchi, Shuji Saito, and Eizi Hirota. Equilibrium structure and potential function of sulfur dioxide from the microwave spectrum in the excited vibrational state. *Journal of Molecular Spectroscopy*, 13(1):95–118, 1964.

[115] Thomas Müller, Michal Dallos, Hans Lischka, Zsófia Dubrovay, and Péter G. Szalay. A systematic theoretical investigation of the valence excited states of the diatomic molecules B_2, C_2, N_2 and O_2. *Theoretical Chemistry Accounts*, 105(3):227–243, 2001.

[116] Robert S. Mulliken. Note on electronic states of diatomic carbon, and the carbon-carbon bond. *Physical Review*, 56(8):778, 1939.

[117] R.S. Mulliken. The lower excited states of some simple molecules. *Canadian Journal of Chemistry*, 36(1):10–23, 1958.

[118] Petr Nachtigall, Jan Hrušák, Ota Bludský, and Suehiro Iwata. Investigation of the potential energy surfaces for the ground $\tilde{X}^1A_1$ and excited $\tilde{C}^1B_2$ electronic states of SO_2. *Chemical Physics Letters*, 303(3):441–446, 1999.

[119] C. Naulin, M. Costes, and G. Dorthe. C_2 radicals in a supersonic molecular beam. Radiative lifetime of the $d^3\Pi_g$ state measured by laser-induced fluorescence. *Chemical Physics Letters*, 143(5):496–500, 1988.

[120] Simon W. North and Gregory E. Hall. Vector and scalar correlations in statistical dissociation: The photodissociation of NCCN at 193 nm. *The Journal of Chemical Physics*, 106(1):60–76, 1997.

[121] Simon W. North, Xiaonan S. Zheng, Ruian Fei, and Gregory E. Hall. Line shape analysis of Doppler broadened frequency-modulated line spectra. *The Journal of Chemical Physics*, 104(6):2129–2135, 1996.

[122] H. Okabe. Photodissociation of acetylene and bromoacetylene in the vacuum ultraviolet: Production of electronically excited C_2H and C_2. *The Journal of Chemical Physics*, 62(7):2782–2787, 1975.

[123] H. Okabe. Photochemistry of acetylene. *Canadian Journal of Chemistry*, 61(5):850–855, 1983.

[124] Hideo Okabe, R.J. Cody, and J.E. Allen. Laser photolysis of C_2H_2 and CF_3C_2H at 193 nm: Production of C_2 ($d^3\Pi_g$) and CH ($A^2\Delta$) and their quenching by Xe. *Chemical Physics*, 92(1):67–73, 1985.

[125] Brian J. Orr and Ian W.M. Smith. Collision-induced vibrational energy transfer in small polyatomic molecules. *Journal of Physical Chemistry*, 91(24):6106–6119, 1987.

[126] D. Papoušek and M.R. Aliev. *Molecular Vibrational-rotational Spectra: Theory and Applications of High Resolution Infrared, Microwave and Raman Spectroscopy of Polyatomic Molecules*. Elsevier, 1982.

[127] G. Barratt Park. Full dimensional Franck-Condon factors for the acetylene $\tilde{\mathrm{A}}^1\mathrm{A}_u$-$\tilde{\mathrm{X}}^1\Sigma_g^+$ transition. I. Method for calculating polyatomic linear–bent vibrational intensity factors and evaluation of calculated intensities for the *gerade* vibrational modes in acetylene. *The Journal of Chemical Physics*, 141(13):134304, 2014.

[128] G. Barratt Park. *Dynamically Motivated Spectroscopy of Small Polyatomic Molecules*. PhD thesis, Massachusetts Institute of Technology, 2015.

[129] G. Barratt Park, Joshua H. Baraban, and Robert W. Field. Full dimensional Franck-Condon factors for the acetylene $\tilde{\mathrm{A}}^1\mathrm{A}_u$-$\tilde{\mathrm{X}}^1\Sigma_g^+$ transition. II. Vibrational overlap factors for levels involving excitation in *ungerade* modes. *The Journal of Chemical Physics*, 141(13):134305, 2014.

[130] G. Barratt Park, Jun Jiang, and Robert W. Field. The origin of unequal bond lengths in the $\tilde{\mathrm{C}}^1\mathrm{B}_2$ state of SO_2: Signatures of high-lying potential energy surface crossings in the low-lying vibrational structure. *The Journal of Chemical Physics*, 144(14):144313, 2016.

[131] G. Barratt Park, Jun Jiang, Catherine A. Saladrigas, and Robert W. Field. Observation of b_2 symmetry vibrational levels of the SO_2 $\tilde{\mathrm{C}}^1\mathrm{B}_2$ state: Vibrational level staggering, Coriolis interactions, and rotation-vibration constants. *The Journal of Chemical Physics*, 144(14):144311, 2016.

[132] G. Barratt Park, Adam H. Steeves, Joshua H. Baraban, and Robert W. Field. Simplified cartesian basis model for intrapolyad emission intensities in the bent-to-linear electronic transition of acetylene. *The Journal of Physical Chemistry A*, 119(5):857–865, 2015.

[133] G. Barratt Park, Caroline C. Womack, Andrew R. Whitehill, Jun Jiang, Shuhei Ono, and Robert W. Field. Millimeter-wave optical double resonance schemes for rapid assignment of perturbed spectra, with applications to the $\tilde{C}^1B_2$ state of SO_2. *The Journal of Chemical Physics*, 142(14):144201, 2015.

[134] John G. Phillips. A new band system of the C_2 molecule. *The Astrophysical Journal*, 107:389, 1948.

[135] John G. Phillips. On the identification of the 3670 Å band of the C_2 molecule. *The Astrophysical Journal*, 112:131, 1950.

[136] Hong Ran, Daiqian Xie, and Hua Guo. Theoretical studies of absorption spectra of SO_2 isotopomers. *Chemical Physics Letters*, 439(4):280–283, 2007.

[137] L.S. Rothman, I.E. Gordon, Y. Babikov, A. Barbe, D. Chris Benner, P.F. Bernath, Manfred Birk, L. Bizzocchi, V. Boudon, L.R. Brown, et al. The HITRAN2012 molecular spectroscopic database. *Journal of Quantitative Spectroscopy and Radiative Transfer*, 130:4–50, 2013.

[138] Y. Saito, T. Hikida, T. Ichimura, and Y. Mori. Fluorescence of excited ethynyl radicals produced by pulsed vacuum ultraviolet photolyses of C_2H_2, C_2D_2, and C_2HBr. *The Journal of Chemical Physics*, 80(1):31–35, 1984.

[139] Tokuei Sako, Akiyoshi Hishikawa, and Kaoru Yamanouchi. Vibrational propensity in the predissociation rate of SO_2 ($\tilde{C}^1B_2$) by two types of nodal patterns in vibrational wavefunctions. *Chemical Physics Letters*, 294(6):571–578, 1998.

[140] T.E. Sharp and H.M. Rosenstock. Franck-Condon factors for polyatomic molecules. *The Journal of Chemical Physics*, 41(11):3453–3463, 1964.

[141] Shing-Kuo Shih, Sigrid D. Peyerimhoff, and Robert J. Buenker. Calculated potential surfaces for the description of the emission spectrum of the C_2H radical. *Journal of Molecular Spectroscopy*, 74(1):124–135, 1979.

[142] V. Sidis and H. Lefebvre-Brion. A 'quasi-diabatic' representation for inelastic collisions. Application to the scattering of He^+ by Ne. *Journal of Physics B: Atomic and Molecular Physics*, 4(8):1040, 1971.

[143] Anthony E. Siegman. *Lasers.* University Science Books, 1986.

[144] Michelle L. Silva. *Spectroscopic Investigations of the $\tilde{X}$ and $\tilde{A}$ State Dynamics of $^{13}C_2H_2$.* PhD thesis, Massachusetts Institute of Technology, 2002.

[145] Sadhu M. Singh and Joel Tellinghuisen. The visible emission spectrum of iodine. *Journal of Molecular Spectroscopy*, 47(3):409–419, 1973.

[146] Felix T. Smith. Diabatic and adiabatic representations for atomic collision problems. *Physical Review*, 179(1):111, 1969.

[147] Thomas E. Sorensen and Walter B. England. Valence states of C_2, Feynman's way. *The Journal of Chemical Physics*, 108(13):5205–5215, 1998.

[148] Osman Sorkhabi, Victor M. Blunt, Hua Lin, Dadong Xu, Jacek Wrobel, Roosevelt Price, and William M. Jackson. Photodissociation of C_2H at 193 nm: Branching ratios for the formation of C_2 in the $X^1\Sigma_g^+$, $A^1\Pi_u$, and $B'^1\Sigma_g^+$ states. *The Journal of Chemical Physics*, 107(23):9842–9851, 1997.

[149] Robert J. Spindler. Franck-Condon factors based on RKR potentials with applications to radiative absorption coefficients. *Journal of Quantitative Spectroscopy and Radiative Transfer*, 5(1):165–204, 1965.

[150] John F. Stanton, Chang-Ming Huang, and Pêter G. Szalay. Stationary points on the S_1 potential energy surface of C_2H_2. *The Journal of Chemical Physics*, 101(1):356–365, 1994.

[151] J. Stark and P. Lipp. The effect of inner molecular relative movement on the intensity of absorption of fluorescent by valence electrons. *Zeitschrift für Physikalische Chemie*, 86:36, 1913.

[152] Daniel A. Steck. *Rubidium 85 D Line Data*, 2013. http://steck.us/alkalidata/.

[153] Daniel A. Steck. *Rubidium 87 D Line Data*, 2013. http://steck.us/alkalidata/.

[154] Adam H. Steeves, Hans A. Bechtel, Anthony J. Merer, Nami Yamakita, Soji Tsuchiya, and Robert W. Field. Stretch-bend combination polyads in the $\tilde{A}^1A_u$ state of acetylene, C_2H_2. *Journal of Molecular Spectroscopy*, 256(2):256–278, 2009.

[155] Adam H. Steeves, Anthony J. Merer, Hans A. Bechtel, Annelise R. Beck, and Robert W. Field. Direct observation of the symmetric stretching modes of $\tilde{A}^1A_u$ acetylene by pulsed supersonic jet laser induced fluorescence. *Molecular Physics*, 106(15):1867–1877, 2008.

[156] L.J. Stief, V.J. DeCarlo, and R.J. Mataloni. Vacuum-ultraviolet photolysis of acetylene. *The Journal of Chemical Physics*, 42(9):3113–3121, 1965.

[157] Masako Suto and L.C. Lee. Quantitative photoexcitation and fluorescence studies of C_2H_2 in vacuum ultraviolet. *The Journal of Chemical Physics*, 80(10):4824–4831, 1984.

[158] Toshinori Suzuki and Nobuhisa Hashimoto. Predissociation of acetylene from the $\tilde{A}^1A_u$ state studied by absorption, laser-induced fluorescence, and H-atom action spectroscopies. *The Journal of Chemical Physics*, 110(4):2042–2050, 1999.

[159] A. Tanabashi, T. Hirao, T. Amano, and P.F. Bernath. The Swan system of C_2: a global analysis of Fourier transform emission spectra. *The Astrophysical Journal Supplement Series*, 169(2):472, 2007.

[160] J.D. Tobiason, A.L. Utz, and F.F. Crim. The direct observation, assignment, and partial deperturbation of ν_5 and $\nu_3 + \nu_5$ in $\tilde{A}^1A_u$ acetylene (C_2H_2). *The Journal of Chemical Physics*, 99(2):928–936, 1993.

[161] J.D. Tobiason, A.L. Utz, E.L. Sibert III, and F.F. Crim. Normal modes analysis of $\tilde{A}$-state acetylene based on directly observed fundamental vibrations. *The Journal of Chemical Physics*, 99(8):5762–5767, 1993.

[162] Kazuhide Tsuji, Naoko Arakawa, Akio Kawai, and Kazuhiko Shibuya. Spectroscopy and predissociation of acetylene in the np gerade Rydberg states. *The Journal of Physical Chemistry A*, 106(5):747–753, 2002.

[163] Kazuhide Tsuji, Kentaro Misawa, Junichi Awamura, Akio Kawai, and Kazuhiko Shibuya. Analysis of low-lying gerade Rydberg states of acetylene using two-photon resonance fluorescence excitation spectroscopy. *The Journal of Physical Chemistry A*, 117(7):1420–1427, 2013.

[164] Kazuhide Tsuji, Chiaki Terauchi, Kazuhiko Shibuya, and Soji Tsuchiya. Trans-cis isomerization of acetylene in the $\tilde{A}^1A_u$ state as studied by dispersed fluorescence spectroscopy. *Chemical Physics Letters*, 306(1):41–47, 1999.

[165] Sylvestre Twagirayezu, Trocia N. Clasp, David S. Perry, Justin L. Neill, Matt T. Muckle, and Brooks H. Pate. Vibrational coupling pathways in methanol as revealed by coherence-converted population transfer fourier transform microwave infrared double-resonance spectroscopy. *The Journal of Physical Chemistry A*, 114(25):6818–6828, 2010.

[166] John Tyson, Howard H. Claassen, and Hyunyong Kim. Molecular potential functions expressed in cartesian coordinates: Application to the orbital valency force field. *The Journal of Chemical Physics*, 54(7):3142–3156, 1971.

[167] R.S. Urdahl, Yihan Bao, and William M. Jackson. Observation of the LIF spectra of C_2 ($a^3\Pi_u$) and C_2 ($A^1\Pi_u$) from the photolysis of C_2H_2 at 193 nm. *Chemical Physics Letters*, 152(6):485–490, 1988.

[168] A.L. Utz, J.D. Tobiason, E. Carrasquillo M., L.J. Sanders, and F.F. Crim. The direct observation, assignment, and partial deperturbation of the ν_4 and ν_6 vibrational fundamentals in $\tilde{A}^1A_u$ acetylene (C_2H_2). *The Journal of Chemical Physics*, 98(4):2742–2753, 1993.

[169] J.C. Van Craen, M. Herman, R. Colin, and J.K.G. Watson. The $\tilde{A}$-$\tilde{X}$ band system of acetylene: Analysis of medium-wavelength bands, and vibration-rotation constants for the levels $n\nu_4''$ ($n = 4 - 6$), $\nu_2' + n\nu_3'$ ($n = 3 - 5$), and $\nu_1' + n\nu_3'$ ($n = 2, 3$). *Journal of Molecular Spectroscopy*, 111(1):185–197, 1985.

[170] J.C. Van Craen, M. Herman, R. Colin, and J.K.G. Watson. The $\tilde{A}$-$\tilde{X}$ band system of acetylene: Bands of the short-wavelength region. *Journal of Molecular Spectroscopy*, 119(1):137–143, 1986.

[171] Jean Vander Auwera, T.R. Huet, Michel Herman, Carl Hamilton, J.L. Kinsey, and R.W. Field. The $\tilde{\mathrm{A}}^1\mathrm{A}_u$ electronic state of monodeuterated acetylene. *Journal of Molecular Spectroscopy*, 137(2):381–395, 1989.

[172] P. Verkerk, M. Pinard, F. Biraben, and G. Grynberg. 1S-3S and 1S-3D Doppler-free two-photon transition in hydrogen and deuterium. *Optics Communications*, 72(3-4):202–204, 1989.

[173] James K.G. Watson. Calculated vibrational intensities in the $\tilde{\mathrm{A}}$-$\tilde{\mathrm{X}}$ electronic transition of acetylene. *Journal of Molecular Spectroscopy*, 207(2):276–284, 2001.

[174] J.K.G. Watson, M. Herman, J.C. Van Craen, and R. Colin. The $\tilde{\mathrm{A}}$-$\tilde{\mathrm{X}}$ band system of acetylene: Analysis of long-wavelength bands, and vibration-rotation constants for the levels $n\nu_4''$ $(n = 0-4)$, $n\nu_3'$ $(n = 0-3)$, and $\nu_2'+n\nu_3'$ $(n = 0-2)$. *Journal of Molecular Spectroscopy*, 95(1):101–132, 1982.

[175] Colin M. Western. *PGOPHER (version 7.1.301), a Program for Simulating Rotational Structure*, 2013. http://pgopher.chm.bris.ac.uk.

[176] Colin M. Western. PGOPHER: A program for simulating rotational, vibrational and electronic spectra. *Journal of Quantitative Spectroscopy and Radiative Transfer*, 186:221–242, 2017.

[177] W.L. Wiese and J.R. Fuhr. Accurate atomic transition probabilities for hydrogen, helium, and lithium. *Journal of Physical and Chemical Reference Data*, 38(3):565–720, 2009.

[178] E.B. Wilson, J.C. Decius, and P.C. Cross. *Molecular Vibrations: The Theory of Infrared and Raman Vibrational Spectra*. McGraw-Hill: New York, 1955.

[179] Alec M. Wodtke and Y. T. Lee. Photodissociation of acetylene at 193.3 nm. *The Journal of Physical Chemistry*, 89(22):4744–4751, 1985.

[180] Lin Xiao and Michael E. Kellman. Catastrophe map classification of the generalized normal-local transition in Fermi resonance spectra. *The Journal of Chemical Physics*, 93(8):5805–5820, 1990.

[181] D.Q. Xie, G.B. Ma, and Hua Guo. Quantum calculations of highly excited vibrational spectrum of sulfur dioxide. III. Emission spectra from the $\tilde{\mathrm{C}}^1\mathrm{B}_2$ state. *The Journal of Chemical Physics*, 111(17):7782–7788, 1999.

[182] Kaoru Yamanouchi, Misaki Okunishi, Yasuki Endo, and Soji Tsuchiya. Laser induced fluorescence spectroscopy of the $\tilde{\mathrm{C}}^1\mathrm{B}_2$-$\tilde{\mathrm{X}}^1\mathrm{A}_1$ band of jet-cooled SO_2: rotational and vibrational analyses in the 235-210 nm region. *Journal of Molecular Structure*, 352:541–559, 1995.